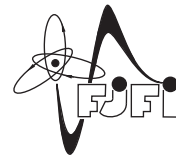Czech Technical University in Prague

Faculty of Nuclear Sciences and Physical Engineering

DOCTORAL THESIS

ULTRASOUND CHARACTERIZATION OF ELASTIC PROPERTIES AND INTERNAL FRICTION IN MATERIALS PREPARED BY PLASMA-BASED TECHNIQUES

Praha 2020   Martin Koller

Bibliographic entry

Author	Ing. Martin Koller Czech Technical University in Prague Faculty of Nuclear Sciences and Physical Engineering Department of Materials
Title of Dissertation	Ultrasound characterization of elastic properties and internal friction in materials prepared by plasma-based techniques
Degree Programme	Applications of Natural Sciences
Field of Study	Physical Engineering
Supervisor	doc. Ing. Hanuš Seiner, Ph.D. Institute of Thermomechanics Czech Academy of Sciences
Supervisor specialist	Ing. Radek Mušálek, Ph.D. Institute of Plasma Physics Czech Academy of Sciences
Academic Year	2019/2020
Number of Pages	160
Keywords	resonant ultrasound spectroscopy, ultrasound wave propagation, elastic properties, anisotropy, internal friction, spark plasma sintering, robocasting

Bibliografický záznam

Autor	Ing. Martin Koller České vysoké učení technické v Praze Fakulta jaderná a fyzikálně inženýrská Katedra materiálů
Název práce	Ultrazvuková charakterizace elastických vlastností a vnitřního tření v materiálech připravených plazmovými technologiemi
Studijní program	Aplikace přírodních věd
Studijní obor	Fyzikální inženýrství
Školitel	doc. Ing. Hanuš Seiner, Ph.D. Ústav termomechaniky AV ČR, v. v. i.
Školitel specialista	Ing. Radek Mušálek, Ph.D. Ústav fyziky plazmatu AV ČR, v. v. i.
Akademický rok	2019/2020
Počet stran	160
Klíčová slova	rezonanční ultrazvuková spektroskopie, šíření ultrazvukových vln, elastické vlastnosti, anizortropie, vnitřní tření, spark plasma sintering, robocasting

Abstract

The doctoral thesis deals with an ultrasound characterization of materials prepared by the spark plasma sintering (SPS) and robocasting techniques. Laser-based resonant ultrasound spectroscopy (RUS) is utilized for determining the elastic and viscoelastic properties of materials from resonant spectra of millimeter-sized samples. In addition, the RUS measurements are for some materials complemented by methods based on propagating ultrasonic waves. The first part of the thesis deals with bulk graphene nanoplatelets and ceramic-matrix composites reinforced by graphene-based fillers, where the preferred orientation of graphene nanoplatelets, perpendicular to the SPS axis, results in anisotropic elastic and acoustic properties. It is observed that with the increasing graphene content within the ceramic matrix, the anisotropy becomes more pronounced, and the elastic moduli gradually decrease. The second part of the thesis reports on the characterization of metal-matrix composites, namely CoNiAl/Ti ferromagnetic composites, and tungsten-based materials, and it shows how the laser-based RUS can be utilized for determining the elastic properties at the elevated temperatures (up to 740 °C). When the composites are well sintered, their macroscopic elastic properties follow the rule of mixtures, corresponding to the elasticity of particular phases, but a significant decrease in elastic moduli indicates an increased porosity and unsintered particles. In addition, the internal friction analysis for the tungsten-based materials proves that the activation energy of the anelastic processes caused by dislocation relaxation can also be reliably determined by the RUS method. The third part of the thesis studies the mechanical properties of robocast scaffolds, where the SPS is utilized for the consolidation of 3D printed ceramic green bodies. The periodic arrangement of ceramic rods within the robocast structure results in the elastic and acoustic anisotropy of several types of scaffolds. The RUS method is used to determine the elastic coefficients and to assess the bonding quality of the scaffolds, while the methods based on propagating waves are utilized for studying the frequency-dependent energy focusing along the rods; in both cases, the experimental results are complemented with numerical simulations elucidating the origin of the observed phenomena.

Anotace v češtině (Abstract in Czech)

Tato dizertační práce se zabývá ultrazvukovou charakterizací materiálů připravených metodami spark plasma sintering (SPS) a robocasting. Pomocí laserové rezonanční ultrazvukové spektroskopie (RUS) jsou z naměřených rezonančních spekter vzorků o velikostech v řádu milimetrů určeny elastické a viskoelastické vlastnosti materiálů. U některých materiálů jsou tato měření doplněna i o metody zkoumající šíření ultrazvukových vln. První část práce se věnuje studiu sintrovaných grafenových destiček a keramických kompozitů zesílených sekundární fází na bázi grafenu. Grafenové destičky jsou orientovány převážně kolmo na osu sintrování, což vede k anizotropním elastickým a akustickým vlastnostem, kde s rostoucím obsahem grafenových výztuh se anizotropie zesiluje a také klesají elastické moduly. Druhá část práce se věnuje charakterizaci kompozitů s kovovou matricí, jmenovitě feromagnetickým kompozitům CoNiAl/Ti a materiálům na bázi wolframu, kde jsou ukázány možnosti využití laserové rezonanční ultrazvukové spektroskopie pro určování elastických vlastností materiálů do vysokých teplot až 740 °C. Pokud jsou kompozity dobře sintrovány, jejich makroskopické elastické vlastnosti odpovídají elasticitě jednotlivých fází, avšak výrazné snížení elastických modulů naznačuje zvýšenou porozitu nebo nedokonale sintrovaná zrna. Analýza vnitřního tření v materiálech na bázi wolframu kromě toho ukazuje, že je možno laserovou rezonanční ultrazvukovou spektroskopií určovat aktivační energii relaxačních procesů, které jsou způsobené pohybem dislokací za vysokých teplot. Třetí část práce se zabývá mechanickými vlastnostmi periodických keramických struktur, připravených metodou robocasting a sintrovaných pomocí SPS. Tyto struktury se skládají z vrstevnatého uspořádání keramických vláken, což vede k elastické a akustické anizotropii některých struktur. Metoda RUS je využita k určení elastických koeficientů a také k potvrzení vysoké kvality sintrovaných struktur a dále je experimentálně zkoumáno, jak je energie šířících se vln s různou frekvencí fokusována podél směrů keramických vláken. Experimentální výsledky získané těmito metodami jsou také porovnány s numerickými simulacemi.

Acknowledgment

Declaration of co-authorship

I confirm that the declaration made by the PhD candidate in the section 1.3 *The extent of the candidate's contribution to the published papers* reflects his contribution to the individual co-authored publications.

Hanuš Seiner [1,2]

on behalf of the co-authors:
Michal Landa [2]
Petr Sedlák [2]
Alena Kruisová [2]
Tomáš Grabec [1]

Radek Mušálek [3]
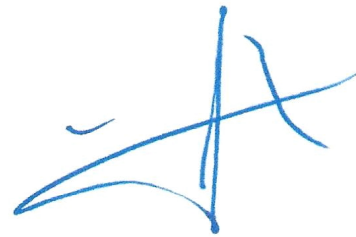
on behalf of the co-authors:
Tomáš Chráska [3]
Jakub Cinert [3]
Jiří Matějíček [3]

Arvind Agarwal [4]

on behalf of the co-authors:
Andy Nieto [4]

Manuel Belmonte [5]

on behalf of the co-authors:
Cristina Ramirez [5]
Pilar Miranzo [5]
María Isabel Osendi [5]
Benito Román-Manso [5,6]
Juan José Moyano [5]
Jesús González-Julián [7]

[1] Faculty of Nuclear Sciences and Physical Engineering, Czech Technical University in Prague

[2] Institute of Thermomechanics, Czech Academy of Sciences

[3] Institute of Plasma Physics, Czech Academy of Sciences
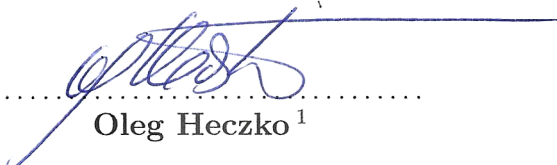
[4] Department of Mechanical and Materials Engineering, Florida International University

[5] Institute of Ceramics and Glass (ICV-CSIC)

[6] School of Engineering and Applied Sciences, Harvard University

[7] Institute of Energy and Climate Research, Forschungszentrum Jülich GmbH
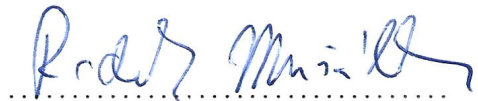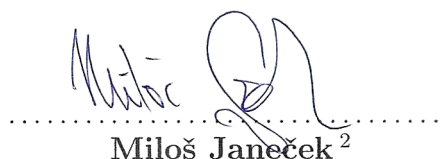
(1/2)

I confirm that the declaration made by the PhD candidate in the section 1.3 *The extent of the candidate's contribution to the published papers* reflects his contribution to the individual co-authored publications.

....
Oleg Heczko[1]

on behalf of the co-authors:
Jaromír Kopeček[1]
Michal Rameš[1]

....
Miloš Janeček[2]

on behalf of the co-authors:
Josef Strácký[2]

....
Monika Vilémová[3]

on behalf of the co-authors:
František Lukáč[2,3]
Přemysl Beran[4,5]
Jakub Čížek[2]
Hynek Hadraba[6]
Jiří Matějíček[3]
Jakub Veverka[3,7]

---

[1] Institute of Physics, Czech Academy of Sciences
[2] Faculty of Mathematics and Physics, Charles University in Prague
[3] Institute of Plasma Physics, Czech Academy of Sciences
[4] Nuclear Physics Institute, Czech Academy of Sciences
[5] European Spallation Source ERIC
[6] Institute of Physics of Materials, Czech Academy of Sciences
[7] Faculty of Nuclear Sciences and Physical Engineering, Czech Technical University in Prague

Table of contents

Symbols and abbreviations

Symbol	Unit	
A	1	anisotropy factor
A_0	1	temperature-independent constant
a_{ij}	1	transformation indices
c_{ij}	Pa	elastic coefficients (2-indices matrix)
C_{ijkl}	Pa	elastic coefficients (4-indices tensor)
d_i	m	dimensions of sample
E	Pa	Young's modulus
E_k	J·m^{-3}	density of kinetic energy
E_p	J·m^{-3}	density of potential energy
f	Hz	frequency
f_v	1	volume fraction
G	Pa	shear modulus
$\mathbf{I}$	-	unit matrix
k	J·K^{-1}, eV·K^{-1}	Boltzmann constant
K	Pa	bulk modulus
l	m	distance, length
L	J	Lagrangian energy
M	Pa	elastic modulus
n_i	1	normal vector
N	1	degree of the polynomial approximation
P_n	1	Legendre polynomials
Q	1	quality factor of resonances
Q^{-1}	1	internal friction
R	J·K^{-1}·mol^{-1}	molar gas constant
s_i	s·m^{-1}	slowness
S	m^2	surface area
S_{ijkl}	Pa^{-1}	stiffness tensor
t	s, min, h	time
$\tan\phi$	1	loss tangent
T	K, °C	temperature
T_i	Pa	traction
U	J, eV, J·mol^{-1}	activation energy
u_i, U_i	m	displacement
v	m·s^{-1}	phase velocity
v_L	m·s^{-1}	longitudinal wave velocity
v_T	m·s^{-1}	transverse wave velocity
v^g	m·s^{-1}	group velocity
V	m^3	volume
W	J	elastic energy
x_i	m	coordinates

Symbol	Unit	
α	m^{-1}	attenuation coefficient
α_{ijkl}	m	Ritz expansion coefficients for displacement
Γ_{ik}	m$^2 \cdot$s^{-2}	Christoffel matrix
$\boldsymbol{\Gamma}$	s^{-2}	forward procedure matrix
δ_{ij}	1	Kronecker delta
ε_{ij}	1	strain tensor
λ	m	wavelength
Λ	J$\cdot$m^{-3}	density of time-averaged Lagrangian energy
Ψ	1	specific damping capacity
Ψ_{jkl}	1	functional basis
ϕ	1	loss angle
ν	1	Poisson's ratio
ρ	kg$\cdot$m^{-3}	mass density
σ_{ij}	Pa	stress tensor
ω	s^{-1}	angular frequency

Abbreviations:

AM	additive manufacturing
BCC	body-centered cubic
CAD	computer-aided design
CMC	ceramic matrix composite
DBT	ductile-to-brittle transition
DBTT	ductile-to-brittle transition temperature
EDS	energy dispersive X-ray spectroscopy
EMAR	electromagnetic acoustic resonance
FCC	face-centered cubic
FEM	finite element method
FFT	fast Fourier transform
GNPs	graphene nanoplatelets
FAST	field-assisted sintering technique
MAX	M$_{n+1}$AX$_n$ compound
qL	quasi-longitudinal
qT	quasi-transverse
rGO	reduced graphite oxide
RPR	rectangular parallelepiped resonance
RUS	resonant ultrasound spectroscopy
SEM	scanning electron microscopy
SPS	spark plasma sintering
XRD	X-ray diffraction

Chapter 1

Introduction

As many newly-developed materials are only available in limited quantities, there is a need for experimental methods capable of detecting the material properties in small amounts or without damaging the measured specimens. This brings opportunity for ultrasonic methods, which are able to determine elastic and anelastic properties entirely from the attributes of ultrasonic waves traveling through materials or from resonant characteristics of small specimens.

This thesis deals with the ultrasound characterization of materials prepared by plasma-based techniques, namely the spark plasma sintering (SPS) technique [1–7], with the main focus on the contactless laser resonant ultrasound spectroscopy (RUS) method [8–13]. The main advantage of this method lies in the fact that all the elastic coefficients of a measured sample can be obtained from its single resonant spectrum, where the applied strains are much lower than the elastic limit of the studied material. Besides that, viscoelastic behavior of the material is also reflected in the resonant spectrum, where internal friction is directly proportional to the widths of the resonant peaks. Moreover, as the laser-based RUS experimental setup is fully contactless due to the utilization of lasers for both generating and detecting the elastic vibrations, the measured sample can be put into a low-pressure nitrogen chamber, where its resonant spectrum can be detected at a wide range of temperatures. This is mostly beneficial for studying temperature-dependent phenomena that are reflected in the temperature evolution of the resonant frequencies or the widths of resonant peaks, such as phase transitions or anelastic relaxation.

All the materials studied in this thesis were produced by utilizing the SPS method, which employs pulsing direct electric current for rapid consolidation of powder compacts. The conventional sintering of powders is performed at very high temperatures for long holding times, which often leads to the deterioration of the mechanical properties of sintered materials. On the other hand, the SPS technique allows the powder consolidation in much shorter times due to rapid heating rates in several hundreds of °C/min, resulting from the Joule effect of the pulsing currents passing through the SPS punches, die, and powders [1].

The thesis is structured as a compilation of eight research papers, which are grouped into three logical sections, complemented with interconnecting comments by the PhD candidate. The first section, numbered 3.1, deals with the anisotropic elastic properties of materials based on graphene sheets (bulk graphene nanoplatelets and silicon nitride/graphene fillers composites). The second section 3.2 describes the elastic properties of three types of metal-matrix composites (CoNiAl/Ti ferromagnetic composites, tungsten/steel composites, and

mechanically alloyed tungsten), including their characterization up to the high-temperature limit (740 °C) of the laser-based RUS apparatus. The third section 3.3 focuses on the mechanical properties of micro-architectured periodic scaffolds, produced by the robocasting method and consolidated by pressureless SPS.

The thesis itself is divided into several chapters. After the introduction in this Chapter 1, theoretical background and experimental methods are summarized in Chapter 2. The first section 2.1 of this chapter reviews the theory of elastic and anelastic properties of solid materials. The following section 2.2 summarizes the principles of the RUS method, including the historical development from the pioneering works in the 1960s up to fully-contactless laser-based RUS, utilized at the Institute of Thermomechanics of the Czech Academy of Sciences. The next section 2.3 shows the general principles of the SPS method in subsection 2.3.1 and the robocasting technique in subsection 2.3.2, where the SPS is utilized for the consolidation of 3D printed ceramic green bodies. Chapter 3 comprises eight research papers, complemented with the comments by the PhD candidate. The papers are grouped into three sections 3.1–3.3. The final Chapter 4 brings the conclusions of the presented thesis.

1.1   Aims of the thesis

The main aim of this thesis was to perform a characterization of newly-produced materials, consolidated by spark plasma sintering technique, by means of ultrasonic methods. Particular topics of the thesis include

- determination of anisotropy in the elastic properties of ceramic-matrix and metal-matrix composites by laser-based RUS,

- detection of temperature-activated processes from temperature evolution of elastic coefficients and internal friction up to the high-temperature limit of the RUS apparatus,

- characterization of acoustic and elastic properties of periodic robocast scaffold depending on their geometry.

1.2 List of the PhD candidate's publications included in this thesis

- **Paper A** (included on page 53):

  Martin Koller, Hanuš Seiner, Michal Landa, Andy Nieto, and Arwind Agarwal: Anisotropic Elastic and Acoustic Properties of Bulk Graphene Nanoplatelets Consolidated by Spark Plasma Sintering. *Acta Physica Polonica A* **128** (4) (2015) 670–674. `doi:10.12693/APhysPolA.128.670`

  Abstract: Elastic anisotropy and acoustic attenuation in bulk material consisting of consolidated graphene nanoplatelets are studied. The material was prepared by spark plasma sintering, and exhibits highly anisotropic microstructure with the graphene nanoplatelets oriented perpendicular to the spark plasma sintering compression axis. The complete tensor of elastic constants is obtained using a combination of two ultrasonic methods: the through-transmission method and the resonant ultrasound spectroscopy. It is shown that the examined material exhibits very strong anisotropy both in the elasticity (the Young moduli in directions parallel to the graphene nanoplatelets and perpendicular to them differ by more than 20 times) and in the attenuation, where the dissipative effect of the internal friction in the graphene nanoplatelets combines with strong scattering losses due to the porosity. The results are compared with those obtained for ceramic-matrix/graphene nanoplatelet composites by the same ultra-sonic methods.

- **Paper B** (included on page 59):

  Hanuš Seiner, Cristina Ramirez, **Martin Koller**, Petr Sedlák, Michal Landa, Pilar Miranzo, Manuel Belmonte, and Maria Isabel Osendi: Elastic properties of silicon nitride ceramics reinforced with graphene nanofillers. *Materials and Design* **87** (2015) 675–680. `doi:10.1016/j.matdes.2015.08.044`

  Abstract: Elastic constants of silicon nitride composites with variable content (3–18 wt.%) of two kinds of graphene fillers (nanoplatelets and reduced graphene oxide sheets) are determined using resonant ultrasound spectroscopy. The corresponding Young's modulus (E), shear modulus (G) and Poisson's ratio (ν) are calculated for each material. Composites show a noticeable anisotropy that grows stronger with the graphene filler content, owing to the preferential alignment of the graphene layers and to their own anisotropy as well. E and G monotonically decrease with the filler concentration for both types of fillers, showing a maximum decrease in E of 75% along the direction perpendicular to the graphene plane for the composite with the highest filler content (Si_3N_4–18 wt.% GNP) and a reduction in G of 63 % for shear along the graphene plane for the same composite. Influence on the fracture pattern of the composites is also addressed.

- **Paper C** (included on page 71):

Martin Koller, Tomáš Chráska, Jakub Cinert, Oleg Heczko, Jaromír Kopeček, Michal Landa, Radek Mušálek, Michal Rameš, Hanuš Seiner, Josef Stráský, and Miloš Janeček: Mechanical and magnetic properties of semi-Heusler/light-metal composites consolidated by spark plasma sintering. *Materials and Design* **126** (2017) 351–357. `doi:10.1016/j.matdes.2017.04.028`

Abstract: Light-weight ferromagnetic Co-Ni-Al:Ti composites were consolidated by spark plasma sintering. Powders of ball-milled Co-Ni-Al and gas atomized α-Ti were mixed together in three different ratios and spark plasma sintered at 950°C, using two sintering times, i.e. dwell times at the maximal temperatures: 1 and 5 min. The composites were successfully compacted and new intermetallic phases were formed at the Co-Ni-Al/Ti interfaces. The composites exhibit favourable flexural strength, excellent high-temperature stability, and relatively high saturation magnetization. On the other hand, the newly emerged intermetallic phases are non-ferromagnetic, which slightly deteriorates the magnetic properties.

- **Paper D** (included on page 79):

Martin Koller, Alena Kruisová, Radek Mušálek, Jiří Matějíček, Hanuš Seiner, and Michal Landa: On the relation between microstructure and elastic constants of tungsten/steel composites fabricated by spark plasma sintering. *Fusion Engineering and Design* **133** (2018) 51–58. `doi:10.1016/j.fusengdes.2018.05.056`

Abstract: Tungsten/steel composites might play an important role in plasma-facing components, especially in joining of tungsten armor to structural parts made of steel. In this work, Young's moduli and shear moduli of a set of tungsten/P91 steel composites fabricated by spark plasma sintering were determined by resonant ultrasound spectroscopy. It was observed that the sintering temperature and the volume fractions of the individual phases have strong effects on the macroscopic elastic constants. The results were interpreted by means of a finite elements numerical model, showing that the regions of imperfectly bonded tungsten particles appearing in the microstructure of some of the composites act effectively as inclusions with very low elastic stiffness. A good correlation between the number of these regions in the microstructure and the elastic constants was observed.

- **Paper E** (included on page 89):

  Martin Koller, Monika Vilémová, František Lukáč, Přemysl Beran, Jakub Čížek, Hynek Hadraba, Jiří Matějíček, Jakub Veverka, and Hanuš Seiner: An ultrasonic study of relaxation processes in pure and mechanically alloyed tungsten. *International Journal of Refractory Metals & Hard Materials* **90** (2020) 105233. `doi:10.1016/j.ijrmhm.2020.105233`

  Abstract: High-temperature internal friction in a pure tungsten single crystal, polycrystals with different grain sizes, and mechanically alloyed tungsten polycrystals was studied. Positron annihilation spectroscopy was used to prove that all studied materials contain a detectable amount of dislocations. Then, resonant ultrasound spectroscopy was applied to determine the internal friction evolution with temperature from room temperature up to 740 °C. For the pure tungsten samples, a sharp increase of internal friction was observed for temperatures above 470 °C (for the single crystal) or above 400 °C (for the polycrystals); the activation energy corresponding to this increase was the same as the activation energy for the ductile-to-brittle transition in tungsten reported in the literature. For the alloyed materials, direct observation of the onset of this relaxation mechanism was impossible due to additional effects resulting from the secondary phases in the material.

- **Paper F** (included on page 107):

  Martin Koller, Alena Kruisová, Hanuš Seiner, Petr Sedlák, Benito Román-Manso, Pilar Miranzo, Manuel Belmonte, and Michal Landa: Anisotropic elasticity of ceramic micro-scaffolds fabricated by robocasting. *Acta Physica Polonica A* **134** (2018) 799–803. `doi:10.12693/APhysPolA.134.799`

  Abstract: Anisotropic elastic and acoustic properties of robocast ceramic scaffolds are calculated by finite element method, utilizing real geometries and material parameters obtained from robocast silicon carbide samples. Six types of robocast geometries are studied, showing different material symmetries given by the arrangement of the ceramic rods in the scaffold structures. Due to the macroscopic periodicity of the structures composed of fully sintered ceramic rods, the robocast scaffolds exhibit metamaterial-like elastic and acoustic properties, never observed for natural materials. The effect of the micro-architecture is shown to be crucial: while for tetragonal and orthorhombic structures, strong acoustic focusing along the directions of the rods appears even in the low-frequency limit, hexagonal structures exhibit no energy focusing up to some frequency limit given by the geometry.

- **Paper G** (included on page 113):

Tomáš Grabec, **Martin Koller**, Petr Sedlák, Alena Kruisová, Benito Román-Manso, Manuel Belmonte, Pilar Miranzo, and Hanuš Seiner: Frequency-dependent acoustic energy focusing in hexagonal ceramic micro-scaffolds. *Wave Motion* **92** (2020) 102417. `doi:10.1016/j.wavemoti.2019.102417`

Abstract: Acoustic properties of an additive-manufactured SiC scaffold with hexagonal symmetry fabricated by the robocasting method are studied both numerically and experimentally. The numerical analysis is based on the finite element method (FEM) using Bloch boundary conditions. The calculations show both angular and frequency dispersion of the acoustic waves with wavelengths comparable to the spacing between the rods, i.e., on a millimeter scale, indicating interesting acoustic properties in the MHz range. The dispersion character leads to focusing of the energy propagation into the directions of the rods of the hexagonal structure. This is illustrated by modal-based calculations of the propagation of longitudinal and out-of-plane shear wave packets with a dominant wavelength. The experimental analysis consists of two steps, the measurement of the resonant spectrum and shear wave propagation character. The measured resonant spectrum is in good agreement with the one calculated using numerically obtained low-frequency properties of the structure, also showing the quality of the overall manufactured structure. The time-domain measurement shows significant changes in the energy propagation between low and high frequencies, as predicted by FEM calculations.

- **Paper H** (included on page 127):

Manuel Belmonte, **Martin Koller**, Juan José Moyano, Hanuš Seiner, Pilar Miranzo, María Isabel Osendi, and Jesús González-Julián: Multifunctional 3D-Printed Cellular MAX-Phase Architectures. *Advanced Materials Technologies* (2019) 1900375. `doi:10.1002/admt.201900375`

Abstract: The development of porous MAX-phase structures from computer-aided design models and 3D printing strategies is of great interest for the fabricating of cellular parts with geometric and material complexities for advanced technological applications. This is reinforced by the joining of the outstanding properties of MAX phases with the benefits of creating lighter materials with a higher surface area. Here, the additive manufacturing of 3D cellular Cr_2AlC MAX-phase architectures using a direct ink writing technique from concentrated MAX aqueous-based inks is presented. These architectures exhibit multifunctional properties; in particular, high strength and good mechanical cycling behavior, excellent electrical conductivity, tailored heat dissipation, and good thermal cycling resistance, a blend that widens the potential engineering applications of these MAX phases through an innovative approach.

1.3 The extent of the candidate's contribution to the published papers

- **Paper A** (*Anisotropic elastic and acoustic properties of bulk graphene nanoplatelets consolidated by spark plasma sintering*):

  The candidate measured the time-amplitude signals of the longitudinal and transverse waves propagating through the samples cut from the sintered pellet and determined the velocities and the attenuation coefficients. Moreover, the candidate performed the RUS measurements, evaluated the polar distribution of Young's modulus, and wrote the paragraphs describing these measurements.

  Co-authors from the Institute of Thermomechanics (H. Seiner and M. Landa) came up with the concept of the paper and supervised the work. Co-authors from the Florida International University (A. Nieto and A. Agarwal) consolidated the SPS pellet and performed its complementary characterization, including the scanning electron micrograph.

- **Paper B** (*Elastic properties of silicon nitride ceramics reinforced with graphene nanofillers*):

  The candidate measured the velocities of longitudinal waves, determined the elastic coefficients from the laser-based RUS measurements, and evaluated the distributions of Young's modulus and Poisson's ratio.

  Co-authors from the Institute of Thermomechanics (H. Seiner, P. Sedlák, M. Landa) came up with the concept of the paper and were responsible for the discussion of the obtained results. Co-authors from the Institute of Ceramics and Glass (C. Ramirez, P. Miranzo, M. Belmonte, and M. I. Osendi) prepared the graphene/ceramic mixture, consolidated and characterized the composites, including the micrographs of the fracture surfaces and the Vickers indents, and coordinated and supervised the work on the paper.

- **Paper C** (*Mechanical and magnetic properties of semi-Heusler/light-metal composites consolidated by spark plasma sintering*):

  The candidate measured the density, elastic coefficients and internal friction temperature evolutions, and was responsible for the submission process of the paper.

  Co-authors from the Institute of Plasma Physics (T. Chráska, J. Cinert, R. Mušálek) consolidated the composites by the SPS method, made the scanning electron micrographs, and measured the flexural strength. Co-authors from the Institute of Physics (O. Heczko, J. Kopeček, M. Rameš) performed the magnetization measurements and the EDS analysis. Co-authors from the Institute of Thermomechanics (M. Landa, H. Seiner) were responsible for discussing the relation between the microstructure and the mechanical properties of the composites. Co-authors from the Faculty of Mathematics and Physics (J. Stráský, M. Janeček) came up with the original concept of the paper and supervised the work on the paper.

- **Paper D** (*On the relation between microstructure and elastic constants of tungsten/steel composites fabricated by spark plasma sintering*):

  The candidate measured the density and the elastic coefficients, co-wrote the manuscript and coordinated the work on the paper.

  Co-authors from the Institute of Thermomechanics (A. Kruisová, H. Seiner, M. Landa) were responsible for the discussion based on FEM modelling. Co-authors from the Institute of Plasma Physics (R. Mušálek, J. Matějíček) consolidated the composites, performed the XRD analysis, and provided the scanning electron micrographs.

- **Paper E** (*An ultrasonic study of relaxation processes in pure and mechanically alloyed tungsten*):

  The candidate performed the RUS measurements, plotted the temperature evolutions of Young's modulus and internal friction, co-wrote the manuscript and coordinated the work on the paper.

  Co-authors from the Institute of Plasma Physics (M. Vilémová, F. Lukáč, J. Matějíček, J. Veverka) prepared the powders by the mechanical alloying, consolidated the materials by the SPS, determined their densities and porosities, and provided the micrographs of the structures. P. Beran was responsible for the neutron powder diffraction measurements. J. Čížek examined the composites by the positron annihilation spectroscopy. H. Hadraba contributed to the analysis of the mechanical test results. H. Seiner contributed to the discussion of the results and supervised the work on the paper.

- **Paper F** (*Anisotropic elasticity of ceramic micro-scaffolds fabricated by robocasting*):

  The candidate calculated and plotted the distributions of phase and group velocities, drew the sketches in Fig. 1, and wrote the paper.

  Co-authors from the Institute of Thermomechanics (A. Kruisová, H. Seiner, P. Sedlák, M. Landa) determined the geometrical parameters of the sintered scaffolds, designed the FEM computational unit cells for each of the studied scaffolds, calculated their elastic coefficients by the FEM method, and supervised the work on the paper. Co-authors from the Institute of Ceramics and Glass (B. Román-Manso, P. Miranzo, M. Belmonte) fabricated and provided the SiC scaffolds.

- **Paper G** (*Frequency-dependent acoustic energy focusing in hexagonal ceramic micro-scaffolds*):

    The candidate measured the RUS spectra and the propagating time-domain signals, co-wrote the manuscript and coordinated the work on the paper.

    T. Grabec performed the modal-based study of the time-domain propagation properties and co-worked on the analysis of the time-domain experimental signals and manuscript preparations. Co-authors from the Institute of Thermomechanics (P. Sedlák, A. Kruisová, H. Seiner) performed the FEM calculations, designed the principles of the modal-based study, and supervised the work on the paper. Co-authors from the Institute of Ceramics and Glass (B. Román-Manso, M. Belmonte, P. Miranzo) fabricated and provided the SiC hexagonal scaffold.

- **Paper H** (*Multifunctional 3D-Printed Cellular MAX-Phase Architectures*):

    The candidate developed the printable ink based on Cr_2AlC ceramic powder and printed green bodies of the scaffolds during his internship at the Institute of Ceramics and Glass.

    Co-authors from the Institute of Ceramics and Glass (M. Belmonte, J. J. Moyano, P. Miranzo, M. I. Osendi) consolidated the scaffolds by SPS and performed their analysis (including differential thermal analysis, scanning electron micrographs, compression tests, electrical and thermal conductivity measurements). H. Seiner organized the internship and supervised the work on the paper. J. González-Julián produced and provided the Cr_2AlC powder.

Chapter 2

Theoretical background and experimental methods

2.1 Elastic and anelastic properties of solids

This section describes the fundamental attributes of elastic, acoustic, and anelastic properties of solid bodies. The first section 2.1.1 gives an introduction to linear elasticity theory [14–16] with the focus on crystallographic symmetry and its influence on the elastic coefficients. The following section 2.1.2 describes the principles of the acoustic waves propagation [15–21] and its relation to the elastic properties of the materials. Section 2.1.3 then deals with relaxation processes in materials [20–24] and discusses some phenomena responsible for internal friction and attenuation of propagating acoustic waves.

2.1.1 Linear elasticity theory

In the continuous elastic media, the deformation in an arbitrary point can be described by a **displacement vector**

$$u_i = x_i' - x_i \,, \tag{2.1}$$

where x_i' are the coordinates of the given point after the deformation when compared to the coordinates x_i before the deformation. After the deformation, the distance $\mathrm{d}l'$ between two points infinitesimally close to each other is[1]

$$\mathrm{d}l' = \mathrm{d}l + \left(\frac{\partial u_i}{\partial x_j} + \frac{\partial u_j}{\partial x_i} + \frac{\partial u_k}{\partial x_i} \frac{\partial u_k}{\partial x_j} \right) \mathrm{d}x_i \, \mathrm{d}x_j \,. \tag{2.2}$$

For small deformations, i. e. when the change of any distance is much smaller than the distance itself, the term $\dfrac{\partial u_k}{\partial x_i} \dfrac{\partial u_k}{\partial x_j}$ can be neglected, as $\dfrac{\partial u_i}{\partial x_j} \ll 1$. The equation (2.2) is then

$$\mathrm{d}l' = \mathrm{d}l + 2\,\varepsilon_{ij}\,\mathrm{d}x_i\,\mathrm{d}x_j \,, \tag{2.3}$$

$$\varepsilon_{ij} = \frac{1}{2} \left(\frac{\partial u_i}{\partial x_j} + \frac{\partial u_j}{\partial x_i} \right) , \tag{2.4}$$

where ε_{ij} is a **strain tensor**. By its definition (2.4), the strain tensor is symmetric ($\varepsilon_{ij} = \varepsilon_{ji}$), and thus the maximum number of independent components ε_{ij} is 6. The diagonal components

---

[1]Einstein summation convention is used throughout this thesis: when the same index appears in two factors in a multiplication equation, a summation of the term is implied, e. g. $a_i x_i = \sum_{i=1}^{3} a_i x_i$.

ε_{11}, ε_{22}, ε_{33} represent the relative longitudinal extensions along the respective axes x_1, x_2, x_3, and their sum $\varepsilon_{ii} = \varepsilon_{11} + \varepsilon_{22} + \varepsilon_{33}$ is equal to the volume dilatation of the elastic body. The components ε_{12}, ε_{13}, ε_{23} represent shear deformations; for example, the ε_{12} component is equal to one half of the change in the angle between the originally perpendicular axes x_1 and x_2.

Internal stresses in the continuous media can be described by a **stress tensor** σ_{ij}, which is defined such that the traction vector **T** on an arbitrary surface with normal vector **n** is

$$T_j = \sigma_{ij}\, n_i\,. \tag{2.5}$$

Stress tensor σ_{ij} is also symmetric due to the conservation of the overall momentum in an arbitrary volume element. In analogy to the strain tensor, the components σ_{11}, σ_{22}, σ_{33} represent the normal stresses to the respective surfaces, while σ_{12}, σ_{13}, σ_{23} represent the shear stresses.

In linearly elastic solids, the stress components σ_{ij} are linearly dependent on the combination of the strain components ε_{kl}, which can be expressed by a generalized **Hooke's law**

$$\sigma_{ij} = C_{ijkl}\, \varepsilon_{kl}\,, \tag{2.6}$$

where C_{ijkl} is the **tensor of elastic coefficients** of the material. The elastic coefficients C_{ijkl} generally acquire 81 combinations, but as both the stress tensor σ_{ij} and the strain tensor ε_{kl} are symmetric ($\sigma_{ij} = \sigma_{ji}$, $\varepsilon_{kl} = \varepsilon_{lk}$), and the potential energy is quadratic in the strains, the number of independent elastic coefficients is reduced to 21.

From the full set of the elastic coefficients, Young's and shear moduli distributions can be obtained. **Young's modulus** E_1 in the direction of the x_1 axis is given [25] as

$$E_1 = \frac{1}{S_{1111}}\,, \tag{2.7}$$

and the **shear modulus** G_{23} in the plane perpendicular to the x_1 axis [26] is

$$G_{23} = \frac{1}{4 S_{2323}}\,, \tag{2.8}$$

where the **stiffness/compliance tensor** S_{ijkl} is inverse to the C_{ijkl} tensor

$$\varepsilon_{ij} = S_{ijkl}\, \sigma_{kl}\,. \tag{2.9}$$

Moreover, Young's modulus can be determined in any arbitrary direction x_i

$$E(x_i) = \frac{1}{S'_{1111}(x'_1 = x_i)}\,, \tag{2.10}$$

when the tensor S_{ijkl} is transformed to S'_{ijkl} such that the chosen direction x_i is parallel to the transformed coordinate axis of x'_1. The transformed tensor is obtained by the equation

$$S'_{ijkl} = a_{im}\, a_{jn}\, a_{kp}\, a_{lq}\, S_{mnpq}\,, \tag{2.11}$$

where

$$a_{im} = \cos(x'_i, x_m) \tag{2.12}$$

are the cosines of the angles between the transformed coordinates x'_i and the original coordinates x_m. The shear modulus in the plane perpendicular to x_i is then

$$G(x_i) = \frac{1}{4 \, S'_{2323}(x'_1 = x_i)} . \tag{2.13}$$

For simplicity, the elastic coefficients are usually written in Voigt notation with two indices as c_{ij}. Hooke's law is then written in the following form

$$
\begin{pmatrix}
\sigma_{11} \\
\sigma_{22} \\
\sigma_{33} \\
\sigma_{23} \\
\sigma_{13} \\
\sigma_{12}
\end{pmatrix}
=
\begin{pmatrix}
c_{11} & c_{12} & c_{13} & c_{14} & c_{15} & c_{16} \\
c_{21} & c_{22} & c_{23} & c_{24} & c_{25} & c_{26} \\
c_{31} & c_{32} & c_{33} & c_{34} & c_{35} & c_{36} \\
c_{41} & c_{42} & c_{43} & c_{44} & c_{45} & c_{46} \\
c_{51} & c_{52} & c_{53} & c_{54} & c_{55} & c_{56} \\
c_{61} & c_{62} & c_{63} & c_{64} & c_{65} & c_{66}
\end{pmatrix}
\begin{pmatrix}
\varepsilon_{11} \\
\varepsilon_{22} \\
\varepsilon_{33} \\
2\,\varepsilon_{23} \\
2\,\varepsilon_{13} \\
2\,\varepsilon_{12}
\end{pmatrix} . \tag{2.14}
$$

The coefficients c_{ij} are here unambiguously associated with the coefficients C_{ijkl}; if assuming index transformation $C_{ijkl} \leftrightarrow c_{\alpha\beta}$, then $\alpha = i$ if $i = j$, and $\alpha = 9 - (i+j)$ if $i \neq j$, and similarly $\beta = k$ if $k = l$, and $\beta = 9 - (k+l)$ if $k \neq l$. Therefore, the indices are reduced by the rule: $11 \rightarrow 1$; $22 \rightarrow 2$; $33 \rightarrow 3$; 23 or $32 \rightarrow 4$; 13 or $31 \rightarrow 5$; 12 or $21 \rightarrow 6$.

The number of independent elastic coefficients depends on the material symmetry [27]. A general *triclinic* solid has 21 independent elastic coefficients, and the number of independent elastic coefficients decreases with an increasing symmetry.

In *monoclinic* materials, two angles between the principal axes are equal to 90°, and thus, the number of independent elastic coefficients is lowered to 13.

In *orthorhombic* materials, all principal axes are mutually perpendicular, which results in 9 independent elastic coefficients

$$
c_{ij} \, (\text{orthorhombic}) =
\begin{pmatrix}
c_{11} & c_{12} & c_{13} & 0 & 0 & 0 \\
c_{12} & c_{22} & c_{23} & 0 & 0 & 0 \\
c_{13} & c_{23} & c_{33} & 0 & 0 & 0 \\
0 & 0 & 0 & c_{44} & 0 & 0 \\
0 & 0 & 0 & 0 & c_{55} & 0 \\
0 & 0 & 0 & 0 & 0 & c_{66}
\end{pmatrix} . \tag{2.15}
$$

In *tetragonal* materials, two axes are equivalent, which leads to $c_{11} = c_{22}$, $c_{13} = c_{23}$, $c_{44} = c_{55}$ (when the equivalent axes are x_1 and x_2). This results in 6 independent elastic coefficients

$$c_{ij} \, (\text{tetragonal}) = \begin{pmatrix} c_{11} & c_{12} & c_{13} & 0 & 0 & 0 \\ c_{12} & c_{11} & c_{13} & 0 & 0 & 0 \\ c_{13} & c_{13} & c_{33} & 0 & 0 & 0 \\ 0 & 0 & 0 & c_{44} & 0 & 0 \\ 0 & 0 & 0 & 0 & c_{44} & 0 \\ 0 & 0 & 0 & 0 & 0 & c_{66} \end{pmatrix}. \tag{2.16}$$

Hexagonal materials have 5 independent coefficients

$$c_{ij} \, (\text{hexagonal}) = \begin{pmatrix} c_{11} & c_{12} & c_{13} & 0 & 0 & 0 \\ c_{12} & c_{11} & c_{13} & 0 & 0 & 0 \\ c_{13} & c_{13} & c_{33} & 0 & 0 & 0 \\ 0 & 0 & 0 & c_{44} & 0 & 0 \\ 0 & 0 & 0 & 0 & c_{44} & 0 \\ 0 & 0 & 0 & 0 & 0 & \frac{1}{2}(c_{11} - c_{12}) \end{pmatrix}. \tag{2.17}$$

In the hexagonal symmetry, all directions within the $x_1 x_2$ plane are equivalent, and thus, the **transverse isotropic** materials also have this kind of symmetry [25]. Then, the Young's moduli in all directions in the isotropic plane $x_1 x_2$ are

$$E_1 = E_2 = \frac{(c_{11} - c_{12})((c_{11} + c_{12}) \, c_{33} - 2 \, c_{13}^2)}{c_{11} \, c_{33} - c_{13}^2}, \tag{2.18}$$

and Young's modulus E_3 in the direction of the anisotropic axis x_3 is

$$E_3 = c_{33} - \frac{2 \, c_{13}^2}{c_{11} + c_{12}}. \tag{2.19}$$

The shear moduli in the principal directions are simply

$$G_{23} = G_{13} = c_{44}, \tag{2.20}$$

$$G_{12} = c_{66} = \frac{1}{2}(c_{11} - c_{12}). \tag{2.21}$$

In **cubic** materials, all three principal directions are equivalent, which decreases the number of independent elastic coefficients to 3

$$c_{ij} \, (\text{cubic}) = \begin{pmatrix} c_{11} & c_{12} & c_{12} & 0 & 0 & 0 \\ c_{12} & c_{11} & c_{12} & 0 & 0 & 0 \\ c_{12} & c_{12} & c_{11} & 0 & 0 & 0 \\ 0 & 0 & 0 & c_{44} & 0 & 0 \\ 0 & 0 & 0 & 0 & c_{44} & 0 \\ 0 & 0 & 0 & 0 & 0 & c_{44} \end{pmatrix}. \tag{2.22}$$

The **anisotropy factor** A is defined for the cubic materials as

$$A = \frac{2\,c_{44}}{c_{11} - c_{12}}\,, \tag{2.23}$$

and it couples the elastic coefficient c_{44} with the elastic coefficient

$$c' = \frac{c_{11} - c_{12}}{2}\,, \tag{2.24}$$

which represents the relation between shear stress and deformation in the diagonal plane, having the normal vector of (1,-1,0).

In **isotropic** materials, all directions are macroscopically equivalent, and thus, the number of independent elastic coefficients is decreased: $c_{11} = c_{22} = c_{33}$, $c_{12} = c_{13} = c_{23}$, and $c_{44} = c_{55} = c_{66} = \frac{1}{2}(c_{11} - c_{12})$, i. e. $A = 1$. Then both Young's modulus E and shear modulus G are equal in all directions:

$$E = c_{44}\,\frac{3\,c_{11} - 4\,c_{44}}{c_{11} - c_{44}} = c_{11} - \frac{2\,c_{12}^2}{c_{11} + c_{12}}\,, \tag{2.25}$$

$$G = c_{44} = \frac{1}{2}(c_{11} - c_{12})\,. \tag{2.26}$$

Alternatively, Hooke's law (2.6) in isotropic solids can also be written as

$$\sigma_{ij} = c_{12}\,\varepsilon_{kk}\,\delta_{ij} + 2\,G\,\varepsilon_{ij}\,, \tag{2.27}$$

where $\varepsilon_{kk} = \varepsilon_{11} + \varepsilon_{22} + \varepsilon_{33}$ is the volume dilatation, δ_{ij} is Kronecker delta ($\delta_{ij} = 1$ for $i = j$ and $\delta_{ij} = 0$ for $i \neq j$). For describing the elastic properties of isotropic solids, two elastic parameters are sufficient; it could be c_{11} and c_{12} coefficients, Young's modulus E (2.25), shear modulus $G = c_{44}$ (2.26), **bulk modulus** K

$$K = \frac{c_{11} + 2\,c_{12}}{3} = c_{11} - \frac{4}{3}c_{44} = \frac{E\,G}{3\,(3\,G - E)}\,, \tag{2.28}$$

or **Poisson's ratio** ν

$$\nu = \frac{c_{12}}{c_{11} + c_{12}} = \frac{c_{11} - 2\,c_{44}}{2\,c_{11} - 2\,c_{44}} = \frac{E - 2\,G}{2\,G}\,. \tag{2.29}$$

Generally, every elastic modulus in the isotropic medium can be expressed as the combination of two other moduli; some of the formulas are given in the above equations, and the remaining ones can be easily derived from them.

Young's modulus E of a two-phase composite material can be estimated as

$$E_{\text{Reuss}} \leq E \leq E_{\text{Voigt}}\,, \tag{2.30}$$

where the lower (Reuss [28]) bound is based on the equal-stress distribution

$$\frac{1}{E_{\text{Reuss}}} = \frac{f_v}{E_f} + \frac{1 - f_v}{E_m}\,, \tag{2.31}$$

and the upper (Voigt [29]) bound is based on the equal-strain distribution

$$E_{\text{Voigt}} = f_v \, E_f + (1 - f_v) \, E_m \,, \tag{2.32}$$

where f_v is the volume fraction of the phase with the Young's modulus E_f, where the other phase has Young's modulus E_m.

2.1.2 Wave propagation in elastic solids

Dynamic equilibrium in an unbounded elastic medium leads to the equation

$$\rho \, \frac{\partial^2 u_i}{\partial t^2} = \frac{\partial \sigma_{ij}}{\partial x_j} \,, \tag{2.33}$$

when external forces such as gravity etc. are neglected; ρ is the **mass density**. As the elastic tensor C_{ijkl} is symmetric in k and l indices, the equation (2.33) yields to

$$\rho \, \frac{\partial^2 u_i}{\partial t^2} = \frac{\partial}{\partial x_j} \left(C_{ijkl} \frac{\partial u_k}{\partial x_l} \right) . \tag{2.34}$$

For homogeneous media, C_{ijkl} is independent on coordinates $\mathbf{x}$, which results in the **wave equation**

$$\rho \, \frac{\partial^2 u_i}{\partial t^2} = C_{ijkl} \, \frac{\partial^2 u_k}{\partial x_j \partial x_l} \,. \tag{2.35}$$

By applying the general formula for harmonic plane waves

$$u_i = U_i \, \mathrm{e}^{-i \, \omega \, (\, t \, - \, s_m \, x_m \,)} \,, \tag{2.36}$$

where $\mathbf{s} = \mathbf{n}/v$ is the **slowness vector**, and v is the **phase velocity**, the wave equation (2.35) leads to the **Christoffel equation**

$$\rho \, v^2 \, U_i = C_{ijkl} \, n_j \, n_l \, U_k. \tag{2.37}$$

By defining Christoffel matrix[2]

$$\Gamma_{ik} = \frac{C_{ijkl}}{\rho} \, n_j \, n_l \,, \tag{2.38}$$

the equation (2.37) leads to

$$(\, \Gamma_{ik} - v^2 \, \delta_{ik} \,) \, U_k = 0 \,, \tag{2.39}$$

which is the eigenvalue equation, and thus, the phase velocities v of the waves propagating in a given direction $\mathbf{n}$ is determined by solving the characteristic equation

$$\det (\, \Gamma_{ik} - v^2 \, \delta_{ik} \,) = 0 \,. \tag{2.40}$$

As the Christoffel matrix is symmetric $\Gamma_{ik} = \Gamma_{ki}$ due to the symmetry of the elastic tensor C_{ijkl}, the eigenvalues v^2 are real, and the eigenvectors U_k, which represent the wave polarization, are

---

[2]Some authors (e.g. Royer et al. [16]) define the Christoffel matrix (also called Christoffel tensor) without the reciprocal density, i. e. $\Gamma_{ik} = C_{ijkl} \, n_j \, n_l$, which thus affects the subsequent equations dealing with Γ_{ik}.

orthogonal. Therefore, in an arbitrary direction, there are generally three plane waves with the orthogonal polarization; the wave with the polarization closest to the propagating direction **n** is called in ***quasi-longitudinal*** (qL), and the other two are called ***quasi-transverse*** (qT) [16]. The ***group velocity*** v_i^g coincides with the energy velocity v_i^e and is given as

$$v_i^g = v_i^e = \frac{C_{ijkl} \, n_k \, U_j \, U_l}{\rho \, v}. \tag{2.41}$$

The scalar product $\mathbf{v}^g \cdot \mathbf{n}$, leads to

$$v_i^g \, n_i = \frac{C_{ijkl} \, n_i \, n_k \, U_j \, U_l}{\rho \, v} = \frac{\rho \, v^2 \, U_l \, U_l}{\rho \, v} = v \,, \tag{2.42}$$

which means that the projection of the group velocity $\mathbf{v}^g$ in the direction of the wave propagation **n** is equal to the phase velocity v. Therefore, the absolute value of the group velocity vector is always higher or equal to the phase velocity v of the plane waves in the elastic media.

The angular dependencies of phase velocity, slowness vector, and group velocity can be visualized by characteristic surfaces. The ***phase velocity surface*** is drawn by the vector $\mathbf{v} = v \, \mathbf{n}$, i. e. the distance between the origin of the coordinate system and the surface is equal to the phase velocity v in the given direction **n**. The ***slowness surface*** is defined by the distribution of the slowness vector $\mathbf{s} = \mathbf{n}/v$, and the ***wave surface*** is given by the group velocity vector $\mathbf{v}^g$ distribution. These surfaces are mutually coupled, where the relation between the phase velocity surface and slowness surface is directly given by the slowness vector definition $\mathbf{s} = \mathbf{n}/v$, and the equation (2.42) yields that the normal vector to the slowness surface is parallel to the direction of the group velocity vector. Generally, there are three distinct surfaces for each type of waves (one quasi-longitudinal and two quasi-transverse waves), and in certain cases depending on the material symmetry, the surfaces can intersect. In the isotropic media, the surfaces representing the transverse waves merge together, as there is only one transverse wave velocity, as shown later in this section.

The above equations can be generally utilized for the calculation of phase and group velocities, but they can be simplified by applying the material symmetry. For *orthorhombic* materials, i. e. the materials with orthogonal principal axes of symmetry, the elements in the first row of the Christoffel matrix (2.38) are

$$\Gamma_{11} = \frac{c_{11}}{\rho} \, n_1^2 + \frac{c_{66}}{\rho} \, n_2^2 + \frac{c_{55}}{\rho} \, n_3^2 \,, \tag{2.43}$$

$$\Gamma_{12} = \frac{c_{12} + c_{66}}{\rho} \, n_1 \, n_2 \,, \tag{2.44}$$

$$\Gamma_{13} = \frac{c_{13} + c_{55}}{\rho} \, n_1 \, n_3 \,, \tag{2.45}$$

and the elements in the remaining rows are analogous to these ones. For the direction of wave propagation along the x_1 principal axis, i. e. $\mathbf{n} = (1, 0, 0)$, the Christoffel matrix is simplified
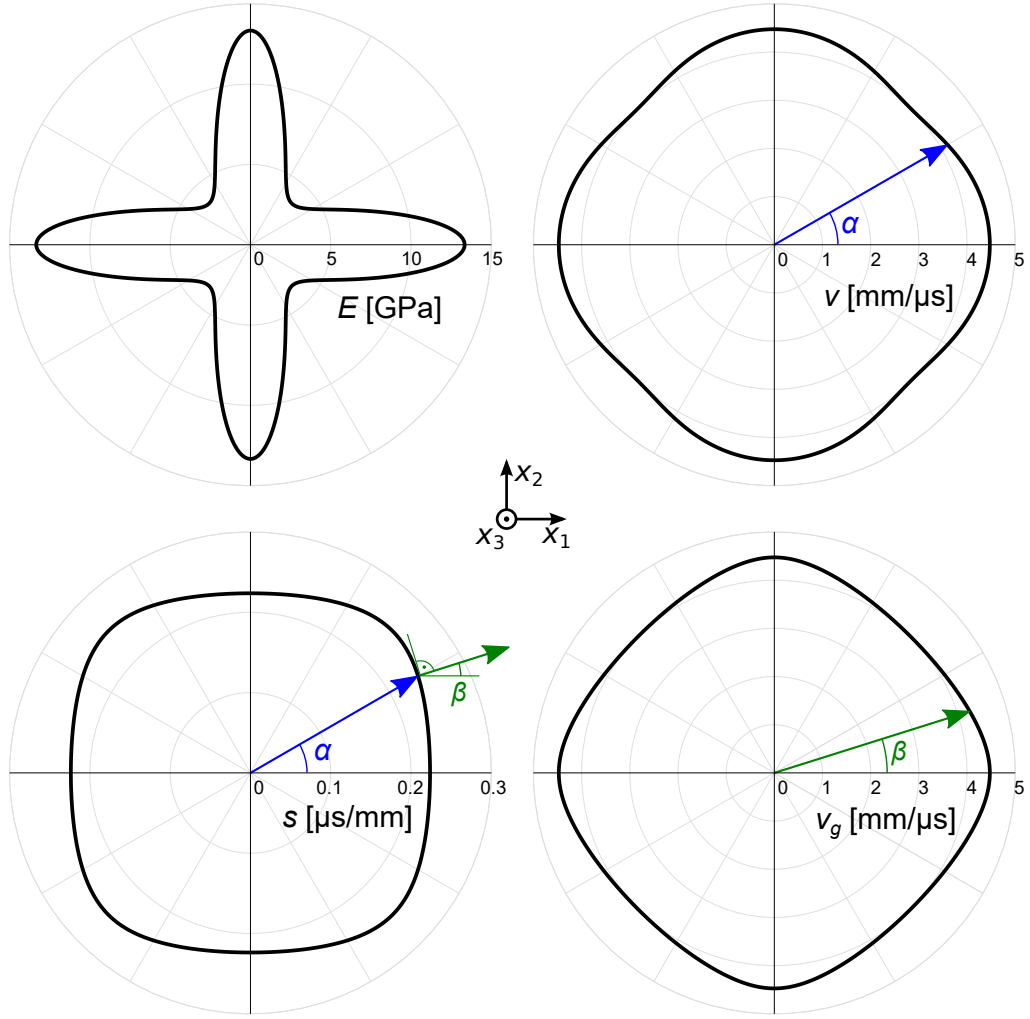
Figure 2.1: Distributions of Young's modulus E, phase velocity v, slowness s and group velocity v_g of quasi-longitudinal waves in the principal x_1x_2 plane for an example of a cubic material with anisotropy factor $A = 0.2$ ($c_{44} = 1$ GPa, $c' = 5$ GPa, $c_{11} = 20$ GPa, $\rho = 1$ g·cm^{-3}). These distributions were plotted by implementing the equations (2.10, 2.37–2.41). For a given direction of wave propagation at an angle of $\alpha = 30°$, the angle between the x_1 axis and the normal vector to the slowness surface (and thus the direction of the group velocity vector) is $\beta \doteq 17.36°$ in this particular case.

to

$$\mathbf{\Gamma} = \begin{pmatrix} c_{11}/\rho & 0 & 0 \\ 0 & c_{66}/\rho & 0 \\ 0 & 0 & c_{55}/\rho \end{pmatrix}, \tag{2.46}$$

which leads to the characteristic equation

$$\left(\frac{c_{11}}{\rho} - v^2\right)\left(\frac{c_{66}}{\rho} - v^2\right)\left(\frac{c_{55}}{\rho} - v^2\right) = 0 \tag{2.47}$$

with three solutions for v^2. The solution $v = \pm\sqrt{c_{11}/\rho}$ leads to the polarization vector $\mathbf{U} = (U, 0, 0)$, which is parallel to the wave propagation $\mathbf{n} = (1, 0, 0)$, i. e. the waves with

this velocity are polarized in the direction of the wave propagation and thus they are often called *pure longitudinal*. The waves with the velocity of $\pm\sqrt{c_{66}/\rho}$ are polarized along the x_2 axis, and the waves with $v = \pm\sqrt{c_{55}/\rho}$ are polarized along the x_3 axis, and thus these are the *pure transverse* waves. If we define v_{ij} as the velocities of the waves which propagate along direction the x_i axis with the polarization along the x_j axis, the velocities are

$$v_{11} = \sqrt{\frac{c_{11}}{\rho}}\,, \qquad v_{12} = \sqrt{\frac{c_{66}}{\rho}}\,, \qquad v_{13} = \sqrt{\frac{c_{55}}{\rho}}\,. \tag{2.48}$$

Only the positive v values are given here (and also later in the thesis) as the negative v values correspond to the waves propagating in the opposite direction that otherwise have exactly the same character. Analogously, it can be shown that

$$v_{21} = \sqrt{\frac{c_{66}}{\rho}} = v_{12}\,, \qquad v_{22} = \sqrt{\frac{c_{22}}{\rho}}\,, \qquad v_{23} = \sqrt{\frac{c_{44}}{\rho}}\,, \tag{2.49}$$

$$v_{31} = \sqrt{\frac{c_{55}}{\rho}} = v_{31}\,, \qquad v_{32} = \sqrt{\frac{c_{44}}{\rho}} = v_{23}\,, \qquad v_{33} = \sqrt{\frac{c_{33}}{\rho}}\,. \tag{2.50}$$

Clearly, the transverse waves propagating in the direction of the x_i axis and polarized along the x_j have the same velocity as the waves propagating in the direction of the x_j axis and polarized along the x_i axis as the properties of such waves result from the shear deformations in the $x_i x_j$ plane. For general orthorhombic symmetry, only these waves propagating in the direction of the principal axes are pure, i. e. the polarization vector is parallel to the direction of propagation $\mathbf{n}$ for the longitudinal waves or perpendicular to $\mathbf{n}$ for the transverse waves. In such cases, the group velocity vector $\mathbf{v}^g$ is parallel to the direction of propagation $\mathbf{n}$, and also $\mathbf{v}^g = v\,\mathbf{n}$, i. e. the group velocity of the pure waves is equal to their phase velocity.

The equations (2.48–2.50) are also clearly valid for the cases of higher symmetry, such as the tetragonal materials with $c_{11} = c_{22}, c_{13} = c_{23}, c_{44} = c_{55}$, and hexagonal materials (2.17) with $c_{66} = \frac{1}{2}(c_{11} - c_{12})$. In the cubic materials (2.22), the principal axes are macroscopically equivalent, which leads to

$$v_{11} = v_{22} = v_{33} = \sqrt{\frac{c_{11}}{\rho}}\,, \tag{2.51}$$

$$v_{12} = v_{13} = v_{21} = v_{23} = v_{31} = v_{32} = \sqrt{\frac{c_{44}}{\rho}}\,. \tag{2.52}$$

These two equations (2.51, 2.52) are also valid in the isotropic materials, and as all directions are equivalent, they directly represent pure longitudinal waves with the velocity

$$v_L = \sqrt{\frac{c_{11}}{\rho}}\,, \tag{2.53}$$

and pure transverse waves with the velocity

$$v_T = \sqrt{\frac{c_{44}}{\rho}}\,. \tag{2.54}$$

From the above equations, it can be seen that some of the elastic coefficients c_{ij} can be determined by measuring the velocities of longitudinal or transverse waves propagating through a material with a known density. When a measured sample is cut such that its faces are parallel to the principal axes of the material symmetry, the coefficients c_{11}, c_{22}, c_{33} can be determined by measuring the velocities of the longitudinal waves, and the coefficients c_{44}, c_{55}, c_{66} can be determined by measuring the velocities of the transverse waves. Therefore, only for isotropic materials (with two independent coefficients c_{11}, c_{44}), the full set of the elastic coefficients can be determined in this way. For the materials with lower symmetry (cubic, hexagonal, etc.), the non-diagonal components c_{12}, c_{13} etc. of the Voigt matrix (2.14) can be determined by measuring the velocities in non-principal directions (e. g. in the face diagonal and body diagonal directions), or more conveniently by resonant ultrasound spectroscopy, as described in section 2.2.

2.1.3   Wave attenuation and internal friction

When the elastic waves propagate through real solid materials, their energy partially dissipates, and the wave amplitude thus gradually decreases. The amount of energy ΔW dissipated during one period of the cycle can be expressed by a ***specific damping capacity*** [20, 23]

$$\Psi = \frac{\Delta W}{W}\,, \tag{2.55}$$

where W is the stored elastic energy at the maximum strain. When the elastic energy dissipated in one cycle ΔW is much smaller than total stored elastic energy W, i. e. $\Psi \ll 1$, the amplitude U of the propagating waves decreases exponentially [16]

$$U = U_0\, \mathrm{e}^{-\alpha x}\,, \tag{2.56}$$

where α is the ***attenuation coefficient***, and $\Psi \approx 2\,\alpha\,\lambda$, where λ is the wavelength.

When the periodic stress

$$\sigma = \sigma_0\, \mathrm{e}^{i\,\omega\,t} \tag{2.57}$$

is imposed onto a linearly elastic system with damping, the strain ε is also periodic with the same frequency, but its phase lags behind the stress [22], i. e.

$$\varepsilon = \varepsilon_0\, \mathrm{e}^{i\,(\omega\,t - \phi)}\,, \tag{2.58}$$

where ϕ is the ***loss angle***. The elastic modulus M, which couples stress and strain (e. g. Young's modulus E etc.), thus becomes complex

$$M^* = \frac{\sigma}{\varepsilon} = \frac{\sigma_0}{\varepsilon_0}\, \mathrm{e}^{i\,\phi} = |M|\, \mathrm{e}^{i\,\phi} = M' + i\,M''\,, \tag{2.59}$$

where $|M|$ is called the absolute dynamic modulus, M' is the storage modulus, and M'' is the loss modulus. Their ratio

$$\tan\phi = \frac{M''}{M'} \tag{2.60}$$

is called the **loss tangent**, and the specific damping capacity Ψ is proportional to it

$$\Psi = \frac{\Delta W}{W} = 2\pi \tan\phi. \tag{2.61}$$

In section 2.2 of this thesis, it is shown how the elastic coefficients c_{ij} can be determined by measuring resonant spectra of small samples. While the resonant frequencies depend mostly on the density and the elastic coefficients, the width of resonant peaks reflects the damping properties of the studied materials. The **quality factor** of resonances Q is defined [11, 30, 31] as

$$Q = \frac{f_r}{f_1 - f_2} = \frac{f_r}{f_{\text{FWHM}}}, \tag{2.62}$$

where f_r is the resonant frequency, and f_1, f_2 are the frequency values at which the amplitude falls to $1/2$ of the maximum amplitude value at f_r, where $f_1 < f_r$ and $f_2 > f_r$. The difference $f_{\text{FWHM}} = f_1 - f_2$ is often called *full width at half maximum*. The reciprocal value of the quality factor is called **internal friction** Q^{-1}. By applying the relation for displacement amplitude of forced vibrations [22], it can be seen that the internal friction is directly equal to the loss angle, $Q^{-1} = \phi$. Therefore, when it is low ($Q^{-1} \ll 1$ and thus $\tan\phi \sim \phi$), internal friction represents the specific damping capacity Ψ (2.61), only scaled by the factor of 2π.

Internal friction in materials results mostly from the inner microstructure and its behavior in relation to elastic deformation. The most important phenomena responsible for the internal friction in common materials are summarized in the following text, and more details can be found e. g. in [22–24].

Point defects, such as interstitial atoms, vacancies, or substitutional atoms, induce distortions of the periodic crystal lattice, which causes several types of characteristic anelastic behavior. *Snoek relaxation* is observed in body-centered cubic (BCC) metals that contain a significant amount of interstitial atoms. These atoms (usually C, N, H, O, etc.) occupy certain positions prescribed by the arrangement of the BCC lattice, creating elastic dipoles with a tetragonal symmetry, i. e. generally lower symmetry than cubic. The reorientation of the elastic dipoles under applied stress leads to mechanical loss, which results in a Snoek relaxation peak. Originally in 1939, Snoek observed a relaxation peak near room temperature at low frequencies in α-iron doped with carbon or nitrogen [32, 33], and later the Snoek relaxation peaks were also recognized in other BCC metals (W, Ta, Nb, Cr, V) with various interstitial atoms [22, 34].

Zener relaxation is observed in substitutional alloys, i. e. those solute solutions, where the atoms (of at least two different elements) are similar in size and thus able to create a single common lattice. When the substitutional atoms form a neighboring pair, the lattice is asymmetrically distorted, and the reorientation of the pairs under applied stress leads to the mechanical loss. Zener first observed this effect in an α-brass (Cu/Zn) crystal, with a relaxation peak near 410 °C at 620 Hz [35, 36], but this type of relaxation was also discovered in many other alloys [22, 37]. Anelastic behavior caused by point defects can also be specifically observed in several types of oxides, or in quasicrystals [38], etc.

Dislocations are other important crystallographic defects that influence the anelastic behavior of the solid materials, as the internal friction is generally very sensitive to the mobility of dislocations. When a dislocation is assumed as a string of length l, which bows between

two pinning points under the applied stress, a *Granato-Lücke vibrating string model* [24, 39] predicts that $Q^{-1} \sim l^4$. i. e. the damping in the material is strongly dependent on the density of pinning points. Besides that, relaxation peaks caused by dislocations can also occur in the internal friction spectra of several materials, such as *Bordoni relaxation* peak [40], often observed in cold-worked face-centered cubic (FCC) solids at low temperatures, caused by a formation of kink pairs and their motion under stress; or *Snoek-Köster relaxation* resulting from the interaction of dislocations with point defects.

For a wide variety of thermally activated relaxation processes, the internal friction in the high-frequency limit increases exponentially with temperature T, following the Arrhenius equation [24, 41]

$$Q^{-1} = A_0 \exp(-\frac{U}{kT}), \qquad (2.63)$$

where A_0 is a temperature-independent constant, U is an activation energy in Joules or eV, k is Boltzmann constant. Alternatively, when the activation energy is determined in J/mol, the equation (2.63) can be rewritten as

$$Q^{-1} = A_0 \exp(-\frac{U}{RT}), \qquad (2.64)$$

where R is molar gas constant. When the internal friction is measured at varying temperatures for a certain resonant mode (such as the case for the resonant ultrasound spectroscopy described in the following section), the activation energy U can be then obtained from the slopes in $\ln Q^{-1}$ vs. $\frac{1}{T}$ coordinates, as the equation (2.63) yields

$$\ln Q^{-1} = \ln A_0 - \frac{U}{k}\frac{1}{T}. \qquad (2.65)$$

The internal friction measurements can also be utilized for determining the temperatures of phase transition, as the internal friction significantly increases near the transition temperatures [24]. Besides that, as the elastic coefficients c_{ij} are second derivatives of free energy with respect to strain [11], there is a sudden change in c_{ij} at the first-order phase transitions and a change of slope in the c_{ij} dependence on temperature for the second-order phase transitions.

2.2 Resonant ultrasound spectroscopy (RUS)

Resonant ultrasound spectroscopy (RUS) is an experimental technique for determining elastic properties of materials based on measuring resonant spectra of free elastic vibrations of small samples [8–13]. The elastic coefficients of the measured sample cannot be, however, obtained directly from its resonant spectrum, but an inverse procedure must be utilized, as shown in Figure 2.2. At first, an initial guess of the elastic coefficients is given, and a resonant spectrum is calculated by a forward problem, as shown in more detail in section 2.2.2. The measured resonant frequencies are associated with the calculated resonant frequencies, and their difference is then iteratively minimized. In this sense, the resulting elastic coefficients are those that correspond to a resonant spectrum that fits best to the resonant spectrum of the measured sample.
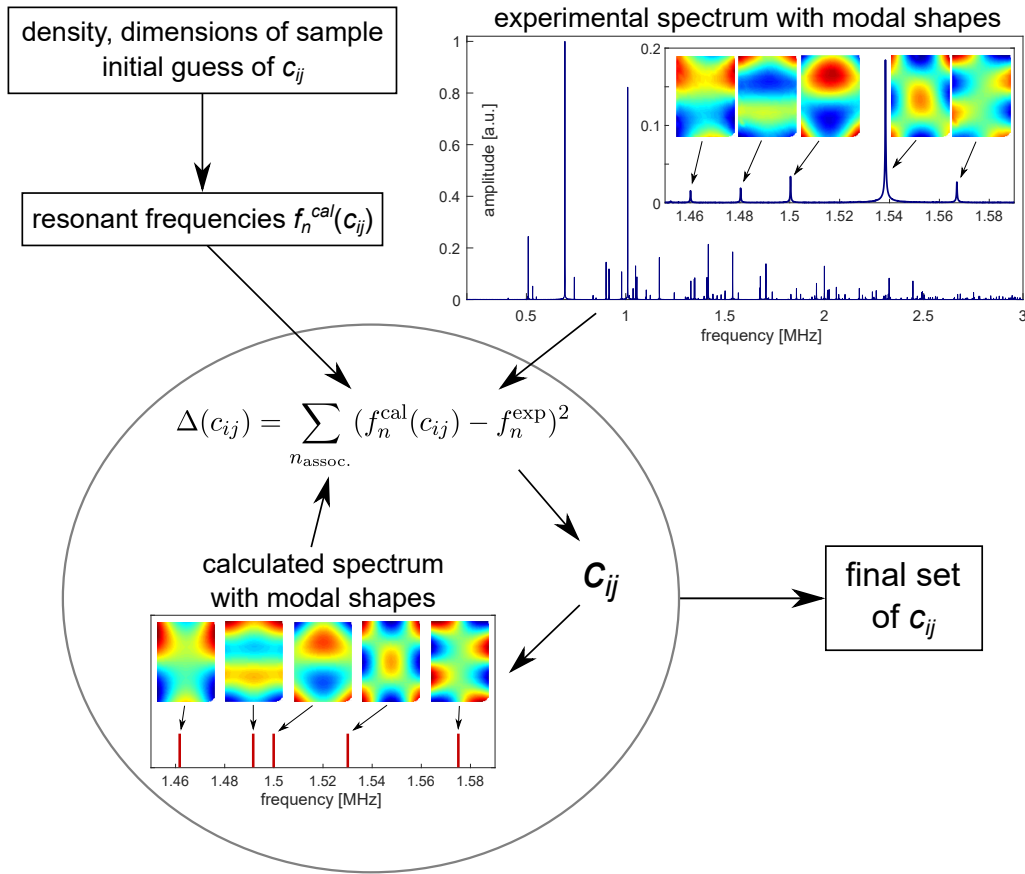

Figure 2.2: Determination of the elastic coefficients c_{ij} by resonant ultrasound spectroscopy (RUS); own work based on the principles of the RUS method [12].

This chapter provides a detailed description of the RUS method and is divided into several sections. The first section 2.2.1 describes the evolution of the RUS method from the pioneering works in the 1960s up to fully contactless laser-based RUS. The theory of the elastic coefficients determination is summarized in section 2.2.2, and the principles of the laser-based RUS employed at the Institute of Thermomechanics of the Czech Academy of Sciences are shown in section 2.2.3. The last section 2.2.4 shows how the experimental data are processed in a custom

toolbox, which was designed in MATLAB computational environment by the colleagues from the Institute of Thermomechanics of the Czech Academy of Sciences. This toolbox was utilized for all the RUS results presented in this thesis.

2.2.1 Historical development of the RUS method

One of the first experimental methods that utilized the measurements of resonant spectra of small samples for the determination of elastic coefficients was the method developed by Frazer and LeCraw [42] in the 1960s. In this method, a sphere with a diameter of several millimeters was freely placed on a shear piezoelectric transducer, which was then driven at varying frequencies up to tens of MHz. The resonant spectrum was detected by measuring the displacement response of the sphere, and the elastic moduli were then determined by comparing the measured resonant frequencies with the analytical solution of resonances of a homogeneous isotropic sphere [43]. Soga and Anderson [44] utilized the similar setup, but the measured sphere was rather placed between two piezoelectric transducers, which was shown to work better for materials with higher acoustic loss; they called this method as *resonant sphere technique*.

The resonance methods utilizing free elastic vibrations of bulk samples were at first limited only to homogeneous isotropic spheres, as there have been no exact analytical solutions for other shapes of the measured samples or for more general symmetry class. In 1971, Demarest [45] proposed a method based on the resonances of a cube, where the resonant frequencies of rectangular parallelepiped samples with isotropic or cubic symmetry were numerically calculated by Rayleigh-Ritz method with Legendre polynomials as basis functions. The resonant frequencies of a small cube of fused quartz were then measured using a similar setup as in [44], where the measured cube was placed between two piezoelectric transducers such that it touched them on the opposite corners in order to minimize the pressure and the contact areas between the transducers and the measured sample. The set of calculated resonant frequencies very well corresponded to the measured resonant frequencies, and the elastic moduli of fused quartz were thus determined with high accuracy.

In 1976, Ohno [46] extended the Demarest's theory to the rectangular parallelepiped bodies with more general symmetry and applied it to the measurement of the elastic coefficients of an orthorhombic single crystal of olivine. This method was referred as *rectangular parallelepiped resonance (RPR) method* to reflect the possibility of measurement on any rectangular parallelepiped samples, i. e. not limited only to the cubes. Later on, the numerical calculation of the resonant frequencies of the rectangular parallelepiped bodies was extended to the cases of trigonal [47] and general triclinic [48, 49] materials. Ohno also extended the theory to the case of piezoelectric crystals [50].

In another paper from 1976, Sumino et al. [51] utilized the RPR method for measuring the elastic coefficients and internal friction of MgO single crystals with cubic symmetry. Also, the effect of clamping force between the measured sample and the transducers was studied here; one of the transducers was connected to one lever of balance scales, which allowed to change the clamping force by simply putting the weights onto the opposite lever of the scales. The resonant frequencies were detected for several values of clamping forces, which corresponded to

the loadings up to several grams. Some resonant frequencies did not show any dependence on the clamping force, but others slightly changed with higher load, where the largest difference between the resonant frequency at the maximum load and the frequency extrapolated to zero force was 0.4 %. Nevertheless, this difference corresponded to a quite high loading force, and the frequency difference was actually significantly below 0.1 % when assuming the usual clamping forces during the RPR measurements. Therefore, the apparatus with the balance scales were not frequently used in the following RPR measurements, and the clamping force was just kept as low as possible in order to increase the accuracy of the elastic coefficients determination.

In 1977, Sumino et al. [52] first applied the RPR method for measuring the elastic coefficients at varying temperatures. A rectangular parallelepiped sample was cut from an orthorhombic single crystal of forsterite along the {100} crystallographic plane, and its resonant spectrum was detected at varying temperatures from -190 °C up to 400 °C. It was also shown here that the coefficients of linear thermal expansion are needed to be known for the accurate determination of the elastic coefficients due to the change of the sample dimensions with temperature. In later works by Sumino et al., the elastic coefficients of a single crystal of MgO up to 1300 K [53] and a single crystal of forsterite Mg_2SiO_4 up to 1200 K [54] were determined by the RPR method, while using single crystals of $LiNbO_3$ as the high-temperature transducers.

The high-temperature applications of the RPR method were limited by temperature thresholds above which the materials utilized for the transducers lose the piezoelectric effect. Goto and Anderson [55–59] tried to overcome this issue by creating a new apparatus based on the RPR method, in which the measured sample was placed into a cylindrical furnace, where it was held between two long alumina buffer rods. The opposite sides of the rods were glued to the piezoelectric transducers outside the furnace, which allowed the sample to be heated up to 1825 K, while the transducers could have been kept at much lower working temperatures. Nevertheless, Gladden et al. [27, 60] later showed that the weight of the buffer rods also caused a significant shift in the resonant frequencies. Moreover, the signal of the weaker resonances can be lost due to the transmission through the buffer rods, or even new resonant peaks, which correspond only to the vibrations of the buffer rods can appear in the measured spectrum.

Around 1990, a research group of A. Migliori at the Los Alamos National Laboratory adopted the RPR method, but they rather called it *resonant ultrasound technique* [61, 62]. Later in the 1990s, the method has eventually become referred as *resonant ultrasound spectroscopy* (RUS) [9, 10, 63–66]; two schematic diagrams of the RUS experimental setup from the 1990s are shown in Figure 2.3. In 1991, a paper by Visscher et al. [67] described the calculation of the vibrational modes of several types of various objects (including cylinders, cones, spheroids, sandwiches or even objects with irregular shapes) with arbitrary anisotropy, where powers of the Cartesian coordinates were used as the basis function $\Phi = x^l y^m z^n$. In 1994, Sarrao et al. [65] showed that the crystallographic orientation does not have to be necessarily known prior to the RUS measurements, but both the orientation and the elastic coefficients can be determined simultaneously from a single RUS measurement. Nevertheless, the knowledge of the crystal orientation can substantially simplify the resonant spectrum calculation, especially when the free surfaces of the sample are parallel to the principal crystallographic planes [10].
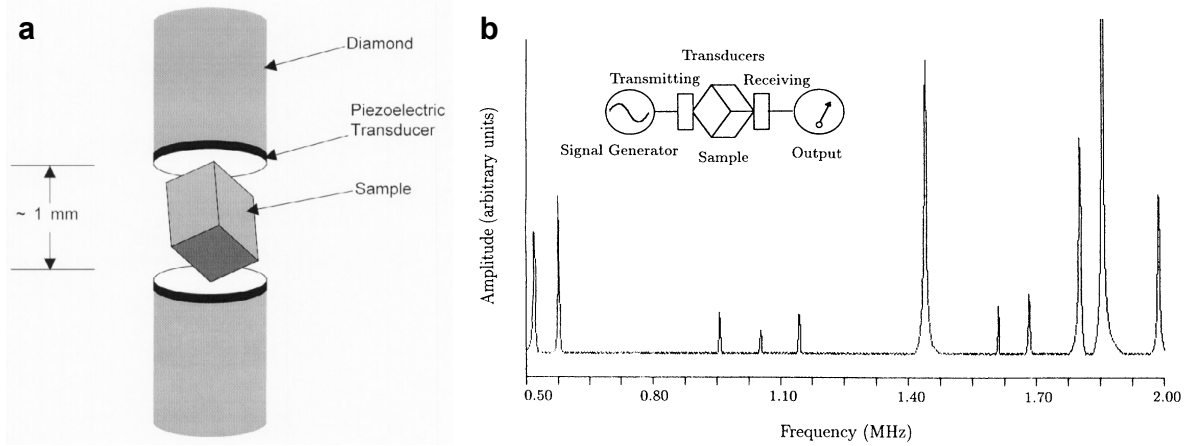
Figure 2.3: a) Arrangement of the sample put between two piezoelectric transducers for the RUS method from the paper [11], b) Resonant spectrum of a monocrystalline $YBa_2Cu_3O_{7-\delta}$ sample at 295 K and the schematic diagram of the RUS setup from the paper [64].

During the 1990s, several modifications of the RUS method were employed. Maynard et al. [8, 68] utilized an apparatus where the measured sample was placed between polyvinylidene fluoride (PVDF) thin-film transducers. This setup was favorably utilized for measurements on fragile samples with sub-millimeter dimensions, as the contact forces induced by the film transducers were significantly lower than those from bulk transducers. Stekel at al. [63] employed another RUS apparatus, which was able to identify the vibrational modes by detecting the displacement amplitudes at 225 points (15×15 array). In the meantime, Kuokkala and Schwarz [69] developed a method where the principles of determining the elastic coefficients were the same as for the RPR/RUS method, but the vibrations of the sample were generated by magnetic field. The measured sample was coated by a magnetostrictive material (unless the sample was magnetostrictive itself), and then its vibrations were excited by magneto-mechanical coupling between an alternating magnetic field and the magnetostrictive coating. A similar method, where the vibrations were also generated by the magnetic field, but the sample was instead inserted in a solenoidal coil, was later adopted by Ogi et al. and called *electromagnetic acoustic resonance* (EMAR) [70–72].

In 1999, Sato el at. [73] showed that a focused laser beam can be utilized for the generation of the vibrations, and a laser interferometer can be utilized for the detection.

In 2001, Guo and Lal [74] utilized the RUS method for measuring the elastic coefficients of a micro-machined silicon nitride membrane, but its resonant frequencies were calculated by finite element method (FEM). Also, many other authors later showed that FEM can be used as an alternative approach to the Rayleigh-Ritz method for calculating the resonant spectra, and it is especially beneficial for more complex shapes of the vibrating bodies [75, 76].

In the early 2000s, Ogi et al. [77–80] developed a new *tripod* setup of the RUS measurements, where the measured samples were freely put onto three pinducers (i. e. needle-like transducers), as shown schematically in Figure 2.4(b). Two pinducers were used for generating and detecting the vibrations of the sample, and the remaining pinducer was used as a support. In addition, the top surface of the measured sample was scanned by a laser Doppler interferometer, which

detected the normal component of the displacement for each resonant frequency. In comparison to the previous RPR/RUS measurements, this setup has several advantages. The sample was no longer constrained between the transducers, so there was no clamping force affecting the measured values of the resonant frequencies anymore. Moreover, the laser vibrometer enables to identify the vibrational modes, which is beneficial for an unambiguous pairing between the measured and calculated resonant frequencies.

Nakamura et al. [80–82] also showed that the RUS can be utilized for the determination of the elastic coefficients of thin coatings deposited on bulk substrates. At first, the elastic coefficients of the substrate were obtained separately, utilizing the RUS tripod setup. Then, the resonant spectrum of a sample with the coating was measured, and the elastic coefficients of the coating were determined from the analysis of the frequency shifts imposed by the deposited layer.

During the 2000s, the RUS technique was employed at the Institute of Thermomechanics of the Czech Academy of Sciences [83–87], and a fully non-contact laser-based RUS apparatus has been utilized there since 2008 [12, 88]; more details about this experimental setup are given in section 2.2.3. The laser-based RUS has been then utilized for measurements on various materials, including

- thin coatings on bulk substrates [89–92] and free-standing coatings [93–95];
- shape memory alloys, such as NiTi [96–98], or ferromagnetic NiMnGa [99–103] and CoNiAl [104] alloys;
- ultrafine-grained polycrystalline copper [105] and ultrafine-grained magnesium alloys [41, 106];
- materials with weak gradients in elastic properties [107];
- $BaTiO_3$ functional ceramics [108, 109] and semiconductors [110];
- metastable titanium alloys [111–114].

Moreover, a paper [13] from 2014 confirmed that the laser-based RUS can be utilized for the determination of all 21 independent elastic coefficients of a general triclinic solid from its single resonant spectrum.

(a) classical scheme   (b) tripod scheme   (c) fully non-contact scheme
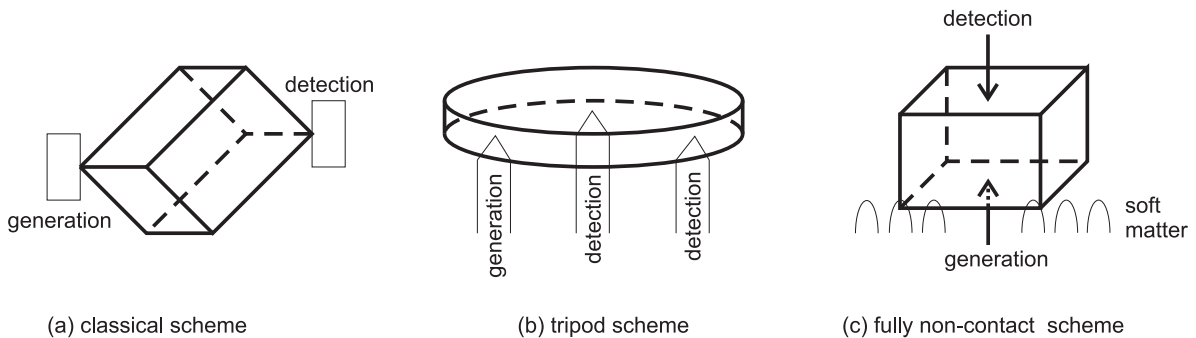
Figure 2.4: Development of RUS devices [12]. In the classical scheme (a), the measured sample is placed between two piezoelectric transducers. In the tripod scheme (b), the sample lies on needle-like transducers. In the fully non-contact scheme (c), the sample lies on a soft underlay, and its vibrations are generated by a pulsing laser and detected by a laser vibrometer.

In the meantime, the laser-based RUS was also employed at the Idaho National Laboratory [115–119]. Other authors have still used the RUS setup where the sample vibrations have been

generated by piezoelectric transducers [120–122], but some of them have also utilized the laser vibrometers for identification of modal shapes of vibration [76, 123, 124].

Schematic diagrams of the fundamental RUS setups, i. e. the classical scheme (where the sample is put between two piezoelectric transducers), the tripod scheme, and the fully non-contact scheme, are shown in Figure 2.4.

2.2.2 Determination of elastic coefficients from measured resonant spectra

This section shows how the elastic coefficients are obtained from the RUS measurements. As already mentioned in the introduction of the section 2.2, the elastic coefficients cannot be determined directly from the measured resonant spectrum but have to be computed inversely, where the experimental resonant frequencies are compared with calculated ones. A *forward procedure* is used for the evaluation of the resonant spectrum of free elastic vibrations, when the mass density ρ of the sample, its dimensions, and the initial values of elastic coefficients c_{ij} are given. The elastic coefficients are then obtained inversely, where the measured resonant frequencies are iteratively compared with the resonant frequencies calculated by the forward procedure, as shown schematically in Figure 2.2.

A forward procedure based on energy minimization and Rayleigh-Ritz method [8–12] is described here, as it has been utilized for the RUS measurements presented in this thesis. In a vibrating linearly-elastic body, the density of potential energy E_p is

$$E_p = \frac{1}{2}\, C_{ijkl}\, \frac{\partial u_i}{\partial x_j}\, \frac{\partial u_k}{\partial x_l}\,, \tag{2.66}$$

and the density of kinetic energy E_k is

$$E_k = \frac{1}{2}\, \rho\, \dot{u}_i\, \dot{u}_i\,. \tag{2.67}$$

The total Lagrangian energy L is given as the difference of the kinetic energy and the potential energy

$$L = \int_V (E_k - E_p)\, \mathrm{d}V = \frac{1}{2} \int_V \left(\rho\, \dot{u}_i\, \dot{u}_i - C_{ijkl}\, \frac{\partial u_i}{\partial x_j}\, \frac{\partial u_k}{\partial x_l} \right) \mathrm{d}V\,. \tag{2.68}$$

Considering displacement to be harmonic, i. e.

$$u_i = U_i \cos(\omega t)\,, \tag{2.69}$$

the total Lagrangian energy (2.68) is

$$L = \frac{1}{2} \int_V \left(\rho\, \omega^2\, U_i\, U_i \sin^2(\omega t) - C_{ijkl}\, \frac{\partial U_i}{\partial x_j}\, \frac{\partial U_k}{\partial x_l} \cos^2(\omega t) \right) \mathrm{d}V\,. \tag{2.70}$$

Following the principle of stationary action

$$\delta \int_{t_1}^{t_2} L\, \mathrm{d}t = 0 \tag{2.71}$$

for arbitrary t_1 and t_2, and setting

$$t_2 = t_1 + \frac{2\,\pi}{\omega}\,, \tag{2.72}$$

the time coordinates can be eliminated due to the equality

$$\int_{t_1}^{t_1 + \frac{2\pi}{\omega}} \cos^2(\omega t)\, \mathrm{d}t = \int_{t_1}^{t_1 + \frac{2\pi}{\omega}} \sin^2(\omega t)\, \mathrm{d}t\,. \tag{2.73}$$

The variation condition (2.71) is then simplified to

$$\delta \frac{1}{2} \int_V \left(\rho\,\omega^2\, U_i\, U_i - C_{ijkl}\, \frac{\partial U_i}{\partial x_j}\, \frac{\partial U_k}{\partial x_l} \right) \mathrm{d}V = 0\,. \tag{2.74}$$

By applying Euler-Lagrange equations and integration by parts, the variation condition yields

$$\frac{1}{2} \int_V \left[\frac{\partial \Lambda}{\partial U_i} - \frac{\mathrm{d}}{\mathrm{d}x_j} \left(\frac{\partial \Lambda}{\partial \left(\frac{\partial U_i}{\partial x_j} \right)} \right) \right] \delta U_i\, \mathrm{d}V + \int_S n_j\, \frac{\partial \Lambda}{\partial \left(\frac{\partial U_i}{\partial x_j} \right)}\, \delta U_i\, \mathrm{d}S = 0\,, \tag{2.75}$$

where

$$\Lambda = \rho\,\omega^2\, U_i\, U_i - C_{ijkl}\, \frac{\partial U_i}{\partial x_j}\, \frac{\partial U_k}{\partial x_l} \tag{2.76}$$

is the density of time-averaged Lagrangian energy from the equation (2.74). As the variations δU_i are arbitrary, the integrands in the brackets must vanish independently. The first bracket leads to the elastic wave equation (see (2.35) for comparison)

$$\frac{\partial \Lambda}{\partial U_i} - \frac{\mathrm{d}}{\mathrm{d}x_j} \left(\frac{\partial \Lambda}{\partial \left(\frac{\partial U_i}{\partial x_j} \right)} \right) = \rho\,\omega^2\, U_i + C_{ijkl}\, \frac{\partial^2 U_k}{\partial x_j\, \partial x_l} = 0\,, \tag{2.77}$$

and the second bracket is a boundary condition at the surface with normal vector $\mathbf{n}$

$$n_j\, \frac{\partial \Lambda}{\partial \left(\frac{\partial U_i}{\partial x_j} \right)} = n_j\, C_{ijkl}\, \frac{\partial U_k}{\partial x_l} = 0\,. \tag{2.78}$$

In the Rayleigh-Ritz method, the displacement field U_i is given in the form of Ritz ansatz function

$$U_i(\mathbf{x}) = \alpha_{ijkl} \Psi_{jkl}(\mathbf{x})\,, \tag{2.79}$$

where $\Psi_{jkl}(\mathbf{x})$ is a chosen functional basis. For the case of rectangular parallelepiped samples, normalized Legendre polynomials

$$P_n(x) = \sqrt{\frac{2n+1}{2}}\, \frac{1}{2^n n!}\, \frac{\mathrm{d}^n}{\mathrm{d}x^n} (x^2 - 1)^n \tag{2.80}$$

are suitable as the functional basis

$$\Psi_{jkl}(\mathbf{x}) = P_j \left(\frac{2x_1}{d_1} \right) P_k \left(\frac{2x_2}{d_2} \right) P_l \left(\frac{2x_3}{d_3} \right) \tag{2.81}$$

for

$$j, k, l = 0, 1, 2, \ldots \qquad j + k + l \leq N\,, \tag{2.82}$$

where N is the degree of the polynomial approximation, d_i is the dimension of the sample in direction x_i, and the origin of the coordinate system is in the centre of symmetry of the parallelepiped sample. This leads to an eigenvalue problem, which can be solved by common numerical algorithms,

$$(\omega^2 \, \mathbf{I} - \mathbf{\Gamma}) \, \boldsymbol{\alpha} = 0 \,, \tag{2.83}$$

where $\mathbf{I}$ is the unit matrix in the form

$$\mathrm{I}_{[abci][defk]} = \delta_{ij} \, \delta_{ad} \, \delta_{be} \, \delta_{cf} \,, \tag{2.84}$$

$\mathbf{\Gamma}$ is the matrix that depends on the density, elastic coefficients and the dimensions of the sample

$$\Gamma_{[abci][defk]} = \frac{C_{ijkl}}{\rho} \, \frac{8}{d_1 \, d_2 \, d_3} \int_{-d_1/2}^{d_1/2} \int_{-d_2/2}^{d_2/2} \int_{-d_3/2}^{d_3/2} \frac{\partial \Psi_{abc}}{\partial x_j} \frac{\partial \Psi_{def}}{\partial x_l} \, \mathrm{d}x_1 \, \mathrm{d}x_2 \, \mathrm{d}x_3 \,, \tag{2.85}$$

and its rank depends of the used degree of the polynomial approximation N

$$\mathrm{rank}(\mathbf{\Gamma}) = \frac{(N+1)(N+2)(N+3)}{2} \,. \tag{2.86}$$

Clearly, the higher N leads to better approximation (2.79), but it also substantially increases the computational time. Migliori et al. [9] suggested in 1993 that $N = 10$ is already a good compromise between the computing time and the computational accuracy, but with modern personal computers, N can be set around 20.

In the inverse procedure, the difference between experimentally measured resonant frequencies f^{exp} and calculated resonant frequencies f^{cal} is compared, and the error function

$$\Delta(c_{ij}) = \sum_{n_{\mathrm{assoc.}}} (f_n^{\mathrm{cal}}(c_{ij}) - f_n^{\mathrm{exp}})^2 \,, \tag{2.87}$$

is iteratively minimized, where only the associated frequencies are taken into account. As the RUS method is more sensitive to the shearing modes, the longitudinal wave velocities in some directions (determined e. g. by the *through-transmission* or *pulse-echo* methods described below) can be also incorporated in the inverse procedure. The final set of elastic coefficients c_{ij} is eventually obtained when the error function reaches a desirable accuracy during the iterative minimization process, which could be performed e. g. by a gradient Levenberg-Marquardt algorithm [12]. The accuracy of the evaluated coefficients is then estimated from the goodness of fit between the experimental spectrum and the calculated resonant frequencies [12, 13].

Besides that, the ultrasonic waves velocities can be utilized for an initial guess of the elastic coefficients, applying the equations (2.48–2.54). Usually, the phase velocities are measured by *through-transmission* or *pulse-echo* methods, where both these methods follow the same principle. In the through-transmission method, a sample is placed between two piezoelectric transducers, where one transducer generates the ultrasonic waves, and the propagating waves are detected by the second transducer at the opposite face of the sample. In the pulse-echo method, one transducer generates the ultrasonic waves and also detects the waves reflected

at the opposite free surface of the sample. The phase velocities are then determined from the times of flight at the given distances.

2.2.3 Laser-based resonant ultrasound spectroscopy

This section describes the principles of contactless laser-based RUS apparatus employed at the Department of Ultrasonic Methods, Institute of Thermomechanics of the Czech Academy of Sciences. As of 2020, three separate RUS devices are utilized at this department; they differ in the operating temperatures at which the resonant spectra of the small samples (with the dimensions of several mm^3) can be detected. As the laser-based RUS is fully contactless, the measured sample can be placed into a temperature chamber with a controlled environment. A RUS device with a so-called *Peltier* chamber has operating temperatures between -40 °C and 120 °C, and a RUS device with a high-temperature chamber allows to measure up to 750 °C. A third RUS device is cooled with liquid nitrogen, which thus allows measurements down to cryogenic temperatures (i. e. slightly higher than the boiling point of nitrogen at -196 °C).
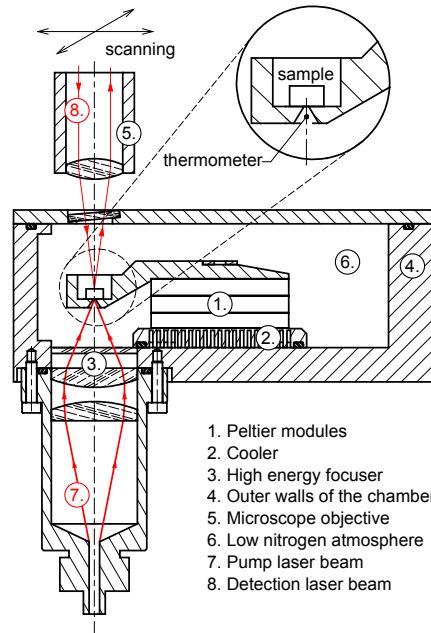
Figure 2.5: Low-pressure *Peltier* chamber of the laser-based resonant ultrasound spectroscopy [13]; in the high-temperature chamber, Peltier modules are replaced by resistive-heating modules.

All RUS measurements presented in this thesis were performed by utilizing either the device with the Peltier chamber or the high-temperature chamber, and these two RUS devices are therefore described in more detail in this section. Both the Peltier chamber and the high-temperature chamber follow the same design, shown in Figure 2.5. The sample is at first placed into the chamber, which is then evacuated (at least to the pressure lower than 10^{-2} mbar) and subsequently filled with nitrogen to approx. 10–20 mbar in order to assure the heat transfer and simultaneously to prevent oxidation of the sample. The sample vibrations are generated by a pulsed-laser beam, which is focused by a high-energy fiber focuser through a small conical hole in the underlay to the bottom surface of the measured sample. The power and duration

of the laser pulses are chosen such that the photothermal generation is mostly provided by the thermoelastic effect [125, 126], where the impact point is quickly heated; the changes in temperature cause rapid expansion in material, resulting in a generation of a broad-band pulse. The vibrations are detected by a laser vibrometer focused on the top side of the sample, and the experimental resonant spectra are then obtained by fast Fourier transform (FFT) of the measured time-amplitude signals.

In the *Peltier* chamber with the operating temperatures between −40 °C and 120 °C, the heating/cooling is arranged by a Peltier cell cascade (numbered 1. in the schematic in Figure 2.5). The laser-based generation of the vibrations is provided by short infrared pulses from Quantel ULTRA Nd:YAG laser (nominal wavelength 1064 nm, pulse duration 8 ns, pulse energy 25 mJ) with a variable repetition rate; usually, a repetition rate of several Hz is used. The vibrations are detected by a scanning laser vibrometer incorporated in Polytec Micro System Analyzer MSA-500, shown in Figure 2.6a, which allows measuring the out-of-plane displacements within the field of view of 3.5 mm × 4.5 mm, when using Mitutoyo M Plan APO 2x/0.055 f=200 objective lens. Usually, a regular mesh with $\sim$ 20 × 20 points on the top surface of the measured sample is used, which allows to properly identify the modal shapes of vibrations for several tens or even hundreds of resonant frequencies. The temperature in the chamber (and between Peltier cells) is monitored by Omega thermocouple sensors and Hayashi Denko PT100 sensor, and the redundant heat is removed by a water-cooling system utilizing JULABO FL1201 recirculating cooler.
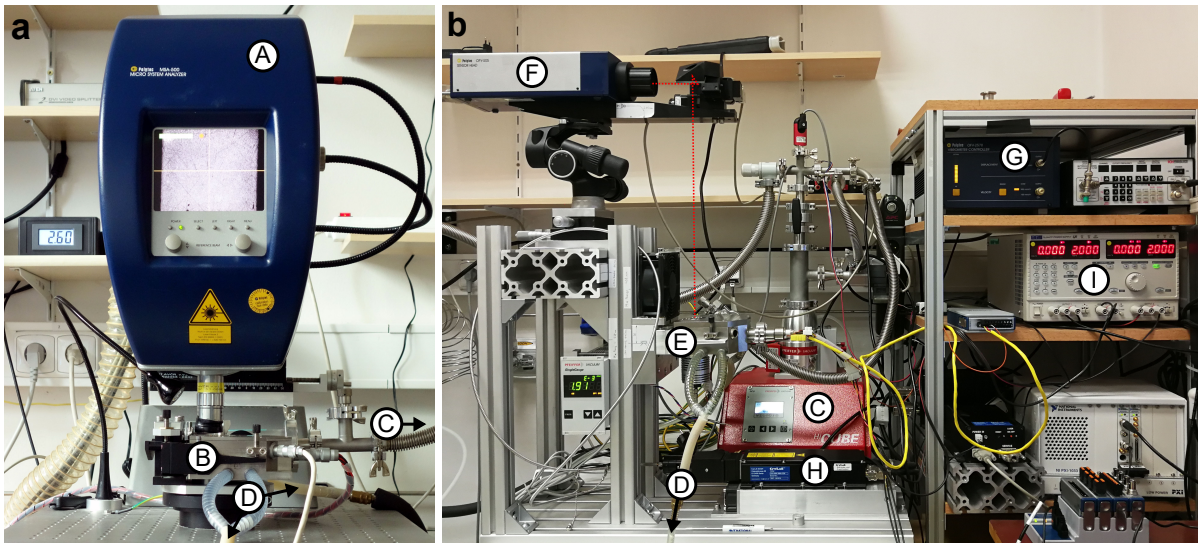

Figure 2.6: Design of the laser-based RUS devices. On the left side, a) Polytec MSA-500 vibrometer head (A) placed above *Peltier* chamber (B) connected to vacuum pumping station (C) and water-cooling system (D). A photo on the right side b) shows the high-temperature chamber (E), Polytec OFV-505 vibrometer head (F), Polytec OFV-2570 vibrometer controller (G), CryLaS DSS 1064-3000 pulsed laser (H), Aim-TTi QL564TP power supply (I). The red dotted line outlines the path of the vibrometer laser beam used for the detection of the sample vibrations.

In the high-temperature chamber, shown in Figures 2.6b and 2.7, the Peltier modules (at position no. 1. in Figure 2.5) are replaced by two OMEGA CSH-202250 cartridge heaters

controlled by Aim-TTi QL564TP power supply. This setup allows measurements from a minimal temperature set by the water-cooling system (usually near the room temperature) up to 750 °C. This temperature is only limited by the working temperature of the cartridge heaters, and thus the measuring temperature of the laser-based RUS could be theoretically even much higher when suitable heating would be utilized; this brings the opportunity for the future development of the RUS devices. The vibrations of the samples are generated by CryLaS DSS 1064-3000 pulsed laser (wavelength 1064 nm, pulse energy 2.8 mJ, pulse length 1.7 ns) with a repetition rate of 5 Hz and detected by Polytec OFV vibrometer system (OFV-2570 vibrometer controller, OFV-505 sensor head).
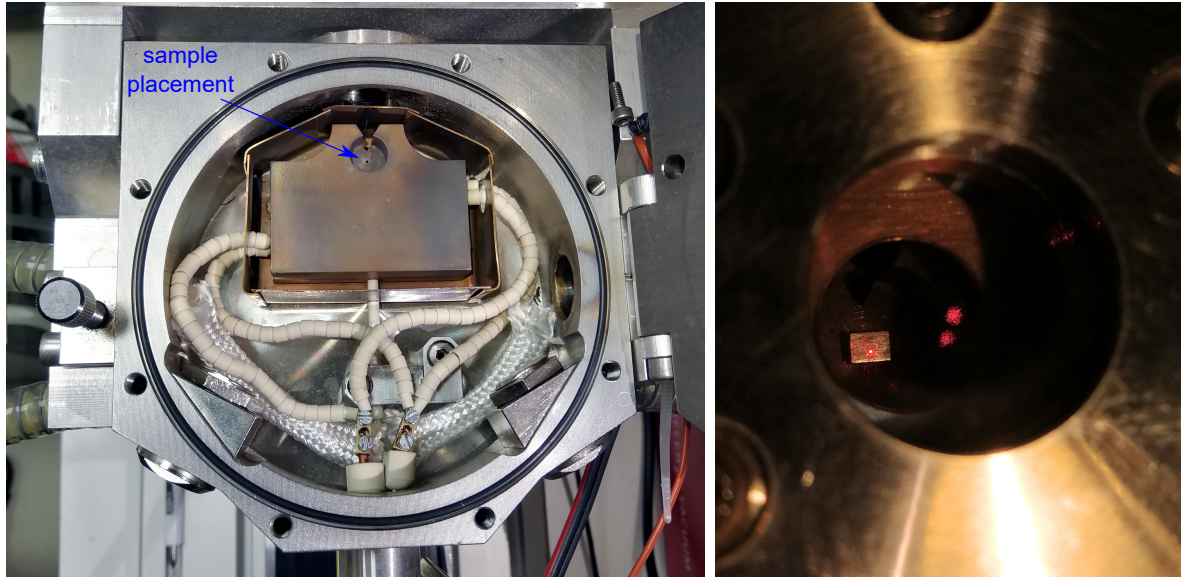
Figure 2.7: The high-temperature RUS chamber. The measured sample is placed over a small hole, as highlighted by a blue arrow in the photo of the open chamber of the left; the pulsed-laser beam, which generates the vibrations of the sample, is focused onto the bottom face of the sample through this hole. The photo on the right side shows a sample placed into the chamber, where the vibrometer laser beam passes through the sapphire window in the top lid of the chamber, and it is focused onto the top face of the sample.

2.2.4 Processing of the experimental data

The measured experimental data are processed in a custom toolbox, running in MATLAB computing environment, which was developed by Dr. Petr Sedlák from the Department of Ultrasonic Methods at the Institute of Thermomechanics. A screenshot of the tool used for the inverse determination of the elastic coefficients from the measured resonant spectrum is shown in Figure 2.8. Figure 2.9 shows a screenshot of another tool, which is utilized for the determination of internal friction Q^{-1} values, where the experimental resonant spectra are fitted with Lorentzian mask, resulting in a quality factor Q values for each of the fitted resonant peaks. This application also allows to upload multiple resonant spectra so that the temperature evolution of the resonant frequencies and Q values can be followed. All results presented in this thesis regarding the RUS measurements were obtained by using this toolbox.
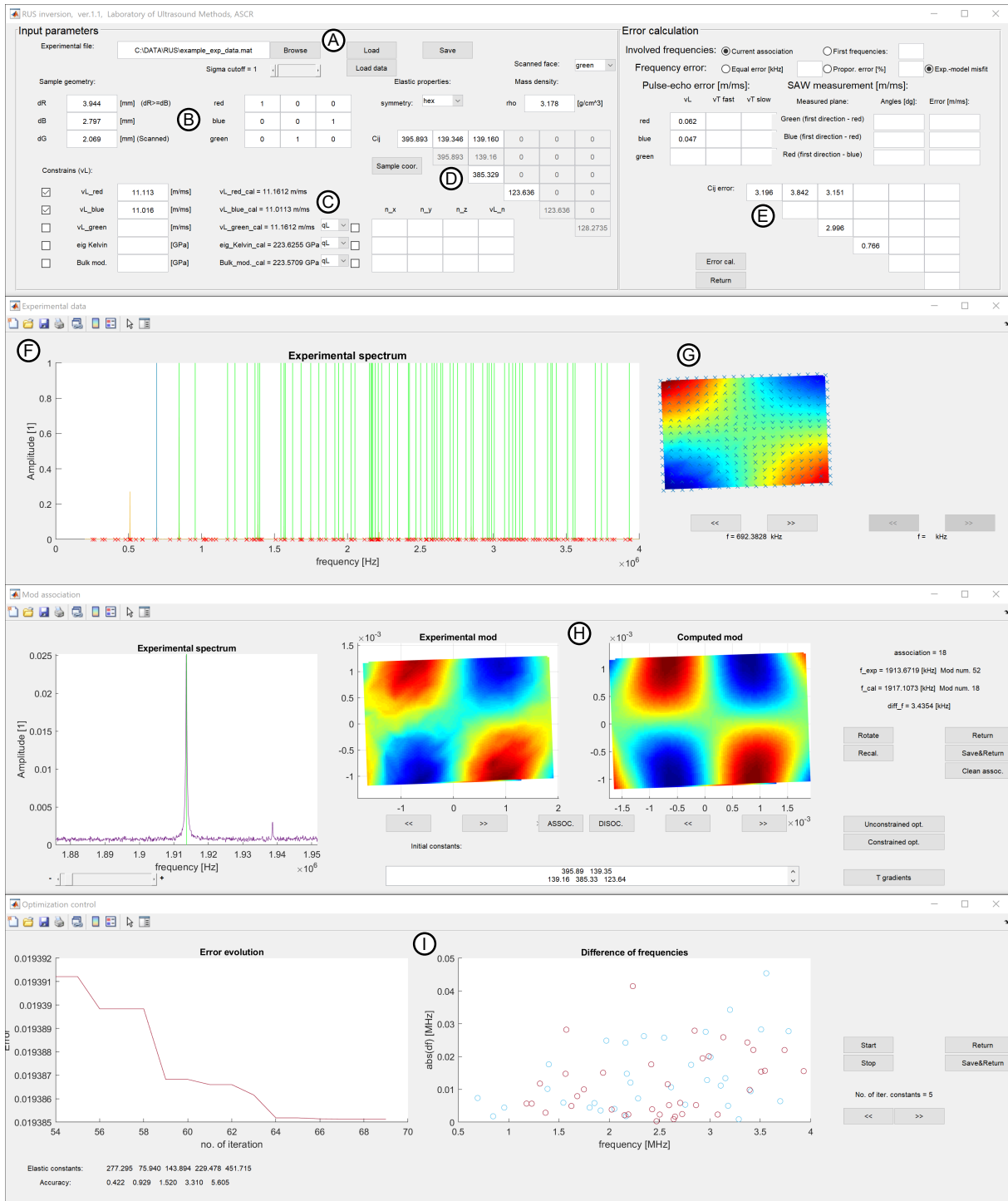
Figure 2.8: Custom MATLAB tool for the inverse determination of elastic coefficients. A file containing the experimental data from the RUS measurement is loaded (A), and the experimental spectrum is shown in (F) with modal shapes of vibrations in (G); also the measuring points are highlighted here. Density, dimensions and crystallographic symmetry of the sample and the orientation of the sample faces are filled in (B). When the velocities of the ultrasonic waves are also measured, they can be filled in (C) and taken into account during the inverse procedure. After an initial guess of the elastic coefficients in (D), the association between the measured and calculated resonant frequencies is performed in (H). Window (I) then depicts the running minimization of the inverse procedure. Each of these steps can be repeated until the best possible association is achieved. The resulting elastic coefficients are then shown in (D), and their errors can be calculated in (E).
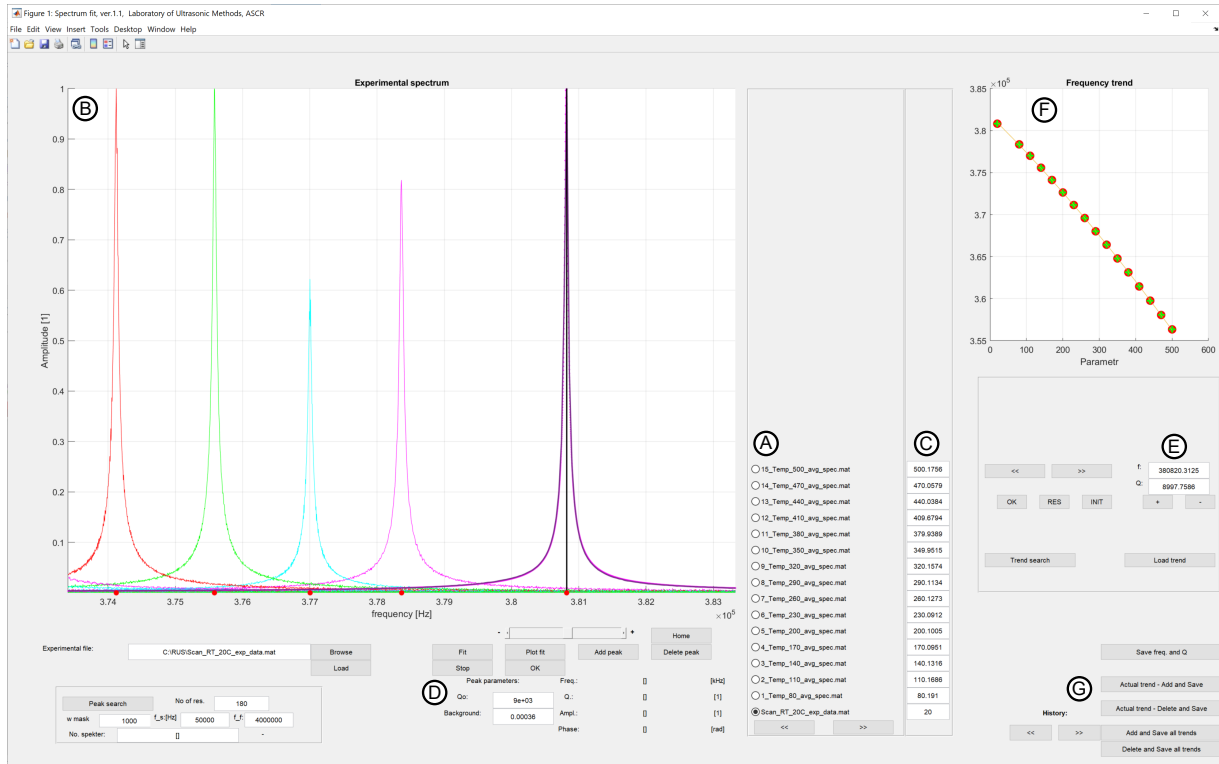
Figure 2.9: A screenshot of a MATLAB tool used for determination of internal friction Q^{-1} and evolution of resonant frequencies. After the experimental files are uploaded to (A), resonant spectra are shown in (B), and the measured temperatures are in (C). Each of the chosen resonant peaks can be then fitted by Lorenztian mask in (D), and the quality factor Q and the frequency of the fitted peak are shown in (E). The temperature evolution of resonant frequencies is shown in (F), and it can be saved in (G), along with the temperature evolution of Q.

2.3 Processing techniques

This section describes the processing techniques that were used for the production of the materials studied in this thesis. The subsection 2.3.1 summarizes the general principles of the spark plasma sintering (SPS) method, and the next subsection 2.3.2 deals with the robocasting method, which has been utilized for producing micro-architectured ceramic scaffolds, where the pressureless SPS is utilized for the consolidation of 3D printed ceramic green bodies.

2.3.1 Spark plasma sintering

Spark plasma sintering (SPS) [1–7, 127–160] (also known as field-assisted sintering technique, FAST [127, 128]) is a sintering technique, where a powder material is consolidated into a bulk pellet by the combination of high temperature, uniaxial pressure, and pulsing direct electric current.

Similarly to the conventional hot pressing, a powder material is placed into a graphite die and uniaxially pressed at a high temperature in a low-pressure environment. In addition, a pulsing direct current, applied through electrodes at top and bottom graphite plungers, passes through the graphite die and the powder compact during the SPS process.
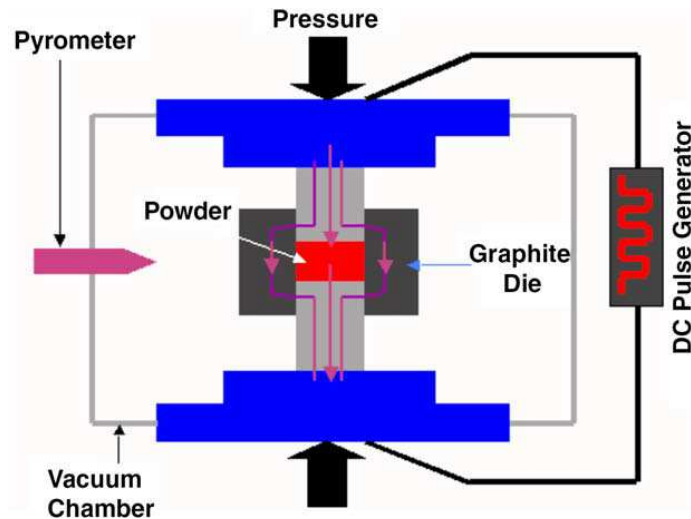

Figure 2.10: Spark plasma sintering apparatus [4].

The heating of the powder samples is induced by resistive Joule heating, resulting from the pulsing direct current distribution, which depends on the die geometry and electrical and thermal conductivities of the die and powder materials [1–3, 129]. For conductive powders, a local increase of temperature by Joule effect at the contacting areas of powder particles is expected to occur, which results in a quick nucleation and the growth of neck connections [130–134]. For non-conductive samples, the Joule heat is generated in the graphite die and the plungers, and is transferred to the powder compact by conduction and radiation. In general, very fast heating rates of hundreds of °C/min can be achieved, and, as a result, almost a full densification is performed in a short holding time, usually in several minutes. Due to the accelerated densification, a wide variety of materials can be fabricated by SPS, including

those that cannot be produced by other powder sintering techniques. Most importantly, grain growth is suppressed, and the microstructure is less affected by the high temperatures when compared to the conventional sintering. Moreover, the SPS is also beneficial from the engineering point of view, as 90–95 % of the total amount of energy can be saved compared to the conventional hot pressing due to the higher productivity and shorter holding times at very high temperatures [135].

The temperature during the SPS consolidation is usually measured either by an optical pyrometer focused on the die surface, or by a thermocouple. Unfortunately, the very fast heating rates of hundreds of °C/min may bring some issues on the proper measurements of the temperature inside the die, as many authors [2, 3, 127, 128, 136–140] have shown that the actual temperature of the powder compact during the sintering can be much higher (even several hundreds of °C higher, depending on the thermal conductivity of the sintered material) than the recorded temperature. It was also shown that a thermocouple inserted in a hole drilled in the graphite die or plunger can indicate more accurate temperatures than an optical pyrometer [2, 136]; nevertheless, it should always be kept in mind that the sintered material could achieve significantly higher temperatures than those detected.

The applied uniaxial pressure helps to enhance the consolidation of the powder [141–143], and if the imposed stress exceeds the yield stress of powder particles, the densification is further accelerated by plastic deformation [7, 144, 145].

The presumed presence of sparks or plasma during the SPS consolidation is still not fully understood. Some authors [5, 7, 131, 137, 145–150] have believed that multiple spark discharges occur at the cavities between the powder particles, where the surrounding gas is ionized, and a high-temperature plasma is created. At the initial stage of sintering, the particles create only small contacts with high local resistivity leading to the intensive Joule heating. Therefore, the temperature of particle surfaces increases and causes local softening, or even melting/evaporation of the surface, which can lead to particles rearrangement by their sliding or rotation. Due to the discharges, the surface is said to be activated and purified, for instance from oxide impurities, which should promote the transfer of material by grain-boundary diffusion and thus enhance the densification.

Nevertheless, Hulbert et al. [151] showed in 2009, using three experimental methods (in situ atomic emission spectroscopy, direct visual observations, and ultrafast in situ voltage measurements), that no type of plasma, arcing or sparking events were observed or detected for a wide variety of powder materials and SPS processing conditions. The measured voltages were approximately one order of magnitude lower than the estimated voltage required for generating plasma in the SPS process. However, the other mechanisms taking place during the SPS processing, such as Joule heating, local softening or melting and intrinsic electric field effects, have been relatively well established [152, 153].

On the other hand, Zhang et al. [146] showed in 2014 that several spark discharges between the graphite plungers occurred during spark plasma sintering, using a SPS apparatus with multiple graphite plungers. When sintering an ultrafine copper powder or the combination of Ti and TiB$_2$ powders, they believed that high-temperature plasma was excited as a result of the electric field of pulsing direct current, since several particles were locally melted. Although it was the first proof that spark discharges really occur during spark plasma sintering, sparking

events taking place directly in the sintered powder materials have not been detected with certainty until now (as of 2020).

As the SPS has been proved as an effective method for producing a wide variety of materials by a rapid consolidation of powders, novel prospective multi-phase composites can be produced by sintering mixtures of different powders. This is highly beneficial for composites made of materials with very dissimilar mechanical or functional properties, which could not be made by the conventional techniques. Several types of such composites are presented in this thesis, namely ceramic composites containing graphene fillers, shown in section 3.1, and metal-matrix composites described in section 3.2.

2.3.2 Robocasting

The last part of this thesis deals with the mechanical properties of periodic ceramic scaffolds, which were produced by an additive-manufacturing direct-ink-writing technique, known as robocasting [161–164]. By this method, the scaffolds are built up layer-by-layer by printing a colloidal gel ink based on a ceramic powder, following a printing route defined by computer aided design (CAD); an example of such a designed scaffold is shown in Figure 2.11a. The printed ceramic bodies are then consolidated by sintering.
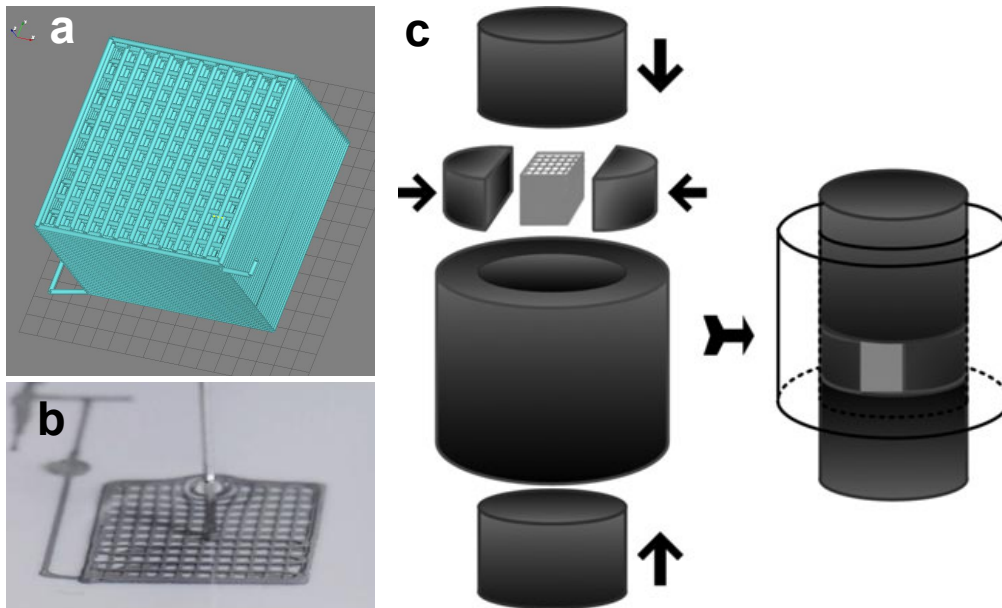

Figure 2.11: a) A tetragonal scaffold designed in RoboCAD 4.0 software [163], b) a photo showing the ink extrusion through a nozzle during the printing process [163], c) a schematic illustration of graphite dies used in the pressureless SPS of the robocast scaffolds [164].

The micro-sized ceramic-based powder is at first mixed with organic additives in order to create a printable ink with shear-thinning pseudo-plastic behavior, which allows to form a thin continuous filament during the printing, but also to preserve the geometry of already-printed previous layers. Depending on the scaffold geometry and the properties of the ink, the printing can be performed in mineral oil, as seen in Figure 2.11b, or directly in air. The printed ceramic green body is dried in air, the organic additives are then burnt out,

and the scaffold is subsequently sintered. When the SPS method is utilized, a pressureless modification of the graphite die is usually used, as shown in Figure 2.11c, where the additional graphite components assure that the scaffolds do not collapse under the external pressure during the sintering. The printed scaffolds well preserve the designed geometry, as can be seen in Figure 2.12, and the ceramic rods are sintered near to full density. However, there is a significant shrinkage during the drying and sintering; depending on the used ceramic powder and the powder/additives ratio of the printable inks, the linear shrinkage could be around 10–30 % [163–165].
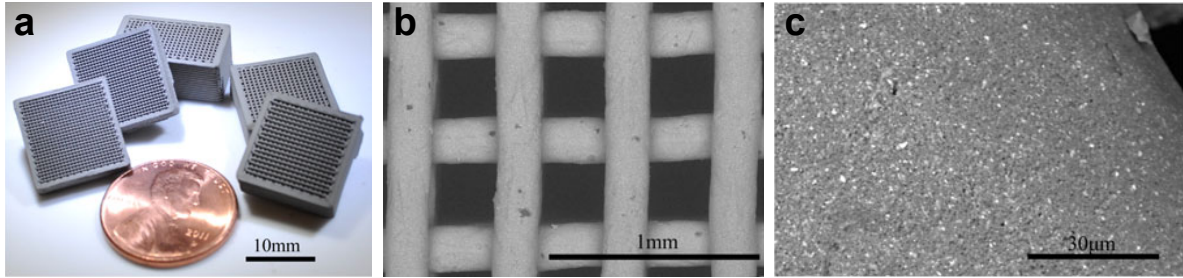

Figure 2.12: Robocast SiC green body scaffolds printed by Cai et al. [164]: a) several types of tetragonal lattices, b) SEM image of a printed green sample from top view, and c) a detail of its surface.

The robocast scaffolds have some unique properties, which result from their specific periodic structure. Due to the high specific surface area, the scaffolds can be utilized in catalytic systems [166–168]. Another possible application of the robocast scaffolds is in bone tissue engineering [169–171], as the micro-architectured scaffolds can meet the structural requirements for the replacements of inner bone tissue.

Elastic and acoustic properties of robocast SiC scaffolds have been already studied at the Institute of Thermomechanics since 2014, which resulted in three publications by Kruisová et al. [172–174]. The first paper [172] has shown that a tetragonal SiC scaffold is highly elastically anisotropic, which also leads to a strong acoustic energy focusing along the direction of the ceramic rods. Acoustic band structure was also studied in this paper and later in [173] by finite element method (FEM), which has shown that this tetragonal scaffold exhibits a phononic-crystal behavior with acoustic band gaps in MHz range. In the next paper [174], the band gap structure of four types of robocast scaffolds (two tetragonal scaffolds and two hexagonal scaffolds with different rod spacing) has been studied both numerically and experimentally, showing how the geometry of the rods within each layer or the orientation of the adjacent layers affect the frequency range of the acoustic band gaps.

The PhD candidate has started working on this topic during his PhD studies, partially following the works of Kruisová et al. [172–174], which has resulted in a publication of three other papers. These papers are included in section 3.3.

Chapter 3

Studied materials and obtained results

This section comprises eight research papers, complemented with interconnecting comments by the PhD candidate. The papers are divided into three sections: the first section 3.1 deals with the anisotropic elastic properties of bulk graphene nanoplatelets and the ceramic-matrix composites reinforced by the graphene fillers. Section 3.2 then deals with metal-matrix composites and their characterization by the laser-based RUS. Section 3.3 describes the mechanical properties of robocast ceramic scaffolds that come from their specific periodic structure. Each of these three sections has the same structure: at first, an introduction to the particular topic is given, describing its relation to the presented thesis; the papers are then included, and the last part of each section summarizes the results obtained by the PhD candidate.

3.1 Sintered graphene nanoplatelets and ceramic composites with graphene fillers

This section includes two research papers that delineate the ability of RUS to characterize spark plasma sintered materials based on graphene nanoplatelets (GNPs). The first paper [A] deals with anisotropic acoustic and elastic properties of sintered GNPs studied by the through-transmission method and the laser-based RUS. In the second paper [B], the anisotropic elastic properties of Si_3N_4-matrix composites with variable content of graphene-based fillers are presented.

Graphene has recently received much attention due to its extraordinary mechanical, electrical and thermal properties [175–179], which makes it a prospective material to be used as a filler in ceramic-matrix composites. As the production of single-layer graphene sheets is still very demanding, graphene nanoplatelets (GNPs), consisting of a few to dozens of graphene layers, are often utilized as graphene-based fillers, as they are much more cost-effective while they still retain many unique properties of graphene.

Spark plasma sintering has been beneficially utilized for producing the ceramic-matrix composites with GNP fillers, as the ceramic matrix is consolidated to a full density in a short time, and degradation of the graphene sheets can be fully avoided [180]. The graphene nanoplatelets often have a preferential orientation perpendicular to the SPS pressure axis, which results in unique anisotropic properties, such as high thermal and electrical conductivity

in the directions parallel to the graphene sheets [181–186]. Moreover, the incorporation of GNPs to the ceramic matrix leads to a significant increase in the fraction toughness [187–196], resulting from a weak bonding between the GNPs and the ceramic matrix. During the crack propagation, GNPs are pulled out from the matrix and a certain amount of energy is thus dissipated due to the friction between the GNPs and the matrix. This results in typical features that can be seen in micrographs of the cracks, such as bridging the cracks by the GNPs, crack deflecting, or branching, as shown in Figure 3.1b.
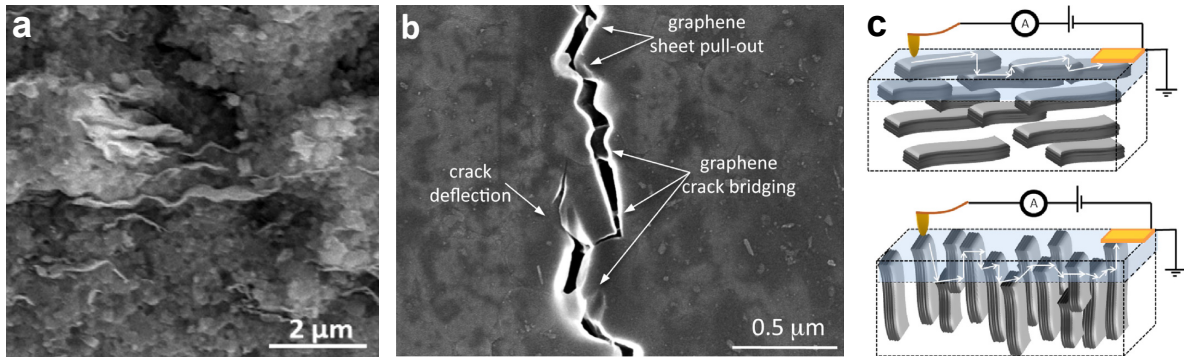

Figure 3.1: a) Microstructure of GNPs/Si$_3$N$_4$ composites produced by Ramírez et al. [184], b) toughening mechanisms in GNPs/Si$_3$N$_4$ composites observed by Walker et al. [187], c) principles of anisotropic electrical conductivity of the GNPs/ceramic composites, as presented by Ramírez et al. [182], with the possible conducting paths highlighted by white arrows.

Elastic properties of Si$_3$N$_4$-GNP composites consolidated by hot isostatic pressing were studied by Kun et al. [197] in 2012, using a four-point bending test. Ramírez et al. [195] later determined the elastic moduli of SPSed Si$_3$N$_4$-GNP composites by indentation testing. The indentation tests were also utilized for determining the elastic properties of other types of SPSed ceramic-matrix composites with graphene-based fillers, e. g. TaC-GNP composites studied by Nieto et al. [192], or Al$_2$O$_3$-rGO composites studied by Fan et al. [198]. All these measurements showed a small decrease in elastic moduli of the composites when compared to the pure sintered ceramics. Nevertheless, these methods could not capture the anisotropy in the elastic coefficients, which results from the preferred orientation of the graphene fillers.

The laser-based RUS has been already utilized for determining a full set of elastic coefficients of a Si$_3$N$_4$-3wt.%GNP composite, where the measurements have been performed by the PhD candidate before the start of his PhD studies, and the results were published in a paper [199] in *Composites Science and Technology* journal. As expected from its microstructure, the composite exhibited the transverse isotropic symmetry with 5 independent elastic coefficients. Figure 3.2 shows Young's modulus distribution of the composite, plotted from the obtained elastic coefficients using the formula (2.10), together with Young's modulus of a pure isotropic Si$_3$N$_4$ sample sintered at the same conditions as the studied composite.

As seen in Figure 3.2, the Si$_3$N$_4$-3wt.%GNP composite has lower Young's modulus E in all directions when compared to the pure Si$_3$N$_4$; the decrease in E along the platelet orientation is about 5 %, while E decreased about 26 % in the direction perpendicular to the platelets. Moreover, the E distribution was shown to be very close to an elliptic approximation [200–203],
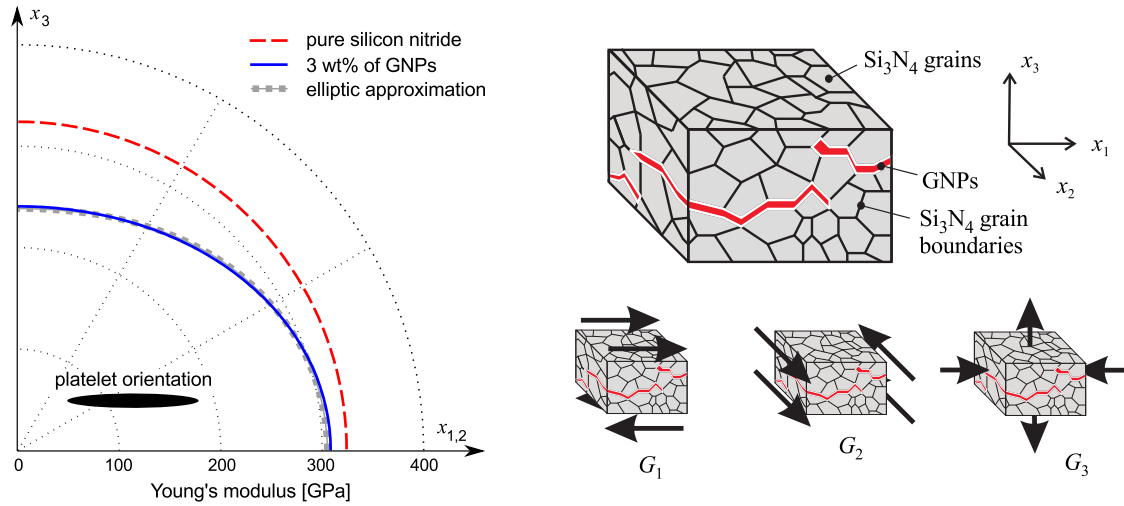
Figure 3.2: Young's modulus of the Si_3N_4-3wt.%GNP composite (solid blue line) and sintered pure Si_3N_4 (dashed red line) distributions, as determined from the elastic coefficients measured by laser-based RUS [199]. A schematic sketch of the micromorphology of the composite is shown on the right, with a geometric interpretation of the three principal shearing modes.

which suggests that the GNPs act as oriented spheroidal voids in the isotropic ceramic matrix; the weak Si_3N_4/GNP bonding results in a slight deviation from this elliptic approximation. The elastic anisotropy was also evident from the shear moduli and internal friction, as the principal shear modulus corresponding to the shear deformations along the preferential plane of the platelets, depicted as G_2 in Figure 3.2, was about 13 % larger than other two principal shear moduli, G_1 and G_3. Moreover, the internal friction Q_2^{-1} value associated with this shearing mode was significantly lower than Q_1^{-1} and Q_3^{-1} values.

In summary, the addition of GNPs to the Si_3N_4 leads to an overall decrease in elastic coefficients, where the GNPs macroscopically act as spheroidal voids, resulting from a weak bonding between the GNPs and the matrix. The anisotropy in the elastic properties was quite pronounced, as the directions with the highest elastic moduli correspond to the directions of the preferential orientation of the platelets; also, the internal friction was the lowest for the shearing mode along the platelets.

During the candidate's PhD studies, the work on graphene-based fillers (motivated by the results obtained in [199]) continued, which has resulted in a publication of two papers in journals with impact factor. The first paper [A] deals with a study of ultrasonic waves propagation and the elastic anisotropy of sintered bulk GNPs. The second paper [B] studies the effect of variable amounts of graphene fillers on the elastic anisotropy of Si_3N_4/graphene composites, where two types of graphene platelets prepared by different methods were used as the fillers [196]. In the composites denoted as Si_3N_4/GNPs, the commercially available graphene nanoplatelets were mixed with the ceramic powder (α-Si_3N_4 with Al_2O_3/Y_2O_3 sintering additives) and consolidated by the SPS. In the composites denoted as Si_3N_4/rGO, the ceramic powder was mixed with graphene oxide sheets, which were subsequently reduced to the graphene during the sintering; the abbreviation rGO stands for *reduced graphene oxide*.

Paper A

Anisotropic elastic and acoustic properties of bulk graphene nanoplatelets consolidated by spark plasma sintering

Martin Koller, Hanuš Seiner, Michal Landa,
Andy Nieto, and Arvind Agarwal

Number of total citations[1]: 4 (excluding self-citations: 2)

Contribution of the PhD candidate and the co-authors:

The candidate measured the time-amplitude signals of the longitudinal and transverse waves propagating through the samples cut from the sintered pellet and determined the velocities and the attenuation coefficients. Moreover, the candidate performed the RUS measurements, evaluated the polar distribution of Young's modulus, and wrote the paragraphs describing these measurements.

Co-authors from the Institute of Thermomechanics (H. Seiner and M. Landa) came up with the concept of the paper and supervised the work. Co-authors from the Florida International University (A. Nieto and A. Agarwal) consolidated the SPS pellet and performed its complementary characterization, including the scanning electron micrograph.

---

[1]According to the Web of Science database `webofknowledge.com` as of August 2020

Anisotropic Elastic and Acoustic Properties of Bulk Graphene Nanoplatelets Consolidated by Spark Plasma Sintering

M. KOLLER[a], H. SEINER[b,*], M. LANDA[b], A. NIETO[c] AND A. AGARWAL[c]

[a]Faculty of Nuclear Sciences and Physical Engineering, Czech Technical University in Prague,
Trojanova 13, 120 00 Prague 2, Czech Republic

[b]Institute of Thermomechanics, Academy of Sciences of the Czech Republic,
Dolejškova 5, 182 00 Prague 8, Czech Republic

[c]Department of Mechanical and Materials Engineering, Florida International University,
10555 West Flagler Str., EC 3464, Miami, FL 33174, USA

Elastic anisotropy and acoustic attenuation in bulk material consisting of consolidated graphene nanoplatelets are studied. The material was prepared by spark plasma sintering, and exhibits highly anisotropic microstructure with the graphene nanoplatelets oriented perpendicular to the spark plasma sintering compression axis. The complete tensor of elastic constants is obtained using a combination of two ultrasonic methods: the through-transmission method and the resonant ultrasound spectroscopy. It is shown that the examined material exhibits very strong anisotropy both in the elasticity (the Young moduli in directions parallel to the graphene nanoplatelets and perpendicular to them differ by more than 20 times) and in the attenuation, where the dissipative effect of the internal friction in the graphene nanoplatelets combines with strong scattering losses due to the porosity. The results are compared with those obtained for ceramic-matrix/graphene nanoplatelet composites by the same ultrasonic methods.

1. Introduction

Graphene exhibits unique mechanical properties, such as superior tensile strength [1] and extremely high in-plane elastic modulus [2]. In order to utilize these properties for enhancement of the mechanical performance of ceramics, graphene nanoparticles (such as nanotubes and nanoplatelets) are often used as fillers for ceramic matrix composites (CMCs) [3–5]. Various CMCs with highly oriented graphene-based filaments were prepared by the spark plasma sintering (SPS) technique [6–8]. These composite materials exhibit, besides the expected improved fracture toughness, also significant anisotropies in electric conductivity [6], thermal conductivity [7, 9], elastic stiffness and internal friction [10]. Recently, Nieto et al. [11] reported on a bulk material consisting purely of the graphene nanoplatelets (GNPs) consolidated together by the SPS. This material was shown to exhibit unique tribological properties, utilizing the lubricating effect of graphene. However, the highly porous anisotropic microstructure of this material can be expected also to induce extremely strong anisotropy of elastic and acoustic properties. Such an analysis is carried out in this paper, with the main aim to show the relation between the orientation of the GNPs and the macroscopic elasticity and elastodynamics of the bulk material.

2. Material and samples

The examined material was a bulk aggregate of GNPs consolidated by SPS. A detailed description of the synthesis and properties of this material can be found elsewhere [11], here we bring only a brief summary: GNPs (XG Sciences, US) with thickness of 6 to 8 nm ($\approx$20 layers of graphene) and average diameter of 15 μm were consolidated by SPS at 1850 °C with pressure 80 MPa for holding time of 10 min. The obtained bulk pellet had the thickness of 3 mm and diameter of 20 mm. The mass density of bulk GNPs was measured as 2.11 g/cm^3 which is significantly higher than the density 1.82 g/cm^3 of the original GNP powder.

After SPS consolidation, GNPs were uniformly oriented with their preferred plane perpendicular to the thickness of the sample, as seen in Fig. 1. The Raman spectroscopy (see [11] for more details) proved that individual GNPs retained their graphene content after SPS consolidation and did not transform to any other allotrope of carbon. Some of the individual GNPs were not strictly straight, but they were bent and folded at some places resulting from high applied pressure during SPS processing.

At the macroscale, the material shown in Fig. 1 can be expected to exhibit transversal isotropy, i.e. rotational symmetry about the SPS compression axis, as usual for SPSed composites with spatially anisotropic arrangement of the individual constituents [10].

The anisotropic elasticity of such a material is describable by five independent elastic coefficients: c_{11}, c_{12}, c_{13},
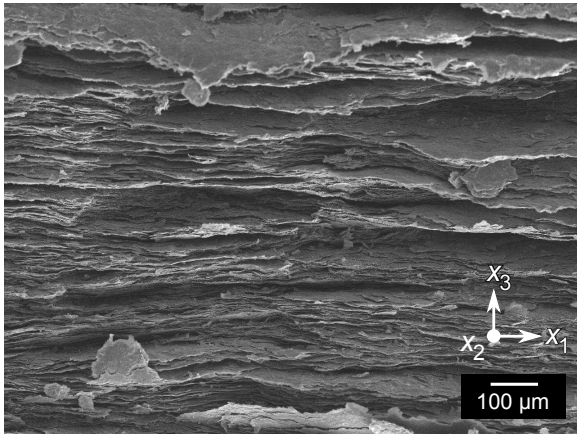
---
*corresponding author; e-mail: hseiner@it.cas.cz

Fig. 1. Scanning electron micrograph of a fracture surface of the examined material. The vertical axis is parallel to the SPS pressing direction, the layered structure outlines the orientation of the GNPs.

c_{33} and c_{44} for the coordinate system oriented such that the axis x_3 is perpendicular to the GNPs. However, in this case it is more illustrative to use $c_{66} = (c_{11} - c_{12})/2$ as one of the independent coefficient instead of c_{12}, as c_{66} represents the shear modulus for shearing perpendicular to the platelets, and can be, thus, directly compared to the shear modulus along the platelets c_{44}.

From the SPS pellet, samples for the ultrasonic characterization were cut out. Two sets of rectangular parallelepiped-like samples were prepared: The first set (4 samples) had the largest faces of the samples parallel to preferred orientation of the GNPs and varying thicknesses (0.52, 0.82, 0.88 and 1.07 mm) in direction perpendicular to this largest face. The second set (3 samples, thicknesses 0.72, 0.88 and 1.25 mm) had the largest faces perpendicular to the GNPs preferred plane. These samples were used for the through-transmission method measurements [12]. Hereafter, the samples from these two sets will be denoted as $T_{1-4}^{\parallel}$ and $T_{1-3}^{\perp}$, respectively, where the symbol in the superscript denotes the orientation of the sample with respect to the GNPs and the number in the subscript is the number of the sample. Additionally, two samples in forms of thin rectangular plates were prepared for the resonant ultrasound spectroscopy (RUS, [13, 14]) measurements. One of these plates (thickness 0.21 mm, lateral dimensions 2.27 mm ×3.40 mm) was oriented parallel to the preferential orientation of the GNPs, the second one (thickness 0.40 mm, lateral dimensions 1.87 mm ×2.81 mm) was oriented perpendicularly to this plane. These samples will be denoted as RUS$^{\parallel}$ and RUS$^{\perp}$, respectively.

3. Experimental

Two ultrasonic methods were applied to the prepared samples. Firstly, the velocities of longitudinal and transverse elastic waves traveling in directions perpendicular

and parallel to the GNPs, were obtained by through-transmission measurements on sets $T_{1-4}^{\parallel}$ and $T_{1-3}^{\perp}$. For the set $T_{1-3}^{\perp}$ (i.e. for the propagation along the GNPs) shear waves polarized both along the GNPs and perpendicular to them were detected; for the set $T_{1-4}^{\parallel}$ (i.e. propagation in direction perpendicular to GNPs), no such distinguishing between the polarization directions was necessary, since all possible polarization directions of the shear waves propagation along the x_3 axis are equivalent due to the transversal isotropy.

Then, the vibrational spectra of free elastic vibrations of samples RUS$^{\parallel}$ and RUS$^{\perp}$ were recorded using the contact-less RUS setup described in details in [14]. As shown for example in [15], the through-transmission method and the RUS are complementary to each other, since the through-transmission method is highly sensitive to the hard (mostly longitudinal) elastic coefficients, while the RUS measurements are suitable mainly for the determination of the softest (mostly shear) elastic coefficients.
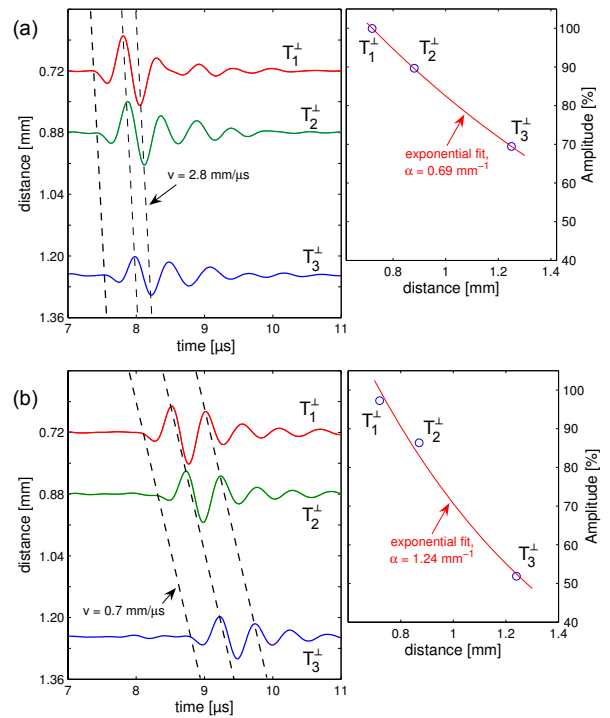

Fig. 2. Experimental data processing examples for transmission through measurements on the samples belonging to the set $T_{1-3}^{\perp}$: (a) shear waves polarized along the GNPs; (b) shear waves polarized parallel to the GNPs.

For the through-transmission measurements, ultrasonic transducers with various nominal frequencies were used, in order to analyze the possible frequency dependence. For the longitudinal wave measurements, transducers at 5 MHz and 10 MHz were used, and for the shear (transversal) measurements, transducers at 2 MHz

and 5 MHz were used. In addition to the velocities of the acoustic waves, the through-transmission measurements enabled also the determination of the acoustic attenuation coefficients α for the individual propagation modes. For each set of the samples, this coefficient was determined from the amplitudes A of the transmitted signals by assuming [12]:

$$A = A_0 \exp(-\alpha d) \tag{1}$$

where A_0 is a constant and d is the traveling distance. Figure 2 shows an example of through-transmission measurement results for determination of the velocity (from the times-of-flight of the waves through the samples) and of the attenuation coefficient (from the amplitudes; the experimental error in α was then determined from the goodness-of-fit of the $A(d)$ data by relation (1)).

The RUS spectra for the samples were recorded in the frequency range 50–500 kHz. Due to the high damping, only a very limited number of resonant peaks was detectable for each sample. In particular, for sample RUS$^\perp$, 7 resonant peaks were detected, and for sample RUS$^\parallel$, 8 resonant peaks were detected. For each detected resonant peak, also the corresponding modal shape of vibrations was determined by a scanning laser vibrometer.

4. Results and discussion

The results of the through-transmission method (the velocities of the propagation and the corresponding attenuation coefficients) for both sets of samples are listed in Tables I and II. It is clearly seen that the velocity of both the longitudinal and the shear waves exhibits strong anisotropy, and so does the attenuation coefficient. Systematically, the velocities of propagation for all modes and at all frequencies in directions along the GNPs are significantly higher than the corresponding velocities in directions perpendicular to the GNPs.

Only the longitudinal waves appear to be frequency-dependent; especially the velocity of propagation along the GNPs and the corresponding attenuation coefficient differ significantly for 10 MHz and for 5 MHz. This indicates that there is some wave-guiding effect of the platelets occurring in the material.

Another interesting phenomenon appears for the shear waves. From assuming the transversal isotropy, the velocity of the shear waves propagating along the x_3 direction (and polarized along the $x_1 x_2$ plane) should be exactly the same as the velocity of the shear waves propagating along the x_1 direction and polarized along the x_3 direction. Similar equality should be valid also between the attenuation coefficients, providing that the viscoelasticity of the material exhibits the same symmetry class as the elasticity. However, as seen in Table II, the waves propagating perpendicularly to GNPs (i.e. along the x_3 direction) and polarized along them are significantly slower and more attenuated than those propagating along GNPs and polarized perpendicular to them. This discrepancy can be easily explained by the fact that the attenuation of the waves propagation perpendicular

Results of longitudinal wave through-transmission measurements: velocities v and attenuation coefficients α.

Frequency	Direction	v [mm/μs]	α [mm^{-1}]
5 MHz	$\parallel$ GNPs	5.6±0.1	0.9±0.3
10 MHz	$\parallel$ GNPs	4.7±0.2	1.4±0.3
5 MHz	$\perp$ GNPs	1.3±0.1	2.9±0.7
10 MHz	$\perp$ GNPs	1.2±0.1	5.2±1.0

Results of shear wave through-transmission measurements: velocities v and attenuation coefficients α for different polarization orientations.

Freq.	Direct.	Polariz.	v [mm/μs]	α[mm^{-1}]
2 MHz	$\perp$ GNPs	$\parallel$ GNPs	0.68±0.03	2.1±0.5
5 MHz	$\perp$ GNPs	$\parallel$ GNPs	0.68±0.02	2.0±0.5
2 MHz	$\parallel$ GNPs	$\perp$ GNPs	0.73±0.03	0.7±0.2
5 MHz	$\parallel$ GNPs	$\perp$ GNPs	0.77±0.03	1.1±0.3
2 MHz	$\parallel$ GNPs	$\parallel$ GNPs	2.8±0.2	1.2±0.5
5 MHz	$\parallel$ GNPs	$\parallel$ GNPs	2.9±0.2	1.3±0.5

to the GNPs is given not only by the viscoelasticity of the material but also by scattering of the waves on flat pores and imperfect bondings between the platelets. This scattering effectively increases the attenuation and decreases the measured velocity of propagation [16]. The observed large difference in both the velocities and the attenuation coefficients indicates that the effect of scattering is very strong; such pronounced anisotropic scattering is expectable with respect to the layered structure of the material.

The outputs of the both experimental methods (i.e. the velocities of longitudinal and shear waves in the given directions and the resonant frequencies of the RUS samples) were recalculated into the elastic coefficients by using a joint inverse procedure described in [17]. This procedure finds such a set of elastic constants that the misfit between the input parameters (i.e. the experimentally obtained velocities and the resonant frequencies) and the values of these parameters calculated for the this set of elastic constants is minimal in the least squares sense. For this procedure, the velocity data obtained at lower frequencies (5 MHz for the longitudinal waves and 2 MHz for the shear waves) were used.

The resulting elastic constants were $c_{11} = (66.17 \pm 2.34)$ GPa, $c_{13} = (9.14 \pm 1.29)$ GPa, $c_{33} = (3.57 \pm 0.51)$ GPa, $c_{44} = (1.15 \pm 0.05)$ GPa, and $c_{66} = (17.76 \pm 1.71)$ GPa, where the errors were calculated by a sensitivity analysis described in [14]. This set of elastic constants confirms the strong anisotropy deduced from the through-transmission measurements: the longitudinal stiffness along the platelets (c_{11}) is significantly stiffer than perpendicular to them (c_{33}); similar difference can be seen between the shear stiffness along the platelets (c_{44}) and perpendicular to them (c_{66}). In Fig. 3, these
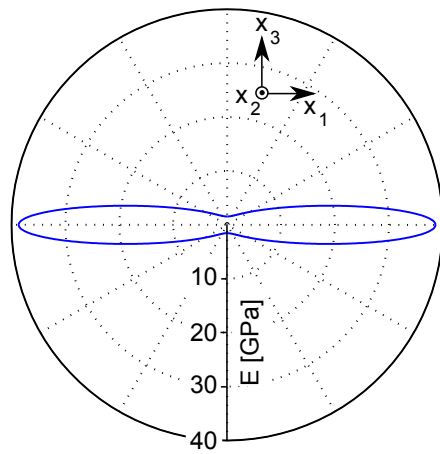
Fig. 3. Directional dependence of the Young modulus in the $x_1 x_3$ plane.

elastic constants are visualized by a plot of the directional dependence of the Young modulus in the $x_1 x_3$ plane. It can be seen that the Young modulus is the highest in the transversely isotropic plane ($E_1 = 38.66$ GPa) and the smallest in direction perpendicular to this plane ($E_3 = 1.55$ GPa). However, the Young moduli both in the in-plane and out-of-plane directions are incomparably smaller than those of graphite ($E_1 = 1.03$ TPa and $E_3 = 36.1$ GPa [18]), probably because of the porosity and the micromechanics of the GNPs in the studied material similar to the one suggested for GNPs embedded in a ceramic matrix in [10]. Nieto et al. [11] reported on the Young moduli of the bulk GNPs measured by nanoindentation with significantly different results ($E_3 = 8.7$ GPa and E_1 exhibiting a bi-modal distribution with the values $E_1 = 10.3$ GPa and $E_1 = 15.2$ GPa). This indicates that the elasticity of the GNP bulk material is strongly amplitude-dependent. The elastic moduli determined by the ultrasonic measurements (amplitudes $\varepsilon \approx 10^{-6}$) correspond to purely elastic straining of the GNPs, including reversible sliding of the platelets, while for much larger strains the material is subjected to under the indenter, the measured elasticity corresponds probably also to folding of the platelets, pore closing and irreversible sliding. As a result, the elasticity determined by nanoindentation is much less anisotropic, since the highly oriented spatial arrangement of the GNPs deteriorates under the large loads induced by the indenter.

The resulting set of elastic coefficients c_{ij} can be possibly also used for rough estimates of the anisotropic elasticity of the CMC including some given amount GNPs by means of some rule of mixtures. For example, for the silicon nitride/GNP composite reported in [10], the Hill averaging method (using $E = 324$ GPa for pure silicon nitride and the above obtained results $E_1 = 38.66$ GPa and $E_3 = 1.55$ GPa for GNPs) gives $E_1 = 273$ GPa and $E_3 = 168$ GPa. However, the experimental results $E_1 = 308$ GPa and $E_3 = 240$ GPa for this CMC [10] are

significantly higher. This difference may indicate either that the GNPs embedded in ceramic matrices are better anchored than those in the examined material, or that the elasticity of the bulk GNPs is still significantly softened by porosity and weak interconnections between the individual platelets.

5. Conclusions

The ultrasonic measurements reported in this paper show that the bulk GNP material under study is highly anisotropic in acoustic properties such as speed of ultrasonic longitudinal and transverse waves and their attenuation.

The corresponding elastic coefficients are significantly more anisotropic than those obtained previously by nanoindentation, but simultaneously much less anisotropic that the elastic constants of graphite.

From the attenuation measurements, it is obvious that the elastic waves propagation in this material is damped at least by two different mechanisms: viscous energy dissipation probably due to mutual sliding of the GNPs (cf. [10]) and scattering of the waves on the layered porous structure. The attenuation coefficients obtained especially for the wave propagation perpendicular to the GNPs are very high, which suggest the possible application of the bulk GNPs as acoustic shock absorbers or as components of materials for acoustic energy redirection or cloaking.

References

[1] C. Lee, X. Wei, J.W. Kysar, J. Hone, *Science* **321**, 385 (2008).

[2] K.H. Michel, B. Verberck, *Phys. Status Solidi B* **245**, 2177 (2008).

[3] A. Nieto, D. Lahiri, A. Agarwal, *Mater. Sci. Eng. A* **582**, 338 (2013).

[4] L.S. Walker, V.R. Marotto, M.A. Rafiee, N. Koratkar, E.L. Corral, *ACS Nano* **5**, 3182 (2011).

[5] O. Malek, J. González-Julián, J. Vleugels, W. Vanderauwera, B. Lauwers, M. Belmonte, *Mater. Today* **14**, 496 (2011).

[6] C. Ramirez, L. Garzón, P. Miranzo, M.I. Osendi, C. Ocal, *Carbon* **49**, 3873 (2011).

[7] G.D. Zhan, J.D. Kuntz, H. Wang, C.M. Wang, A.K. Mukherjee, *Philos. Mag. Lett.* **84**, 419 (2004).

[8] C. Ramírez, S.M. Vega-Diaz, A. Morelos-Gómez, F.M. Figueiredo, M. Terrones, M.I. Osendi, M. Belmonte, P. Miranzo, *Carbon* **57**, 425 (2013).

[9] P. Miranzo, E. García, C. Ramírez, J. González-Julián, M. Belmonte, M.I. Osendi, *J. Eur. Ceram. Soc.* **32**, 1847 (2012).

[10] H. Seiner, P. Sedlák, M. Koller, M. Landa, C. Ramírez, M.I. Osendi, M. Belmonte, *Compos. Sci. Technol.* **75**, 93 (2013).

[11] A. Nieto, D. Lahiri, A. Agarwal, *Carbon* **50**, 4068 (2012).

[12] M. Levy, H.E. Bass, R.R. Stern, *Handbook of Elastic Properties of Solids, Liquids, and Gases*, Vol. 1, *Dynamic Methods for Measuring the Elastic Properties of Solids*, Academic Press, New York 2000.

[13] R.G. Leisure, F.A. Willis, *J. Phys. Condens. Matter* **9**, 6001 (1997).

[14] P. Sedlák, H. Seiner, J. Zídek, M. Janovská, M. Landa, *Exp. Mech.* **54**, 1073 (2014).

[15] M. Landa, P. Sedlák, H. Seiner, L. Heller, L. Bicanová, P. Šittner, V. Novák, *Appl. Phys. A* **96**, 557 (2009).

[16] R. Truell, C. Elbaum, B.B. Chick, *Ultrasonic Methods in Solid State Physics*, Academic Press, New York 1969.

[17] M. Janovská, P. Sedlák, H. Seiner, M. Landa, P. Marton, P. Ondrejkovič, J. Hlinka, *J. Phys. Condens. Matter* **24**, 385404 (2012).

[18] E.J. Seldin, C.W. Nezbeda, *J. Appl. Phys.* **41**, 3389 (1970).

Paper B

Elastic properties of silicon nitride ceramics reinforced with graphene
nanofillers

Hanuš Seiner, Cristina Ramirez, **Martin Koller**, Petr Sedlák, Michal Landa,
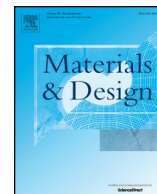Pilar Miranzo, Manuel Belmonte, Maria Isabel Osendi

Number of total citations[1]: 28 (excluding self-citations: 25)

Contribution of the PhD candidate and the co-authors:

The candidate measured the velocities of longitudinal waves, determined the elastic coefficients from the laser-based RUS measurements, and evaluated the distributions of Young's modulus and Poisson's ratio.

Co-authors from the Institute of Thermomechanics (H. Seiner, P. Sedlák, M. Landa) came up with the concept of the paper and were responsible for the discussion of the obtained results. Co-authors from the Institute of Ceramics and Glass (C. Ramirez, P. Miranzo, M. Belmonte, and M. I. Osendi) prepared the graphene/ceramic mixture, consolidated and characterized the composites, including the micrographs of the fracture surfaces and the Vickers indents, and coordinated and supervised the work on the paper.

---

[1]According to the Web of Science database `webofknowledge.com` as of August 2020

Elastic properties of silicon nitride ceramics reinforced with graphene nanofillers

Hanuš Seiner [b], Cristina Ramirez [a], Martin Koller [c], Petr Sedlák [b], Michal Landa [b], Pilar Miranzo [a], Manuel Belmonte [a], Maria Isabel Osendi [a,*]

[a] *Institute of Ceramics and Glass (ICV), CSIC, Campus Cantoblanco, 28049 Madrid, Spain*
[b] *Institute of Thermomechanics, Academy of Sciences of the Czech Republic, Dolejškova 5, 18200 Prague, Czech Republic*
[c] *Faculty of Nuclear Sciences and Physical Engineering, Czech Technical University in Prague, Trojanova 13, 12000 Prague, Czech Republic*

A B S T R A C T

Elastic constants of silicon nitride composites with variable content (3–18 wt.%) of two kinds of graphene fillers (nanoplatelets and reduced graphene oxide sheets) are determined using resonant ultrasound spectroscopy. The corresponding Young's modulus (E), shear modulus (G) and Poisson's ratio (ν) are calculated for each material. Composites show a noticeable anisotropy that grows stronger with the graphene filler content, owing to the preferential alignment of the graphene layers and to their own anisotropy as well. E and G monotonically decrease with the filler concentration for both types of fillers, showing a maximum decrease in E of 75% along the direction perpendicular to the graphene plane for the composite with the highest filler content (Si_3N_4–18 wt.% GNP) and a reduction in G of 63% for shear along the graphene plane for the same composite. Influence on the fracture pattern of the composites is also addressed.

© 2015 Elsevier Ltd. All rights reserved.

1. Introduction

Ceramic composites reinforced with multilayer graphene nanofillers and consolidated by spark plasma sintering (SPS) can reach significant toughening enhancement and exhibit electrical conduction as well, thus becoming attractive multifunctional composites. Most of the studies about these composites are devoted to the toughness enhancement in a gamut of ceramic matrices owing to these fillers [1–4]. Nevertheless, not much attention has been paid to examine their elastic properties [5–7], which are fundamental for their structural performance. Actually, this performance can be particularly affected when a preferential orientation of the fillers occurs, such as it happens for graphene/ceramic composites fabricated by SPS [5,8]. It has been shown that the preferred orientation of the graphene layers induces anisotropy of the electrical and thermal properties of Si_3N_4/graphene composites [9,10] but also of their elastic constants [6].

Silicon nitride (Si_3N_4) polycrystalline ceramics display basically isotropic elastic behavior with two independent elastic constants [6]. In the absence of any crystallographic texture, the anisotropy of α- and β-Si_3N_4 single crystals [11,12] homogenizes into fully isotropic elasticity of the polycrystalline ceramics. In this paper, we discuss the change of this bulk isotropic behavior due to the presence of two different types of graphene nanofillers: the so-called graphene nanoplatelets (GNPs) and reduced graphene oxide (rGO). Both types of nanofillers consist in stacks of graphene layers – pristine in the case of GNPs and defective for rGOs – with a range of thickness that varies from the monolayer up to more than 300 layers in some cases. A finite graphene sheet can be expected to exhibit an orthotropic behavior [13]; however, if we consider stacks with a certain number of graphene sheets, we could assume transversely isotropic elastic characteristics with five independent elastic constants, approaching those of highly oriented pyrolytic carbon [14]. In addition to this intrinsic elastic anisotropy, these fillers exhibit also anisotropy of spatial arrangement within the matrix, which is then reflected by the macro-scale properties of the composite. Therefore, it seems reasonable to look into the effect of these nanofillers on the elastic constants of an essentially isotropic matrix; especially when there is only one paper addressing this matter [6], formerly reported by the present authors. In that work the transversely isotropic nature of Si_3N_4 with 3 wt.% GNPs was established by means of resonant ultrasound spectroscopy (RUS), observing a reduction of 23% of the elastic modulus in the SPS compression direction [6]. In the present paper, we go one step further studying the variation of the elastic constants and elastic moduli of silicon nitride ceramics as a function of filler content for two types of graphene

* Corresponding author.
E-mail address: miosendi@icv.csic.es (M.I. Osendi).
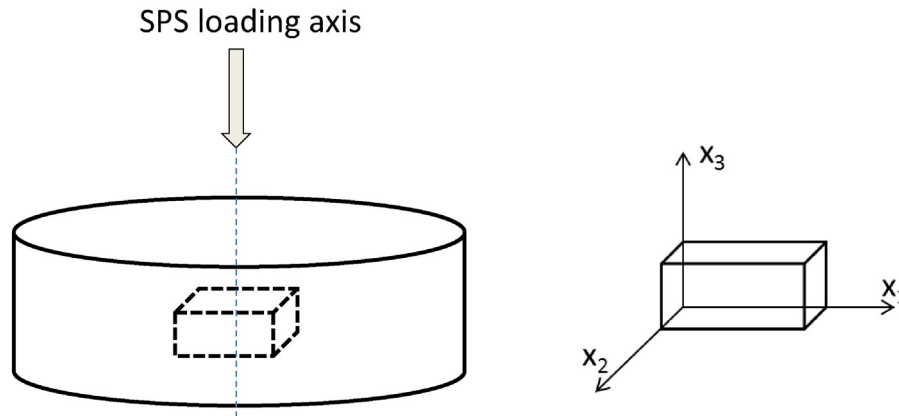
SPS loading axis

Fig. 1. Scheme showing orientation of RUS specimens with reference to the SPS disk.

fillers, i.e. GNP and rGO, and for contents beyond the contacting limit for those fillers.

2. Experimental details

2.1. Materials

The composites were prepared using GNPs and GO sheets, respectively, following the same route as described elsewhere [15]. In short, the matrix composition, equal in both cases, was a blend of α-Si$_3$N$_4$ (E-10, Ube Corp.) powders plus 2 wt.% Al$_2$O$_3$ (Baikalox-SM8) and 5 wt.% Y$_2$O$_3$ (HC-Starck) used as sintering aids, all dispersed in alcohol media. GNPs are commercial nanoplatelets (N002 from Angstron Materials) that were dispersed in isopropyl alcohol using a sonication bath and then mixed with the ceramic powder dispersions in the same media. GO sheets prepared by the modified Hummers method [16] were re-dispersed in ethanol and blended with the matrix slurry – ethanol media – by sonication and blade mixing. Densification took place by spark plasma sintering (SPS) (Dr. Sinter, SPS-510CE) at 1625 °C for 5 min under vacuum of ~4 Pa and 50 MPa of uniaxial pressure. Five compositions were prepared, with three of them having 3, 10 and 18 wt.% of GNPs and the other two with 3 and 5 wt.% of rGO — GO sheets become reduced during the SPS. The reason for the lower filler concentration used in rGO composites is their higher exfoliation, as rGO composites are electrically connected for contents ~4 wt.% [17] whereas in GNP composites the connected network occurs at ~8 wt.% [9]. Therefore, concentration of 18 wt.% GNPs is well beyond the connecting limit.

Parallelepipeds of $4 \times 3 \times 2$ mm^3 were machined from the sintered disks (20×3 mm^2) as shown in Fig. 1. Density of composites was determined by the water immersion method. The microstructure of fractured specimens was observed using field emission scanning electron microscopy (FE-SEM, Hitachi S-4700).

2.2. RUS method

These parallelepiped-shaped samples were used for resonant ultrasound spectroscopy (RUS) [18,19] measurements. Resonant spectra of free elastic vibrations of these samples were recorded by a laser-based, fully non-contact RUS setup [20], and then these spectra were processed to calculate the elastic constants by numerical inverse algorithms described also in detail in Ref. [20]. For each sample, at least 20 resonant modes were identified in the measured frequency range 100 kHz–2 MHz, which enabled the calculation of all independent elastic constants for each material under the assumed transversal isotropy (see the next section). To increase the experimental accuracy, the RUS measurements were complemented by pulse-echo measurements of velocity of longitudinal acoustic waves in directions perpendicular to the individual faces of the samples [20]. All acoustic measurements were performed at 20 °C in a temperature-controlled chamber and in a low-pressure (20 mbar) nitrogen atmosphere.

3. Results and discussion

Relative densities of the Si$_3$N$_4$ and the composites were in the range 99.7–99.9% and matrix consisting in a blend of α and β phases (β-Si$_3$N$_4$
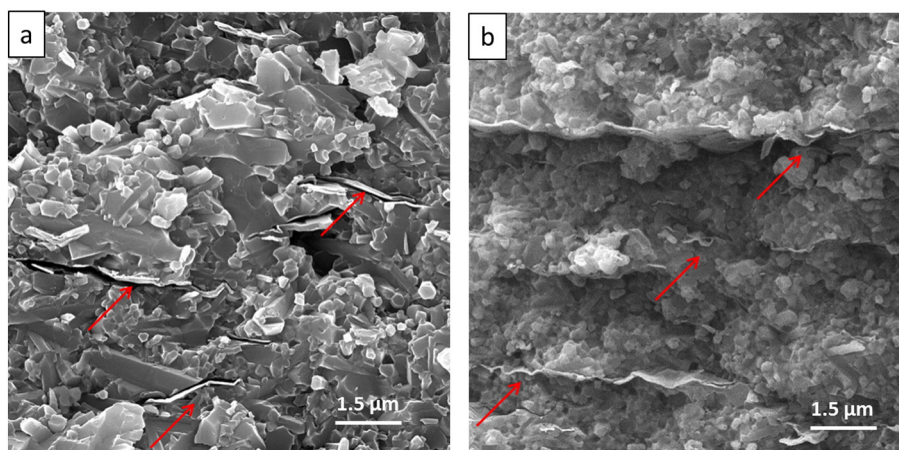

Fig. 2. FE-SEM micrographs of fracture surfaces for Si$_3$N$_4$ with 3 wt.% of (a) GNP and (b) rGO fillers. Vertical axis in the images coincides with SPS loading axis.

Table 1
Elastic constants calculated from RUS experiments for the examined materials.

	Pure Si$_3$N$_4$ [6]	3 wt.% GNP	10 wt.% GNP	18 wt.% GNP	3 wt.% rGO	5 wt.% rGO
c_{11} [GPa]	396.2 ± 0.4	367.9 ± 0.8	295.7 ± 0.7	238 ± 5	361 ± 1	312 ± 4
c_{12} [GPa]	133.8 ± 0.4	121 ± 1	82.6 ± 0.9	61 ± 5	120 ± 1	100 ± 5
c_{13} [GPa]	133.8 ± 0.4	108.0 ± 0.4	58.6 ± 0.6	33 ± 2	112 ± 1	70 ± 5
c_{33} [GPa]	396.2 ± 0.4	286 ± 1	141.3 ± 0.5	87 ± 3	299 ± 1	201 ± 6
c_{44} [GPa]	128.6 ± 0.4	107.3 ± 0.2	69.1 ± 0.1	47.5 ± 0.3	102.5 ± 0.2	78.7 ± 0.8

ratio between 55 and 80%). Owing to the overall flatness of the graphene fillers and the SPS fabrication method, these composites experience a certain degree of alignment showing the graphene plane mostly perpendicularly oriented to the SPS pressing axis (see Fig. 2). Observation of these fracture surfaces also reveals the waviness of both fillers, more pronounced for rGO sheets.

Accordingly, all composites have a symmetry axis defined by the vertical loading axis (x$_3$ axis, see Fig. 1), displaying transversely isotropic elastic behavior. For this symmetry only five independent elastic constants of the stiffness matrix are defined [6]. These constants obtained by the RUS measurements are summarized in Table 1 for each composite, also including the corresponding data for the monolithic Si$_3$N$_4$ material taken from Ref. [6]. This material is isotropic and thus has only two independent elastic constants c_{11} and c_{44}. For the 3 wt.% GNP composite, the elastic constants are very close to those reported for the same material in Ref. [6], although a different newly prepared sample was used. The experimental errors for the elastic constants were determined from the final misfit between the measured resonant frequencies and the frequencies calculated for the given set of elastic constants using the sensitivity analysis procedure described in Ref. [20]. These errors are very low (Table 1) for the materials with 3 and 10 wt.% of GNP as well as for the 3 wt.% rGO composite; whereas for the 18 wt.% GNP and 5 wt.% rGO specimens measurements are much less accurate. Hence, the higher experimental error for the percolated materials could indicate the occurrence of some softened heterogeneous regions in these composites due to clusters of interconnected fillers. However, even for those composites, the resulting experimental accuracy is sufficient to allow for a discussion of the elasticity evolution with the content of fillers.

From the coefficients c_{ij}, the elastic moduli E (Young's modulus) and G (the shear modulus) in different directions were calculated. For a matrix $c_{ij}(\mathbf{n})$ obtained by a rotation of the tensor of elastic coefficients such that the unit vector $\mathbf{n}$ coincides with the x$_1$ direction in the rotated system, the Young's modulus in the direction $\mathbf{n}$ and the shear modulus for shearing in the plane perpendicular to $\mathbf{n}$ were obtained as

$$E(\mathbf{n}) = 1/s_{11}(\mathbf{n}) \tag{1}$$

and

$$G(\mathbf{n}) = 1/s_{44}(\mathbf{n}), \tag{2}$$

where $s_{ij}(\mathbf{n})$ is an inverse matrix to the matrix $c_{ij}(\mathbf{n})$. Also Poisson's ratios were determined using this approach as

$$v(\mathbf{n}, \mathbf{m}) = -s_{12}(\mathbf{n})/s_{11}(\mathbf{n}), \tag{3}$$

which gives a ratio between the lateral contraction in direction $\mathbf{m}$ (perpendicular to $\mathbf{n}$) and the extension along the uniaxial loading direction $\mathbf{n}$, where $\mathbf{m}$ coincides with the x$_2$ axis in the rotated coordinate system.

For the isotropic pure Si$_3$N$_4$ material, the elastic modulus E of 324 GPa, shear modulus G of 129 GPa and Poisson's ratio (v) of 0.26 were obtained. The determined E value calculations are compared as a function of the filler content in Fig. 1 for the two significant directions — along the preferred orientation of the fillers (x$_{1,2}$) and the direction perpendicular to it (x$_3$). A drastic decrease of E with filler content is observed for the x$_3$ direction (Fig. 3); see for example E_3 (75 GPa) versus E_1 (225 GPa) for the 18 wt.% GNP composite, these values are also lower than the E of the blank Si$_3$N$_4$ about 75 and 27%, respectively. For the higher filler concentration, E_3 seems to level off (Fig. 3b), and most probably related to the formation of a fully contacted graphene network [8].

These E data are rather low if we consider the in-plane elastic modulus (0.6–1 TPa) reported for either graphite or graphene [13,21,22]; and although numerical modeling indicates a decrease of E with the number of graphene layers, values always remain above 0.9 TPa [23, 24]. Therefore, the reason for the enhanced flexibility in the composites along the x$_1$ direction must be either caused by the lack of connection to the matrix as discussed in the earlier work [6], or rather attributable to the micro-waviness of the graphene fillers (Fig. 2 a,b). This effect would not be so relevant for the x$_3$ direction, where probably the dominant effect is from the low out-of-plane modulus of multi-layered graphene. What's more, E of graphene for increased number of layers along the c-axis remains almost constant but as low as 50–60 GPa according to computational modeling [25]. Also for measurements in bulks of compressed expanded graphite in the direction perpendicular to the flakes E is ~70 MPa [26], which is ~13 times lower than E reported for the in-plane orientation, and for a plain GNP consolidated by SPS [27], the E reported along the x$_{1,2}$ ~ 38 GPa and x$_3$ ~ 2 GPa directions is also rather low [28].

The E plots for rGO and GNP composites display similar trends as shown in Fig. 3. Actually, for the 3 wt.% of nanofillers both composites
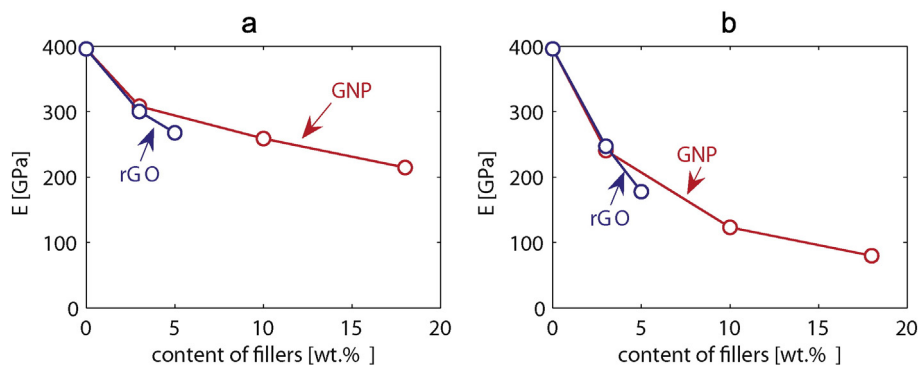

Fig. 3. Elastic modulus as a function of the filler content for the two types of fillers and both orientations, a) x$_1$, i.e. along the graphene plane and b) x$_3$, i.e. perpendicular to the graphene plane.
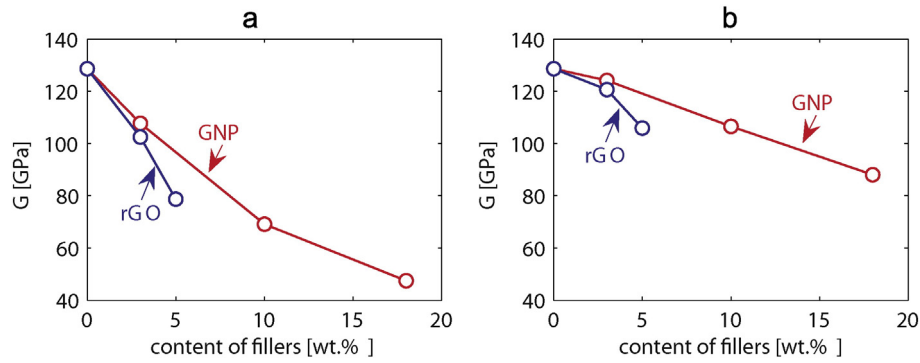
Fig. 4. Shear modulus as a function of the filler content for the two types of fillers and both orientations, a) shear along the graphene plane x_3 and b) along graphene edges x_1 plane.

show similar E, although a faster decay is anticipated for rGO materials along both principal directions for higher contents, owing in the first place to the higher exfoliation of this filler (at ~5 wt.% rGO concentration, fillers are already connected) and to the intrinsic lower E of the rGO sheets. Average E of 250 GPa was reported by indentation atomic force microscopy (AFM) measurements for the GO monolayer reduced by treatment in a H_2 plasma [29]. Corresponding E values of 253–582 GPa for 8 nm thick GO films were stated by Brillouin spectroscopy [30] as a function of thermal treatment (100–200 °C range under vacuum), which are also in good agreement with first-principles computations showing strong dependence with the oxygen coverage and the degree of ordering in the monolayer [31].

Comparing with data for other graphene/ceramic composites, smaller E reductions have been reported for Al_2O_3-graphene composites with fillers obtained by liquid exfoliation of graphite (≤5 vol.% filler) [5] – ultrasonic measurements and in-plane orientations – and also for

rGO composites (<2 vol.% of filler) by nanoindentation tests [7]. More recently, a higher decrease of E (~30%) has been reported [32] for an Al_2O_3–rGO composite (~2 vol.% filler) by measuring deformation under bending tests, which is more in consonance with present data (Fig. 3).

Regarding the shear modulus G, a declining trend is perceived for both composites (Fig. 4), more relevant for shearing along the isotropy plane x_3 (G_{12}) coincident with the graphene plane, and reaching a minimum value of 47 GPa for the 18 wt.% of GNP composite, about a half of the value for shear along the edge of the nano-platelets (Fig. 4). Compared to the G of pure Si_3N_4 (129 GPa), reductions of 63 and 30%, respectively, are observed. Again, rGO composites show similar behavior but with faster decays. Computed shear modulus (G_3) of graphene and graphite report numbers of 300 GPa [13, 21], larger than G_3 for the present composites, although for single crystal graphite in the c-direction, G_{12} of only 4 GPa has been stated
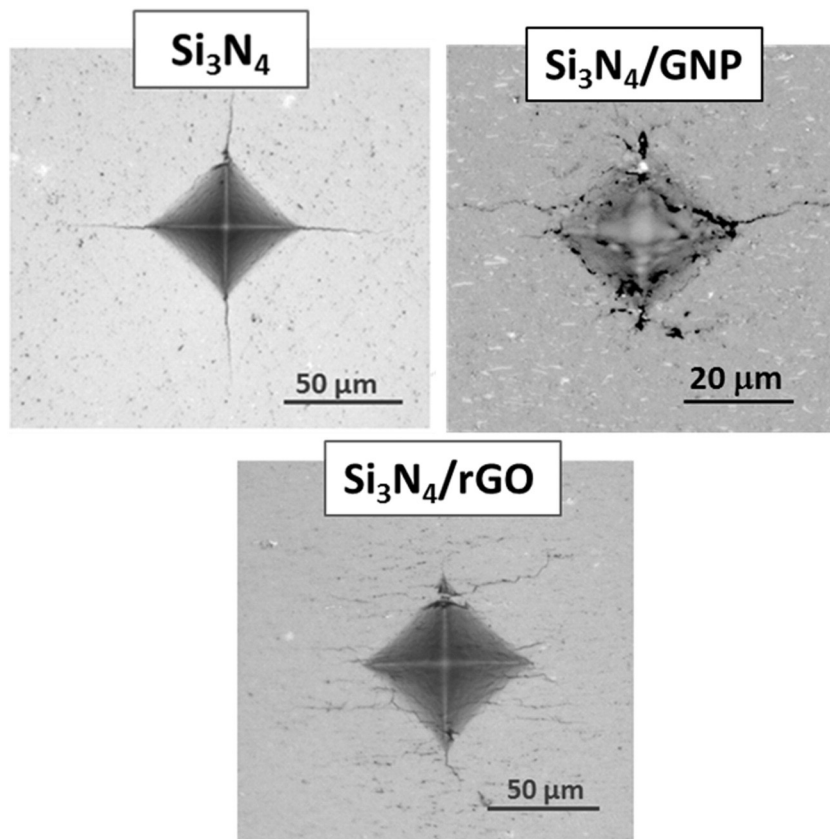

Fig. 5. Optical images comparing Vickers indentation imprints for Si_3N_4 material, 10 wt.% GNP and 3 wt.% rGO composites (x_2 plane).
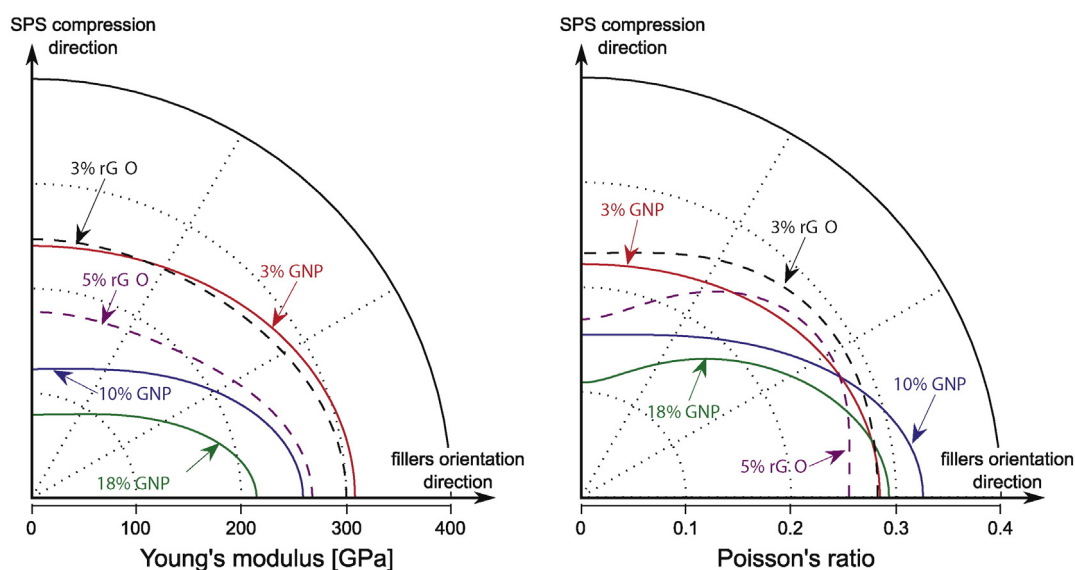
Fig. 6. Angular plots of E and ν for directions ranging from the filler orientation direction (x_1) to the SPS compression orientation direction (x_3).

[33]. All these results suggest favorable shear deformation along the graphene plane (G_{12}) for both composite types when fillers are connected.

Such a significant softening of G may, in principle, have an effect also on the fracture properties of these composites. Actually, the indentation imprints shown in Fig. 5 reveal that while for pure Si_3N_4 the cracks develop according to lines of the maximal tensile stress, several microcracks nucleate along the graphene/ceramic interface (plane x_3) within the imprints for the composites, suggesting that the crack formation may be affected by enhanced shear deformation along this plane. Ogata et al. [34] have proposed the concept of shearability as a crystal property that indicates its tendency to break bonds by shear compared to tension. Generally, ceramics show a larger ratio of shear to bulk moduli, which indicates their poor ductility [34]. For Si_3N_4 single crystals the G/B ratio is ~0.7 (where B is the bulk modulus), and for graphite [35] is as low as 0.1. The addition of the graphene fillers may be thus expected to decrease this ratio in the composites and consequently enable easier shear-induced cracking.

However, increasing the content of graphene fillers simultaneously leads to a significant decrease of B. For the monolithic Si_3N_4, the G/B ratio is 0.57; whereas for GNP composites G/B along $x_{1,2}$ increases to 0.58 for 3 wt.% of GNPs and further to 0.63 and 0.68 for the materials with 10 wt.% of GNPs and 18 wt.% of GNPs, respectively. For rGO composites, however, the increase is less pronounced, $G/B = 0.58$ for 5 wt.% of rGO. In other words, we can presume that the change of the cracking pattern behavior observed in the Vickers indented specimens (see Fig. 5) is due to other effects, most probably associated with the growth of local stresses at the wavy graphene interfaces than with the decrease of the shear modulus. Most probably the toughening effect of these fillers prevents the formation/propagation of cracks in directions perpendicular to the isotropy plane.

To visualize the allover anisotropy of the present composites, plots of E and ν are displayed in Fig. 6 for the loading directions ranging from the isotropy plane (the approximate plane of the preferred orientation of the fillers) to the SPS compression orientation. We can observe how E decreases as direction departs from the graphene plane, more drastically for higher filler contest. Similarly, Poisson's ratio ν is lower along the direction perpendicular to the graphene plane, indicating that stretching along the graphene plane is accompanied by a strong length reduction in the out of plane perpendicular direction, probably favored by an accordion effect on the fillers.

Furthermore, anisotropy in the composites with the concentration of graphene nanostructures becomes more pronounced once they are percolated, e.g. above 8 wt.% GNP and 4 wt.% rGO. Above the percolation limit, in addition, the directional dependence of Young's modulus does not follow the elliptic degeneracy observed for the 3 wt.% GNP composite [6] and approximately also for the 3 wt.% rGO composite. For higher contents of both fillers, the square root of Young's modulus cannot be well approximated by an ellipse, which means that the anisotropy of the composite cannot be understood as induced by an oriented array of non-interacting defects [36]. This is expectable, as the percolation necessarily results in mutual interactions between the fillers.

4. Conclusions

Ceramic composites containing graphene fillers –pristine GNP and defective rGO – densified by SPS methods show an anisotropic behavior regarding elastic constants, with symmetry axis defined by the SPS loading direction. This anisotropy is enhanced when fillers are fully contacted. Elastic and shear moduli experience a steady decrease with the increasing content of fillers. The decreasing ratio is mostly controlled by the exfoliation degree of the nanofillers as it determines the percolation limit. Although the ratio of the shear modulus to the bulk modulus increases for the composites compared with pure Si_3N_4 ceramics, shear induced fracture is present in the composites; this proves the strength of the toughening effect of the fillers that prevent tension-induced fracture in given directions even though the shearability of the composites decreases.

Acknowledgments

References

[1] A. Nieto, D. Lahiri, A. Agarwal, Graphene NanoPlatelets reinforced tantalum carbide consolidated by spark plasma sintering, Mater. Sci. Eng. A 582 (2013) 338–346.
[2] J. Liu, H. Yan, M.J. Reece, K. Jiang, Toughening of zirconia/alumina composites by the addition of graphene platelets, J. Eur. Ceram. Soc. 32 (2012) 4185–4193.
[3] J. Dusza, J. Morgiel, A. Duszova, L. Kvetkova, M. Nosko, P. Kun, et al., Microstructure and fracture toughness of Si_3N_4 + graphene platelet composites, J. Eur. Ceram. Soc. 32 (2012) 3389–3397.

[4] L.S. Walker, V.R. Marotto, M.A. Rafiee, N. Koratkar, E.L. Corral, Toughening in graphene ceramic composites, ACS Nano 5 (2011) 3182–3190.

[5] H. Porwal, P. Tatarko, S. Grasso, J. Khaliq, I. Dlouhy, M.J. Reece, Graphene reinforced alumina nano-composites, Carbon 64 (2013) 359–369.

[6] H. Seiner, P. Sedlak, M. Koller, M. Landa, C. Ramirez, M. Isabel Osendi, et al., Anisotropic elastic moduli and internal friction of graphene nanoplatelets/silicon nitride composites, Compos. Sci. Technol. 75 (2013) 93–97.

[7] Y. Fan, M. Estili, G. Igarashi, W. Jiang, A. Kawasaki, The effect of homogeneously dispersed few-layer graphene on microstructure and mechanical properties of Al$_2$O$_3$ nanocomposites, J. Eur. Ceram. Soc. 34 (2014) 443–451.

[8] C. Ramirez, L. Garzon, P. Miranzo, M.I. Osendi, C. Ocal, Electrical conductivity maps in graphene nanoplatelet/silicon nitride composites using conducting scanning force microscopy, Carbon 49 (2011) 3873–3880.

[9] C. Ramirez, F.M. Figueiredo, P. Miranzo, P. Poza, Osendi M. Isabel, Graphene nanoplatelet/silicon nitride composites with high electrical conductivity, Carbon 50 (2012) 3607–3615.

[10] P. Miranzo, E. Garcia, C. Ramirez, J. Gonzalez-Julian, M. Belmonte, Osendi M. Isabel, Anisotropic thermal conductivity of silicon nitride ceramics containing carbon nanostructures, J. Eur. Ceram. Soc. 32 (2012) 1847–1854.

[11] R. Vogelgesang, M. Grimsditch, J.S. Wallace, The elastic constants of single crystal beta-Si$_3$N$_4$, Appl. Phys. Lett. 76 (2000) 982–984.

[12] N. Hirosaki, S. Ogata, C. Kocer, H. Kitagawa, Y. Nakamura, Molecular dynamics calculation of the ideal thermal conductivity of single-crystal alpha- and beta-Si$_3$N$_4$, Phys. Rev. B 65 (2002).

[13] C.D. Reddy, S. Rajendran, K.M. Liew, Equilibrium configuration and continuum elastic properties of finite sized graphene, Nanotechnology 17 (2006) 864–870.

[14] J.M. Gebert, B. Reznik, R. Piat, B. Viering, K. Weidenmann, A. Wanner, et al., Elastic constants of high-texture pyrolytic carbon measured by ultrasound phase spectroscopy, Carbon 48 (2010) 3647–3650.

[15] C. Ramirez, P. Miranzo, M. Belmonte, M.I. Osendi, P. Poza, S.M. Vega-Diaz, et al., Extraordinary toughening enhancement and flexural strength in Si$_3$N$_4$ composites using graphene sheets, J. Eur. Ceram. Soc. 34 (2014).

[16] S. Gilje, S. Han, M. Wang, K. Wang, R. Kaner, A chemical route to graphene for device applications, Nano Lett. 7 (2007) 3394–3398.

[17] C. Ramirez, S.M. Vega-Diaz, A. Morelos-Gomez, F.M. Figueiredo, M. Terrones, M.I. Osendi, et al., Synthesis of conducting graphene/Si$_3$N$_4$ composites by spark plasma sintering, Carbon 57 (2013) 425–432.

[18] R.G. Leisure, F.A. Willis, Resonant ultrasound spectroscopy, J. Phys. Condens. Matter 9 (1997) 6001–6029.

[19] J.D. Maynard, Resonant ultrasound spectroscopy, Conference on Ultrasonic Transducer Engineering — Medical Imaging 1998. San Diego, Ca 1998 1998, pp. 132–142.

[20] P. Sedlak, H. Seiner, J. Zidek, M. Janovska, M. Landa, Determination of all 21 independent elastic coefficients of generally anisotropic solids by resonant ultrasound spectroscopy: benchmark examples, Exp. Mech. 54 (2014) 1073–1085.

[21] J.-L. Tsai, J.-F. Tu, Characterizing mechanical properties of graphite using molecular dynamics simulation, Mater. Des. 31 (2010) 194–199.

[22] M.M. Shokrieh, R. Rafiee, Prediction of Young's modulus of graphene sheets and carbon nanotubes using nanoscale continuum mechanics approach, Mater. Des. 31 (2010) 790–795.

[23] A.R. Golkarian, M. Jabbarzadeh, The density effect of van der Waals forces on the elastic modules in graphite layers, Comput. Mater. Sci. 74 (2013) 138–142.

[24] C. Lee, X. Wei, Q. Li, R. Carpick, J.W. Kysar, J. Hone, Elastic and frictional properties of graphene, Phys. Status Solidi B Basic Solid State Phys. 246 (2009) 2562–2567.

[25] S.K. Georgantzinos, G.I. Giannopoulos, N.K. Anifantis, Numerical investigation of elastic mechanical properties of graphene structures, Mater. Des. 31 (2010) 4646–4654.

[26] A. Celzard, J.F. Mareche, G. Furdin, Modelling of exfoliated graphite, Prog. Mater. Sci. 50 (2005) 93–179.

[27] A. Nieto, D. Lahiri, A. Agarwal, Synthesis and properties of bulk graphene nanoplatelets consolidated by spark plasma sintering, Carbon 50 (2012) 4068–4077.

[28] Koller M SH, Landa M, Nieto A, Agarwal A. Anisotropic elastic and acoustic properties of bulk graphene nanoplatelets consolidated by spark plasma sintering. Acta Physica Polonica A.

[29] C. Gomez-Navarro, M. Burghard, K. Kern, Elastic properties of chemically derived single graphene sheets, Nano Lett. 8 (2008) 2045–2049.

[30] R.J.J. Rioboo, E. Climent-Pascual, X. Diez-Betriu, F. Jimenez-Villacorta, C. Prieto, A. de Andres, Elastic constants of graphene oxide few-layer films: correlations with interlayer stacking and bonding, J. Mater. Chem. C 3 (2015) 4868–4875.

[31] L. Liu, J. Zhang, J. Zhao, F. Liu, Mechanical properties of graphene oxides, Nanoscale 4 (2012) 5910–5916.

[32] Y. Fan, G. Igarashi, W. Jiang, L. Wang, A. Kawasaki, Highly strain tolerant and tough ceramic composite by incorporation of graphene, Carbon 90 (2015) 274–283.

[33] A. Bosak, M. Krisch, M. Mohr, J. Maultzsch, C. Thomsen, Elasticity of single-crystalline graphite: inelastic x-ray scattering study, Phys. Rev. B 75 (2007).

[34] S. Ogata, J. Li, N. Hirosaki, Y. Shibutani, S. Yip, Ideal shear strain of metals and ceramics, Phys. Rev. B 70 (2004).

[35] K.H. Michel, B. Verberck, Theory of the elastic constants of graphite and graphene, Phys. Status Solidi B 245 (2008).

[36] M. Kachanov, On the concept of approximate elastic symmetry and its application to materials with defects, Int. J. Fract. 74 (1996) R33–R38.

Summary of the presented articles

The papers [A,B] show that the laser-based RUS combined with the through-transmission/ pulse-echo method is able to determine the full set of elastic coefficients of macroscopically heterogeneous materials with hexagonal symmetry, which is induced by the preferential orientation of the graphene-based fillers in the studied materials. The resulting distributions of Young's modulus are shown in Figure 3.3.
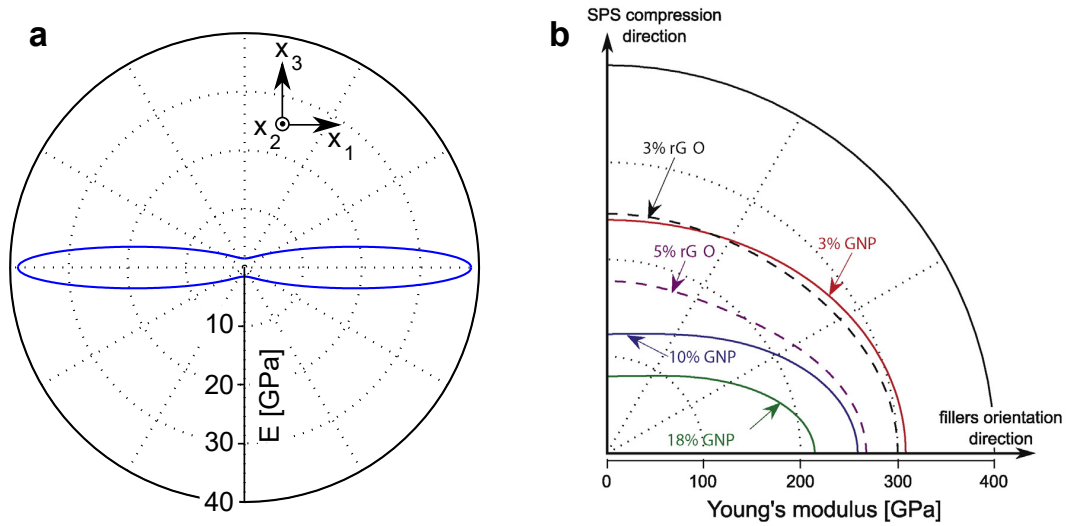

Figure 3.3: Directional dependence of Young's modulus in the x_1x_3 plane, the x_3 axis corresponds to the SPS compression direction, which is perpendicular to the preferential orientation of the graphene platelets: a) Young's modulus of the pure sintered GNPs [A], b) Young's modulus of the silicon nitride reinforced with graphene fillers [B].

The paper [A] also shows that the propagation of ultrasonic waves in pure sintered GNPs is both direction-dependent and frequency-dependent. The longitudinal waves have much higher velocities along the preferential orientation of the rods when compared to the perpendicular x_3 direction (as expected from the strong anisotropic structure of the sintered GNPs), but they are also more attenuated at the higher frequency. For the case of the shear waves, the velocity v_{13}, corresponding to the waves propagating in the GNPs direction and polarized perpendicular to the GNPs, is significantly higher than the velocity v_{31} of the waves propagating in the perpendicular direction to the GNPs and polarized along the GNPs. This is in contradiction to the equations (2.49, 2.50), as the studied material consists of an oriented structure of the GNPs and pores between them. The ultrasonic waves propagating in the direction perpendicular to the GNPs are scattered on the flat pores, which effectively increases the attenuation and decreases the measured velocity. Therefore, this effect further emphasizes the strong acoustic anisotropy of the sintered GNPs.

The paper [B] shows that the elastic coefficients of the Si_3N_4/graphene fillers composites decrease with the increasing graphene content for both types of graphene fillers (denoted here as GNPs and rGOs); the obtained Young's modulus distributions are shown in Figure 3.3b. Due to the preferred orientation of the graphene fillers, Young's moduli are significantly lower in the SPS compression direction, which is perpendicular to the orientation of the fillers. As the rGOs

(reduced graphene oxide sheets) are more exfoliated than the GNPs due to different processing methods, they also have a slightly stronger effect on the macroscopic elastic properties of the resulting composites. The elliptic approximation of the Young's moduli is shown to be valid only for lower content of graphene fillers. After a certain threshold ($\sim$4 wt.% for rGOs and $\sim$8 wt.% for GNPs), the fillers start to form an interconnected network and thus, they cannot be further considered as spheroidal voids.

Since their publication in 2015, the papers [A,B] has received quite some attention. Nieto et al. [204] have cited both papers in a 2017 review on graphene reinforced metal- and ceramic-matrix composites, emphasizing the anisotropic properties induced by the GNPs. Another 2017 review article by Miranzo et al. [205] has demonstrated how the addition of graphene fillers incorporates the anisotropic elastic properties, citing the results of papers [199,B]. A 2020 review by Zhou et al. [206] has cited the strong elastic anisotropy of sintered GNPs from the paper [A], along with the anisotropic elastic behavior of the composites from the paper [199]. Other papers that cited the paper [B] mostly referred to the anisotropic nature of the graphene-fillers composites, e. g. [207–213], or to the toughening effect of graphene to the ceramic matrix, e. g. [214–217].

3.2 Spark plasma sintered metal-matrix composites

This section consists of three research papers studying the mechanical properties of metal-matrix composites consolidated by SPS, including the characterization of their elastic properties by the laser-based RUS. The work presented in this section was supported by Czech Science Foundation project no. GB14-36566G called *Multidisciplinary research centre for advanced materials (AdMat)*, which comprised six Czech research institutions from the field of materials science. One of the main aims of the AdMat centre was to develop novel materials and to perform their fundamental characterization. The PhD candidate has been involved in this project, particularly in the topic of ultrasound characterization of the newly produced materials. The collaboration between the research institutes, namely the Institute of Plasma Physics (where the materials were produced by the SPS method) and the Institute of Thermomechanics (where the RUS characterization was performed), has resulted in three papers on the topic of metal-matrix composites, included in this thesis.

The first paper [C] shows the ability of SPS to produce a light-weight ferromagnetic material by sintering a powder mixture consisting of CoNiAl Heusler ferromagnetic alloy and gas-atomized α-Ti powder particles. The interconnection of the CoNiAl and Ti grains has been accomplished by a formation of an intermetallic layer with a rather complicated structure, which results mostly from an Al, Co, and Ni diffusion into the Ti particles [218]. The elastic properties and internal friction evolutions of three Co-Ni-Al/Ti composites (consolidated from powder mixtures with 2:1, 1:1 and 1:2 Co-Ni-Al:Ti volume ratios) were measured by the PhD candidate, utilizing the laser-based RUS method from room temperature up to 740 °C.
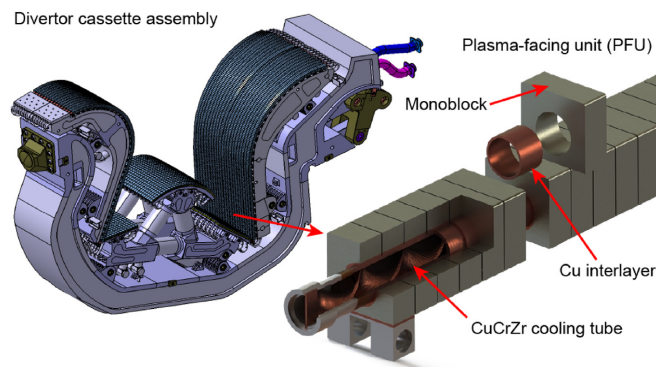

Figure 3.4: ITER tungsten divertor design: a single cassette assembly unit (one of total 54 units) and a detailed view of one of the plasma-facing units made of tungsten monoblocks surrounding CuCrZr cooling tubes [219].

The next two papers [D, E] deal with tungsten-based materials, where the motivation for this work is the possible application of tungsten as a plasma-facing material in fusion devices [219–224]. As seen in Figure 3.4, plasma-facing units of ITER fusion reactor (which is currently being assembled) are made of tungsten monoblocks, which are joined to the copper-alloy cooling tubes. However, reduced-activation ferritic-martensitic steels are considered as the structural materials in future fusion devices, such as DEMO fusion reactor [225–227].

Paper [D] studies the elastic properties of tungsten/steel composites, showing that the SPS method is capable of joining these two dissimilar materials. The relation between the microstructure and elastic properties of tungsten/steel composites is described, where the effective elastic coefficients measured on the bulk composite samples were also utilized for determining the effective elasticity of the individual phases based on the FEM modelling. Several types of materials are studied here: a pure steel sample and three composites with variable W contents (20 vol. %, 43 vol. %, or 69 vol. % of tungsten powder in the initial mixtures) sintered at 1100 °C; moreover, the powder mixtures with 69 vol. % of W were also sintered at different temperatures: 1200 °C, 1300 °C, and 1400 °C. Similarly as in the Co-Ni-Al/Ti composites, an intermetallic compound (Fe_7W_6 in this case) is formed during the sintering, affecting the mechanical and functional properties of the steel/tungsten composites. The total amount of the intermetallic phase within the composite structure strongly depends on the sintering temperature and sintering time. Therefore, another sintered material was studied, where the composition of the powder mixture and the sintering parameters were designed such that the amount of the intermetallic compound is maximized. The room-temperature elastic coefficients of these eight materials were determined by the PhD candidate by the laser-based RUS method. The obtained results were then utilized for a FEM study of effective elastic moduli of the tungsten agglomerations within the composite structures.

The third paper [E] studies the properties of pure tungsten and mechanically alloyed tungsten composites, including the laser-based RUS characterization up to 740 °C, and it shows that the internal friction measurements can detect the relaxation processes at elevated temperatures. The studied composites (W-1wt.%Y_2O_3 and W-2.5wt.%TiC) were processed by mechanical alloying [228], where the powder mixtures were mixed in a planetary ball mill (which is schematically shown in Figure 3.5) for several tens of hours and then consolidated by the SPS. This leads to the formation of composites with ultrafine second-phase particles dispersed in the tungsten matrix, which should improve the high-temperature performance of tungsten-based materials. For comparison, three pure tungsten samples were also studied: a tungsten single crystal and two tungsten SPSed compacts that differed in the treatment before the sintering (one sample was directly sintered from the original powder, while for the second sample, the powder was also processed in the planetary ball mill before the sintering).
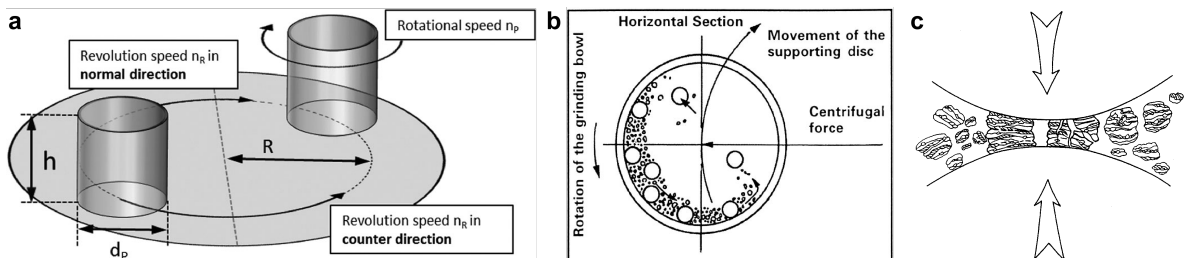

Figure 3.5: Principles of mechanical alloying, utilizing a planetary ball mill: a) disk movement in a planetary ball mill [229], b) ball motion inside the ball mill from a top view [228], c) ball–powder–ball collision of powder mixture leading to the mechanical alloying [228].

Paper C

Mechanical and magnetic properties of semi-Heusler/light-metal composites consolidated by spark plasma sintering

Martin Koller, Tomáš Chráska, Jakub Cinert, Oleg Heczko, Jaromír Kopeček, Michal Landa, Radek Mušálek, Michal Rameš, Hanuš Seiner, Josef Stráský, Miloš Janeček
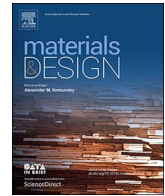
Number of total citations[1]:   4 (excluding self-citations: 2)

Contribution of the PhD candidate and the co-authors:

The candidate measured the density, elastic coefficients and internal friction temperature evolutions, and was also responsible for the submission process of the paper.

Co-authors from the Institute of Plasma Physics (T. Chráska, J. Cinert, R. Mušálek) consolidated the composites by the SPS method, made the scanning electron micrographs, and measured the flexural strength. Co-authors from the Institute of Physics (O. Heczko, J. Kopeček, M. Rameš) performed the magnetization measurements and the EDS analysis. Co-authors from the Institute of Thermomechanics (M. Landa, H. Seiner) were responsible for discussing the relation between the microstructure and the mechanical properties of the composites. Co-authors from the Faculty of Mathematics and Physics (J. Stráský, M. Janeček) came up with the original concept of the paper and supervised the work on the paper.

---

[1]According to the Web of Science database `webofknowledge.com` as of August 2020

CrossMark

Mechanical and magnetic properties of semi-Heusler/light-metal composites consolidated by spark plasma sintering

Martin Koller[a,*], Tomáš Chráska[b], Jakub Cinert[b], Oleg Heczko[c], Jaromír Kopeček[c], Michal Landa[d], Radek Mušálek[b], Michal Rameš[c], Hanuš Seiner[d], Josef Stráský[e], Miloš Janeček[e]

[a] Faculty of Nuclear Sciences and Physical Engineering, Czech Technical University in Prague, Trojanova 13, 120 00 Praha 2, Czech Republic
[b] Institute of Plasma Physics, Czech Academy of Sciences, Za Slovankou 1782/3, 182 00 Praha 8, Czech Republic
[c] Institute of Physics, Czech Academy of Sciences, Na Slovance 1999/2, 182 21 Praha 8, Czech Republic
[d] Institute of Thermomechanics, Czech Academy of Sciences, Dolejškova 1402/5, 182 00 Praha 8, Czech Republic
[e] Faculty of Mathematics and Physics, Charles University in Prague, Ke Karlovu 2026/5, 121 16 Praha 2, Czech Republic

ARTICLE INFO

ABSTRACT

Light-weight ferromagnetic Co-Ni-Al:Ti composites were consolidated by spark plasma sintering. Powders of ball-milled Co-Ni-Al and gas atomized α-Ti were mixed together in three different ratios and spark plasma sintered at 950 °C, using two sintering times, i.e. dwell times at the maximal temperatures: 1 and 5 min. The composites were successfully compacted and new intermetallic phases were formed at the Co-Ni-Al/Ti interfaces. The composites exhibit favourable flexural strength, excellent high-temperature stability, and relatively high saturation magnetization. On the other hand, the newly emerged intermetallic phases are non-ferromagnetic, which slightly deteriorates the magnetic properties.

1. Introduction

Modern powder metallurgy methods such as spark plasma sintering (SPS) enable fabrication of fully dense metal–metal composites consisting of components of very dissimilar mechanical or functional properties. For example, Tang et al. [1] utilized SPS to consolidate a functionally graded Cu / W composite, combining machinability of copper with superior hardness and temperature resistance of tungsten; the same concept was discussed for steel / W composites by Matějíček et al. [2]. Xie et al. [3] used a mixture of Ni-based and Fe-based glassy alloy powders to prepare a dual-phase composite with unique high-strength properties, Mizuuchi et al. [4] designed a NiTi-reinforced AZ31 Mg alloy matrix composite, and Lazurenko et al. [5] used SPS for fabrication of layered titanium / Al₃Ti composite. Other examples of application of SPS for fabrication of metal-matrix composites with enhanced functionality comprise Mg / Ni-Mn-Ga [6], Ti / Ti-Nb-Ta-Zr-O [7], and Al / WC [8] systems.

This paper explores the possibility of combining a light metal with a ferromagnetic alloy, in order to obtain a light-weight metallic composite with a local ferromagnetic behavior, i.e. a composite the structural damage of which could be detectable by Barkhausen noise recording [9–11], or a composite usable for light-weight magnetic shielding applications.

For the design of this composite, commercially pure α-titanium was selected as the light-metal component, since the α-Ti powders were shown recently as apparently suitable for consolidation by SPS [12]. Moreover, α-Ti exhibits structural stability up to much higher temperatures than aluminium or magnesium, which enables the use of higher sintering temperatures required for full sintering of the ferromagnetic component. As the ferromagnetic component, the cubic B2 phase of a semi-Heusler Co-Ni-Al ferromagnetic alloy [13–15] was used. This alloy has a significantly lower mass density ($\rho = 6.95 \text{ g·cm}^{-3}$) than single-element ferromagnetic metals (Ni, Fe, Co), which makes it beneficial for designing light-weight composites. Simultaneously, this alloy exhibits a structural stability to much higher temperatures than most of the classical Heusler alloys, such as Cu₂MnAl. The Co-Ni-Al alloy is often studied as a ferromagnetic shape memory alloy (FSMA), as it undergoes a cubic-to-tetragonal transition at low temperatures around −70 °C [16]. However, this transition can be observed only in Co-Ni-Al samples annealed at temperatures above 1000 °C, while the as-cast bulk material (later milled to produce the powder used for the composites reported in this paper) is stable in the cubic B2 phase down to −263 °C (10 K) [16].

The composites reported in this paper exhibit mass density comparable to or below 6 g·cm⁻³, flexural strength comparable with conventional SPSed α-Ti, structural stability at elevated temperatures, and

* Corresponding author.
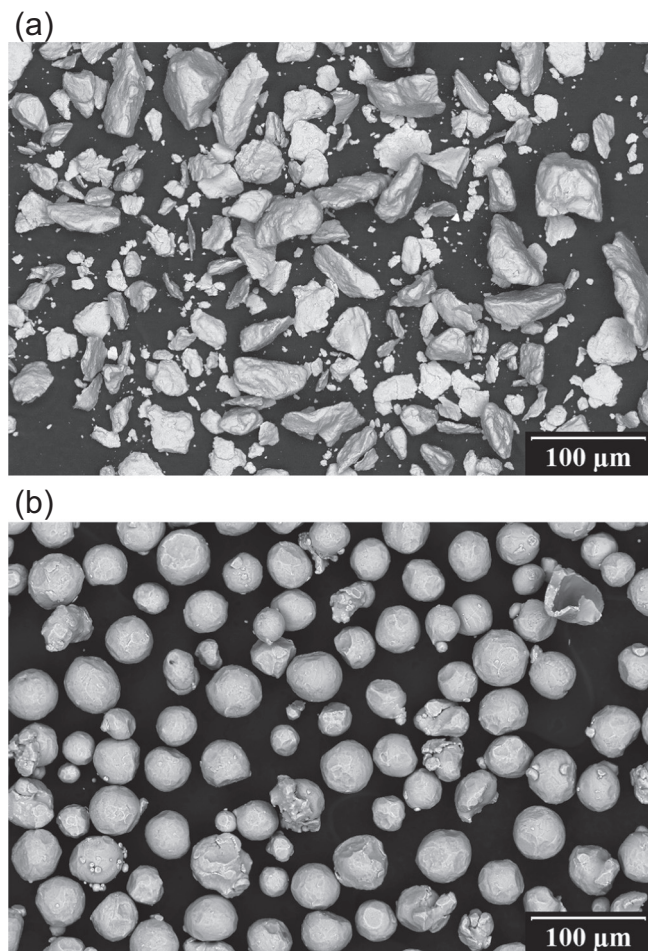*E-mail address:* martin.koller@fjfi.cvut.cz (M. Koller).

(a)

(b)

Fig. 1. Scanning electron micrographs of the initial powders: ball-milled Co-Ni-Al powder (a); gas atomized Ti powder (b).

measurable magnetization in external magnetic field. The presented results outline the possibility of preparing novel materials with unique combination of mechanical and magnetic properties. Moreover, as the semi-Heusler alloys have several potential applications for energy conversion as thermoelectric materials [17–20], their ability to retain their properties in SPSed composites documented in this paper can also outline a path for development of new thermoelectric composites. This concept was partially explored by Gelbstein et al. [21] who used SPS for preparation of an in-situ thermoelectric composite composed of the Ti-Ni-Sn semi-Heusler alloy and other residual metallic and intermetallic phases.

2. Material preparation

The Co-Ni-Al powder was prepared in two steps. First, coarse chips were prepared by mechanical grinding from a cast ingot with a coarse dendritic structure. In the second step, the size of the particles was reduced by planetary milling. Milling resulted in ablated grains of irregular shapes. For the sintering, a sieved fraction of diameter 20–63 μm (Fig. 1) was used. The composition of the powder was determined by energy dispersive X-ray spectroscopy (EDS) analysis as follows: $X_{Co} = (39.9 \pm 0.4)$ at.%, $X_{Ni} = (33.8 \pm 0.4)$ at.%, $X_{Al} = (24.8 \pm 0.3)$ at.%. An additional iron admission originating from milling $X_{Fe} = (1.5 \pm 0.1)$ at.% was found; this admission was heterogeneously distributed among the grains.

The used gas atomized α-Ti (grade 2 commercially pure titanium) powder was purchased from TLS Technik GmbH & Co. Spezialpulver KG (Bitterfeld, Germany). The mean size of titanium particles was 40.7 μm

and the particle distribution had 10th and 90th percentiles of 29.0 μm and 56.7 μm, respectively, as measured by Mastersizer 3000 (Malvern, UK) laser particle size analyser. The titanium-based powder contained small impurities of iron (0.08 wt.%) and oxygen (0.14 wt.%). The powders were stored in air.

Bulk Co-Ni-Al:Ti composite pellets were produced by spark plasma sintering of mixed powders at volume ratios of 2:1, 1:1, 1:2. The mixing was performed in a mechanical blender for several minutes. The mixtures were then sintered at 950 °C by applying uniaxial stress of 80 MPa at two various sintering times (1 min or 5 min), using a 10-4 SPS device (Thermal Technologies LLC).

3. Experimental characterization

Density of the sintered pellets was determined by Archimedes' method (weighting the samples of the materials on air and in deionized water). Microstructure of the samples was investigated on the cross-sections, which were ground and polished by using diamond suspensions down to 1 μm. The final polishing was done using OP-S mixed with H_2O_2 and diluted Kroll's reagent (HNO_3 and HF). Scanning electron micrographs were taken by employing a scanning electron microscope Zeiss EVO MA 15; the same device was used also for the micrographs of the original powders in Fig. 1.

Flexural strength was evaluated using a modified ASTM C1161 method. Beams of approx. 4×4 mm^2 in cross-section were cut out from the compacted samples, using a precision saw, chamfered and ground with P600 SiC paper. The beams were then loaded by 3-point bending with the span of outer supports of 14.55 mm and loading rate of 0.2 mm/min. From the maximum loads at fracture, flexural strengths were computed.

Magnetic properties of all composites were measured by a vibrating sample magnetometer (VSM) PAR at room temperature in the magnetic field up to 1.5 T. Additional VSM measurements from 97 °C down to − 263 °C were done for the 1:1 composite (5 min dwell time) using a PPMS (Quantum Design). In this set-up, low-field magnetization at 0.01 T and saturation magnetization at 9 T were measured. These measurements intended to detect a martensitic transition in the Co-Ni-Al components of the composites and to estimate the Curie point.

The elastic properties of the composites were determined using resonant ultrasound spectroscopy (RUS, [22,23], see also [24] for a comprehensive report on application of RUS for semi-Heusler materials). This method is based on the measurements of vibrational spectra of small samples of the examined materials. For this purpose, cuboidal samples with dimensions of approximately $3 \times 2 \times 1$ mm^3 were cut from central parts of the SPS compacts; only the materials sintered for 5 min were used for these measurements. For each sample, Young's modulus and internal friction parameter at room temperature and at elevated temperatures up to 740 °C were measured using contactless laser-based RUS apparatus described in detail in [25]. Temperature evolutions both on heating and on cooling were recorded in low-pressure nitrogen atmosphere, at 30 °C steps with the heating and cooling rates of approx. 3 °C/min, in order to analyze the possible irreversible changes occurring in the material during the temperature cycles.

4. Results

Selected sintering conditions led to an effective formation of dense Co-Ni-Al:Ti composites with homogeneously dispersed constituents and negligible porosity, as seen in scanning electron micrographs in Fig. 2. At the Co-Ni-Al/Ti interfaces, the formation of a new phase (or, more precisely, a mixture of new phases) was observed; its volume fraction increased with increasing dwell time at maximum sintering temperature, as seen in Fig. 3. An EDS analysis revealed that the structure of these newly formed interfacial layers is relatively complicated. It was observed that the titanium content continuously changes over the layer,
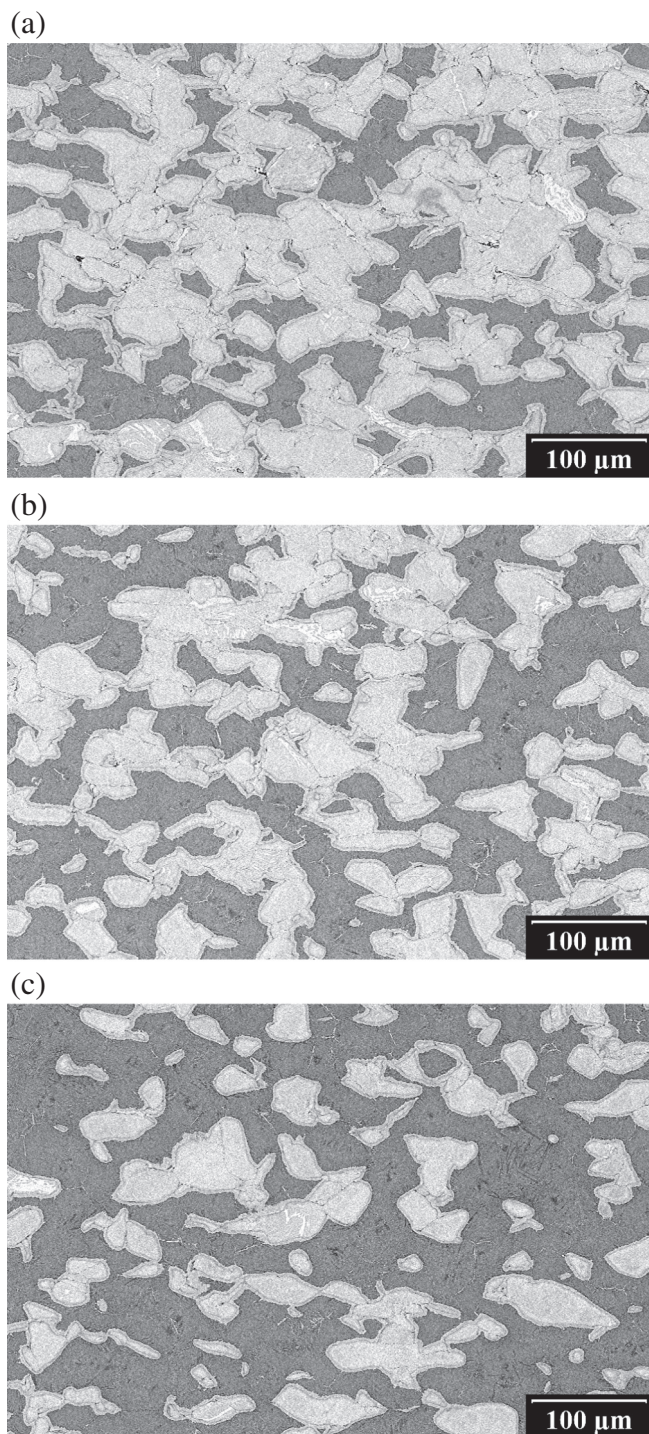
(a)

(b)

(c)

Fig. 2. Microstructure of Co-Ni-Al:Ti composites with 2:1 (a), 1:1 (b), and 1:2 (c) volume ratios (dwell time 1 min).

(a)

(b)

Fig. 3. Microstructures of Co-Ni-Al:Ti 1:1 composites for dwell times of 1 min (a) and 5 min (b).

Table 1
Mass densities of the examined composites determined by Archimedes' method.

Co-Ni-Al:Ti ratio	Dwell time [min]	Density [g·cm^{-3}]
2:1	1	6.12 ± 0.07
1:1		5.75 ± 0.07
1:2		5.36 ± 0.07
2:1	5	6.22 ± 0.08
1:1		5.66 ± 0.06
1:2		5.37 ± 0.06

starting from pure hexagonal close-packed α-Ti in the Ti-powder particles, over cubic C9 (Co,Ni)Ti$_2$ and B2 (Co,Ni)Ti phases, to L2$_1$ (Co,Ni)AlTi phase, which neighbors to a surface layer of B2 (Co,Ni)Al surrounding the initial Co-Ni-Al grains, which contain A1 (Co,Ni,Al) face-centered cubic solid solution particles in B2 (Co,Ni)Al matrix. A detailed description of the results of this structural analysis, as well as the instrumental and experimental details, will be published elsewhere. For the scope of this paper, the main conclusion drawn from this analysis was that the newly appearing phases can be assumed as non-magnetic.

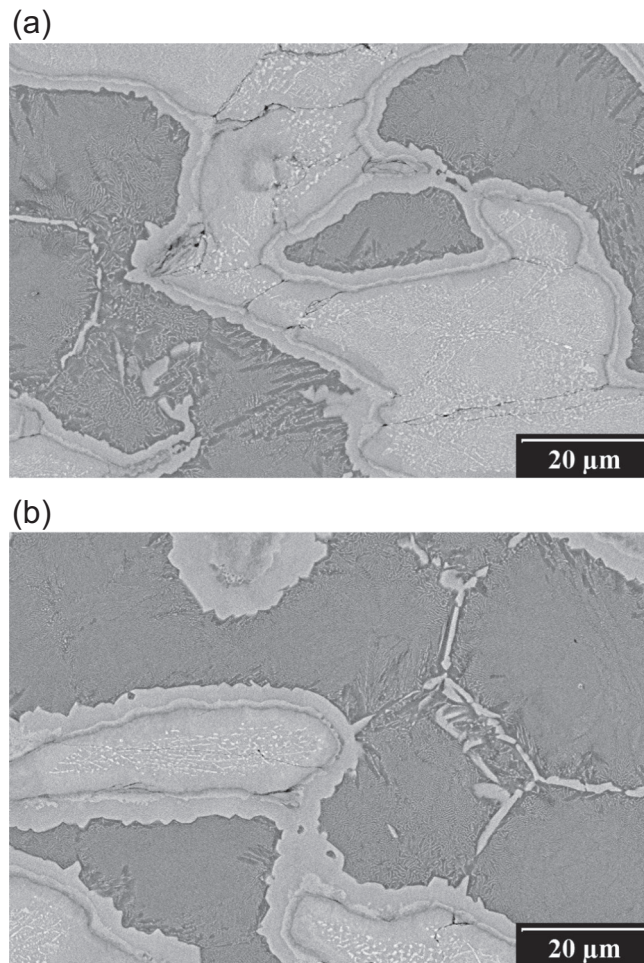Despite the formation of the new phases, the density of the samples exhibited a gradual evolution with the changes of the Co-Ni-Al:Ti volume ratios, with only a negligible effect of the dwell time. As seen in Table 1, the 2:1 composite has the density above 6 g·cm^{-3}, but the densities of the 1:1 and 1:2 composites are significantly below 6 g·cm^{-3}, and only by 22 % and 15 % higher than density of pure titanium (4.7 g·cm^{-3}). Thus, these composites can be considered as light-weight materials.

The flexural strengths of the prepared composites showed excellent repeatability and ranged from 520 MPa to 860 MPa depending on the Co-Ni-Al content, as shown in Fig. 4. In general, the flexural strength decreased with increasing Co-Ni-Al content. Moreover, the longer sintering time (5 min) was observed to produce composites with slightly higher flexural strength than the samples sintered for 1 min. Analysis of the fractured specimens revealed that in all cases, the cracks propagated dominantly along the boundaries of the original powder particles, i.e. through the newly formed brittle phase, as seen in Fig. 5. Numerous secondary cracks were also observed in the vicinity of the
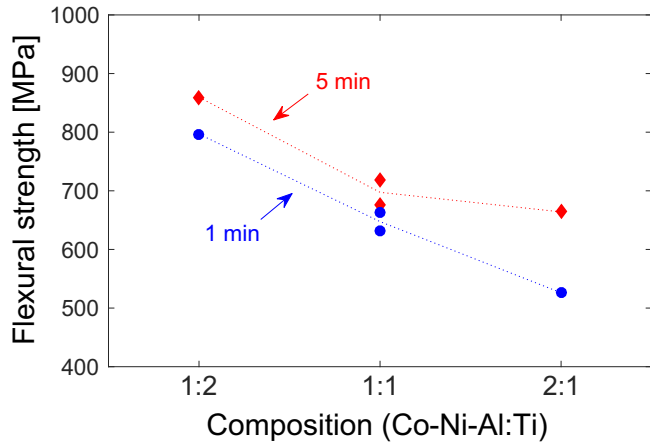
Fig. 4. Flexural strength of the studied Co-Ni-Al:Ti composites. Repeatability of the flexural strength evaluation is documented for 1:1 composites.
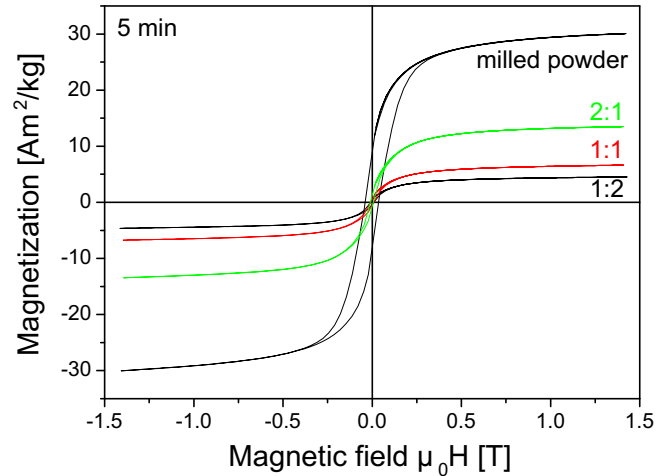

Fig. 5. Fracture surface (a) and cross-section (b) of a fractured sample (1:1 composite, 1 min dwell time).

Fig. 6. Magnetization curves for the SPS compacts compared with the magnetization curve for the initial Co-Ni-Al powder.
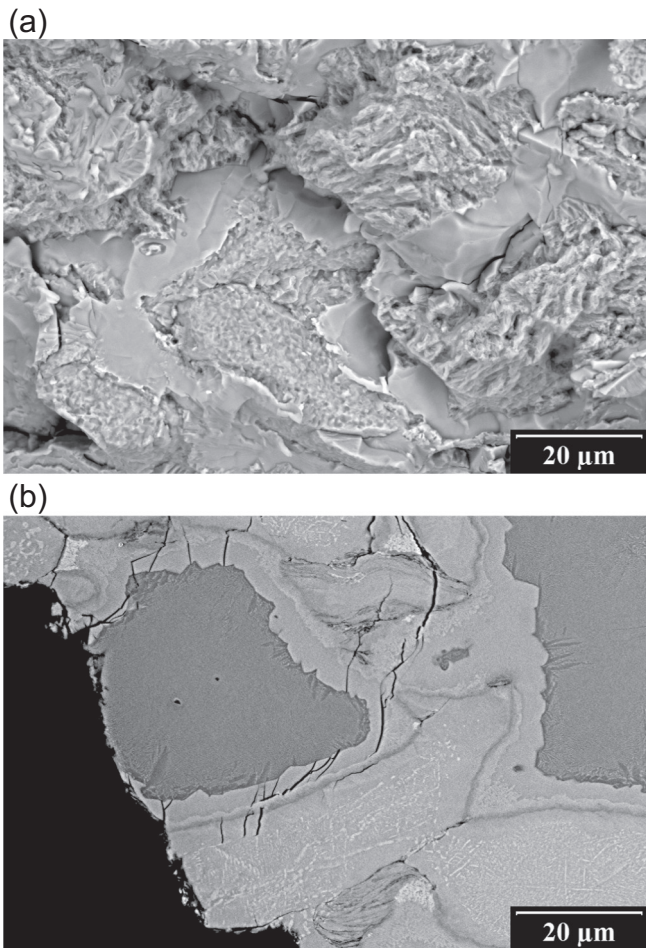

Fig. 7. Difference in magnetization curves of SPS 1:1 composites of Co-Ni-Al:Ti with different dwell time.

magistral crack (up to about 50 μm), which may indicate an intensive dissipation of the energy during the crack propagation.

The magnetization curves at room temperature of the sintered composites together with the initial pure Co-Ni-Al powder are shown in Fig. 6. The most distinctive changes are the decrease of magnetization in the composites, and a high magnetic hysteresis of the powder compared to much smaller hysteresis of the composites. The high hysteresis indicates that there are large internal stresses induced during powder milling. These stresses were mostly eliminated during the SPS
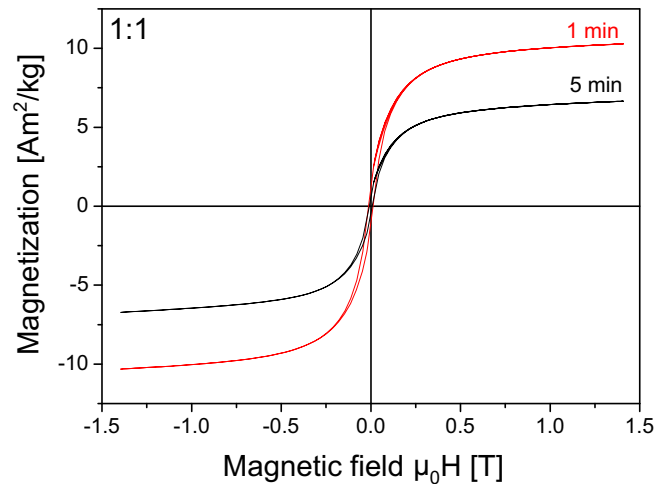
process and the hysteresis strongly decreased, about five times. The hysteresis significantly decreases already during the first minute of the sintering, as seen in Fig. 7, which indicates that the SPS process is effective for the structure relaxation. However, the hysteresis of the composites is still much higher than for a single crystal (about 0.001 T, not shown). Surprisingly, the coercivity does not depend on the volume fraction of the ferromagnetic phase, which suggests that the magnetization process takes place in each grain separately. The enhanced coercivity of the SPS compacts compared to the single crystal can be ascribed to grain boundaries which may act as effective pinning sites for domain walls.

The shapes of the magnetization curves of the different composites prepared at the same conditions (Fig. 6) are very similar and can be scaled to a single curve using saturation magnetization value as a scaling parameter. This indicates that the remaining magnetic phases in the composites are the same or at least they have very similar properties. Also the curves of the composites prepared with 1 and 5 min dwell times do not differ significantly apart from the saturation magnetization as shown in Fig. 7 for the 1:1 composite. The decrease of the saturation magnetization with longer SPS time indicates the higher intermixing with Ti and more intensive formation of the non-magnetic phases.

The values of the magnetization at 1.5 T for all composites are summarized in Fig. 8. In general, the observed differences in saturation magnetization between the different composites and between the
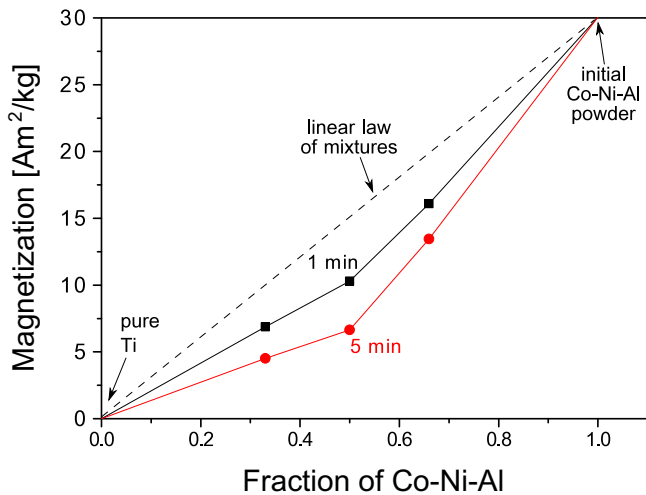
Fig. 8. The changes of magnetization at 1.5 T with changing volume ratio and different time as marked in the figure. The dashed line represents a linear law of mixtures for initial Ti (non-magnetic) and Co-Ni-Al (ferromagnetic) powders.
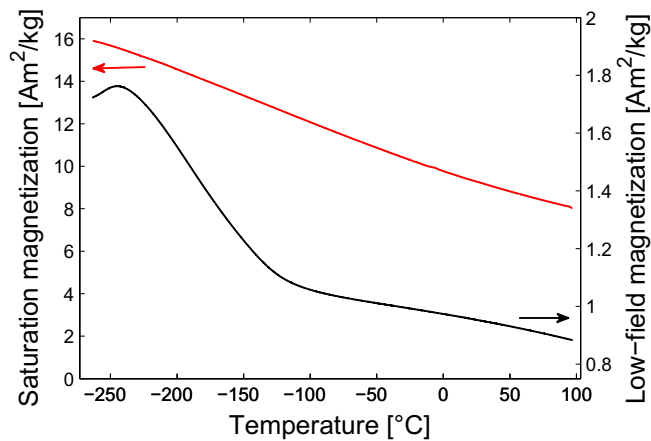

Fig. 9. Low-field magnetization at 0.01 T (lower curve, right vertical axis) and saturation magnetization at 9 T (upper curve, left vertical axis) of the 1:1 composite (5 min dwell time). The increase of the low-field magnetization, i.e. the increase of susceptibility, below − 120 °C can be tentatively ascribed to the onset of the martensitic transformation. The finish of the transformation is marked by slope levelling at about − 250 °C.

composites and pure Co-Ni-Al powder follow the changes in volume of the ferromagnetic phase in the studied samples. The decrease is, however, larger than what can be expected from a linear law of mixtures (outlined by the dashed line in Fig. 8). This indicates the phase intermixing and is consistent with the observed formation of the new non-magnetic phases. Clearly, the difference from the law of mixtures increases with the dwell time and it is the highest for the 1:1 composite. For this composite, the density of the Co-Ni-Al/Ti interfaces is the highest, and thus, the growth of the new non-magnetic phase is the most massive.

Low-field magnetization measured during cooling (Fig. 9) indicated an increase in susceptibility below the temperature of − 120 °C. This temperature can be therefore regarded as the martensite start temperature (M_s). Martensite finish temperature (M_f) can be inferred from the curve being at around − 250 °C. Estimated M_s of the investigated material is lower than the transformation temperature of about − 70 °C observed in the as-cast bulk Co-Ni-Al [16,26]. The very broad temperature range of the transformation compared to the single crystal material [16] can be associated with the heterogeneity in the size of Co-Ni-Al particles, the absence of free surface of the transforming grains and chemical inhomogeneities of the composite. Simultaneously, there is no sudden change of saturation magnetization upon indicated transformation, which is consistent with the behavior of the bulk Co-Ni-Al material [16].

From the magnetization measurements, it can be also concluded that the Curie ferromagnetic point is above 100 °C, which is somehow higher than for the annealed single crystal but similar to the as-cast material [16]. Nevertheless for the as-cast material, the magnetic transformation is smeared over a broad region and the ferromagnetic ordering persists above 90 °C [16].

The elastic constants of the Co-Ni-Al:Ti composites were determined at room temperature and at elevated temperatures up to 740 °C. The results of RUS measurements are shown in Fig. 10: the Young's moduli for all composites exhibit pronounced softening with the increasing temperature, Fig. 10 (a), which is typical for α-Ti. Even in the 2:1 composite, where there is a majority of the Co-Ni-Al grains, there is no indication of the phonon stiffening of Co-Ni-Al with increasing temperature [16]. Nevertheless, the dE/dT slope for this material is the smallest. For the 2:1 composite, there is an additional measurable hysteresis between the heating and cooling runs. For the 1:1 and 1:2 materials, the hysteresis further decreases, and becomes comparable to the resolution limit of the used method (± 1 GPa). It is obvious that this hysteresis cannot be ascribed to further growth of the new phase, as this phase can be expected to grow with the fastest rate for the 1:1
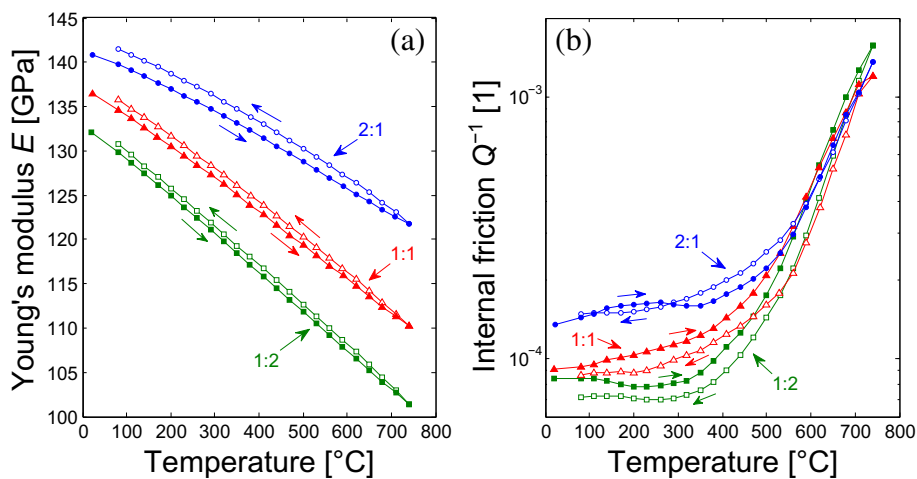

Fig. 10. Young's modulus (a) and internal friction (b) evolutions with 20 °C → 740 °C → 80 °C thermal cycles.

composite. Instead, the observed slight increase of the Young's modulus may be attributed to further annealing of the Co-Ni-Al particles during the thermal cycle. As shown in [16], annealing leads to a slight decrease in the c' shear elastic coefficient of the Co-Ni-Al single crystal, but to an increase in the c_{44} shear elastic coefficient ($c' = 7.32$ GPa and $c_{44} = 114$ GPa for the as-cast material vs. $c' = 4.81$ GPa and $c_{44} = 123$ GPa for the annealed material). Hence, assuming that the Young's modulus of the SPSed polycrystalline material is dominantly given by the Voigt's average of these principal shear moduli ($c' + c_{44}$)/2, a slight increase due to the used thermal cycle could be expected.

It can be also seen that the room-temperature Young's modulus slightly decreases with the increasing content of α-Ti (from 141 GPa for the 2:1 material to 132 GPa for the 1:2 material). This agrees well with the fact that the elastic moduli of polycrystalline α-Ti ($E = 114$ GPa [27]) and polycrystalline as-cast Co-Ni-Al ($E \leq 187$ GPa, Voigt's average of single-crystal data [16]) are relatively close to each other, and the values of Young's moduli for the composites lie between them.

An additional information about the elastic performance of the studied composites is obtained from the internal friction data, Fig. 10 (b). It is seen that all composites exhibit a thermally activated character of the internal friction with a steep increase above approximately 400 °C. Both the value of the internal friction and the slope of the increase at the high temperatures are approximately the same for all compositions, with the activation energies of (0.65 ± 0.10) eV. This internal friction might be attributed to dislocation slip in α-Ti, whose activation energy is between 0.18 and 1.3 eV [28].

A difference is, however, seen between the internal friction coefficients of the individual composites at the room temperature and up to 500 °C. The 2:1 sample exhibits the highest internal friction and the highest increase of the internal friction with temperature in this region. With an increasing content of α-Ti, the internal friction decreases and the dQ^{-1}/dT slope vanishes to zero. This indicates that there is a low-temperature relaxation mechanism related to Co-Ni-Al grains that is suppressed with increasing titanium content. One of the possible explanations of this effect is the magneto-elastic attenuation.

5. Conclusion

The mixtures of Co-Ni-Al and α-Ti powders were compacted by SPS with the aim to produce fully dense ferromagnetic materials with decreased mass density and favourable mechanical properties. The resulting compacts exhibit the desired properties: the flexural strength is acceptable for a structural material, the ferromagnetic response is satisfyingly strong, and the density can be as low as 5.4 g·cm^{-3}. However, the macro-scale properties (both mechanical and magnetic) are affected by the formation of new intermetallic phases during the sintering process. The layers of these new phases appearing at the boundaries between initial Co-Ni-Al and Ti grains thicken with increasing dwell time, which leads to deterioration of the magnetic properties, as the new phases are non-magnetic. On the other hand, the increase in the dwell time leads to better compaction of the powders, and consequently, to higher flexural strengths of the resulting materials. A suitable compromise in the processing parameters must be therefore sought to obtain an optimal combination of mechanical and magnetic properties.

The magnetic and ultrasonic measurements confirmed a structural stability of the prepared composites in a temperature interval at least from -120 °C to 400 °C, whereto the magnetic properties are maintained at least to 100 °C. Below this interval, the Co-Ni-Al grains start martensitically transforming, which may lead to pronounced changes in both mechanical and magnetic properties. Above 400 °C, some thermally activated process occurs in the material, which is indicated by a rapid increase of internal friction. Hence, the mechanical performance of the material above this point may be questionable. Nevertheless, the application window for the newly developed material is still relatively broad, which brings sufficient motivation for further research in the field of light-metal / (semi-)Heusler composites.

References

[1] X. Tang, H. Zhang, D. Du, D. Qu, C. Hu, R. Xie, Y. Feng, Fabrication of W-Cu functionally graded material by spark plasma sintering method, Int. J. Refract. Met. Hard Mater. 42 (2014) 193–199, http://dx.doi.org/10.1016/j.ijrmhm.2013.09.005.

[2] J. Matějíček, B. Nevrlá, M. Vilémová, H. Boldyryeva, Overview of processing technologies for tungsten-steel composites and FGMs for fusion applications, Nukleonika 60 (2) (2015) 267–273, http://dx.doi.org/10.1515/nuka-2015-0049.

[3] G. Xie, D.V. Louzguine-Luzgin, L. Song, H. Kimura, A. Inoue, Dual phase metallic glassy composites with large-size and ultra-high strength fabricated by spark plasma sintering, Intermetallics 17 (7) (2009) 512–516, http://dx.doi.org/10.1016/j.intermet.2009.01.003.

[4] K. Mizuuchi, K. Inoue, K. Hamada, M. Sugioka, M. Itami, M. Fukusumi, M. Kawahara, Processing of TiNi SMA fiber reinforced AZ31 Mg alloy matrix composite by pulsed current hot pressing, Mater. Sci. Eng. A 367 (1-2) (2004) 343–349, http://dx.doi.org/10.1016/j.msea.2003.10.286.

[5] D.V. Lazurenko, V.I. Mali, I.A. Bataev, A. Thoemmes, A.A. Bataev, A.I. Popelukh, A.G. Anisimov, N.S. Belousova, Metal-Intermetallic Laminate Ti-Al$_3$Ti Composites produced by spark plasma sintering of titanium and aluminum foils enclosed in titanium shells, Metall. Mater. Trans. A 46 (9) (2015) 4326–4334, http://dx.doi.org/10.1007/s11661-015-3002-5.

[6] B. Tian, Z.G. Cheng, Y.X. Tong, L. Li, Y.F. Zheng, Q.Z. Li, Effect of enhanced interfacial reaction on the microstructure, phase transformation and mechanical property of Ni-Mn-Ga particles/Mg composites, Mater. Des. 82 (2015) 77–83, http://dx.doi.org/10.1016/j.matdes.2015.05.051.

[7] W.-D. Zhang, Y. Liu, B. Liu, X.-F. Li, H. Wu, J.-W. Qiu, A new titanium matrix composite reinforced with Ti-36Nb-2Ta-3Zr-0.35O wire, Mater. Des. 117 (2017) 289–297, http://dx.doi.org/10.1016/j.matdes.2016.12.029.

[8] A. Pakdel, A. Witecka, G. Rydzek, D.N.A. Shri, A comprehensive microstructural analysis of Al-WC micro- and nano-composites prepared by spark plasma sintering, Mater. Des. 119 (2017) 225–234, http://dx.doi.org/10.1016/j.matdes.2017.01.064.

[9] D.-W. Kim, D. Kwon, Quantification of the Barkhausen noise method for the evaluation of time-dependent degradation, J. Magn. Magn. Mater. 257 (2-3) (2003) 175–183, http://dx.doi.org/10.1016/S0304-8853(02)00575-9.

[10] F. Kun, G.B. Lenkey, N. Takács, D.L. Beke, Structure of magnetic noise in dynamic fracture, Phys. Rev. Lett. 93 (22) (2004) 227204, http://dx.doi.org/10.1103/PhysRevLett.93.227204.

[11] P. Haušild, K. Kolařík, M. Karlík, Characterization of strain-induced martensitic transformation in A301 stainless steel by Barkhausen noise measurement, Mater. Des. 44 (2013) 548–554, http://dx.doi.org/10.1016/j.matdes.2012.08.058.

[12] R. Chaudhari, R. Bauri, Microstructure and mechanical properties of titanium processed by spark plasma sintering (SPS), Metallography, Microstructure, and Analysis 3 (1) (2014) 30–35, http://dx.doi.org/10.1007/s13632-013-0112-6.

[13] K. Oikawa, T. Ota, F. Gejima, T. Ohmori, R. Kainuma, K. Ishida, Phase equilibria and phase transformations in new B2-type ferromagnetic shape memory alloys of Co-Ni-Ga and Co-Ni-Al systems, Mater. Trans. 42 (11) (2001) 2472–2475, http://dx.doi.org/10.2320/matertrans.42.2472.

[14] K. Oikawa, T. Omori, Y. Sutou, R. Kainuma, K. Ishida, Development of the Co-Ni-Al ferromagnetic shape memory alloys, J. Phys. IV France 112 (2003) 1017–1020, http://dx.doi.org/10.1051/jp4:20031054.

[15] J. Kopeček, F. Yokaichiya, F. Laufek, M. Jarošová, K. Jurek, J. Drahokoupil, S. Sedláková-Ignácová, P. Molnár, O. Heczko, Martensitic transformation in Co-based ferromagnetic shape memory alloy, Acta Phys. Pol., A 122 (3) (2012) 475–477, http://dx.doi.org/10.12693/APhysPolA.122.475.

[16] H. Seiner, J. Kopeček, P. Sedlák, L. Bodnárová, M. Landa, P. Sedmák, O. Heczko, Microstructure and martensitic transformation and anomalies in c'-softening in Co-Ni-Al ferromagnetic shape memory alloys, Acta Mater. 61 (15) (2013) 5869–5876, http://dx.doi.org/10.1016/j.actamat.2013.06.035.

[17] G.S. Nolas, J. Poon, M. Kanatzidis, Recent developments in bulk thermoelectric materials, MRS Bull. 31 (3) (2006) 199–205, http://dx.doi.org/10.1557/mrs2006.45.

[18] J. Yang, H. Li, T. Wu, W. Zhang, L. Chen, J. Yang, Evaluation of half-Heusler compounds as thermoelectric materials based on the calculated electrical transport properties, Adv. Funct. Mater. 18 (19) (2008) 2880–2888, http://dx.doi.org/10.1002/adfm.200701369.

[19] C. Fu, S. Bai, Y. Liu, Y. Tang, L. Chen, X. Zhao, T. Zhu, Realizing high figure of merit in heavy-band p-type half-Heusler thermoelectric materials, Nat. Commun. 6

(2015) 8144, http://dx.doi.org/10.1038/ncomms9144.

[20] T. Zhu, C. Fu, H. Xie, Y. Liu, X. Zhao, High efficiency half-Heusler thermoelectric materials for energy harvesting, Adv. Energy Mater. 5 (19) (2015) 1500588, http://dx.doi.org/10.1002/aenm.201500588.

[21] Y. Gelbstein, N. Tal, A. Yarmek, Y. Rosenberg, M.P. Dariel, S. Ouardi, B. Balke, C. Felser, M. Köhne, Thermoelectric properties of spark plasma sintered composites based on TiNiSn half-Heusler alloys, J. Mater. Res. 26 (15) (2011) 1919–1924, http://dx.doi.org/10.1557/jmr.2011.107.

[22] J. Maynard, Resonant ultrasound spectroscopy, Phys. Today 49 (1) (1996) 26–31, http://dx.doi.org/10.1063/1.881483.

[23] R.G. Leisure, F.A. Willis, Resonant ultrasound spectroscopy, J. Phys. Condens. Matter 9 (28) (1997) 6001–6029, http://dx.doi.org/10.1088/0953-8984/9/28/002.

[24] G. Rogl, A. Grytsiv, M. Gürth, A. Tavassoli, C. Ebner, A. Wünschek, S. Puchegger, V. Soprunyuk, W. Schranz, E. Bauer, H. Müller, M. Zehetbauer, P.

Rogl, Mechanical properties of half-Heusler alloys, Acta Mater. 107 (2016) 178–195, http://dx.doi.org/10.1016/j.actamat.2016.01.031.

[25] P. Sedlák, H. Seiner, J. Zídek, M. Janovská, M. Landa, Determination of all 21 independent elastic coefficients of generally anisotropic solids by resonant ultrasound spectroscopy: benchmark examples, Exp. Mech. 54 (6) (2014) 1073–1085, http://dx.doi.org/10.1007/s11340-014-9862-6.

[26] J. Kopeček, V. Kopecký, M. Landa, O. Heczko, Structural changes in Co-based F-SMA, European Symposium on Martensitic Transformations Vol. 738-739 of Materials Science Forum, Trans Tech Publications, 2013, pp. 416–420, , http://dx.doi.org/10.4028/www.scientific.net/MSF.738-739.416.

[27] M. Tane, Y. Okuda, Y. Todaka, H. Ogi, A. Nagakubo, Elastic properties of single-crystalline ω phase in titanium, Acta Mater. 61 (20) (2013) 7543–7554, http://dx.doi.org/10.1016/j.actamat.2013.08.036.

[28] H. Conrad, Thermally activated derfomation of α titanium below 0.4 T_M, Can. J. Phys. 45 (2) (1967) 581–590, http://dx.doi.org/10.1139/p67-050.

Paper D

On the relation between microstructure and elastic constants of
tungsten/steel composites fabricated by spark plasma sintering

Martin Koller, Alena Kruisová, Radek Mušálek, Jiří Matějíček, Hanuš Seiner,
Michal Landa

Number of total citations[1]:   5 (excluding self-citations: 3)

Contribution of the PhD candidate and the co-authors:

The candidate measured the density and the elastic coefficients, co-wrote the manuscript
and coordinated the work on the paper.

Co-authors from the Institute of Thermomechanics (A. Kruisová, H. Seiner, M. Landa)
were responsible for the discussion based on FEM modelling. Co-authors from the Institute of
Plasma Physics (R. Mušálek, J. Matějíček) consolidated the composites, performed the XRD
analysis, and provided the scanning electron micrographs.

---

[1]According to the Web of Science database `webofknowledge.com` as of August 2020
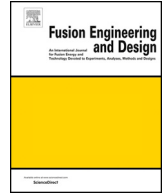
On the relation between microstructure and elastic constants of tungsten/steel composites fabricated by spark plasma sintering

Martin Koller[a],*, Alena Kruisová[b], Radek Mušálek[c], Jiří Matějíček[c], Hanuš Seiner[b], Michal Landa[b]

[a] *Faculty of Nuclear Sciences and Physical Engineering, Czech Technical University in Prague, Trojanova 13, 120 00 Praha 2, Czech Republic*
[b] *Institute of Thermomechanics, Czech Academy of Sciences, Dolejškova 1402/5, 182 00 Praha 8, Czech Republic*
[c] *Institute of Plasma Physics, Czech Academy of Sciences, Za Slovankou 1782/3, 182 00 Praha 8, Czech Republic*

A B S T R A C T

Tungsten/steel composites might play an important role in plasma-facing components, especially in joining of tungsten armor to structural parts made of steel. In this work, Young's moduli and shear moduli of a set of tungsten/P91 steel composites fabricated by spark plasma sintering were determined by resonant ultrasound spectroscopy. It was observed that the sintering temperature and the volume fractions of the individual phases have strong effects on the macroscopic elastic constants. The results were interpreted by means of a finite elements numerical model, showing that the regions of imperfectly bonded tungsten particles appearing in the microstructure of some of the composites act effectively as inclusions with very low elastic stiffness. A good correlation between the number of these regions in the microstructure and the elastic constants was observed.

1. Introduction

Extreme conditions in fusion reactors require the use of advanced materials with enhanced materials properties. Tungsten is considered as a primary candidate plasma-facing material due to its high resistance to sputtering, high melting point, and high thermal conductivity [1–3]. On the other hand, pure bulk tungsten cannot be usually utilized as a structural material due to its brittle nature with a high temperature of brittle-to-ductile transition, and due to difficult processing and machining. Therefore, to fulfill high demands put on the components of the fusion reactors, novel advanced materials have to be developed.

Plasma-facing components, primarily based on tungsten, have to be joined with the supporting structure. Due to the high amount of energy absorbed from the plasma, the heat has to be efficiently removed from the exposed surfaces of plasma-facing components, in order to minimize armor erosion [1]. In the current ITER design, the adjacent water-cooled heat sink is made of CuCrZr pipes, and joined to the tungsten divertor by a copper interlayer [4–8]. Similar divertor design with the water-cooled copper-based heat sink is also one of the options for future fusion devices, such as DEMO [8–10]. However, cracking and delamination can occur between the tungsten components and the copper-based heat sink due to a large difference in thermal expansion coefficients [11–14]. Alternatively, a helium gas-cooled modular divertor is considered, in which the tungsten components are joined with a steel heat sink [9,15–17]. Nevertheless, the difference in thermal expansion

coefficients of tungsten and steel is also significant, which results in high stresses at the interface [15–18]. Therefore, in order to assure the best interconnection and to reduce stress concentration at tungsten/steel interfaces, several joining techniques of steel and tungsten have been presented [19]. Tungsten may be deposited on steel substrates as a plasma-sprayed coating [11,20–23]. Kruszewski et al. [18] designed possible bonding of tungsten and P91 steel elements through WL10 (W – 1 wt.% La_2O_3) interlayer and successfully fabricated W/WL10 and WL10/steel joints by pulse plasma sintering. Weber et al. [17] produced functionally graded tungsten/steel coatings by vacuum plasma spraying and magnetron sputtering. Zhong et al. [24] produced tungsten/ferritic steel joints with a Ni interlayer by diffusion bonding. Rasinski et al. [25] prepared Fe/W binary coatings by magnetron sputtering deposition technique. Powder metallurgy techniques have also been used. Qu et al. [26] used resistance sintering at ultra-high pressure. Despite very short processing times, intermetallic layer formation at the steel/tungsten interfaces was observed. Tan et al. [27] used mechanical alloying and spark plasma sintering. It was found that increased milling times lead to particle refinement and more homogeneous mixing, but increased amount of intermetallics upon sintering. In both cases, only very basic characterization was performed.

In this paper, tungsten/P91 steel composites fabricated by spark plasma sintering (SPS) [28–30] are addressed. In a fusion reactor (such as DEMO) with significant neutron fluxes, Ni-containing stainless steel cannot be used due to activation. Therefore, reduced activation ferritic-

martensitic steels such as Eurofer 97 [31,32] are foreseen as structural materials. P91 steel was chosen because of a wide availability and similar composition (~9% Cr) to Eurofer.

The aim of this paper is to show how the different processing conditions (different volume fractions of the constituents, sintering times and temperatures) affect the microstructure and, consequently, the macroscopic elastic constants of the composites, and to analyze the microstructural origin of these effects. In principle, the macro-scale mechanical performance of the composite results not only from the volume fractions of P91 and tungsten, but also from several microstructural features, such as micro-cracking, imperfect bondings of the particles, and formation of intermetallic phases. We show that all these features are sensitively reflected by the elastic constants, and use finite elements modelling (FEM) to identify the contribution of these individual features to the macroscopic elastic behavior.

2. Materials and methods

2.1. Materials fabrication and microstructural characterization

One P91 steel sample and seven types of tungsten/steel composites were consolidated by spark plasma sintering (SPS), using a 10-4 SPS device from Thermal Technology, USA (see [29] for more details). Powders of tungsten (Osram Sylvania, USA) and P91 steel (Karlsruhe Institute of Technology, Germany) were sieved to < 20 μm size. The powders were mechanically mixed at various volume ratios (ranging from 0/100 to 69/31, as summarized in the first column of Table 1), put into a graphite die lined with a graphite foil, and sintered in a pulsed current regime in He atmosphere of 50 Pa under a uniaxial pressure of 80 MPa. The sintering was controlled by a pyrometer sensing the process temperature in a hollow cavity made in the graphite die only about 1 mm from the sintered material. This characteristic processing temperature ranged from 1100 to 1400 °C, and the samples are always referred in this paper with the respect to this temperature. The sintering times were 2 min for all composites, except for the 53/47 composite sintered for 30 min, as seen in Table 1. The heating rate up to the maximum temperature and cooling rate down to 800 °C were 100 °C/min, followed by free cooling. The sintered compacts had a diameter of 19 mm and thickness of 3 mm; the surface affected by a contact with graphite was ground away.

The W/P91 volume ratio as well as the long sintering time for the last sample was chosen with the aim to maximize the formation of the Fe_7W_6 intermetallic compound in order to facilitate the characterization of its properties. This intermetallic phase typically appears in tungsten/steel composites between steel grains and tungsten grains due to diffusion [26–29], and it has much higher yield strength than steel and tungsten, but its thermal conductivity is low, which is unfortunately not desirable for plasma-facing components [29]. Moreover, as a typical intermetallic compound, Fe_7W_6 is brittle, and thus, its

formation embrittles the resulting material [15].

The rapid growth of an intermetallic phase is one the features of spark plasma sintering of a mixture of materials. As shown by Anselmi-Tamburini et al. [33] for the case of sintering of Si and Mo layers, the electric current taking place during SPS enhances the growth rate of an intermetallic $MoSi_2$ phase. Similarly, in the papers by Kondo et al. [34] and Li et al. [35], the diffusion growth of thick intermetallic layers is observed after the SPS of samples consisting of two plates of different materials (Nb and C, or Fe and Al, respectively), with the strong dependence on sintering temperature and time. Moreover, the growth rate of an interphase layer is not linear, as the thickness of the layer follows square-root dependence in time [33–35]; therefore, the SPS of a powder mixture can lead to a formation of thick inter-granular layers only after a few minutes when utilizing a sufficient temperature. Such behavior was observed e.g. for the SPS of Ni and Ti powders [36], where thick layers surrounding the Ni grains were observed after 10 min of sintering; or for the SPS of CoNiAl and Ti powders [37], where intermetallic layers with the thickness of several μm were formed after the sintering for only 1 min.

The microstructures of the composites were studied by scanning electron microscopy (SEM, EVO MA15, Carl Zeiss SMT, Germany) at the polished cross-sections. The phase identification was performed using X-ray diffraction (D8 Discover, Bruker AXS, Germany); their volume fractions were determined by image analysis of the SEM micrographs.

2.2. Resonant ultrasound spectroscopy measurements

From the sintered pellets of tungsten/steel composites, samples with dimensions of approx. 2 mm × 3 mm × 4 mm were cut. Density of the composites was determined by weighting and measuring the volume of the samples. Room-temperature elastic properties were determined by the combination of pulse-echo method and resonant ultrasound spectroscopy. By the pulse-echo method, velocities of longitudinal and shear ultrasonic waves propagating through the samples were measured.

Laser-based contactless resonant ultrasound spectroscopy [38] was utilized for determining elastic constants of the tungsten/steel composites. In this method [39,40], elastic constants are determined by measuring resonant spectra of free elastic vibrations of small samples. The vibrations of the samples are generated by a pulsing infrared laser beam focused on one side of the sample, and they are detected on the other side by a scanning laser vibrometer. The resonant spectrum is then obtained by Fourier transform of the time-amplitude signals. The elastic constants are determined inversely, i.e. by an iterative comparison of the measured resonant spectrum with a resonant spectrum calculated from given elastic coefficients, density and dimensions of the sample. The final set of elastic constants is obtained after the sum of squared differences between measured and calculated resonant frequencies is iteratively minimized.

For all examined SPSed samples, more than 20 resonant frequencies were taken into account for the inverse calculation. It was assumed that the examined materials are macroscopically isotropic, i.e. they can be described by two independent elastic constants only: the Young's modulus E and the shear modulus G. This assumption was verified by measuring the longitudinal wave propagation velocity in directions perpendicular to the individual faces of the samples using the pulse-echo method. For all samples, the differences between velocity values obtained in different direction were smaller than the experimental accuracy of the pulse-echo method (~ 0.05 mm·μs^{-1}), which confirms that the materials do not exhibit any measurable anisotropy. The velocities of ultrasonic waves measured by the pulse-echo method were also used as initial values for the RUS iteration and as a complementary information for the inverse procedure [38].

Table 1
Volume ratios of W and P91 steel powders prior to sintering, sintering temperatures T, sintering times t, and phase compositions of sintered tungsten/steel composites.

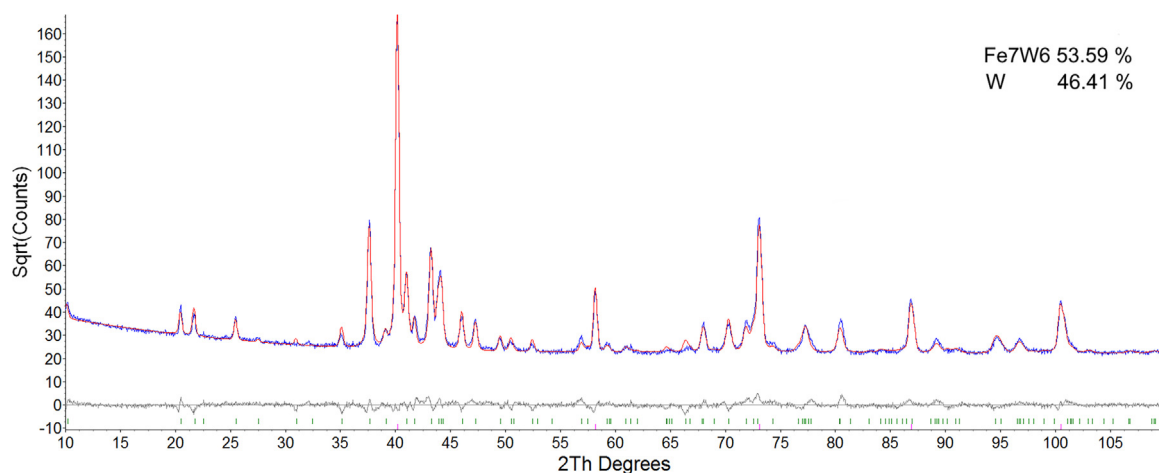| Sintering parameters			Sintered compact		
vol. % W/P91	T [°C]	t [min]	vol. % W	vol. % P91	vol. % Fe_7W_6
0/100	1100	2	0	100	0
20/80	1100	2	11	68	21
43/57	1100	2	37	51	12
69/31	1100	2	61	26	13
69/31	1200	2	52	23	25
69/31	1300	2	47	9	44
69/31	1400	2	41	0	59
53/47	1400	30	15	0	85

Fig. 1. XRD spectrum taken on a cross section of 69/31 sample sintered at 1400 °C. The numbers in the top right corner represent weight fractions of the phases determined by Rietveld refinement of the whole pattern.

3. Results

3.1. Microstructure

All samples exhibited dense structures with negligible porosity. The determined volume fractions of the individual constituents (tungsten, P91 steel and Fe_7W_6-type intermetallic compound) are given in Table 1. The intermetallic phase was identified by X-ray diffraction as having the Fe_7W_6 structure (Fig. 1). For simplicity, the crystallographic designation Fe_7W_6 is used throughout this paper; however, it contained both iron and chromium in a ratio similar to the P91 steel. Energy-dispersive spectroscopy indicated the following composition: 54.1 at.% of Fe, 40.6 at.% of W, and 5.3 at.% of Cr [29].

The representative SEM images of all 8 samples, Fig. 2, were taken in the middle of polished cross-sections. The pure P91 sample, Fig. 2(a), exhibited a homogeneous compact structure of well sintered steel grains, the microstructure of the 53/47 sample sintered for 30 min at 1400 °C, Fig. 2(h), consisted of isolated residual tungsten grains (15% volume fraction) embedded in a homogeneous Fe_7W_6 matrix.

The 20/80 composite, Fig. 2(b), consisted of tungsten grains separated from the steel matrix by thick layers of the Fe_7W_6 compound. The volume fraction of this compound for the 20/80 sample was the highest among all composites sintered at 1100 °C. The structure of this composite was compact, without any visible microcracks or other defects.

Similar structure was also seen for the 43/57 composite, Fig. 2(c), where, however, the intermetallic layer was much thinner and had a dispersed, dendritic-like structure. At some places where clusters of W grains were formed, the gaps between the original tungsten particles were clearly visible (arrows in Fig. 2(c)), which indicates imperfect bonding. At other places, the tungsten grains appeared to be connected by thin layers of the Fe_7W_6 compound.

With increasing volume fraction of tungsten, the increased number of unconnected or loosely connected W grains inside of larger clusters was observed. In the microstructure of the 69/31 composite sintered at 1100 °C, Fig. 2(d), large areas of such grains were visible, while the Fe_7W_6 compound was observed only in thin layers surrounding the W clusters.

For the same volume ratio, the bonding between W grains was improved by increasing the sintering temperature. As seen in Fig. 2(e, f), higher temperatures led simultaneously also to thickening of the Fe_7W_6 layer encapsulating the agglomerated W grains. Finally, for the 1400 °C sintering temperature, Fig. 2(g), the steel practically completely disappeared and the microstructure consisted of well sintered tungsten regions surrounded by the Fe_7W_6 matrix. There were few microcracks observed in the Fe_7W_6 regions, typically between W grains.

Let us mention that this microstructure is very similar to the one observed for the 53/47 sample sintered at 1400 °C/30 min, Fig. 2(h), for which, however, no microcracks were observed.

In summary, it can be concluded that there are two concurrent processes taking place in the composites with high volume fraction of tungsten when sintered at higher temperatures and/or for longer times: one is the improvement of bonding quality between W particles, which is favorable, the second one is the rapid growth of the brittle intermetallic compound, which is in principle not desirable. The interplay of these two processes then determines the macro-scale mechanical properties of the composites.

3.2. Density and elastic constants

The results of the density measurements and of the RUS measurements of elastic constants are listed in Table 2 and also shown in Fig. 3. The density exhibits a monotonous increase with increasing W content, which is expectable due to significantly higher density of tungsten in comparison with steel. For the P91 sample, the resulting density is very close to the density of the bulk material (7.76 g cm^{-3}), which confirms that the chosen temperature and sintering time were sufficient for the full compaction of the steel powder. For the tungsten/steel composites, the density increases both with increasing temperature and sintering time. This takes place together with the growth of the Fe_7W_6-type phase (pure Fe_7W_6 has bulk density of 14.89 g cm^{-3} [41]). This growth is dominantly at the expense of P91, as the volume fraction of P91 decreases faster than of W (see Table 1) with the increasing temperature. On the other hand, as the evolution of density with the W content is approximately linear, and the increase in density with increasing sintering temperature is not very pronounced, it appears that the density evolution is not very sensitive to the imperfect bondings between the tungsten grains. As seen in the micrographs in Fig. 2, the imperfectly bonded W grains are closely packed, with only narrow gaps between them; hence, only a weak effect on the density evolution can be expected. Nevertheless, the overall density values are slightly lower than what would correspond to the mixing rule of the individual phases with the measured volume fractions, as given in Table 2. As the composition of the newly formed phases, especially the Fe_7W_6-type phase, is affected by the presence of other alloying elements, such as chromium, their density could be different than the table value of pure Fe_7W_6 intermetallic phase. Moreover, the real densities of fully sintered phases prepared by SPS can be still lower than those of cast polycrystalline materials, which could also affect the overall density.

A completely different behavior is observed for the elastic constants. The elastic stiffness for composites with imperfectly bonded tungsten
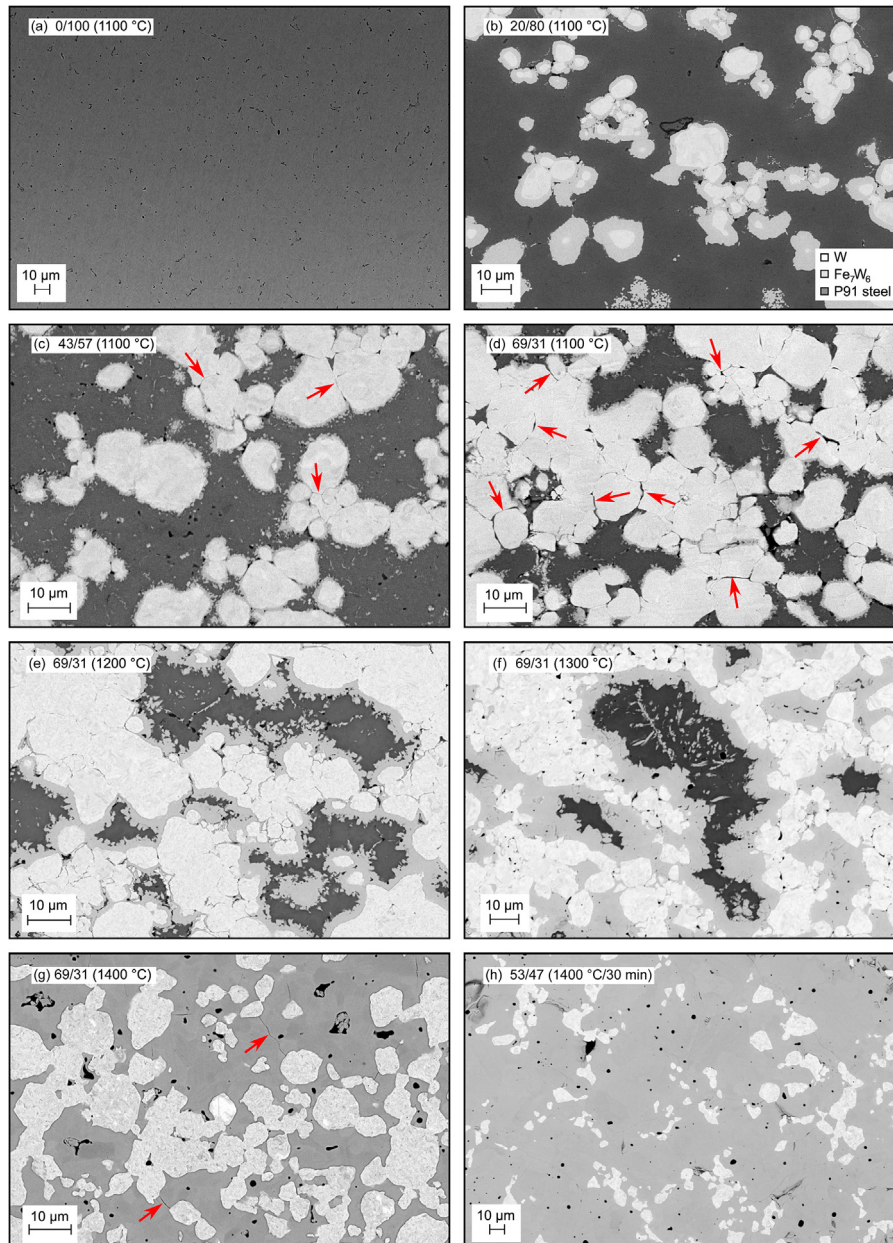
Fig. 2. Microstructures of the examined tungsten/steel composites. In (a), the structure of sintered P91 steel in shown. In (b–f), the brightest regions are the W particles, the medium-gray regions are the Fe_7W_6 compound and the darkest regions are the P91 steel; in (g–h) the brighter regions are W particles and the darker regions are the Fe_7W_6 matrix. The arrows in subfigures (c) and (d) indicate the locations where the imperfect bonding between the W particles is the most evident; the arrows in subfigure (g) show the location of sparse microcracks.

grains is obviously decreased, as the weak bonds between the grains cannot fully transmit the stresses and can relax the strains by mutual sliding of the grains along each other. By increasing the sintering temperature or time, the elastic constants are significantly increased. Both the Young's modulus E and the shear modulus G are two times higher for sintering at 1400 °C than for 1100 °C, while the change in density is about 20%. In summary, the E/ρ ratio of the composite significantly increases with increasing sintering temperature. As the E/ρ ratios of the individual bulk components (P91, W and Fe_7W_6) are rather comparable, this massive increase cannot be explained by changes in the phase composition only, but must be ascribed to the change of the bonding quality.

4. Discussion based on FEM modelling

To discuss quantitatively the effect of the concurrent growth of the Fe_7W_6 compound and the improving quality of the bonds between the tungsten grains, the macroscale elasticity of the composites was studied by finite elements (FEM) simulations. The main aim was to analyze what was the effective elasticity of the individual components, in particular of the weakly bonded tungsten agglomerates.

For this analysis, several simplifying assumptions were made. Among these assumptions, the most important were:

1 the elastic weakening was ascribed only to the tungsten grains, i.e. the Fe_7W_6 and P91 elastic constants were assumed the same for all composites. It was further assumed that the granular-like matter consisting of imperfectly bonded W grains behaved as a

Table 2

Density (ρ) and elastic constants (E and G) of the examined materials. The given experimental errors for ρ were obtained by repeated weighting and measuring of the sample dimensions; the experimental errors in E and G were obtained via the RUS sensitivity analysis described in [38].

| Sample (W/P91)	ρ [g cm^{-3}]	E [GPa]	G [GPa]
pure P91 (1100 °C/2 min)	7.65 ± 0.09	211.91 ± 1.17	79.09 ± 0.24
20/80 (1100 °C/2 min)	9.95 ± 0.12	239.35 ± 2.08	91.15 ± 0.51
43/57 (1100 °C/2 min)	12.14 ± 0.14	243.20 ± 1.67	91.69 ± 0.38
69/31 (1100 °C/2 min)	12.94 ± 0.16	172.83 ± 1.72	66.60 ± 0.43
69/31 (1200 °C/2 min)	13.59 ± 0.17	205.87 ± 3.01	76.74 ± 0.58
69/31 (1300 °C/2 min)	14.85 ± 0.19	288.08 ± 1.97	108.87 ± 0.50
69/31 (1400 °C/2 min)	15.62 ± 0.18	344.99 ± 3.43	127.80 ± 0.74
53/47 (1400 °C/30 min)	14.32 ± 0.18	305.02 ± 3.96	112.26 ± 0.76
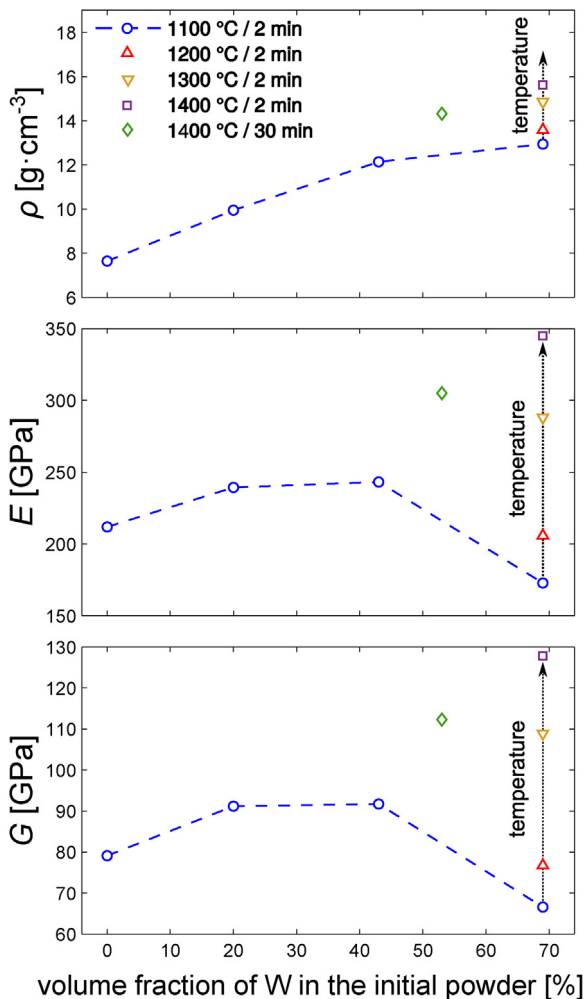
Fig. 3. Density (ρ) and elastic constants (E and G) of the examined materials, plotted with respect to the volume fraction of W in the initial powder. The dashed lines outline the evolutions with increasing tungsten content, the dotted arrows outline the evolutions for fixed volume fraction of tungsten and increasing sintering temperature.

homogeneous, linearly elastic isotropic material, i.e. when there are some structural defects, such as porosity or poor bonding between the tungsten grains, they will be reflected in the macroscopic elastic

weakening. Hence, the inaccuracy in density determination discussed above does not have any effect on the FEM model.

2 a simplified geometry was considered; it was assumed that the whole microstructure can be represented by a volume element consisting of a spherical region of tungsten, separated from the P91 matrix by an interlayer (spherical shell) of Fe$_7$W$_6$, Fig. 4(a). Diameters of the inner sphere and the spherical shell where determined in such a way that the ratios of the volumes of particular domains corresponded to the phase compositions of every sample as given in Table 1. A periodic repetition of this element in all three spatial dimensions was considered. For the samples with only the tungsten and Fe$_7$W$_6$ components, no interlayer was assumed; instead, the considered microstructure was a tungsten sphere embedded in a homogeneous Fe$_7$W$_6$ matrix, Fig. 4(b). For the samples with small volume fraction of P91, the Fe$_7$W$_6$ interlayers in the individual elements were mutually connected along the principal directions, i.e. along the directions of the edges of the representative element, Fig. 4(c). All interfaces were considered sharp and smooth, i.e. the dispersed, dendritic-like structure observed for some of the P91–Fe$_7$W$_6$ interfaces was not taken into account.

3 as the structure composed of these representative volume elements had a cubic symmetry, also the elastic constants exhibited a weak cubic anisotropy. It was assumed that the elastic constants of an isotropic composite can be then calculated from these anisotropic constants using the Hill's averaging scheme. Nevertheless, for all calculated structures, the upper (Voigt) and lower (Reuss) bounds for the isotropic elastic constants did not differ by more than 1 GPa, i.e. the use of Hill's homogenizing scheme was fully justified.

Under these assumptions, a FEM model was constructed and solved using the Comsol Multiphysics computational environment. Tetrahedral quadratic Lagrangian elements were used for the calculation. Three basic loading modes, in particular the unidirectional compressive strain, the simple shear and the pure shear, were considered to obtain three independent material parameters under the assumption of cubic anisotropy: c_{11}, c_{12} and c_{44}. These loading modes were achieved in the FEM model by prescription of relative displacements of corresponding nodes on the opposite faces of the mesh and periodical boundary conditions on the unloaded opposite faces. The respective elastic constants were then obtained from the sum of the deformation energy calculated over the volume of the unit representative cell.

By using this FEM model, the elastic constants of the examined phases were determined inversely, i.e. by minimizing the misfit function

$$F = (E^{\text{exp.}} - E^{\text{calc.}}(E^*, G^*, E\dagger, G^\dagger))^2 + (G^{\text{exp.}} - G^{\text{calc.}}(E^*, G^*, E^\dagger, G^\dagger))^2, \quad (1)$$

where $E^{\text{exp.}}$ and $G^{\text{exp.}}$ are the experimentally determined elastic constants of the composite, and $E^{\text{calc.}}$ and $G^{\text{calc.}}$ are the elastic constants calculated for this composite via the FEM model. The $(E, G)^{\text{calc.}}$ constants were taken as dependent on the sought elastic coefficients $(E, G)^*$ of one of the components of the composite and the known elastic coefficient $(E, G)^\dagger$ of all other components. The minimization was then performed with respect to $(E, G)^*$.

As the first step, the elastic constants of the Fe$_7$W$_6$ intermetallic phase were determined from the elastic constants of the composites consisting only of this phase and the tungsten grains embedded in the Fe$_7$W$_6$ matrix, i.e. the 69/31 (1400 °C/2 min) and 53/47 (1400 °C/ 30 min) samples. The elastic constants of polycrystalline tungsten were taken as $E = 400$ GPa and $G = 155$ GPa according to [42]. The same value of the Young's modulus was recently reported for SPSed tungsten [29], and is also well consistent with other literature [15,43,44], where typically the values between 390 GPa and 410 GPa are used.

The results are given in the first two rows of Table 3. The obtained values of E and G for both materials are satisfyingly similar (differences
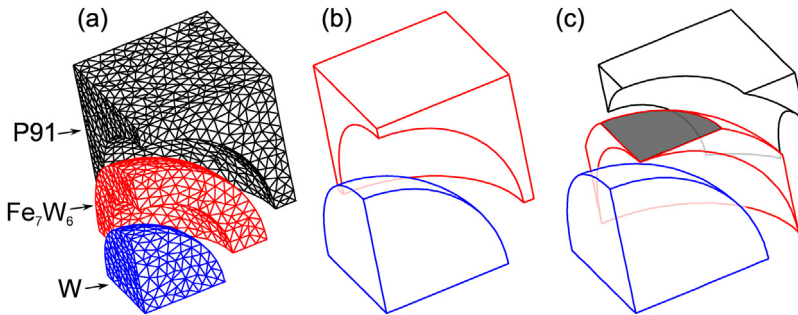
Fig. 4. One octant of the representative volume element (the computational domain) used for the FEM simulations: (a) the basic spatial arrangement of the individual phases, showing also the used computational mesh with tetrahedral element; (b) the simplified geometry of composites with only two phases (W and Fe_7W_6); (c) the representative volume element for the case where the Fe_7W_6 interlayer penetrates the faces of the computational domain and connects with the neighboring element. The shading indicates the contact area in the vertical direction (contact areas in the horizontal directions are not visible).

Table 3

Elastic constants of the Fe_7W_6 phase and of imperfectly sintered tungsten obtained by inverse calculations for the given samples. The parentheses for the 69/31 (1100 °C/2 min) sample denote that these values were obtained with high uncertainty.

Material	Sample (W/P91 ratio, T, t)	E [GPa]	G [GPa]
Fe_7W_6	69/31 (1400 °C/2 min)	309	111
	53/47 (1400 °C/30 min)	291	106
W	69/31 (1300 °C/2 min)	291	116
	69/31 (1200 °C/2 min)	171	64
	69/31 (1100 °C/2 min)	142	56
	43/57 (1100 °C/2 min)	276	108
	20/80 (1100 °C/2 min)	(340)	(148)

~5%), especially when taking into account the simplifications of the model and the inaccuracy in the determination of the volume fractions from the SEM micrographs. For further calculations, the average values $E = 300$ GPa and $G = 109$ GPa were taken.

In the second step, the FEM model was used to analyze the deterioration of the elastic properties due to imperfect bonding of the W particles. The elastic constants of the P91 steel matrix were known from the measurements, the elastic constants of the Fe_7W_6 phase were known from the above analysis, and the elastic constants of tungsten were sought by the inverse procedure. Such an inverse calculation was possible for all 69/31 composites (sintered at 1100 °C, 1200 °C, and 1300 °C) and for the 43/57 composite. For the 20/80 composite, the inverse calculation was not reliable due to the low volume fraction of tungsten. The elastic constants E^* and G^* minimizing the misfit function were found even for this material, however, these results should be understood as only very rough approximations.

All results are given in the lower part of Table 3. A clear correlation between the elastic constants and the microstructure can be seen, Fig. 5: the lowest elastic constants are for the 69/31 (1100 °C composite), where the bonding between the W grains is obviously the weakest. With increasing sintering temperature, the elastic constants rapidly increase. Similarly, a significant increase is observed with decreasing volume fraction of W; this is again consistent with the microstructural observations, as in the composites with reduced volume fraction of tungsten, most of the tungsten particles are neighboring to the P91 matrix (over the newly forming Fe_7W_6 interlayers), and the weakly bonded W–W interfaces are less likely to appear. Let us point out that the changes in E and G of tungsten obtained by this calculation are much stronger than the corresponding changes of the elastic constants of the composites. Hence, it can be concluded that the observed evolutions of the elastic constants of the composites can be dominantly ascribed to the unsintered W particles, rather than to the changes of the volume fractions of the individual components due to the growth of the Fe_7W_6 phase.

5. Conclusion

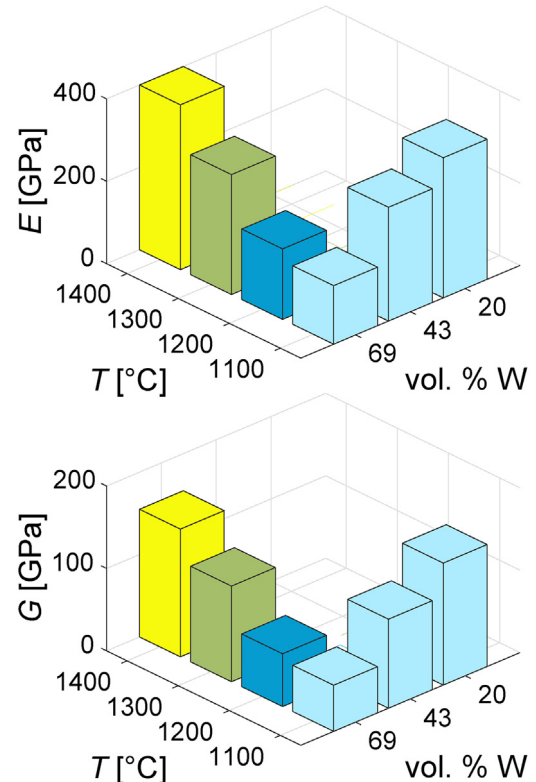We have shown that the elastic moduli (E and G) are sensitive to

Fig. 5. Evolutions of elastic moduli of the tungsten agglomerations with sintering temperature and the volume fraction of tungsten in the initial powder. With increasing temperature the moduli increase due to improved bonding between the particles, with the decreasing volume fraction of tungsten the moduli increase due to decreasing number of W–W interfaces (at W–P91 interfaces, good bonding appears due to formation of the Fe_7W_6 interlayers). The values for $T = 1400$ °C are the literature data [42], all other values were determined from RUS results inversely via the FEM model.

several microstructural features in spark plasma sintered tungsten/steel composites, in particular that their reduction can indicate imperfect bonding between the W particles. For composites with high volume fraction of tungsten and, simultaneously, low sintering temperature, the agglomerations of W particles were shown to behave effectively as regions with elastic moduli more than two times smaller than for a bulk polycrystalline tungsten. On the other hand, the elastic response of these regions was not limiting to zero, i.e. the weakly bonded W agglomerations can still transmit some part of the mechanical stresses and contribute to the macro-scale elastic stiffness of the composite, as expectable for a granular-like medium encapsulated in a matrix.

The result have also shown that the bonding quality in the tungsten/steel composites is strongly dependent not only on the technological parameters (sintering temperature, time, etc.), but also on the volume fraction ratios of the initial powders. For composites with low content

of tungsten, good bonding is provided by formation of the Fe_7W_6 phase at the interfaces between tungsten and steel particles. For higher contents of W, however, the density of non-sintered W–W interfaces increases and higher sintering temperatures are required to ensure good bonding. This, on the other hand, leads to an accelerated growth of the brittle Fe_7W_6 phase, which can be also monitored by elasticity measurements.

Acknowledgement

References

[1] I. Smid, M. Akiba, G. Vieider, L. Plöchl, Development of tungsten armor and bonding to copper for plasma-interactive components, J. Nucl. Mater. 258–263 (Part 1) (1998) 160–172, http://dx.doi.org/10.1016/S0022-3115(98)00358-4.

[2] V. Philipps, Tungsten as material for plasma-facing components in fusion devices, J. Nucl. Mater. 415 (1 Suppl) (2011) S2–S9, http://dx.doi.org/10.1016/j.jnucmat.2011.01.110 Proceedings of the 19th International Conference on Plasma-Surface Interactions in Controlled Fusion.

[3] Y. Ueda, J.W. Coenen, G.D. Temmerman, R.P. Doerner, J. Linke, V. Philipps, E. Tsitrone, Research status and issues of tungsten plasma facing materials for ITER and beyond Proceedings of the 11th International Symposium on Fusion Nuclear Technology-11 (ISFNT-11), Barcelona, Spain, 15–20 September, 2013, Fusion Eng. Des. 89 (7–8) (2014) 901–906, http://dx.doi.org/10.1016/j.fusengdes.2014.02.078.

[4] V. Barabash, A. Peacock, S. Fabritsiev, G. Kalinin, S. Zinkle, A. Rowcliffe, J.-W. Rensman, A.A. Tavassoli, P. Marmy, P.J. Karditsas, F. Gillemot, M. Akiba, Materials challenges for ITER – current status and future activities Proceedings of the Twelfth International Conference on Fusion Reactor Materials (ICFRM-12), J. Nucl. Mater. 367–370 (Part A) (2007) 21–32, http://dx.doi.org/10.1016/j.jnucmat.2007.03.017.

[5] R.A. Pitts, S. Carpentier, F. Escourbiac, T. Hirai, V. Komarov, A.S. Kukushkin, S. Lisgo, A. Loarte, M. Merola, R. Mitteau, A.R. Raffray, M. Shimada, P.C. Stangeby, Physics basis and design of the ITER plasma-facing components Proceedings of the 19th International Conference on Plasma-Surface Interactions in Controlled Fusion, J. Nucl. Mater. 415 (1 Suppl) (2011) S957–S964, http://dx.doi.org/10.1016/j.jnucmat.2011.01.114.

[6] P. Gavila, B. Riccardi, G. Pintsuk, G. Ritz, V. Kuznetsov, A. Durocher, High heat flux testing of EU tungsten monoblock mock-ups for the ITER divertor Proceedings of the 28th Symposium On Fusion Technology (SOFT-28), Fusion Eng. Des. 98–99 (2015) 1305–1309, http://dx.doi.org/10.1016/j.fusengdes.2014.12.006.

[7] Y. Seki, K. Ezato, S. Suzuki, K. Yokoyama, H. Yamada, T. Hirayama, A study of plasma facing tungsten components with electrical discharge machined surface exposed to cyclic thermal loads Proceedings of the 12th International Symposium on Fusion Nuclear Technology-12 (ISFNT-12), Fusion Eng. Des. 109–111 (Part B) (2016) 1148–1152, http://dx.doi.org/10.1016/j.fusengdes.2016.01.001.

[8] F. Crescenzi, H. Greuner, S. Roccella, E. Visca, J.H. You, ITER-like divertor target for DEMO: design study and fabrication test, Fusion Eng. Des. (2017), http://dx.doi.org/10.1016/j.fusengdes.2017.02.014.

[9] D. Stork, P. Agostini, J.L. Boutard, D. Buckthorpe, E. Diegele, S.L. Dudarev, C. English, G. Federici, M.R. Gilbert, S. Gonzalez, A. Ibarra, C. Linsmeier, A.L. Puma, G. Marbach, P.F. Morris, L.W. Packer, B. Raj, M. Rieth, M.Q. Tran, D.J. Ward, S.J. Zinkle, Developing structural, high-heat flux and plasma facing materials for a near-term DEMO fusion power plant: the EU assessment Proceedings of the 16th International Conference on Fusion Reactor Materials (ICFRM-16), J. Nucl. Mater. 455 (1–3) (2014) 277–291, http://dx.doi.org/10.1016/j.jnucmat.2014.06.014.

[10] J.-H. You, Copper matrix composites as heat sink materials for water-cooled divertor target, Nucl. Mater. Energy 5 (2015) 7–18, http://dx.doi.org/10.1016/j.nme.2015.10.001.

[11] S.Y. Moon, C.H. Choi, H.S. Kim, P. Oh, B.G. Hong, S.K. Kim, D.W. Lee, Thick tungsten coating on ferritic-martensitic steel applied with a vacuum plasma spray coating method, Surf. Coat. Technol. 280 (2015) 225–231, http://dx.doi.org/10.1016/j.surfcoat.2015.09.008.

[12] I.S. Batra, G.B. Kale, T.K. Saha, A.K. Ray, J. Derose, J. Krishnan, Diffusion bonding of a Cu-Cr-Zr alloy to stainless steel and tungsten using nickel as an interlayer, Mater. Sci. Eng. A 369 (1) (2004) 119–123, http://dx.doi.org/10.1016/j.msea.2003.10.296.

[13] A. Herrmann, H. Greuner, M. Balden, H. Bolt, Design and evaluation of an optimized W/Cu interlayer for W monoblock components, Fusion Eng. Des. 86 (1) (2011) 27–32, http://dx.doi.org/10.1016/j.fusengdes.2010.07.018.

[14] H. Greuner, A. Zivelonghi, B. Bösirth, J.-H. You, Results of high heat flux testing of W/CuCrZr multilayer composites with percolating microstructure for plasma-facing components Proceedings of the 28th Symposium On Fusion Technology (SOFT-28), Fusion Eng. Des. 98–99 (2015) 1310–1313, http://dx.doi.org/10.1016/j.fusengdes.2015.02.011.

[15] J.M. Missiaen, J.J. Raharijaona, A. Antoni, C. Pascal, M. Richou, P. Magaud, Design of a W/steel functionally graded material for plasma facing components of DEMO,

[16] J. Nucl. Mater. 416 (3) (2011) 262–269, http://dx.doi.org/10.1016/j.jnucmat.2011.05.054.

[16] T. Weber, M. Härtelt, J. Aktaa, Considering brittleness of tungsten in failure analysis of helium-cooled divertor components with functionally graded tungsten/EUROFER97 joints, Eng. Fract. Mech. 100 (2013) 63–75, http://dx.doi.org/10.1016/j.engfracmech.2012.07.024 Crack growth in brittle materials.

[17] T. Weber, M. Stüber, S. Ulrich, R. Vaßen, W.W. Basuki, J. Lohmiller, W. Sittel, J. Aktaa, Functionally graded vacuum plasma sprayed and magnetron sputtered tungsten/EUROFER97 interlayers for joints in helium-cooled divertor components, J. Nucl. Mater. 436 (1–3) (2013) 29–39, http://dx.doi.org/10.1016/j.jnucmat.2013.01.286.

[18] M.J. Kruszewski, L. Ciupinski, M. Rosinski, A. Michalski, K.J. Kurzydlowski, Pulse plasma sintering of a tungsten/steel divertor module Proceedings of the 27th Symposium on Fusion Technology (SOFT-27); Liège, Belgium, September 24–28, 2012, Fusion Eng. Des. 88 (9–10) (2013) 2573–2576, http://dx.doi.org/10.1016/j.fusengdes.2013.05.018.

[19] M. Rieth, S.L. Dudarev, S.M.G. de Vicente, J. Aktaa, T. Ahlgren, S. Antusch, D.E.J. Armstrong, M. Balden, N. Baluc, M.-F. Barthe, W.W. Basuki, M. Battabyal, C.S. Becquart, D. Blagoeva, H. Boldyryeva, J. Brinkmann, M. Celino, L. Ciupinski, J.B. Correia, A.D. Backer, C. Domain, E. Gaganidze, C. García-Rosales, J. Gibson, M.R. Gilbert, S. Giusepponi, B. Gludovatz, H. Greuner, K. Heinola, T. Höschen, A. Hoffmann, N. Holstein, F. Koch, W. Krauss, H. Li, S. Lindig, J. Linke, C. Linsmeier, P. López-Ruiz, H. Maier, J. Matejicek, T.P. Mishra, M. Muhammed, A. Mu noz, M. Muzyk, K. Nordlund, D. Nguyen-Manh, J. Opschoor, N. Ordás, T. Palacios, G. Pintsuk, R. Pippan, J. Reiser, J. Riesch, S.G. Roberts, L. Romaner, M. Rosinski, M. Sanchez, W. Schulmeyer, H. Traxler, A. Ure na, J.G. van der Laan, L. Veleva, S. Wahlberg, M. Walter, T. Weber, T. Weitkamp, S. Wurster, M.A. Yar, J.H. You, A. Zivelonghi, Recent progress in research on tungsten materials for nuclear fusion applications in Europe, J. Nucl. Mater. 432 (1–3) (2013) 482–500, http://dx.doi.org/10.1016/j.jnucmat.2012.08.018.

[20] H. Bolt, V. Barabash, W. Krauss, J. Linke, R. Neu, S. Suzuki, N. Yoshida, A.U. Team, Materials for the plasma-facing components of fusion reactors Proceedings of the 11th International Conference on Fusion Reactor Materials (ICFRM-11), J. Nucl. Mater. 329–333 (Part A) (2004) 66–73, http://dx.doi.org/10.1016/j.jnucmat.2004.04.005.

[21] Y. Yahiro, M. Mitsuhara, K. Tokunakga, N. Yoshida, T. Hirai, K. Ezato, S. Suzuki, M. Akiba, H. Nakashima, Characterization of thick plasma spray tungsten coating on ferritic/martensitic steel F82H for high heat flux armor Proceedings of the Thirteenth International Conference on Fusion Reactor Materials, J. Nucl. Mater. 386–388 (2009) 784–788, http://dx.doi.org/10.1016/j.jnucmat.2008.12.219 Fusion reactor materials.

[22] T. Otsuka, T. Tanabe, K. Tokunaga, Behaviour of tritium in plasma-sprayed tungsten coating on steel exposed to tritium plasma, Phys. Scr. 2011 (T145) (2011) 014035, http://dx.doi.org/10.1088/0031-8949/2011/t145/014035.

[23] Y.J. Lee, H.-M. Sung, Y. Jin, K. Lee, C.R. Park, G.-H. Kim, H.N. Han, Improvement of mechanical property of air plasma sprayed tungsten film using pulsed electric current treatment, Int. J. Refract. Met. Hard Mater. 60 (2016) 99–103, http://dx.doi.org/10.1016/j.ijrmhm.2016.07.001.

[24] Z. Zhong, T. Hinoki, A. Kohyama, Effect of holding time on the microstructure and strength of tungsten/ferritic steel joints diffusion bonded with a nickel interlayer, Mater. Sci. Eng. A 518 (1) (2009) 167–173, http://dx.doi.org/10.1016/j.msea.2009.04.043.

[25] M. Rasinski, S. Möller, J. Steffens, B. Unterberg, K. Sugiyama, T. Schwarz-Selinger, A. Kreter, C. Linsmeier, Morphology and composition of Fe-W coatings after deuterium plasma exposure as a model system for RAFM steels, Phys. Scr. 2016 (T167) (2016) 014013, http://dx.doi.org/10.1088/0031-8949/2016/t167/014013.

[26] D. Qu, Z. Zhou, J. Tan, J. Aktaa, Characterization of W/Fe functionally graded materials manufactured by resistance sintering under ultra-high pressure, Fusion Eng. Des. 91 (2015) 21–24, http://dx.doi.org/10.1016/j.fusengdes.2014.12.014.

[27] C. Tan, G. Wang, L. Ji, Y. Tong, X.-M. Duan, Investigation on 316L/W functionally graded materials fabricated by mechanical alloying and spark plasma sintering, J. Nucl. Mater. 469 (2016) 32–38, http://dx.doi.org/10.1016/j.jnucmat.2015.11.024.

[28] J. Matějíček, B. Nevrlá, M. Vilémová, H. Boldyryeva, Overview of processing technologies for tungsten-steel composites and FGMs for fusion applications, Nukleonika 60 (20) (2015) 267–273, http://dx.doi.org/10.1515/nuka-2015-0049.

[29] J. Matějíček, B. Nevrlá, J. Čech, M. Vilémová, V. Klevarová, P. Haušild, Mechanical and thermal properties of individual phases formed in sintered tungsten-steel composites, Acta Phys. Polonica A 128 (4) (2015) 718–721, http://dx.doi.org/10.12693/aphyspola.128.718.

[30] O. El-Atwani, D.V. Quach, M. Efe, P.R. Cantwell, B. Heim, B. Schultz, E.A. Stach, J.R. Groza, J.P. Allain, Multimodal grain size distribution and high hardness in fine grained tungsten fabricated by spark plasma sintering, Mater. Sci. Eng. A 528 (18) (2011) 5670–5677, http://dx.doi.org/10.1016/j.msea.2011.04.015.

[31] P. Fernandez, A.M. Lancha, J. Lapena, M. Serrano, M. Hernandez-Mayoral, Reduced activation ferritic/martensitic steel Eurofer 97 as possible structural material for fusion devices, Metallurgical Characterization on As-Received Condition and after Simulated Services Conditions, Centro de Investigaciones Energeticas, Medioambientales y Tecnologicas (CIEMAT) (2004) URL https://inis.iaea.org/search/search.aspx?orig_q=RN:36026402.

[32] M. Eddahbi, M.A. Monge, T. Leguey, P. Fernández, R. Pareja, Texture and mechanical properties of EUROFER 97 steel processed by ECAP, Mater. Sci. Eng. A 528 (18) (2011) 5927–5934, http://dx.doi.org/10.1016/j.msea.2011.04.006.

[33] U. Anselmi-Tamburini, J. Garay, Z. Munir, Fundamental investigations on the spark plasma sintering/synthesis process: III. Current effect on reactivity, Mater. Sci. Eng. A 407 (1) (2005) 24–30, http://dx.doi.org/10.1016/j.msea.2005.06.066.

[34] T. Kondo, M. Yasuhara, T. Kuramoto, Y. Kodera, M. Ohyanagi, Z.A. Munir, Effect of

pulsed DC current on atomic diffusion of Nb-C diffusion couple, J. Mater. Sci. 43 (19) (2008) 6400–6405, http://dx.doi.org/10.1007/s10853-008-2758-z.

[35] R. Li, T. Yuan, X. Liu, K. Zhou, Enhanced atomic diffusion of Fe-Al diffusion couple during spark plasma sintering, Scr. Mater. 110 (2016) 105–108, http://dx.doi.org/10.1016/j.scriptamat.2015.08.012.

[36] B.A. Obadele, O.O. Ige, P.A. Olubambi, Fabrication and characterization of titanium-nickel-zirconia matrix composites prepared by spark plasma sintering, J. Alloys Compd. 710 (2017) 825–830, http://dx.doi.org/10.1016/j.jallcom.2017.03.340.

[37] M. Koller, T. Chráska, J. Cinert, O. Heczko, J. Kopeček, M. Landa, R. Mušálek, M. Rameš, H. Seiner, J. Stráský, M. Janeček, Mechanical and magnetic properties of semi-heusler/light-metal composites consolidated by spark plasma sintering, Mater. Des. 126 (2017) 351–357, http://dx.doi.org/10.1016/j.matdes.2017.04.028.

[38] P. Sedlák, H. Seiner, J. Zídek, M. Janovská, M. Landa, Exp. Mech. 54 (6) (2014) 1073–1085, http://dx.doi.org/10.1007/s11340-014-9862-6.

[39] J. Maynard, Resonant ultrasound spectroscopy, Phys. Today 49 (1) (1996) 26–31, http://dx.doi.org/10.1063/1.881483.

[40] R.G. Leisure, F.A. Willis, Resonant ultrasound spectroscopy, J. Phys. Condens. Matter 9 (28) (1997) 6001–6029, http://dx.doi.org/10.1088/0953-8984/9/28/002.

[41] Fe7w6 (w6fe7 rt) Crystal Structure: Datasheet from "pauling file multinaries edition – 2012" in springermaterials, copyright 2016 Springer-Verlag Berlin Heidelberg & Material Phases Data System (MPDS), Switzerland & National Institute for Materials Science (NIMS), Japan. URL http://materials.springer.com/isp/crystallographic/docs/sd_0553642.

[42] B.T. Bernstein, Elastic properties of polycrystalline tungsten at elevated temperatures, J. Appl. Phys. 33 (6) (1962) 2140, http://dx.doi.org/10.1063/1.1728910.

[43] Y. Itoh, M. Takahash, H. Tanako, Design of tungsten/copper graded composite for high heat flux components, Fusion Eng. Des. 31 (4) (1996) 279–289, http://dx.doi.org/10.1016/0920-3796(95)00432-7.

[44] A. Hartmaier, P. Gumbsch, Thermal activation of crack-tip plasticity: the brittle or ductile response of a stationary crack loaded to failure, Phys. Rev. B 71 (2005) 024108, http://dx.doi.org/10.1103/PhysRevB.71.024108.

Paper E

An ultrasonic study of relaxation processes in pure and mechanically alloyed tungsten

Martin Koller, Monika Vilémová, František Lukáč, Přemysl Beran, Jakub Čížek, Hynek Hadraba, Jiří Matějíček, Jakub Veverka, Hanuš Seiner

Number of total citations[1]:   0 (excluding self-citations: 0)

Contribution of the PhD candidate and the co-authors:

The candidate performed the RUS measurements, plotted the temperature evolutions of Young's modulus and internal friction, co-wrote the manuscript and coordinated the work on the paper.

Co-authors from the Institute of Plasma Physics (M. Vilémová, F. Lukáč, J. Matějíček, J. Veverka) prepared the powders by the mechanical alloying, consolidated the materials by the SPS, determined their densities and porosities, and provided the micrographs of the structures. P. Beran was responsible for the neutron powder diffraction measurements. J. Čížek examined the composites by the positron annihilation spectroscopy. H. Hadraba contributed to the analysis of the mechanical test results. H. Seiner contributed to the discussion of the results and supervised the work on the paper.

---

[1]According to the Web of Science database `webofknowledge.com` as of August 2020

An ultrasonic study of relaxation processes in pure and mechanically alloyed tungsten

Martin Koller[a,b,*], Monika Vilémová[c], František Lukáč[c,d], Přemysl Beran[e,f], Jakub Čížek[d], Hynek Hadraba[g], Jiří Matějíček[c], Jakub Veverka[a,c], Hanuš Seiner[a]

[a] Faculty of Nuclear Sciences and Physical Engineering, Czech Technical University in Prague, Trojanova 13, 120 00, Praha 2, Czechia
[b] Institute of Thermomechanics, Czech Academy of Sciences, Dolejškova 5, 182 00 Praha 8, Czechia
[c] Institute of Plasma Physics, Czech Academy of Sciences, Za Slovankou 3, 182 00 Praha 8, Czechia
[d] Faculty of Mathematics and Physics, Charles University, V Holešovičkách 2, 180 00 Praha 8, Czechia
[e] Nuclear Physics Institute, Czech Academy of Sciences, Husinec - Řež 130, 250 68 Řež, Czechia
[f] European Spallation Source ERIC, Box 176, SE-221 00, Lund, Sweden
[g] Institute of Physics of Materials, Czech Academy of Sciences, Žižkova 22, 616 62 Brno, Czechia

ARTICLE INFO

ABSTRACT

High-temperature internal friction in a pure tungsten single crystal, polycrystals with different grain sizes, and mechanically alloyed tungsten polycrystals was studied. Positron annihilation spectroscopy was used to prove that all studied materials contain a detectable amount of dislocations. Then, resonant ultrasound spectroscopy was applied to determine the internal friction evolution with temperature from room temperature up to 740 °C. For the pure tungsten samples, a sharp increase of internal friction was observed for temperatures above 470 °C (for the single crystal) or above 400 °C (for the polycrystals); the activation energy corresponding to this increase was the same as the activation energy for the ductile-to-brittle transition in tungsten reported in the literature. For the alloyed materials, direct observation of the onset of this relaxation mechanism was impossible due to additional effects resulting from the secondary phases in the material.

1. Introduction

Due to its exceptionally high melting point and high density, tungsten is used in a wide range of applications. Among others, tungsten can be used as electron emission source, welding electrodes for resistance, inert gas and plasma welding, products for radiation and medical applications such as electrodes in X-ray tubes and components for shielding. Other specific properties such as high temperature strength, low tritium retention, or low thermal expansion favour tungsten for plasma facing applications in future fusion reactors. However, throughout the decades of research and development on tungsten and tungsten-based materials, major drawbacks were discovered. Among the most serious are high ductile-to-brittle transition temperature (DBTT) [1–4] and mechanical properties degradation resulting from grain coarsening at high temperatures and radiation damage [5,6]. This leads to efforts for improving tungsten properties. Various methods have been proposed including alloying, thermo-mechanical post-processing, or application of fast sintering methods [1,7]. Introduction of second-phase particles to tungsten grain boundaries by

alloying and subsequent sintering was shown to be an effective way of grain growth hindering [8]. However, to fulfill the requirements for advanced fusion materials in a reasonable time schedule, there is a need for development of reliable non-destructive methods for studying the ductile-to-brittle behavior and its evolution with processing parameters, irradiation or chemical composition.

The DBTT in tungsten and tungsten-based alloys is typically studied by high-temperature three-point bending (3PB), Charpy impact testing, tensile testing, etc. [9], which are all destructive methods, requiring a direct mechanical contact between a testing device and the sample under controlled temperature. On the other hand, several works indicate that the DBTT can be detected from internal friction measurements [10,11], as the enhancement of the dislocation motion above the DBTT leads to increased dislocation damping. However, there were only few attempts to apply this approach to tungsten documented in the literature so far. A remarkable observation was done by Ziebart and Schultz [12], who reported a low-frequency internal friction study of high purity tungsten single crystals using a torsional pendulum. They observed a rapid increase of the internal friction above approximately

---

350 °C. According to the detailed flow-stress analysis of tungsten single crystals by Brunner and Glebovsky [13], this temperature marks the threshold above which the strain-rate sensitivity starts to decrease with increasing temperature, i.e. above which the thermal activation becomes less and less important for the plastic flow. The strain-rate sensitivity reaches zero at the so-called knee temperature $T_K \approx 470$ °C [14]; a temperature above which the screw dislocations can move without thermal activation.

The relation between T_K and DBTT is very complex and depends on the particular cracking mechanism [15–17]. For tungsten, intergranular fracture has been reported as the main source of brittleness, and, closely related to that, it is well known that the DBTT is strongly correlated with the grain size and grain boundary impurities. Therefore, it is very important to control grain boundary chemistry [18]. An improvement in grain boundary purity is enabled by grain size refinement. Larger area of grain boundaries leads to dilution of impurities [19]. However, to preserve small grain size especially during high temperature sintering, it is necessary to introduce particles into the material that provide pinning effect. Thus, the second-phase particles are known to strengthen the grain boundaries; however, also to increase DBTT [8,20]. This opens the question of how the grain size or the dispersion of the particles affect the internal friction behavior, and T_K in particular.

In this paper, we report on utilization of contactless laser-based ultrasonic measurements for internal friction characterization of tungsten in different conditions: a single crystal, two polycrystalline materials with different grain size, and two mechanically alloyed materials, i.e., polycrystals of tungsten with second-phase particle dispersions. The aim of the research was to explore the sensitivity of this approach to T_K, to discuss the relation between T_K and the microstructure. As the internal friction measurements can be a priori considered as non-destructive methods, such measurements cannot directly capture the DBTT. However, as the mobility of the dislocations may play a key role in the ductile-to-brittle transition, such a study may still be valuable for understanding the DBTT origins in the studied materials.

2. Materials and methods

Two types of tungsten-based materials with second-phase particle dispersion W-1wt.%Y_2O_3 (W-3.7vol.%Y_2O_3), W-2.5wt.%TiC (W-9.6vol.%TiC), and a pure tungsten pellet were prepared by mechanical alloying and subsequently consolidated by spark plasma sintering (SPS). The powders were alloyed in a planetary ball mill Pulverisette 5 (Fritsch, Germany) using WC-Co milling bowls and balls. The powders of W (2 μm average powder size, 99.95% purity), Y_2O_3 (0.7 μm average powder size, 99.99% purity) and TiC (17 μm average powder size, 99.5% purity) were mixed in the corresponding ratios and processed in the planetary ball mill for several tens of hours under argon protective atmosphere, which prevents oxidation during the milling process. The milling speed was set to 240 rpm, and the ball-to-powder ratio was 9:1 for the W-1Y_2O_3 powder, 11:1 for the W-2.5TiC powder, and 7:1 for the pure tungsten powder. These three ball-milled powders and also the unmilled tungsten powder were then consolidated by spark plasma sintering SPS 10–4 device (Thermal Technology, USA) under vacuum with the identical sintering conditions: heating rate of 100 °C/min, sintering temperature of 1800 °C, and dwell time of 2 min.

Moreover, a single-crystalline tungsten sample (see [21] for more details) was studied for comparison. All the studied samples are summarized in Table 1.

Images of the microstructure were acquired using a scanning electron microscope EVO MA 15 (Carl Zeiss SMT, Germany).

Neutron powder diffraction measurements at room temperature were performed on diffractometer MEREDIT@NPI of CANAM infrastructure. Powder samples were placed in the vanadium containers with a diameter of 10 mm. Sintered samples were joined to the exchangeable carousel allowing the rotation along the vertical sample axis to

minimize the possible texture influence in the refinement process. Diffraction patterns were collected between 4° and 144° of 2Θ with the step of 0.8° and using Cu(220) mosaic crystal monochromator producing neutrons with a wavelength of 1.46 Å. An instrument resolution function (IRF) describing the reflection shape given by the instrument obtained from pattern fitting of a SiO_2 standard using the same monochromator setting was used for the refinement. Full pattern refinement was performed using FullProf software [22].

The presence and distribution of lattice defects in the studied samples were examined by positron annihilation spectroscopy. Positron lifetime spectra were measured by high-resolution digital spectrometer described in [23,24] equipped with two Hamamatsu H3378 photomultipliers coupled with BaF_2 scintillators. Detector pulses were sampled in real time by two ultra-fast 8-bit digitizers Acqiris DC211 with a sampling frequency of 4 GHz. The digitized pulses are acquired in a PC and worked out off-line by a software using a new algorithm for integral constant fraction timing. The time resolution of the digital LT spectrometer was 145 ps (FWHM, ^{22}Na). At least 10^7 annihilation events were accumulated in each LT spectrum. The source contribution to the LT spectra consisted of two components with lifetimes of 368 ps and 1.5 ns and corresponding relative intensities 11% and 1% representing contributions of positrons annihilating in the ^{22}Na source spot and the covering mylar foil, respectively.

High-temperature elastic properties were measured by contactless laser-based resonant ultrasound spectroscopy (RUS) [25,26]. From the measured materials, samples with the volume of several mm^3 were cut, and their resonant spectra of free elastic vibrations were measured at room temperature and then at temperatures from 80 °C to 740 °C with 30 °C temperature step. The elastic moduli were obtained inversely, where the measured resonant spectra were iteratively compared with calculated resonant spectra. Moreover, temperature dependencies of internal friction parameter Q^{-1} were determined by measuring the widths of several resonant peaks (full widths at half maximum) in the measured spectra. All samples were assumed to be elastically isotropic, which was verified by measuring ultrasonic wave velocities in three mutually rectangular directions by pulse-echo method. The single-crystalline tungsten sample was also assumed to be elastically isotropic, as the anisotropy ratio of crystalline tungsten, which generally exhibits cubic material symmetry, is very close to 1 [21,27,28].

3. Results

Neutron diffraction patterns revealed the phase composition of the tungsten with particle dispersion in comparison with the spectra of pure tungsten. For the W-PC and W-PCM (only W-PCM shown in Fig. 1) samples, only cubic W phase was found. However, W-1Y_2O_3 consists of cubic tungsten and cubic Y_2O_3 and W-2.5TiC of cubic tungsten, TiC and W_2C. Lattice parameters of titanium carbide can be correlated to non-stochiometric $TiC_{0.6}$. The diffraction patterns with indexed main Bragg diffraction positions of respective phases are shown in Fig. 1. W_2C phase present in the W-2.5TiC sample is likely the result of TiC addition and/or carbon contamination from the sintering die. Phase fractions calculated from the neutron diffraction data are noted in Table 2.

Microstructure comparison of the polycrystalline tungsten materials is provided in Fig. 2. Sintered tungsten consists of larger grains (W-PC, 4 μm average grain size) when compared to milled + sintered tungsten (W-PCM, 1.5 μm average grain size). The dark areas within the microstructure are pores. It is apparent that the W-PC (6%) is more porous than W-PCM (3%). The microstructure of W-2.5TiC composite consists of ultrafine tungsten grains (about 300 nm), and TiC and W_2C particles are located mainly at grain boundaries (dark spots and areas). The particle sizes observable by SEM range from several tens of nanometers to occasional large particles having diameters up to 500 nm. Majority of the particles are however smaller than 150 nm. The microstructure of W-1Y_2O_3 composite (Fig. 2d) has relatively larger tungsten grains (about 700 nm) and Y_2O_3 particles are located at grain boundaries

Table 1
Parameters of the studied materials.

Sample	Initial materials	Processing method	Sample description
W-SC	single-crystalline W	Bridgman growth	single-crystalline W
W-PC	W powder (2 μm)	SPS	polycrystalline W
W-PCM	W powder (2 μm)	ball milling for 25 h + SPS	polycrystalline W
W-2.5TiC	W powder (2 μm) + TiC powder (17 μm)	ball milling for 26 h + SPS	polycrystalline W with TiC particle dispersion
W-1Y$_2$O$_3$	W powder (2 μm) + Y$_2$O$_3$ powder (0.7 μm)	ball milling for 21 h + SPS	polycrystalline W with Y$_2$O$_3$ particle dispersion

(dark areas). The particle size ranges from tens of nm up to about 200 nm; most of them are smaller than 100 nm.

Positron annihilation spectroscopy results on SPS compacts are summarized in Fig. 3. Spectra of positron lifetimes are composed of three components:

- Component 1 (T_1) corresponding to free positrons annihilating in the matrix. Positron lifetime in pure tungsten is ~ 105–100 ps [29,30] and between 90 and 100 ps after annealing above 1000 °C [31]. W-2.5TiC sample exhibits shorter component than the other samples, which is probably caused by the contribution of annihilations at misfit defects associated with TiC particles.
- Component 2 (T_2) identified as positrons annihilating as trapped in dislocations with positron lifetime close to 166 ps. Positron lifetimes in dislocations are close to the monovacancies [32]. Dislocations represent a weak trap for positrons; once the positron is trapped at the dislocation, it quickly diffuses along the dislocation line to be subsequently trapped at a point-like defect.
- Component 3 (T_3) originating from positrons annihilating as trapped in large vacancy clusters and pores. Positron lifetime for a cluster of 40 vacancies is reported to be near 550 ps [31].

As seen in Fig. 3, the spectra for all studied samples include lifetimes of approximately 170 ps, which indicates that dislocations are present in all materials, and also that the character of the dislocations is the same for the alloyed and pure samples. Moreover, the intensities corresponding to these lifetimes are always approximately 50%, which means that the dislocation density is not significantly higher or lower in any of the samples. As expected, the relative intensity of the T_2 lifetime

Table 2
Phase fractions calculated from neutron diffraction data.

Sample	W (vol.%)	Y$_2$O$_3$ (vol.%)	TiC (vol.%)	W$_2$C (vol.%)
W-PCM	100	–	–	–
W-1Y$_2$O$_3$	98.5(5)	1.5(2)	–	–
W-2.5TiC	89.5(6)	–	2.1(1)	8.4(4)

compared with T_1 (annihilation in the tungsten matrix) is the lowest for the single crystal sample W-SC, i.e., the dislocation density is the lowest here. Notice that for the W-SC sample, the T_3 lifetime is completely absent in the spectrum, as the single crystal contains no pores or large vacancy clusters.

Temperature dependencies of Young's moduli E, as measured by laser-based RUS, are shown in Fig. 4. For all measured materials, the Young's modulus E gradually decreases with temperature without any sudden change in the E values or in the slope of the temperature dependence. This means that in the examined temperature range, i.e. up to 740 °C, the materials do not undergo any phase transitions or other structural changes. Due to this, any significant variations of the internal friction in this temperature range must be ascribed solely to relaxation-like processes with relaxation times much longer than the period of the used ultrasonic vibrations (~ 1 μs), because for such processes the relaxation does not anyhow affect the dynamic elastic moduli, but affects directly the internal friction parameters [33,34]. For dislocation damping, the relaxation times are typically by more than four orders of magnitude longer [33], so this condition is satisfied.

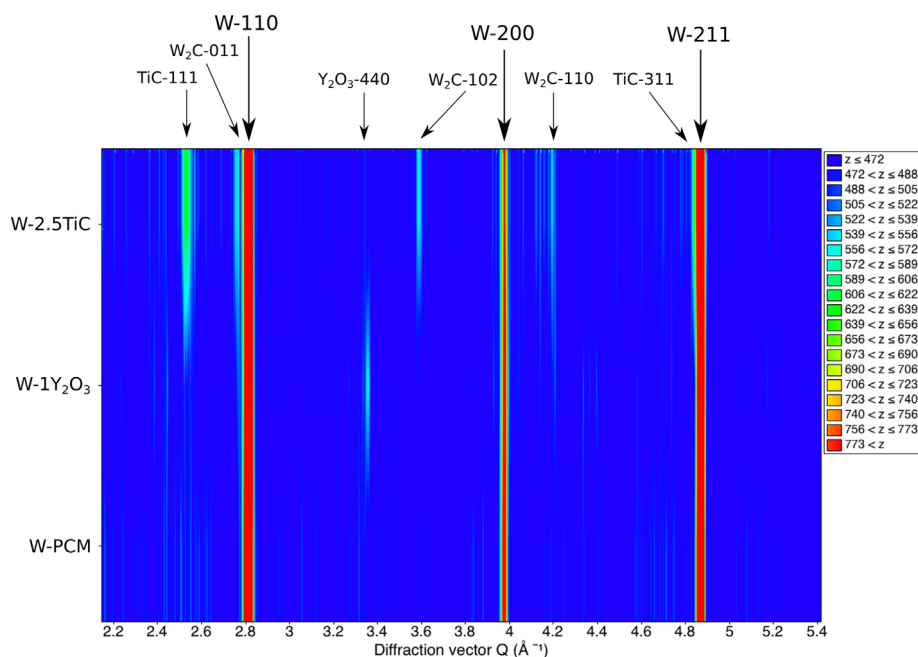The highest values of Young's moduli among the pure tungsten

Fig. 1. Colour map representation of the stacked diffraction patterns for sintered samples. Positions of the main Bragg reflections for individual phases are also pointed out.
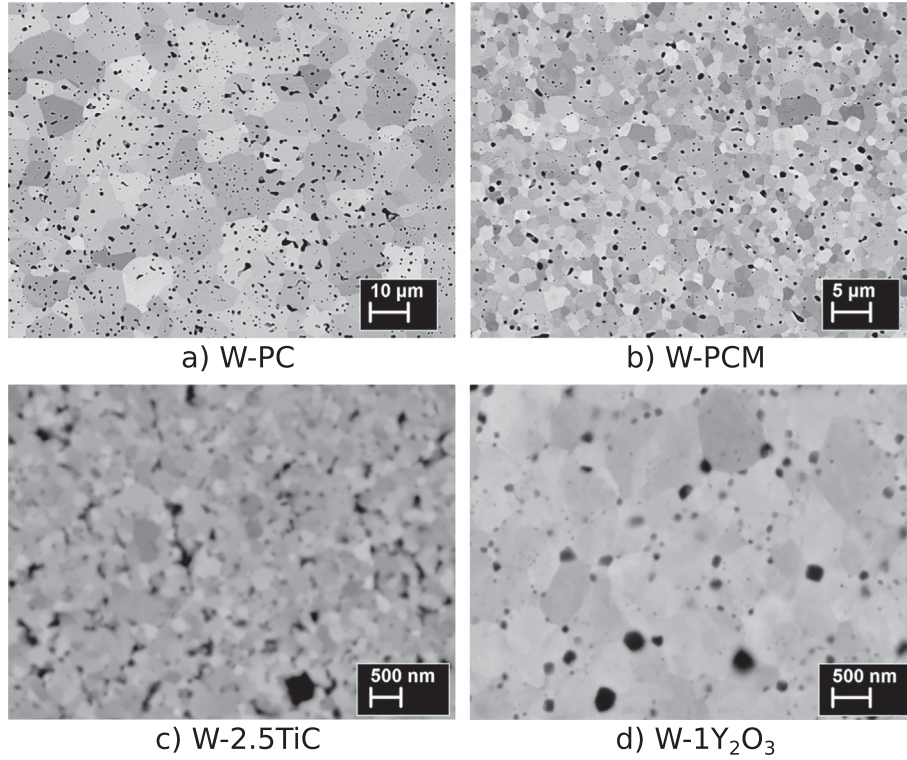
a) W-PC
b) W-PCM
c) W-2.5TiC
d) W-1Y$_2$O$_3$

Fig. 2. Microstructures of the studied sintered samples.
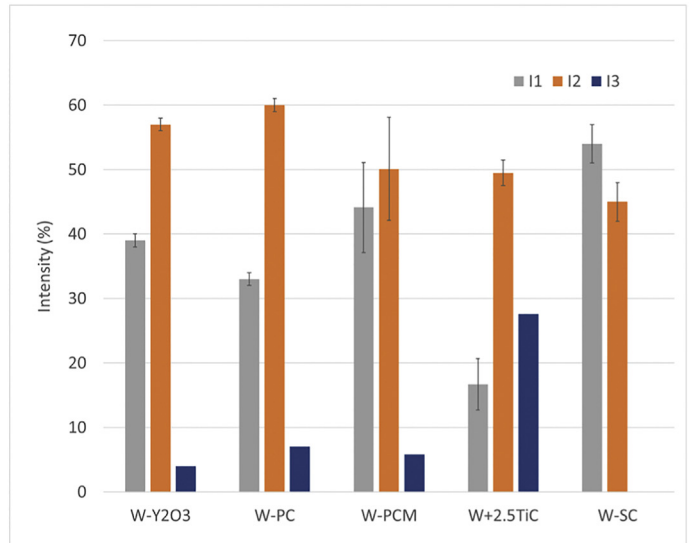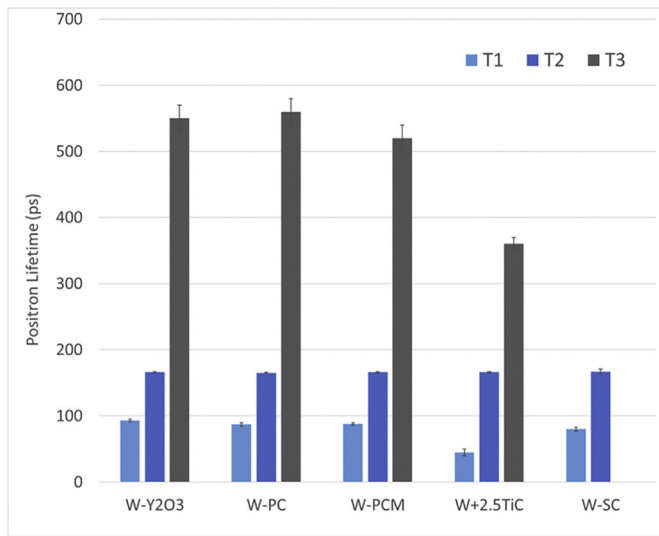

Fig. 3. Comparison of positron lifetimes (on the left) and their intensities (on the right).

samples were measured for the single-crystalline W-SC sample, while the lowest Young's modulus was measured for the W-PC sample, i.e. the sample lacking the milling step. The low values of Young's moduli can be attributed to the relatively large porosity (Table 3) that was confirmed by density measurements as well as by positron annihilation (low I_1 signal compared to W-SC, Fig. 3). However, W-2.5TiC with similar porosity content reaches much higher Young's modulus. All the mechanically alloyed/milled materials reached similar values of Young's modulus close to the values of W-SC disregarding the different amount of porosity and different particle dispersion (E_{Y2O3} = 155.5 GPa [35], E_{TiC} = 410–510 GPa [36], E_W = 411 GPa [37]). Thus, the beneficial effect of mechanical alloying is superior to the factors leading to the decrease of Young's modulus such as grain boundaries,

porosity, or introduction of particles with lower modulus.

In Fig. 5, internal friction parameter Q^{-1} vs. temperature T are plotted in the coordinates of $\ln(Q^{-1})$ vs. $1/T$. As described e.g. in [34], when a relaxation damping is thermally activated, it usually follows the Arrhenius formula, with the internal friction as

$$Q^{-1} = A \cdot \exp\left(-\frac{U}{RT}\right), \tag{1}$$

where A is a temperature-independent function, U is activation energy, R is molar gas constant. Then, in the coordinates of $\ln(Q^{-1})$ vs. $1/T$, activation energy U can be easily determined from the slopes of the measured data.

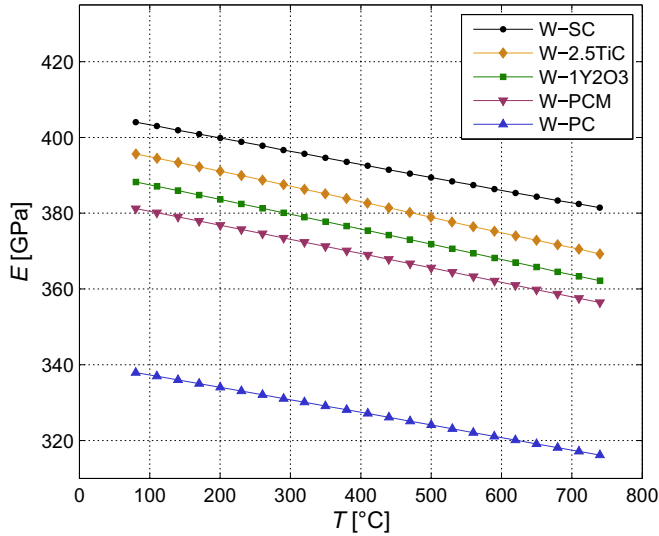As seen in Fig. 5(a), the simplest and most directly interpretable

Fig. 4. Young's moduli E temperature evolution measured by resonant ultrasound spectroscopy.

Table 3
Densities, porosities and grain sizes of the studied samples. For tungsten with particle dispersion, theoretical density is calculated by the rule of mixture, the measured density was estimated by precise volume and weight measurements and porosity was estimated from the theoretical and measured density.

Sample	Theoretical density	Measured density	Porosity	Grain size
W-SC	19.3 g/cm^3	19.3 g/cm^3	0%	–
W-PC	19.3 g/cm^3	17.6 g/cm^3	8.8%	(4 ± 0.35) μm
W-PCM	19.3 g/cm^3	18.6 g/cm^3	3.6%	(1.48 ± 0.14) μm
W-2.5TiC	19.0 g/cm^3	17.4 g/cm^3	8.4%	(0.33 ± 0.05) μm
W-1Y$_2$O$_3$	18.9 g/cm^3	18.4 g/cm^3	2.6%	(0.67 ± 0.15) μm

behavior of the internal friction is seen for polycrystalline W-PC and W-PCM samples. For both these materials, Q^{-1} is temperature-independent below approximately 400 °C and exhibits a linear increase with a slope corresponding approximately to $U \approx 20$ kJ/mol ≈ 0.2 eV above this temperature T_0. The exact values of the T_0 temperature and the activation energy corresponding to the linear slope are listed in Table 4 for the pure tungsten materials. As shown by Gumbsch et al. [4,38], the activation energy for ductile-to-brittle transition in pure tungsten is 0.17–0.20 eV; this value is given by the crack tip activation energy and is significantly lower than the activation energy for homogeneous plastic flow in tungsten, which is 0.35 eV [15]. Hence, we can clearly identify that the internal friction increase above T_0 is due to activation of dislocations at microcrack tips or other defects in the sintered materials; also the value of T_0 for the W-PC and W-PCM samples is very consistent with the experimentally observed DBT temperatures. Let us notice that although the values of Q^{-1} for both materials are comparable, the W-PC sample consistently exhibits slightly higher internal friction, despite the expected lower dislocation density. According to the classical theory of dislocation relaxation, the internal friction due to dislocations is proportional to the dislocation density times the mean length of unpinned segments of dislocations squared. Hence, it seems like the larger grain size in W-PC enabling longer freely gliding segments of dislocations is the decisive factor, outweighing the increased dislocation density.

Such assumption is further justified by the fact that the internal friction in the W-SC sample is even higher. Similarly to the polycrystalline materials, the $Q^{-1}(T)$ dependence for this sample at the highest temperature follows a linear trend with the slope corresponding to $U \approx 20$ kJ/mol. There is also a sharp change of the trend located at
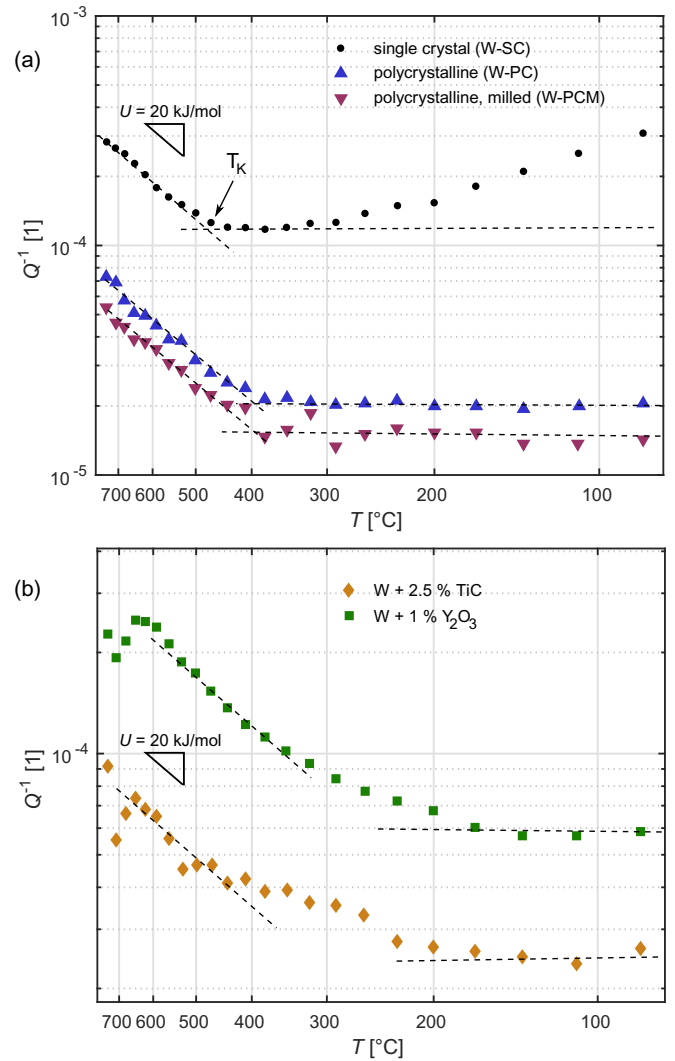

Fig. 5. Internal friction parameter Q^{-1} measured by resonant ultrasound spectroscopy: (a) pure tungsten samples; (b) mechanically alloyed materials.

Table 4
Temperatures T_0 of the sudden slope change in the $\ln(Q^{-1})$ vs. $1/T$ dependence, and activation energies U determined from linear interpolation above T_0 for pure tungsten samples.

Sample	W-PCM	W-PC	W-SC
T_0	(400 ± 30) °C	(400 ± 30) °C	(470 ± 20) °C
U	(17.9 ± 1.6) kJ/mol	(20.5 ± 1.8) kJ/mol	(18.3 ± 1.8) kJ/mol
	(0.185 ± 0.017) eV	(0.213 ± 0.019) eV	(0.190 ± 0.018) eV

approximately 470 °C; however, the internal friction is not temperature independent below this point. Instead, another (rather gradual) slope change is observed below 350 °C, and the internal friction at the room temperature reaches values comparable to those at high temperatures. This result is somehow consistent with low-frequency observations by Ziebart and Schultz [12], who reported nearly temperature-independent behavior of internal friction at moderately elevated temperatures, but an increase towards the room temperature, ascribed to the presence of the so-called α peak (relaxation due to kink-pair formation in 71° dislocations). While at the low frequencies used by Ziebart and Schultz [12] this peak appeared at temperatures as low as -90 °C, Rieu [39] observed the shift of this peak to approximately 30 °C at 45 kHz, which is a frequency comparable to those used in RUS.

Hence, we can assume that the increase of the internal friction at room temperature can be ascribed to the α peak. Surprisingly, however, this increase is not observed for the polycrystalline materials; the reason for this discrepancy is unclear, and this fact has to be verified by further measurements, as most of the available literature data were obtained on single crystals [12,39] or large-grained polycrystals [40] only.

The fact that the sudden change of the slope for the W-SC sample is located at 470 °C, i.e. exactly at the expected knee temperature T_K, may indicate that the observed relaxation mechanism may be related to the enhanced mobility of screw dislocation above this temperature. However, this mechanism seems to be active in the polycrystalline samples already at much lower temperatures, where the dislocation relaxation at micro-crack tips can take place even if the dislocation motion is still partially thermally activated. The higher onset temperature for the single crystal also indicates the rather complex relation between the knee temperature and DBTT, as single crystals often exhibit lower DBTT than polycrystals [41].

For the mechanically alloyed samples W-1Y$_2$O$_3$ and W-2.5TiC (Fig. 5(b)), the low-temperature internal friction appears to be temperature independent as well. However, there is no sudden change in the slope of internal friction throughout the whole temperature range. Instead, the slope changes gradually, starting from temperatures as low as 150 °C. The slope reaches the value approximately corresponding to $U \approx 20\,\mathrm{kJ/mol}$ at about 450 °C, and there appears to be an internal friction peak at 650 °C for both materials. As this peak is not observed in the pure materials, it could be related to the presence of interstitial impurity atoms in the matrix, i.e. it can be a Snoek-like relaxation effect [42]. For example, the carbon Snoek peak in pure tungsten appears at approximately 420 °C at 1 Hz [12], so expecting it to appear at about 600–700 °C for the ~ 500 kHz frequency used in RUS seems realistic. This additional effect probably smears out the internal friction profile and disables direct identification of T_0 for the alloyed materials. Nevertheless, regardless of the internal friction added by this extra relaxation mechanism, the slope does not reach $U \approx 20\,\mathrm{kJ/mol}$ until 400 °C, and thus, the dislocation relaxation observed in the pure samples above T_0 does not take place in the alloyed materials at lower temperatures. This means that the second phase particles probably do not anyhow enhance the dislocation mobility, and their effect on the DBT temperature and increased ductility at lower temperatures [43,44] can be ascribed solely to strengthening the grain boundaries.

4. Conclusion

The presented results show that the internal friction measurements in the ultrasonic frequency range can detect the relaxation processes taking place in tungsten and tungsten-based materials. Most importantly, above temperatures of ~ 400 °C, one dominant internal friction mechanism can be identified in pure tungsten materials, and the activation energy for this relaxation mechanism agrees perfectly with the activation energy for DBT reported in [4,38]. The onset temperature of this mechanism appears to be correlated with the grain size (it is lower for the polycrystals than for the single crystal), and for the single crystal, it perfectly matches the expected knee temperature.

For the materials with second phase particles, direct identification of the onset temperature is impossible, most probably due to relaxation processes related to impurities coming from the alloying. The obtained results bring no direct evidence that the alloying, unlike the grain refinement, could significantly affect the onset temperature for the observed relaxation mechanism. In this sense, taking into account the complex character of DBT in tungsten, the proposed experimental approach may enable deeper insight into the different factors affecting the DBTT. While the factors directly modifying the dislocation dynamics in the material have measurable effects on the internal friction profile, this measurement may be completely insensitive to those affecting DBT in other ways, e.g. by grain boundary strengthening.

Declaration of interests

The authors declare that they have no known competing financial interests or personal relationships that could have appeared to influence the work reported in this paper.

Author statement

Martin Koller: Investigation, Visualization, Analysis, Writing - Original Draft, Writing - Review & Editing;

Monika Vilémová: Conceptualization, Investigation, Resources, Writing - Original Draft, Writing - Review & Editing, Supervision;

František Lukáč: Investigation, Visualization, Writing - Original Draft;

Přemysl Beran: Investigation, Visualization, Analysis;

Jakub Čížek: Investigation, Visualization;

Hynek Hadraba: Investigation, Visualization;

Jiří Matějíček: Supervision, Writing - Review & Editing;

Jakub Veverka: Investigation, Writing - Original Draft;

Hanuš Seiner: Conceptualization, Methology, Resources, Writing - Original Draft, Supervision.

References

[1] J. Reiser, J. Hoffmann, U. Jäntsch, M. Klimenkov, S. Bonk, C. Bonnekoh, M. Rieth, A. Hoffmann, T. Mrotzek, Ductilisation of tungsten (W): On the shift of the brittle-to-ductile transition (BDT) to lower temperatures through cold rolling, International Journal of Refractory Metals and Hard Materials 54 (2016) 351–369. doi:https://doi.org/10.1016/j.ijrmhm.2015.09.001. URL http://www.sciencedirect.com/science/article/pii/S0263436815301475. 1.

[2] A. Wronski, A. Fourdeux, The ductile-brittle transition in polycrystalline tungsten, Journal of the Less Common Metals 8 (3) (1965) 149–158. doi:https://doi.org/10.1016/0022-5088(65)90042-1. URL http://www.sciencedirect.com/science/article/pii/0022508865900421. 1.

[3] H. G. Mellor, A. S. Wronski, The effects of precompression and pressurization on the ductile–brittle transition of polycrystalline cast chromium, molybdenum, and tungsten, Metal Science Journal 4 (1) (1970) 108–113. doi:https://doi.org/10.1179/030634570790444112. URL doi:https://doi.org/10.1179/030634570790444112. 1.

[4] P. Gumbsch, J. Riedle, A. Hartmaier, H. F. Fischmeister, Controlling factors for the brittle-to-ductile transition in tungsten single crystals, Science 282 (5392) (1998) 1293–1295. doi:https://doi.org/10.1126/science.282.5392.1293. URL https://science.sciencemag.org/content/282/5392/1293 1, 3.

[5] V. Budaev, Y. Martynenko, A. Karpov, N. Belova, A. Zhitlukhin, N. Klimov, V. Podkovyrov, V. Barsuk, A. Putrik, A. Yaroshevskaya, R. Giniyatulin, V. Safronov, L. Khimchenko, Tungsten recrystallization and cracking under ITER-relevant heat loads, Journal of Nuclear Materials 463 (2015) 237–240. doi:https://doi.org/10.1016/j.jnucmat.2014.11.129. URL http://www.sciencedirect.com/science/article/pii/S0022311514009362 1.

[6] O. El-Atwani, S. Gonderman, M. Efe, G. D. Temmerman, T. Morgan, K. Bystrov, D. Klenosky, T. Qiu, J. Allain, Ultrafine tungsten as a plasma-facing component in fusion devices: effect of high flux, high fluence low energy helium irradiation, Nuclear Fusion 54 (8) (2014) 083013. doi:https://doi.org/10.1088/0029-5515/54/8/083013. URL https://doi.org/10.1088%2F0029-5515%2F54%2F8%2F083013 1.

[7] M. Vilémová, F. Lukáč, J. Veverka, K. Illková, J. Matějíček, Controlling the carbide formation and chromium depletion in W-Cr alloy during field assisted sintering, International Journal of Refractory Metals and Hard Materials 79 (2019) 217–223. doi:https://doi.org/10.1016/j.ijrmhm.2018.11.010. URL http://www.sciencedirect.com/science/article/pii/S0263436818306656 1.

[8] H. Kurishita, H. Arakawa, S. Matsuo, T. Sakamoto, S. Kobayashi, K. Nakai, G. Pintsuk, J. Linke, S. Tsurekawa, V. Yardley, K. Tokunaga, T. Takida, M. Katoh, A. Ikegaya, Y. Ueda, M. Kawai, N. Yoshida, Development of nanostructured tungsten based materials resistant to recrystallization and/or radiation induced embrittlement, Mater. Trans. 54 (4) (2013) 456–465, https://doi.org/10.2320/matertrans.MG201209. 1.

[9] D. Rupp, S. M. Weygand, Loading rate dependence of the fracture toughness of polycrystalline tungsten, Journal of Nuclear Materials 417 (1) (2011) 477–480, Proceedings of ICFRM-14. doi:https://doi.org/10.1016/j.jnucmat.2010.12.118.

URL http://www.sciencedirect.com/science/article/pii/S0022311510009402 1.

[10] R. Smith, W. Reynolds, The correlation of ultrasonic attenuation, microstructure and ductile to brittle transition temperature in very low carbon steels, Journal of Materials Science 17 (1982) 1420–1426. doi:https://doi.org/10.1007/BF00752255. URL https://link.springer.com/article/10.1007%2FBF00752255 1.

[11] B. Kardashev, A. Nefagin, G. Ermolaev, M. Leonтeva-Smirnova, M. Potapenko, V. Chernov, Internal friction and brittle–ductile transition in structural materials, Technical Physics Letters - TECH PHYS LETT 32 (2006) 799–801. doi:https://doi.org/10.1134/S1063785006090197. 1.

[12] U. Ziebart, H. Schultz, Dislocation relaxation peaks in high purity tungsten single crystals, J. Phys. Colloques 44 (C9) (1983) C9–691–C9–696. doi:https://doi.org/10.1051/jphyscol:19839104. URL doi:https://doi.org/10.1051/jphyscol:19839104 1, 3, 3.

[13] D. Brunner, V. Glebovsky, Analysis of flow-stress measurements of high-purity tungsten single crystals, Materials Letters 44 (3) (2000) 144–152. doi:https://doi.org/10.1016/S0167-577X(00)00017-3. URL http://www.sciencedirect.com/science/article/pii/S0167577X00000173 1.

[14] B. G. Butler, J. D. Paramore, J. P. Ligda, C. Ren, Z. Z. Fang, S. C. Middlemas, K. J. Hemker, Mechanisms of deformation and ductility in tungsten – A review, International Journal of Refractory Metals and Hard Materials 75 (2018) 248–261. doi:https://doi.org/10.1016/j.ijrmhm.2018.04.021. URL http://www.sciencedirect.com/science/article/pii/S0263436818300866 1.

[15] A. Hartmaier, P. Gumbsch, Thermal activation of crack-tip plasticity: the brittle or ductile response of a stationary crack loaded to failure, Phys. Rev. B 71 (2005) 024108, , https://doi.org/10.1103/PhysRevB.71.024108. URL https://link.aps.org/doi/10.1103/PhysRevB.71.024108. 1.

[16] E. Tarleton, S. Roberts, Dislocation dynamic modelling of the brittle-ductile transition in tungsten, Philos. Mag. 89 (2009) 2759–2769, https://doi.org/10.1080/14786430902992619. 1.

[17] D. Cereceda Señas, Multiscale modeling of the plastic behaviour in single crystal tungsten: from atomistic to crystal plasticity simulations, PhD thesis, Universidad Politécnica de Madrid (2015). 1.

[18] J. R. Stephens, Effect of oxygen on mechanical properties of tungsten, Tech. Rep. D-1581, National Aeronautics and Space Administration (Apr. 1963). URL https://ntrs.nasa.gov/search.jsp?R=19630004527 1.

[19] K. Ren, L. Chen, Y. Cheng, J. Wang, H. Duan, A grain level model for deformation and failure of ultrafine-grained tungsten, Science China Technological Sciences 62 (5) (2019) 755–761. doi:https://doi.org/10.1007/s11431-018-9439-4. URL doi:https://doi.org/10.1007/s11431-018-9439-4 1.

[20] M. Rieth, S. Dudarev, S. G. de Vicente, J. Aktaa, T. Ahlgren, S. Antusch, D. Armstrong, M. Balden, N. Baluc, M.-F. Barthe, W. Basuki, M. Battabyal, C. Becquart, D. Blagoeva, H. Boldyryeva, J. Brinkmann, M. Celino, L. Ciupinski, J. Correia, A. D. Backer, C. Domain, E. Gaganidze, C. García-Rosales, J. Gibson, M. Gilbert, S. Giusepponi, B. Gludovatz, H. Greuner, K. Heinola, T. Höschen, A. Hoffmann, N. Holstein, F. Koch, W. Krauss, H. Li, S. Lindig, J. Linke, C. Linsmeier, P. López-Ruiz, H. Maier, J. Matejicek, T. Mishra, M. Muhammed, A. Munoz, M. Muzyk, K. Nordlund, D. Nguyen-Manh, J. Opschoor, N. Ordás, T. Palacios, G. Pintsuk, R. Pippan, J. Reiser, J. Riesch, S. Roberts, L. Romaner, M. Rosiński, M. Sanchez, W. Schulmeyer, H. Traxler, A. U. na, J. van der Laan, L. Veleva, S. Wahlberg, M. Walter, T. Weber, T. Weitkamp, S. Wurster, M. Yar, J. You, A. Zivelonghi, Recent progress in research on tungsten materials for nuclear fusion applications in Europe, Journal of Nuclear Materials 432 (1) (2013) 482–500. doi:https://doi.org/10.1016/j.jnucmat.2012.08.018. URL http://www.sciencedirect.com/science/article/pii/S0022311512004278 1.

[21] K. Skotnicová, V. M. Kirillova, O. I. Zaporozhets, J. Drápala, I. Szurman, Investigation of physical properties of tungsten-based single crystals using an ultrasonic method, Materials and Technologies 48 (6) (2014) 823–826. URL http://hdl.handle.net/10084/106439 2, 2.

[22] J. Rodríguez-Carvajal, Recent advances in magnetic structure determination by neutron powder diffraction, Physica B: Condensed Matter 192 (1) (1993) 55–69. doi:https://doi.org/10.1016/0921-4526(93)90108-I. URL http://www.sciencedirect.com/science/article/pii/092145269390108I 2.

[23] F. Bečvář, J. Čížek, I. Procházka, J. Janotová, The asset of ultra-fast digitizers for positron-lifetime spectroscopy, Nuclear Instruments and Methods in Physics Research Section A: Accelerators, Spectrometers, Detectors and Associated Equipment 539 (1) (2005) 372–385. doi:https://doi.org/10.1016/j.nima.2004.09.031. URL http://www.sciencedirect.com/science/article/pii/S0168900204021862 2.

[24] F. Bečvář, J. Čížek, I. Procházka, High-resolution positron lifetime measurement using ultra fast digitizers Acqiris DC211, Applied Surface Science 255 (1) (2008) 111–114, Proceedings of the Eleventh International Workshop on Slow Positron Beam Techniques for Solids and Surfaces. doi:https://doi.org/10.1016/j.apsusc.2008.05.184. URL http://www.sciencedirect.com/science/article/pii/S0169433208012129 2.

[25] R. G. Leisure, F. A. Willis, Resonant ultrasound spectroscopy, Journal of Physics: Condensed Matter 9 (28) (1997) 6001–6029. doi:https://doi.org/10.1088/0953-8984/9/28/002. URL doi:10.1088%2F0953-8984%2F9%2F28%2F002 2.

[26] P. Sedlák, H. Seiner, J. Zídek, M. Janovská, M. Landa, Determination of all 21 independent elastic coefficients of generally anisotropic solids by resonant ultrasound spectroscopy: Benchmark examples, Experimental Mechanics 54 (2014)

1073–1085. doi:https://doi.org/10.1007/s11340-014-9862-6. URL https://link.springer.com/article/10.1007%2Fs11340-014-9862-6 2.

[27] Z. A. Lethbridge, R. I. Walton, A. S. Marmier, C. W. Smith, K. E. Evans, Elastic anisotropy and extreme Poisson's ratios in single crystals, Acta Materialia 58 (19) (2010) 6444–6451. doi:https://doi.org/10.1016/j.actamat.2010.08.006. URL http://www.sciencedirect.com/science/article/pii/S1359645410005100 2.

[28] P. W. Bridgman, Certain physical properties of single crystals of tungsten, antimony, bismuth, tellurium, cadmium, zinc, and tin, Proceedings of the American Academy of Arts and Sciences 60 (6) (1925) 305–383. doi:https://doi.org/10.2307/25130058. URL http://www.jstor.org/stable/25130058 2.

[29] S. Zhu, Y. Xu, Z. Wang, Y. Zheng, D. Zhou, E. Du, D. Yuan, M. Fukuda, M. Mihara, K. Matsuta, T. Minamisono, Positron annihilation lifetime spectroscopy on heavy ion irradiated stainless steels and tungsten, Journal of Nuclear Materials 343 (1) (2005) 330–332, Proceedings of the 6th International Workshop on Spallation Materials Technology. doi:https://doi.org/10.1016/j.jnucmat.2004.11.024. URL http://www.sciencedirect.com/science/article/pii/S0022311505001728 3.

[30] K. Sato, R. Tamiya, Q. Xu, H. Tsuchida, T. Yoshiie, Detection of deuterium trapping sites in tungsten by thermal desorption spectroscopy and positron annihilation spectroscopy, Nuclear Materials and Energy 9 (2016) 554–559. doi:https://doi.org/10.1016/j.nme.2016.09.014. URL http://www.sciencedirect.com/science/article/pii/S2352179115300764 3.

[31] X. Hu, T. Koyanagi, M. Fukuda, Y. Katoh, L. L. Snead, B. D. Wirth, Defect evolution in single crystalline tungsten following low temperature and low dose neutron irradiation, Journal of Nuclear Materials 470 (2016) 278–289. doi:https://doi.org/10.1016/j.jnucmat.2015.12.040. URL http://www.sciencedirect.com/science/article/pii/S0022311515304098 3.

[32] T. Troev, E. Popov, N. Nankov, T. Yoshiie, Model calculation of positron states in tungsten containing hydrogen and helium, Journal of Physics: Conference Series 207 (2010) 012033. doi:https://doi.org/10.1088/1742-6596/207/1/012033. URL https://iopscience.iop.org/article/10.1088/1742-6596/207/1/012033 3.

[33] A. Nowick, B. Berry, Anelastic Relaxation in Crystalline Solids, Academic Press, 1972, https://doi.org/10.1016/B978-0-12-522650-9.X5001-0. 3.

[34] M. Koller, P. Sedlák, H. Seiner, M. Ševčík, M. Landa, J. Stráská, M. Janeček, An ultrasonic internal friction study of ultrafine-grained AZ31 magnesium alloy, Journal of Materials Science 50 (2015) 808–818. doi:https://doi.org/10.1007/s10853-014-8641-1. URL https://link.springer.com/article/10.1007%2Fs10853-014-8641-1 3, 3.

[35] M. Levy, H. E. Bass, R. R. Stern, V. Keppens, Handbook of Elastic Properties of Solids, Liquids, and Gases. Vol.2: Elastic properties of solids: theory, elements and compounds, novel materials, technological materials, alloys, and building materials, Academic Press, 2001. 3.

[36] H. O. Pierson, Carbides of group IV: Titanium, zirconium, and hafnium carbides, in: H. O. Pierson (Ed.), Handbook of Refractory Carbides and Nitrides, William Andrew Publishing, Westwood, NJ, 1996, pp. 55–80. doi:https://doi.org/10.1016/B978-081551392-6.50005-2. URL http://www.sciencedirect.com/science/article/pii/B9780815513926500052 3.

[37] H.E. Boyer, Metals Handbook: Desk edition, American Society for Metals 3 (1984).

[38] P. Gumbsch, Brittle fracture and the brittle-to-ductile transition of tungsten, Journal of Nuclear Materials 323 (2) (2003) 304–312, Proceedings of the Second IEA Fusion Materials Agreement Workshop on Modeling and Experimental Validation. doi:https://doi.org/10.1016/j.jnucmat.2003.08.009. URL http://www.sciencedirect.com/science/article/pii/S0022311503003738 3, 4.

[39] G. Rieu, Micro and macro strain-induced damping and dislocation structures in tungsten and molybdenum single crystals, Acta Metallurgica 26 (1) (1978) 1–13. doi:https://doi.org/10.1016/0001-6160(78)90197-9. URL http://www.sciencedirect.com/science/article/pii/0001616078901979 3.

[40] R. Chambers, J. Schultz, Dislocation relaxation spectra in plastically deformed refractory b.c.c. metals, Acta Metallurgica 10 (4) (1962) 466–483. doi:https://doi.org/10.1016/0001-6160(62)90031-7. URL http://www.sciencedirect.com/science/article/pii/0001616062900317 3.

[41] J. Stephens, Review of deformation behavior of tungsten at temperature less than 0.2 absolute melting temperature, Tech. Rep. N–72-14550, National Aeronautics and Space Administration (1972). URL https://ntrs.nasa.gov/search.jsp?R=19720006900 3.

[42] M. Weller, The Snoek relaxation in bcc metals–From steel wire to meteorites, Materials Science and Engineering: A 442 (1) (2006) 21–30, Proceedings of the 14th International Conference on Internal Friction and Mechanical Spectroscopy. doi:https://doi.org/10.1016/j.msea.2006.02.232. URL http://www.sciencedirect.com/science/article/pii/S092150930601166X 3.

[43] S. Matsuo, H. Kurishita, H. Arakawa, T. Takida, M. Kato, Y. Yamamoto, K. Takebe, M. Kawai, N. Yoshida, Deformability enhancement in ultra-fine grained, Ar-contained W compacts by TiC additions up to 1.1%, Materials Science and Engineering: A 492 (1) (2008) 475–480. doi:https://doi.org/10.1016/j.msea.2008.05.012. URL http://www.sciencedirect.com/science/article/pii/S0921509308005510 3.

[44] T. Palacios, A. Jiménez, A. Muñóz, M. Monge, C. Ballesteros, J. Pastor, Mechanical characterisation of tungsten–1wt.% yttrium oxide as a function of temperature and atmosphere, Journal of Nuclear Materials 454 (1) (2014) 455–461. doi:https://doi.org/10.1016/j.jnucmat.2014.09.012. URL http://www.sciencedirect.com/science/article/pii/S0022311514006023 3.

Summary of the presented articles

The laser-based RUS was utilized for measuring the elastic properties of several types of metal-matrix composites produced by the SPS method, which has resulted in three publications [C,D,E] included above.

Temperature evolution of Young's modulus and internal friction up to 740 °C of CoNiAl/Ti composites were studied in the paper [C] for the composites denoted as 2:1, 1:1, and 1:2, corresponding to the CoNiAl:Ti volume ratios of the powder mixtures before the sintering. The resulting temperature evolutions of the sintered composites, obtained by the PhD candidate, are shown in Figure 3.6.
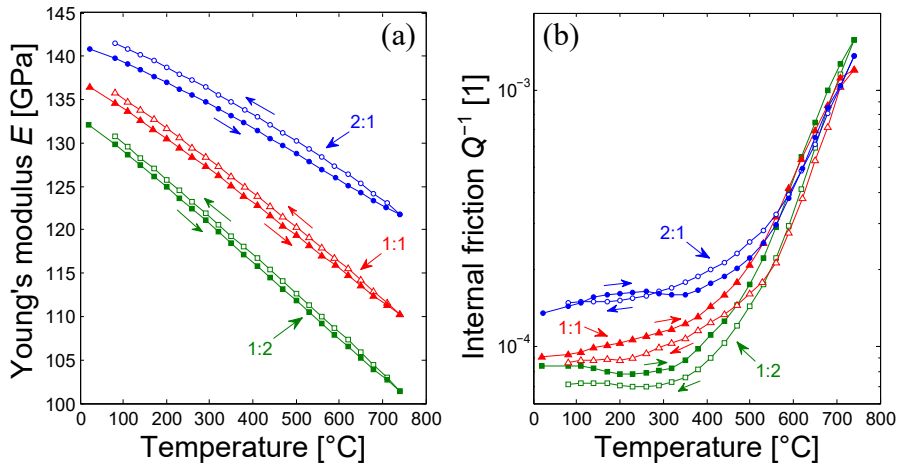

Figure 3.6: Young's modulus (a) and internal friction (b) evolutions of the CoNiAl/Ti composites with 20 °C → 740 °C → 80 °C thermal cycles [C].

The Young's moduli of all three studied CoNiAl/Ti composites exhibit pronounced softening with the increasing temperature, which is typical for the majority of metallic materials, including the α-Ti [230]. On the other hand, the softest c' coefficient (see (2.24) for its definition) of the single-crystalline cubic CoNiAl alloy increases with temperature, as determined by the previous RUS study of Seiner et al. [104]. As seen in Figure 3.6(a), the slope in the E temperature evolution is the smallest for the 2:1 composite (i.e. the one with the highest content of the CoNiAl phase), which could be a direct effect of this c' temperature evolution. Nevertheless, as the E values measured by the RUS method correspond to the macroscopic response of the whole polycrystalline composite sample, the elastic softening of the Ti particles and the softening in c_{44} coefficient of the CoNiAl phase outweigh the effect of this c' behavior. Besides that, as the c_{44} coefficient of the CoNiAl phase significantly increases during annealing [104], a measurable hysteresis (most pronounced for the 2:1 composite with the highest CoNiAl content) can be seen in the E temperature evolution of the composites. Since the temperature cycle was measured with the average heating/cooling rate of $\sim$ 3 °C/min, the CoNiAl particles were exposed to the elevated temperatures for several hours, i. e. for much longer time than during the sintering. This probably resulted in a slight evolution of the macroscopic elastic coefficients of the studied composites due to the annealing effect on the CoNiAl grains during the RUS measurement.

97

The temperature evolution of internal friction, shown in Figure 3.6(b), has a similar character for all three studied CoNiAl/Ti composites. In the lower temperature range (up to ∼ 400 °C), the internal friction is practically temperature-independent, but it is overall higher for the higher content of the CoNiAl phase. On the other hand, the internal friction rapidly increases above the threshold temperature of ∼ 400 °C for all three composites during both the heating and cooling. The activation energy, corresponding to the slopes of the internal friction evolution (2.63) in this high-temperature range, is about $U = (0.65 \pm 0.10)$ eV for all three composites, which suggests that this rapid increase in the internal friction is attributed to the dislocation slip in α-Ti [231].

Elastic properties of another type of two-phase metal–metal composites, the tungsten/steel composites, were studied in the paper [D]. Figure 3.7 shows the measured density ρ and Young's modulus E for the eight studied samples: four samples sintered at 1100 °C with variable tungsten content (pure steel sample with 0 vol. % W and samples with 20, 43, 69 vol. % W in the initial powder mixtures), three additional samples with 69 vol. % W sintered at 1200 °C, 1300 °C, 1400 °C (highlighted by the vertical arrow in Figure 3.7), and a sample intentionally sintered for much longer time (30 minutes) in order to maximize the amount of the Fe_7W_6 intermetallic compound.
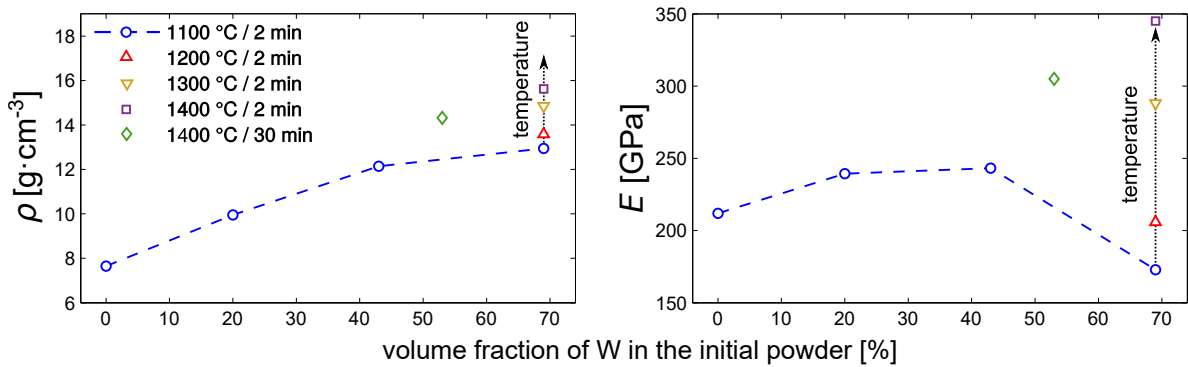

Figure 3.7: Density ρ and Young's modulus E of the tungsten/steel composites, plotted with respect to the volume fraction of tungsten in the initial powder mixture [D].

For the pure steel sample, both the density ρ and Young's modulus E were very close to the values of the bulk material, confirming the good consolidation of the steel powder by the SPS. As expected from the ρ and E values of pure tungsten, there was an increase both in ρ and E for the 20 vol. % W composite, when compared to the steel sample. Nevertheless, for the higher W content, the ρ and E values deflected from the expected linear trend, and the Young's modulus of the 69 vol. % W sample was even much smaller than for the 43 vol. % W sample. Besides that, both the density and elastic moduli of the composites sintered from 69 vol. % W powders substantially increased with the higher sintering temperature, as highlighted by the vertical arrows in Figure 3.7.

These results clearly indicate that the sintering temperature of 1100 °C is rather low for the full compaction of the tungsten particles but sufficient for the steel particles. As seen in the micrographs shown in Fig. 2 of the paper [D], the bonding between the steel and tungsten grains is achieved by formation of the Fe_7W_6 intermetallic compound. In the 20 vol. % W

composite, this Fe_7W_6 interlayer surrounds practically all the tungsten grains that are also quite well dispersed within the steel matrix, which thus leads to the expected increase in both the density and the elastic moduli when compared to the pure steel sample. However, in the microstructure of the 43 vol. % W composite, it can be seen that tungsten clusters are occasionally formed, and there are clearly visible voids/gaps between the neighboring tungsten particles. In the 69 vol. % W composite, there are much more loosely connected tungsten grains, which slightly affect the overall density, but more importantly, this leads to a rapid decrease of the elastic moduli, as these disconnected grains cannot fully transfer the mechanical load. With the increasing sintering temperature for the 69 vol. % W composite, the bonding between the tungsten grains is gradually improved, which is also accompanied by the growth of the Fe_7W_6 interlayer, surrounding the tungsten and steel grains. This leads to a ∼20 % increase in the density (when comparing the 69 vol. % W composite sintered at 1400 °C vs. the composite sintered at 1100 °C) and almost to a 100 % increase in the elastic moduli. However, the Fe_7W_6 intermetallic phase is brittle and not desirable in the prospective plasma-facing composite, so its amount should be minimized as much as possible.

The second part of the paper [D] deals with a FEM study of the contribution of the individual phases to the macroscopic elastic behavior of the composites. This study has utilized the elastic coefficients measured by the PhD candidate, but it was performed by other co-authors of this paper. It has been found out that the low Young's modulus of this composite can be indeed associated with the unsintered, weakly bonded tungsten grains. For example, for the 69 vol. % W composite sintered at 1100 °C (with the lowest detected Young's modulus value of $E \approx 172$ GPa), this FEM study has determined that the Young's modulus of the tungsten agglomerations is only ∼142 GPa, which thus effectively decreases the macroscopic elastic coefficients. Besides that, the elastic moduli of the tungsten agglomeration of the 69 vol. % W composites increased with the higher sintering temperature, which confirmed the crucial role of the sintering temperature for a good powder consolidation by the SPS technique.

The paper [E] deals with an ultrasonic study of five types of tungsten-based materials, where the laser-based RUS method was utilized to determine their elastic properties and internal friction up to 740 °C. The five studied samples include a tungsten single crystal (denoted as W-SC), a polycrystalline sample consolidated directly from the tungsten powder by the SPS (denoted as W-PC), and three additional samples which were treated in a planetary ball mill. The W-2.5TiC and the W-1Y_2O_3 samples were mechanically alloyed in the planetary ball mill and then sintered, where the second-phase particles (TiC or Y_2O_3) were uniformly distributed throughout the fine-grained tungsten matrix. The pure tungsten powder was also processed in the planetary ball mill, which has resulted in a pure tungsten polycrystalline sample (denoted as W-PCM) with finer grains than the W-PC sample.

The temperature evolutions of Young's modulus and internal friction, obtained by the PhD candidate by utilizing the laser-based RUS, are shown in Figure 3.8. Young's modulus of all studied samples gradually decreases with temperature, which means that no phase transitions or other structural changes were detected in the studied temperature range. Among the pure tungsten samples, the lowest Young's modulus was detected for the W-PC sample, i. e. the sample that was sintered directly from the original tungsten powder (without the milling prior
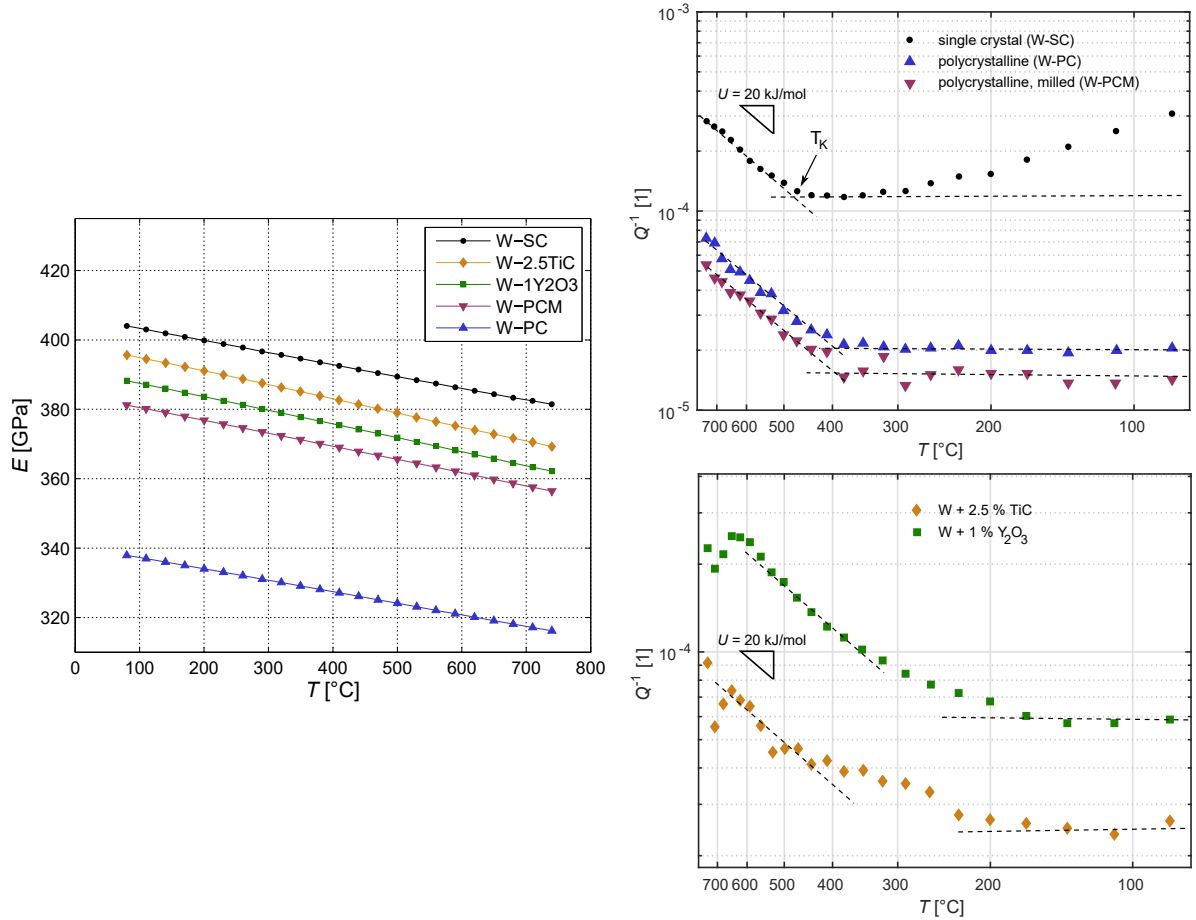
Figure 3.8: Temperature evolutions of Young's modulus E and internal friction Q^{-1} of the tungsten-based materials studied in paper [E].

to the sintering). As a result, this sample had higher porosity than other studied materials, which effectively decreases its Young's modulus. Young's modulus of the W-PCM sample, which was treated in the ball mill prior the sintering, is significantly higher, and it is closer to the Young's modulus of the single-crystalline (W-SC) sample than to the W-PC sample. Young's modulus values of the mechanically alloyed tungsten-based materials (W-2.5TiC and W-1Y$_2$O$_3$) lie between the W-PC and W-SC values, which confirms the good consolidation and incorporation of the second-phase particles into the tungsten matrix.

In the internal friction temperature evolutions in Figure 3.8, the horizontal axis is plotted in $1/T$ coordinates, according to (2.65), which allows to directly visualize the activation energy U. In the upper Q^{-1} plot in Figure 3.8 for the pure tungsten samples, the internal friction temperature behavior can be divided into two parts. In the low-temperature range up to ~400 °C, the internal friction is temperature-independent for the polycrystalline samples (W-PC, W-PCM) and it only slightly evolves for the single-crystalline W-SC sample, which is probably associated to a kink-pair formation relaxation [232]. Above the temperature of ~400 °C for the W-PC, W-PCM samples, and ~470 °C for the W-SC sample, the internal friction rapidly grows, following the Arrhenius equation (2.63) with the activation energy of ~20 kJ/mol. This value well agrees with the activation energy for ductile-to-brittle transition (DBT) reported by Gumbsch et al. [233, 234], which suggests the high-temperature internal

friction in the pure tungsten samples is attributed to the dislocation relaxation at elevated temperatures, when the ductile behavior is allowed by the dislocation mobility. For the W-2.5TiC and W-1Y$_2$O$_3$ composites, the internal friction evolves more gradually without the sudden change in the slope in the Q^{-1} vs. $1/T$ plots, but it also reaches the $\sim$20 kJ/mol activation energy at the elevated temperatures. Moreover, an internal friction peak appears to be near 600–700 °C for both these samples, which is likely associated with a Snoek-like relaxation effect caused by the interstitial atoms in the tungsten body-centered cubic lattice.

In summary, this section shows the ability of the laser-based RUS method to characterize several types of metal-matrix composites. Some important characteristics can be determined from the comparisons of obtained Young's moduli for composites with variable compositions. When the composites are well sintered, and if there are only limited amounts of newly formed phases, the macroscopic elastic moduli well correspond to the rule of mixtures of the powder compact (2.30). This is the case for the CoNiAl/Ti composites in [C], or the 20 vol. % W composite vs. the pure sintered steel sample in [D]. Young's moduli of the composites with higher amounts of the tungsten content in [D] have not followed the rule of mixtures, which means that there are some other features that effectively influence the elastic properties of these materials, mainly porosity and unsintered particles. Similarly in W-PC vs. W-PCM samples from [E], the Young's modulus of W-PCM sample was significantly higher than for the W-PC sample. Both these samples were consolidated from the same pure tungsten powder, which was, however, additionally milled for more than 20 hours before the sintering in the case of the W-PCM sample. As a result, the W-PCM sample was better compacted than the W-PC sample, as it was sintered from a finer tungsten powder, and this was also reflected in the macroscopic elastic properties of these materials.

Temperature evolutions of the elastic coefficients can also detect some material processes that depends on temperature, such as phase transitions. However, it is not the case in the materials studied in this thesis, as the Young's moduli of both the CoNiAl/Ti composites [C] and tungsten-based materials [E] gradually decreases with temperature, showing that there were no structural changes up to 740 °C (which is near the high-temperature limit of the currently used laser-based RUS devices). On the other hand, additional information can be obtained from the internal friction temperature evolutions, where the dislocation relaxation causes its rapid increase at elevated temperatures.

3.3 Acoustic and elastic properties of robocast scaffolds

This section includes three papers studying mechanical properties of micro-architectured scaffolds fabricated by the robocasting method. The robocast scaffolds consist of periodic arrangements of thin (sub-millimeter) ceramic rods. Paper [F] shows how the scaffold geometry strongly affects its acoustic properties, where the acoustic energy can be focused along the principal direction of the rods for the case of scaffolds with tetragonal and orthorhombic symmetry. Paper [G] deals with acoustic properties of a SiC scaffold with hexagonal symmetry, and it shows how the acoustic energy propagation differs at various frequencies. Paper [H] describes a fabrication of newly developed Cr_2AlC scaffolds and a characterization of their mechanical properties.

The work presented in the papers [F,G] partially follows and extends the work performed earlier by Kruisová et al. [172–174]. In [172], elastic properties of a robocast SiC scaffold were studied by the laser-based RUS. A parallelepiped sample, shown in Figure 3.9d, was cut from the central part of a SPSed silicon carbide (SiC) scaffold with a tetragonal lattice, which is shown in Figure 3.9a. The experimental resonant spectra, shown in Figure 3.9(e), consisted of resonant peaks with relatively low internal friction (average Q^{-1} value was about $2 \cdot 10^{-3}$), which confirmed that the individual rods within the scaffold were well interconnected and sintered together, as there were no friction-like contacts between the rods at the intersections.
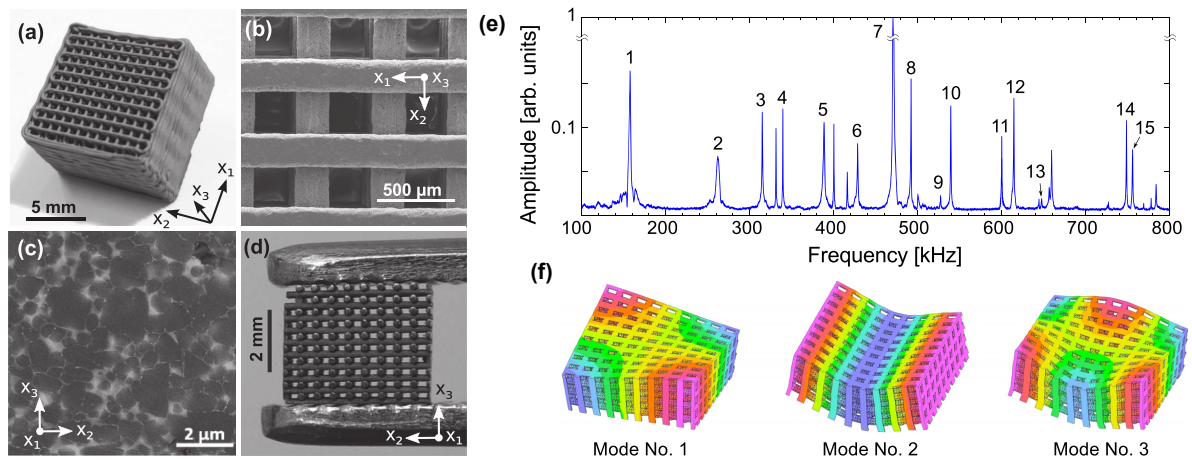

Figure 3.9: The robocast structure studied in [172]: (a) an optical image of the sintered scaffold; (b) a scanning electron micrograph showing a detail of the periodic lattice, (c) the microstructure of a ceramic rod, (d) a sample used for the ultrasonic measurements, (e) an experimental spectrum of the measured sample, (f) visualizations of the modal shapes of vibrations for the first three resonant frequencies.

The FEM method was utilized here for determining the elastic coefficients from the RUS measurement (i. e. instead of the Rayleigh-Ritz forward procedure described in section 2.2.2). As seen in Figure 3.10, a computational unit cell representing the tetragonal scaffold was designed, where its geometric parameters were obtained from the optical micrographs of the sintered scaffolds. By applying the six straining modes seen in Figure 3.10, the six independent elastic coefficients of the tetragonal scaffold were obtained. The resulting elastic coefficients

exhibited a strong elastic anisotropy, where Young's modulus in the diagonal direction in the tetragonal x_1x_2 plane, i. e. in the direction between the rods, was about ten times lower than Young's modulus in the principal direction of the rods, as seen in Figure 3.11a. Moreover, angular dependencies of phase velocities v_ϕ and group velocities v_G were also determined, using the equations (2.37–2.41), where the macroscopic effective density given by the scaffold geometry was taken for the calculation. In the resulting phase and group velocity plots in the tetragonal plane, shown in Figure 3.11b and 3.11c, it can be seen that strong elastic anisotropy also leads to the strong acoustic energy focusing along the principal direction of the rods.
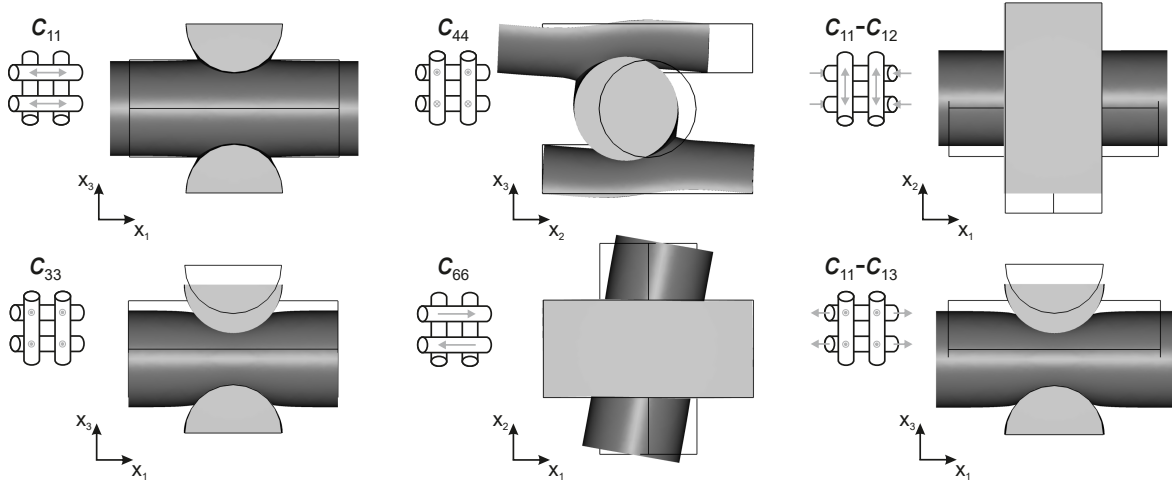

Figure 3.10: Straining modes used for the FEM calculation of effective elastic constants of a tetragonal scaffold [173].
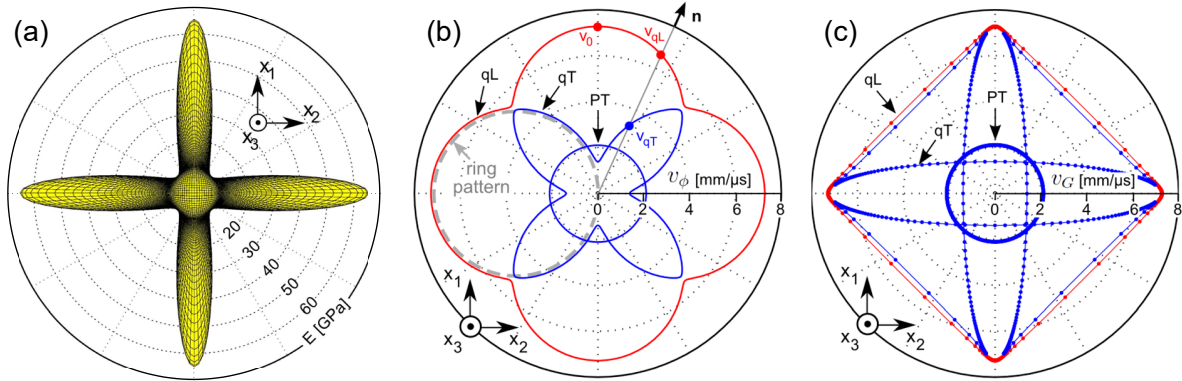
Figure 3.11: Elastic and acoustic properties of the tetragonal scaffolds studied in [172]: (a) directional dependence of Young's modulus E, (b) phase velocities v_ϕ, and (c) group velocities v_G in the tetragonal plane x_1x_2 of the scaffold structure.

The FEM method was also utilized for calculating a frequency band structure of the robocast scaffolds [172–174]. The calculated acoustic branches of the tetragonal scaffold [172], i. e. the wave number dependence on the frequency, were practically linear in the frequency range of the RUS measurements (up to 800 kHz in this case), which confirmed that the approximation of the scaffold structure by the effective anisotropic medium was fully justified. In another paper by Kruisová et al. [174], the band gap structure was calculated for four

different types of SiC scaffolds (two tetragonal scaffolds and two hexagonal scaffolds with different in-plane spacings between the rods), showing several frequency band gaps in the 2–12 MHz frequency range. This was confirmed experimentally by studying the propagation of longitudinal waves through the scaffolds along the direction of the rods by the through-transmission method, where the transmitted amplitude rapidly decreased (about several orders of magnitude) when the input frequency of the generated longitudinal waves fell within the frequency band gaps.

The paper [F], included in this thesis, partially continues in the work of Kruisová et al. [172–174], where the FEM method was utilized for a theoretical calculation of the elastic and acoustic properties of six types of robocast SiC scaffolds. Two tetragonal scaffolds and two hexagonal scaffolds with different in-plane spacings between the rods, as similar to the scaffolds studied in [174], and two additional scaffolds with an orthorhombic symmetry were studied in this paper. For each type of the scaffolds, a FEM computational unit was designed, using the geometrical parameters of sintered scaffolds, and the elastic coefficients were obtained by the other co-authors from the Institute of Thermomechanics by the FEM analysis. The distributions of phase and group velocities were then calculated by the PhD candidate, utilizing the equations given in section 2.1.2.

The paper [G] studies the SiC scaffold with the hexagonal symmetry in more detail both experimentally and theoretically. The experimental measurements described in this paper were done by the PhD candidate, while the numerical analysis was performed by the co-authors of the paper. As seen in Figure 3.12, two experimental setups were utilized for studying the elastic and acoustic properties of the hexagonal scaffold. A modification of RUS method was utilized, where the studied scaffold sample was put between piezoelectric transducers and its vibrations were detected by the laser vibrometer.
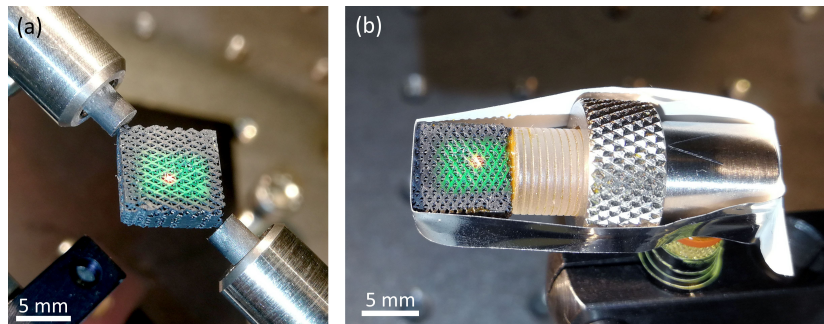
Figure 3.12: Experimental setups from [G]: (a) RUS measurement utilizing the classical scheme (where the sample is put between the piezoelectric transducers) and (b) measurement of the propagation of shear waves. In both these measurements, the out-of-plane displacement was measured by the Polytec MSA-500 vibrometer, where the green-illuminated rectangle highlights the area accessible by the laser vibrometer detection spot.

In the second experiment, the scaffold sample was contacted to a shear wave probe such that the shear waves propagated either along the direction of the rods or in the direction between the rods. The shear waves were polarized vertically, and their propagation could be thus detected by the scanning laser vibrometer at the top layer of the scaffold, as seen in Figure 3.12(b). The experimental results were compared with the numerical simulations of the

shear wave behavior, showing that the wave propagation is also directionally-dependent in the hexagonal scaffold at the higher frequencies.

The last paper [H] covers a slightly different subject within the topic of the robocast scaffolds, as it summarizes the development of robocast scaffolds based on a Cr_2AlC ceramic compound. These scaffolds were fabricated during the PhD candidate's Erasmus+ internship at the Institute of Ceramics and Glass (ICV-CSIC in Madrid, Spain) during the academic year 2017/2018.

Paper F

Anisotropic elasticity of ceramic micro-scaffolds fabricated by robocasting

Martin Koller, Alena Kruisová, Hanuš Seiner, Petr Sedlák, Benito Román-Manso,
Pilar Miranzo, Manuel Belmonte, Michal Landa

Number of total citations[1]: 1 (excluding self-citations: 0)

Contribution of the PhD candidate and the co-authors:

The candidate calculated and plotted the distributions of phase and group velocities, drew the sketches in Fig. 1, and wrote the paper.

Co-authors from the Institute of Thermomechanics (A. Kruisová, H. Seiner, P. Sedlák, M. Landa) determined the geometrical parameters of the sintered scaffolds, designed the FEM computational unit cells for each of the studied scaffolds, calculated their elastic coefficients by the FEM method, and supervised the work on the paper. Co-authors from the Institute of Ceramics and Glass (B. Román-Manso, P. Miranzo, M. Belmonte) fabricated and provided the SiC scaffolds.

---

[1]According to the Web of Science database `webofknowledge.com` as of August 2020

Anisotropic Elasticity of Ceramic Micro-Scaffolds Fabricated by Robocasting

M. Koller[a,*], A. Kruisová[b], H. Seiner[b], P. Sedlák[b], B. Román-Manso[c], P. Miranzo[d], M. Belmonte[d] and M. Landa[b]

[a]Faculty of Nuclear Sciences and Physical Engineering, Czech Technical University in Prague, Trojanova 13, 120 00 Praha 2, Czech Republic

[b]Institute of Thermomechanics, Czech Academy of Sciences, Dolejškova 1402/5, 182 00 Praha 8, Czech Republic

[c]School of Engineering and Applied Sciences, Harvard University, 52 Oxford Str., 02318 Cambridge MA, USA

[d]Institute of Ceramics and Glass (ICV-CSIC), Kelsen 5, 28049 Madrid, Spain

Anisotropic elastic and acoustic properties of robocast ceramic scaffolds are calculated by finite element method, utilizing real geometries and material parameters obtained from robocast silicon carbide samples. Six types of robocast geometries are studied, showing different material symmetries given by the arrangement of the ceramic rods in the scaffold structures. Due to the macroscopic periodicity of the structures composed of fully sintered ceramic rods, the robocast scaffolds exhibit metamaterial-like elastic and acoustic properties, never observed for natural materials. The effect of the micro-architecture is shown to be crucial: while for tetragonal and orthorhombic structures, strong acoustic focusing along the directions of the rods appears even in the low-frequency limit, hexagonal structures exhibit no energy focusing up to some frequency limit given by the geometry.

1. Introduction

Additive manufacturing methods are capable of producing novel advanced materials by layer-by-layer deposition, following a printing route defined by computer-aided design (CAD) [1–4]. Due to their artificial, highly symmetric structure, the fabricated scaffolds exhibit unique acoustic properties, which are not observed in natural materials, e.g. acoustic frequency bandgaps [5–9] and strong acoustic energy focusing [10]. Moreover, such materials can be utilized as light-weight structural materials [11–13] or in bone tissue engineering [1, 14].

Robocasting is an additive manufacturing technique in which the microscaffolds consisting of thin rods are fabricated from a powder slurry [15, 16]. In this paper, robocast silicon carbide (SiC) samples were used as templates for the finite element method (FEM) modeling of elastic and acoustic properties of such microarchitectured scaffolds. It is shown that several types of ceramic scaffolds exhibit anisotropic elastic and acoustic properties leading to strong acoustic energy focusing along the principal symmetry axes of the robocast samples.

2. Materials and methods

A detailed description of SiC scaffolds fabrication by the robocasting method can be found in [15, 16]. In brief, a colloidal gel ink, based on SiC powder, is extruded

―――――

*corresponding author; e-mail: martin.koller@fjfi.cvut.cz
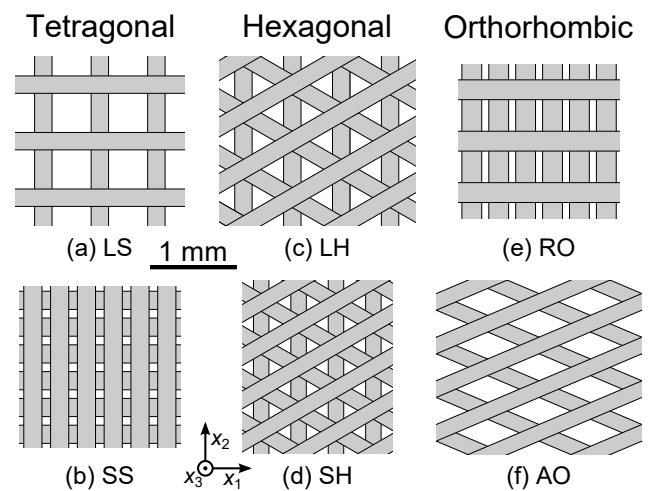
Fig. 1. Geometry of microarchitectures of robocast silicon carbide scaffolds used for the FEM calculations. Tetragonal structures are denoted as (a) LS and (b) SS, meaning *large square* and *small square*, respectively. Hexagonal structures are denoted as (c) LH and (d) SH, meaning *large hexagonal* and *small hexagonal*, respectively. Orthorhombic structures are denoted as (e) RO and (f) AO, meaning *rectangular orthorhombic* and *angular orthorhombic*, respectively.

through a nozzle in an oil bath, following a layer-by-layer printing route defined by CAD. After drying and burning-out of the organic additives, the scaffolds are consolidated by presureless spark plasma sintering.

Six types of robocast SiC scaffolds, as shown in Fig. 1, are used as templates for FEM. Within each layer of every scaffold, the rods with diameter d are mutually

Geometric characteristics of robocast SiC scaffolds: angles between rods in neighbouring layers, in-plane spacings between rods l, rod diameters d, out-of-plane spacings h between rods in neighboring layers; and effective densities ρ computed by FEM

Symmetry	Sample	Angle	l [μm]	d [μm]	h [μm]	ρ [g cm^{-3}]
tetragonal	LS	90°	650	210	137.5	1.212
	SS	90°	308	219	130.5	2.555
orthorhombic	RO	90°	591 / 309.3	238	148.7	2.165
	AO	46°	462	186	125	1.458
hexagonal	LH	60°	562	210	182	1.117
	SH	60°	430	188	150	1.391

parallel with in-plane spacing l, and the arrangement of neighboring layers is also modified, resulting in three types of material symmetries. For the two samples with tetragonal symmetry, an angle between rods of neighboring layers is equal to 90°; and for the two samples with hexagonal symmetry, an angle between rods of neighboring layers is equal to 60°. One of the samples exhibiting orthorhombic symmetry has two different values of in-plane spacing of the rods with an angle between rods of neighboring layers equal to 90°, Fig. 1e, and the direction of the rods in the other sample alternates positively/negatively by 46° with the equal in-plane spacing and the periodicity of two layers, Fig. 1f. Out-of-plane spacings of the rods h between the neighboring layers are smaller than the rod diameters d for all scaffolds, which indicates significant overlapping of the SiC rods at their intersections. The geometric parameters l, d, h of the sintered scaffolds are summarized in Table I.

Elastic coefficients C_{ijkl} of all six types of robocast scaffolds were obtained by FEM, utilizing COMSOL Multiphysics software, as described in [10, 17]. Computational unit cells were designed from the real geometry parameters shown in Table I, to represent periodic structures of the robocast scaffolds. Elastic responses were then calculated by utilizing pure tensile or pure shear straining modes along the principal directions of the unit cells. The density of 3.34 g cm^{-3}, Young's modulus of 305 GPa, and Poisson's ratio of 0.19 of SiC [6, 10] were set as inputs for the calculations.

From the elastic coefficients C_{ijkl}, phase velocity v_ϕ and group velocity vector $\boldsymbol{v_G}$ are calculated. Using the Christoffel equation

$$\left(C_{ijkl}n_j n_l - \rho v_\phi^2 \delta_{ik}\right) U_k = 0, \tag{1}$$

phase velocities v_ϕ are obtained in a given direction of propagation $\boldsymbol{n}$, where ρ is the effective mass density, δ_{ik} is Kronecker's delta, and U_k is polarization vector. For each direction of propagation $\boldsymbol{n}$, three phase velocities v_ϕ with three different polarization vectors are obtained. Then, the group velocity vector is calculated as

$$v_{Gi} = C_{ijkl}n_k U_j U_l/(\rho v_\phi). \tag{2}$$

3. Results and discussion

In Fig. 2 and Fig. 3, the polar plots of phase and group velocities in $x_1 x_2$ plane are shown for the tetragonal samples. The outer velocity curves (red in color

version) represent quasi-longitudinal waves (qL) and the other two curves (blue in color version) represent quasitransverse waves (qT) with horizontal and vertical polarizations. The group velocities are plotted as discrete points, in order to clearly demonstrate acoustic energy focusing.

Fig. 2. Phase velocity v_ϕ and group velocity v_G in the $x_1 x_2$ plane for the LS sample. Number of group velocity data points: 3×480.

Fig. 3. Phase velocity v_ϕ and group velocity v_G in the $x_1 x_2$ plane for the SS sample. Number of group velocity data points: 3×240.

For the LS sample, phase velocity values of qL and qT waves are very close to each other in the 45° direction, as a result of relatively low values of c_{12} and c_{13} coefficients due to the weak interlinking between rods. Very similar results were obtained, when the elastic coefficients of another robocast tetragonal sample [10] were determined by measuring resonant spectra of free elastic vibrations by resonant ultrasound spectroscopy method. This sample had similar average rod diameter d, slighty higher

out-of-plane spacings of the rods h, and slightly smaller in-plane spacings of the rods l than the LS sample. For both the LS sample and the sample described in [10], the qL and qT phase velocity values form ring-like patterns in the x_1x_2 symmetry plane, suggesting that the acoustic waves can be expected to propagate nearly independently in the individual rods.

For the SS sample, the phase velocities values of qL and qT waves significantly differ even in the 45° direction, as seen in Fig. 3, suggesting that there is a much higher interlinking in this sample. As the both rod diameters d and out-of-plane spacings of the rods h are almost identical for the LS and SS samples, the stronger energy focusing for the LS sample has to be attributed to the much higher in-plane spacing between the rods l.

The acoustic energy focusing along the principal axes of the rods, x_1 and x_2, is also seen from the group velocity plots, where the vast majority of group velocity vectors of the qL waves lie along these principal axes. Only when the direction of propagation $\boldsymbol{n}$ is very close to the 45° angle for the LS sample, the acoustic energy propagates between the rectangular rods, but with much smaller group velocity. The focusing of qL waves is more pronounced for the LS sample, as compared to the SS sample, which could be demonstrated from the density of group velocity points.

The strong acoustic energy focusing is also evident for the qT waves of the LS sample. Similarly to the longitudinal waves, the directions of group velocity vector of one of the qT waves lie along the principal axes for the majority of the directions of propagation $\boldsymbol{n}$. The group velocities of the second qT wave are equidistantly distributed with a constant value, indicating an independent projection to x_1x_2 symmetry plane, which suggests that the polarization vector of this qT wave lies along the x_3 principal axis; in Ref. [10], such waves are designated as pure transverse (PT). Likewise for the qL waves, the energy focusing of the qT waves is more pronounced for LS sample, when compared to SS sample.

Similar velocity curves with the qL energy focusing along the principal axes are observed for the RO sample, in Fig. 4. Since this sample has two different in-plane spacings of the rods, the group velocities along the principal axes differ, where the higher group velocity value corresponds to the direction with a closer arrangement of parallel rods in the x_1 axis. Moreover, the pattern of the second qT wave is not circle-like for this sample, unlike for the tetragonal samples, indicating that this wave is not pure transverse, but rather quasi-transverse as a result of the lower symmetry class of the orthorhombic sample.

For the AO sample, Fig. 5, distinguished energy focusing in the directions between the smaller angle between rods, which the axis x_1 intersect in half, is observed for both qL and qT waves.

For the hexagonal samples, Figs. 6 and 7, no energy focusing in the x_1x_2 plane is observed, since the group velocity vectors are uniformly distributed in this
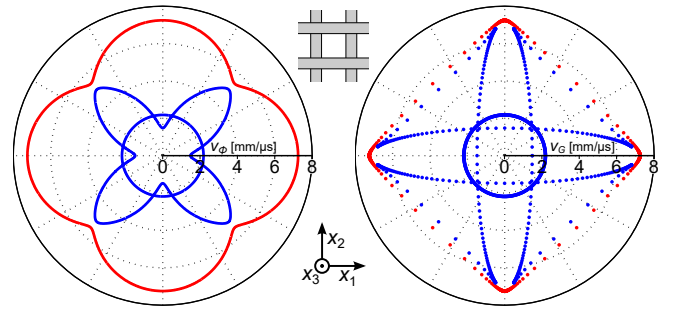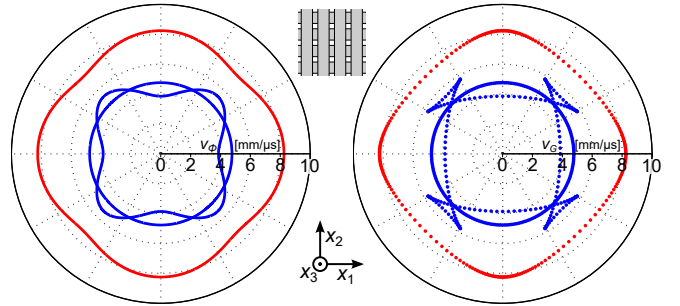

Fig. 4.   Phase velocity v_ϕ and group velocity v_G in the x_1x_2 plane for the RO sample. Number of group velocity data points: 3×480.

Fig. 5.   Phase velocity v_ϕ and group velocity v_G in the x_1x_2 plane for the AO sample. Number of group velocity data points: 3×200.

Fig. 6.   Phase velocity v_ϕ and group velocity v_G in the x_1x_2 plane for the LH sample. Number of group velocity data points: 3×160.
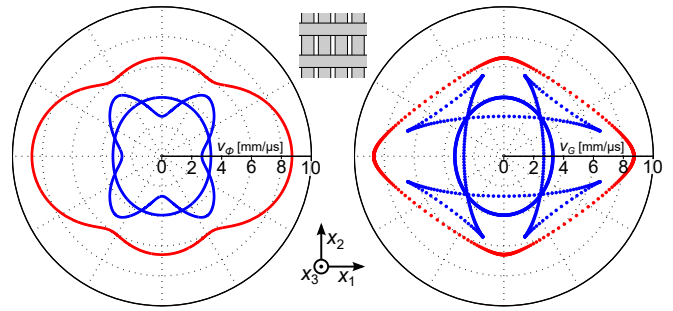

Fig. 7.   Phase velocity v_ϕ and group velocity v_G in the x_1x_2 plane for the SH sample. Number of group velocity data points: 3×160.
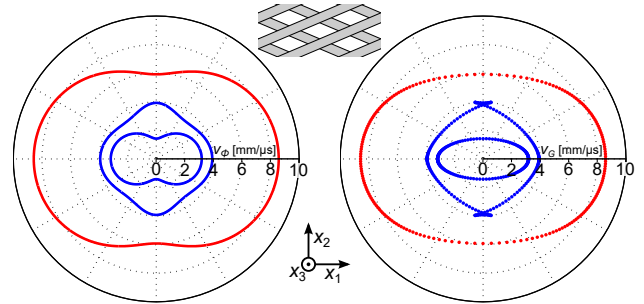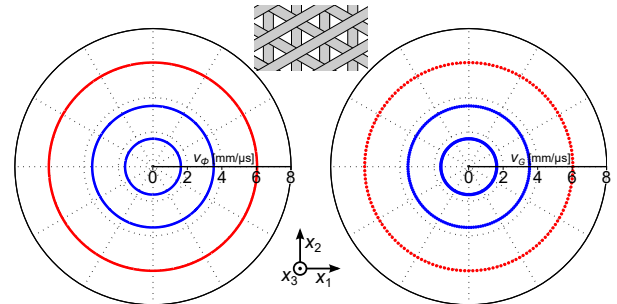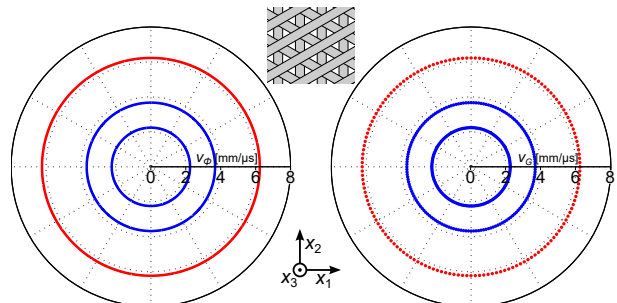
plane with constant magnitudes. This is an expected result, because hexagonal materials have the same macroscopic symmetry, with 5 independent elastic coefficients, as transverse isotropic materials, in which the material properties are independent of direction in the isotropic plane of $x_1 x_2$ [18].

Nevertheless, some acoustic energy focusing can be still expected due to the macroscopic heterogeneous nature of the LH sample, if the wavelengths are comparable to the spacing of the rods. Therefore, the FEM was also utilized for calculating properties of planar waves, where the displacement field $\boldsymbol{u}$ can be assumed in the form

$$\boldsymbol{u}(\boldsymbol{x}, t) = \boldsymbol{U}(\boldsymbol{x}, \boldsymbol{k}) \exp\left[i\left(\boldsymbol{k} \cdot \boldsymbol{x} - 2\pi f t\right)\right]. \qquad (3)$$

$\boldsymbol{k}$ is wave vector, f is frequency, and $\boldsymbol{U}(\boldsymbol{x}, \boldsymbol{k})$ is the Bloch waveform having the same spatial periodicity as the scaffold. Due to the 12 symmetry planes of the LH sample, Fig. 1c, the directions of wave propagation $\boldsymbol{k}$ were chosen as $\alpha = 0°, 5°, 10°, 15°, 20°, 25°, 30°$ angles with respect to the x_1 axis. For each direction, the set of wave vector magnitudes $|\boldsymbol{k}|$, ranging from 0 to $\pi/(l \cos \alpha)$, was taken. Using Eq. (3), the frequencies f corresponding to particular $\boldsymbol{k}$ were calculated on the basic computational unit cells with the complex phase-shift periodic boundary conditions. The phase shift was given by the phase factor $\exp(i(\boldsymbol{k} \cdot \boldsymbol{x}))$ from Eq. (3).

In Fig. 8, frequency dependence on the wave vector magnitudes is shown for all three types of acoustic waves (one qL wave and two qT waves). As seen in this figure, if the $\boldsymbol{k}$ magnitudes are much smaller than π/l, e.g. if the wavelength is significantly longer than the in-plane spacing of the rods l, all directions of propagation lead to very similar frequency values, and thus the hexagonal structure seems to be isotropic in the $x_1 x_2$ plane in the low-frequency limit. With the increasing $\boldsymbol{k}$ magnitudes, the frequency curves become dependent on direction of wave propagation, where the highest frequency at given wave vector and thus the largest phase velocity value corresponds to the propagation along the principal axes of the SiC rods. Therefore, when the wavelengths become comparable to the in-plane spacing of the rods, acoustic energy is more focused along the ceramic rods. The energy focusing is also demonstrated in the polar plots of phase and group velocities at the frequency of 1 MHz, as shown in Fig. 9.

4. Conclusion

Acoustic wave propagation in robocast SiC scaffolds was calculated by FEM, utilizing real scaffold geometries and SiC material properties. The geometry of the tetragonal and orthorhombic scaffolds is shown to be crucial for acoustic energy focusing along the principal axes of SiC rods. The strongest acoustic focusing was observed for the tetragonal sample with the highest value of in-plane spacings between rods, suggesting that the acoustic energy is more focused in the least dense structures. For the hexagonal scaffolds, the effect of the geometry is significant only when the wavelengths are comparable to the
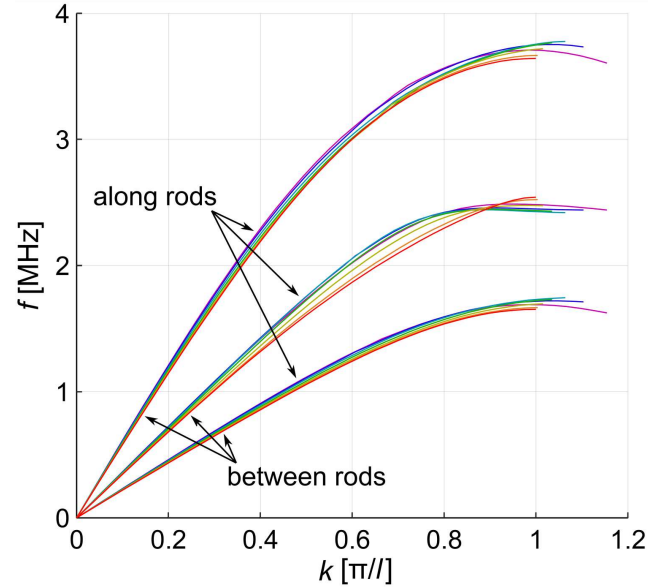
Fig. 8. Frequency f vs. the magnitudes k of wave vector at several directions of wave propagation $\boldsymbol{n}$. The top group of curves represents quasi-londitudinal waves and the other two groups of curves represent quasi-transverse waves.
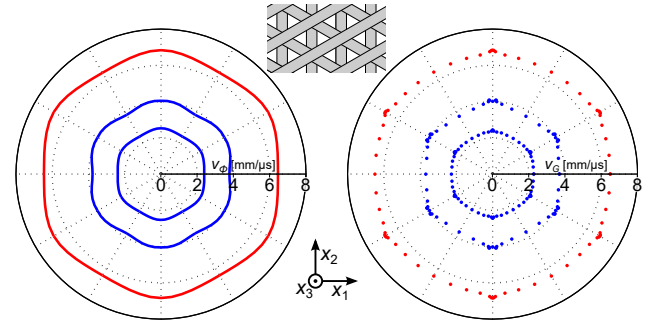
Fig. 9. Phase velocity v_ϕ and group velocity v_G in the $x_1 x_2$ plane for the LH sample, as calculated from the acoustic wave propagation at the frequency of 1 MHz.

spacings between rods, e.g. when the wave frequency is sufficiently high. In the low-frequency limit, the hexagonal scaffolds are isotropic in the hexagonal plane due to their higher degree of macroscopic material symmetry.

The presented result prove that the acoustic properties of robocast materials can be effectively tailored by designing the geometry of the scaffolds. These materials are therefore prospective candidates for applications as smart materials for focusing and redirecting of acoustic energy.

Acknowledgments

References

[1] Q. Fu, E. Saiz, M.N. Rahaman, A.P. Tomsia, *Mater. Sci. Eng. C Mater. Biol. Appl.* **31**, 1245 (2011).

[2] B.G. Compton, J.A. Lewis, *Adv. Mater.* **26**, 5930 (2014).

[3] J.R. Raney, J.A. Lewis, *MRS Bull.* **40**, 943 (2015).

[4] M.K. Thompson, G. Moroni, T. Vaneker, G. Fadel, R.I. Campbell, I. Gibson, A. Bernard, J. Schulz, P. Graf, B. Ahuja, F. Martina, *CIRP Ann. Manuf. Technol.* **65**, 737 (2016).

[5] F. Lucklum, M.J. Vellekoop, *Proced. Eng.* **120**, 1095 (2015).

[6] A. Kruisová, M. Ševčík, H. Seiner, P. Sedlák, B. Román-Manso, P. Miranzo, M. Belmonte, M. Landa, *Ultrasonics* **82**, 91 (2018).

[7] T. Delpero, S. Schoenwald, A. Zemp, A. Bergamini, *J. Sound Vibrat.* **363**, 156 (2016).

[8] K.H. Matlack, A. Bauhofer, S. Krödel, A. Palermo, C. Daraio, *Proc. Natl. Acad. Sci. USA* **113**, 8386 (2016).

[9] H. Seiner, P. Sedlák, M. Ševčík, A. Kruisová, M. Landa, B. Román-Manso, P. Miranzo, M. Belmonte, in: *Proc. VIII ECCOMAS Thematic Conf. on Smart Structures and Materials SMART 2017*, Eds. A. Güemes, A. Benjeddou, J. Rodellar, J. Leng, CIMNE, Barcelona 2017, p. 1702.

[10] A. Kruisová, H. Seiner, P. Sedlák, M. Landa, B. Román-Manso, P. Miranzo, M. Belmonte, *Appl. Phys. Lett.* **105**, 211904 (2014).

[11] R. Huang, M. Riddle, D. Graziano, J. Warren, S. Das, S. Nimbalkar, J. Cresko, E. Masanet, *J. Clean. Prod.* **135**, 1559 (2016).

[12] Y. Tang, Y.F. Zhao, *Rapid Prototyp. J.* **22**, 569 (2016).

[13] C.B. Williams, J.K. Cochran, D.W. Rosen, *Int. J. Adv. Manuf. Technol.* **53**, 231 (2011).

[14] P. Miranda, E. Saiz, K. Gryn, A.P. Tomsia, *Acta Biomater.* **2**, 457 (2006).

[15] K. Cai, B. Román-Manso, J.E. Smay, J. Zhou, M.I. Osendi, M. Belmonte, P. Miranzo, *J. Am. Ceram. Soc.* **95**, 2660 (2012).

[16] B. Román-Manso, Á. de Pablos, M. Belmonte, M.I. Osendi, P. Miranzo, *Bol. Soc. Esp. Ceram. Vidr.* **53**, 93 (2014).

[17] A. Kruisová, H. Seiner, P. Sedlák, M. Landa, B. Román-Manso, P. Miranzo, M. Belmonte, *Appl. Mech. Mater.* **821**, 364 (2016).

[18] H. Seiner, C. Ramirez, M. Koller, P. Sedlák, M. Landa, P. Miranzo, M. Belmonte, M.I. Osendi, *Mater. Des.* **87**, 675 (2015).

Paper G

Frequency-dependent acoustic energy focusing in hexagonal ceramic micro-scaffolds

Tomáš Grabec, **Martin Koller**, Petr Sedlák, Alena Kruisová, Benito Román-Manso, Manuel Belmonte, Pilar Miranzo, Hanuš Seiner

Number of total citations[1]: 1 (excluding self-citations: 0)

Contribution of the PhD candidate and the co-authors:

The candidate measured the RUS spectra and the propagating time-domain signals, co-wrote the manuscript and coordinated the work on the paper.

T. Grabec performed the modal-based study of the time-domain propagation properties and co-worked on the analysis of the time-domain experimental signals and manuscript preparations. Co-authors from the Institute of Thermomechanics (P. Sedlák, A. Kruisová, H. Seiner) performed the FEM calculations, designed the principles of the modal-based study, and supervised the work on the paper. Co-authors from the Institute of Ceramics and Glass (B. Román-Manso, M. Belmonte, P. Miranzo) fabricated and provided the SiC hexagonal scaffold.

---

[1]According to the Web of Science database `webofknowledge.com` as of August 2020
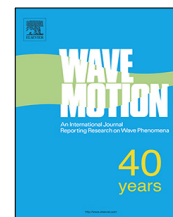
Frequency-dependent acoustic energy focusing in hexagonal ceramic micro-scaffolds

Tomáš Grabec [a], Martin Koller [a,*], Petr Sedlák [b], Alena Kruisová [b],
Benito Román-Manso [c,d,1], Manuel Belmonte [d], Pilar Miranzo [d], Hanuš Seiner [b]

[a] *Faculty of Nuclear Sciences and Physical Engineering, Czech Technical University in Prague, Trojanova 13, 120 00 Praha 2, Czechia*
[b] *Institute of Thermomechanics, Czech Academy of Sciences, Dolejškova 1402/5, 182 00 Praha 8, Czechia*
[c] *School of Engineering and Applied Sciences, Harvard University, 52 Oxford Str, 02138 Cambridge MA, USA*
[d] *Institute of Ceramics and Glass (ICV-CSIC), Kelsen 5, 28049 Madrid, Spain*

ABSTRACT

Acoustic properties of an additive-manufactured SiC scaffold with hexagonal symmetry fabricated by the robocasting method are studied both numerically and experimentally. The numerical analysis is based on the finite element method (FEM) using Bloch boundary conditions. The calculations show both angular and frequency dispersion of the acoustic waves with wavelengths comparable to the spacing between the rods, i.e., on a millimeter scale, indicating interesting acoustic properties in the MHz range. The dispersion character leads to focusing of the energy propagation into the directions of the rods of the hexagonal structure. This is illustrated by modal-based calculations of the propagation of longitudinal and out-of-plane shear wave packets with a dominant wavelength. The experimental analysis consists of two steps, the measurement of the resonant spectrum and shear wave propagation character. The measured resonant spectrum is in good agreement with the one calculated using numerically obtained low-frequency properties of the structure, also showing the quality of the overall manufactured structure. The time-domain measurement shows significant changes in the energy propagation between low and high frequencies, as predicted by FEM calculations.

© 2019 Elsevier B.V. All rights reserved.

1. Introduction

Micro-architectured periodic structures often exhibit phononic-crystal behavior with acoustic phenomena taking place in frequency ranges much lower than those of crystalline materials found in nature, such as frequency band gaps in the MHz range [1–5]. Moreover, due to their highly ordered periodical arrangement, these structures are able to focus the acoustic waves along certain principal directions given by the geometry [6–9].

With the rise of additive manufacturing (AM) methods, phononic crystals with various geometries can be easily produced [10–12]. Robocasting is a direct ink writing AM method, by which periodic structures consisting of layers of thin rods are printed from colloidal gel inks based on micro-sized powders [13,14]. Silicon carbide (SiC) is often utilized for robocast scaffolds due to its favorable thermomechanical properties. Cai et al. [15] produced robocast scaffolds based on SiC with Al_2O_3 and Y_2O_3 sintering additives, utilizing pressure-less spark plasma sintering (SPS) for consolidation.

---

* Corresponding author.
  E-mail address: martin.koller@fjfi.cvut.cz (M. Koller).

[1] Present address: School of Engineering and Applied Sciences, Harvard University, 52 Oxford Str, 02138, Cambridge, MA, USA.

The sintered scaffolds exhibited significant linear shrinkage when compared to green bodies, and the SPS led to almost fully dense scaffolds with uniform microstructure while maintaining the geometric alignment of the rods. Román-Manso et al. [16] produced several SiC-based robocast scaffolds which differed in the mean size of the used SiC powders or compositional ratios between SiC and Al_2O_3 and Y_2O_3 sintering additives. These scaffolds also preserved the designed geometry after the sintering and exhibited low porosity and high indentation hardness. Furthermore, SiC was chosen as a material for the manufacture of electrically functionalized robocast scaffolds with the addition of graphene fillers [17], or for Fe-doped scaffolds for catalytic purposes [18].

Kruisová et al. [19] studied elastic and acoustic properties of the SiC-based scaffolds exhibiting macroscopic tetragonal symmetry by resonant ultrasound spectroscopy (RUS) and finite element method (FEM) modeling. In subsequent works by Koller et al. [20,21], acoustic properties of six types of scaffolds with three different types of material symmetry were studied. It was shown that in tetragonal scaffolds, where the rods in neighboring layers are perpendicular, focusing of the acoustic energy along the rods is observed. Much stronger focusing occurs when the in-plane spacing between the rods is increased.

In another work by Kruisová et al. [22], the transmission of ultrasonic waves through four types of SiC-based scaffolds was studied. Longitudinal ultrasonic waves with frequencies varying from 2 MHz to 12 MHz were sent through scaffolds along one of the directions of the ceramic rods, and the amplitudes of transmitted waves were measured. The wave propagation in these structures was also studied by FEM. It was shown both theoretically and experimentally that these scaffolds, with characteristic dimensions of 0.1–1 mm, exhibit frequency band gaps in the MHz range. Thus, the ability of the robocasting method for fabricating the phononic crystals was confirmed.

In this paper, we investigate a scaffold with the orientation of the rods in neighboring layers of 60° and the periodicity of 3 layers, and thus exhibiting macroscopic hexagonal symmetry. Since all directions in the hexagonal plane are macroscopically equivalent, no energy focusing is observed in the long-wavelength limit. However, when the acoustic wavelength decreases and becomes comparable to the in-plane spacing between the rods, the energy becomes focused along the rods, implying a frequency-dependent angular-dispersive character. A full FEM study of the acoustic behavior of a structure consisting of thousands of unit cells would be computationally very demanding. This problem was addressed by Hyun et al. [23], who developed an efficient and stable basis-vector-based model reduction scheme based on adaptive quasi-static Ritz vector (AQSRV), and described its use for analysis and design of acoustic metamaterials. Similarly, a continuum model for the description of high-frequency behavior was developed by Rosi et al. [24] and tested on hexagonal and hexachiral structures [25]. However, in this paper, we propose a combination of FEM study of a unit cell with special, complex phase-shift boundary conditions in specific angles, followed by a simulation based on modal analysis. The numerical results are supported by laser–ultrasonic measurements of the sample resonances via the RUS method and by propagation characteristics of low- and high-frequency pulses of out-of-plane shear waves, showing the difference in the propagation of wave energy.

2. Materials and methods

2.1. Robocast structure

The studied hexagonal scaffold structure was fabricated by the robocasting technique. At first, a colloidal gel ink, based on β-SiC powder with Al_2O_3 and Y_2O_3 sintering additives, was produced by mechanical mixing of the powder mixture with ultrapure water and organic flocculants and viscosifiers. This is required because the ink needs to have highly shear-thinning rheological behavior, in order to form a thin filament when extruded through a nozzle following a computer-aided-design (CAD) printing route, and also to provide support for the already-printed free-standing structure. In each layer, the rods are mutually parallel with constant in-plane spacing between them, and the rods in the neighboring layers are oriented in a different angle of 60° to form a hexagonal structure. The out-of-plane spacings between the layers are significantly lower than the diameters of the individual rods, producing scaffolds where the rods of adjacent layers partially intersect at crossing points. After the printing, the green bodies were dried in air, the organic additives were then burnt out, and the scaffolds were subsequently consolidated by SPS.

The studied hexagonal scaffold structure, shown in Fig. 1, consists of a layered arrangement of the rods with diameter $d = 215$ μm, which are mutually parallel with constant in-plane spacing $l = 576$ μm in each layer. The orientation angle between the rods in neighboring layers is equal to 60° and the rods partially intersect at the crossing points with the out-of-plane spacing z between the layers. This arrangement thus leads to a periodic hexagonal structure, having the out-of-plane periodicity of 3 layers, $h = 3z = 385$ μm.

2.2. Numerical methods

2.2.1. FEM study

Acoustic properties of the scaffold were studied by finite element method (FEM) using COMSOL Multiphysics software. A representative unit cell of the periodic structure was meshed with tetrahedral Lagrangian elements, as shown in Fig. 2(a).

For the calculation, material properties of SiC were utilized [19]: a density of 3.34 g·cm^{-3}, Young's modulus of 305 GPa, and Poisson's ratio of 0.19. As the studied structure occupies a relative space of 44.4%, the effective density is 1.483 g·cm^{-3}.
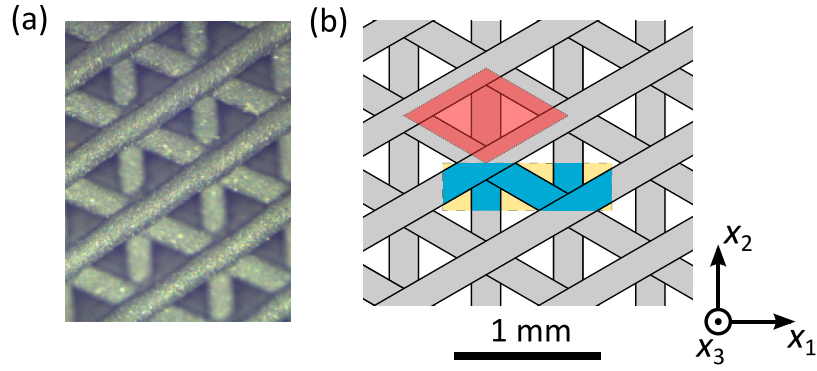
Fig. 1. Top-view of the hexagonal structure, (a) optical micrographs of the consolidated scaffold, (b) geometric arrangement of the periodic structure. The sketches in (b) show the primitive cell (red-colored parallelogram with 60° and 120° angles) of the hexagonal structure with six-fold screw axis of symmetry and the placement of the rectangular computational domain (yellow–blue region) used for FEM calculations. (For interpretation of the references to color in this figure legend, the reader is referred to the web version of this article.)
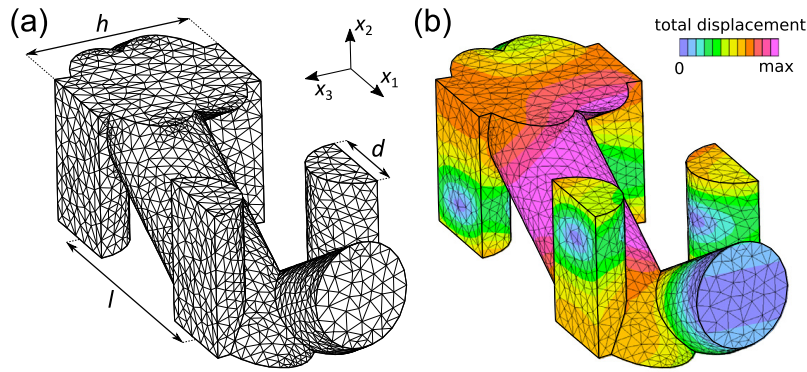

Fig. 2. (a) Computational unit cell used for FEM. (b) Illustrative example of the calculated displacement field for the propagation of a wave with high wavenumber ($k \approx 6.54$ mm^{-1}) in the direction corresponding to $\alpha = 20°$.

As described in [26], applying various types of periodic boundary conditions with prescribed displacements in the principal directions of the computation unit corresponds to macroscopic homogeneous straining of the structure and can be thus used for evaluation of macroscopic elastic coefficients of the hexagonal structure. The resulting constants obeying hexagonal symmetry for the studied structure are:

$$c_{ij} = \begin{pmatrix} 66.05 & 19.45 & 8.80 & 0 & 0 & 0 \\ 19.45 & 66.05 & 8.80 & 0 & 0 & 0 \\ 8.80 & 8.80 & 44.32 & 0 & 0 & 0 \\ 0 & 0 & 0 & 9.30 & 0 & 0 \\ 0 & 0 & 0 & 0 & 9.30 & 0 \\ 0 & 0 & 0 & 0 & 0 & 23.30 \end{pmatrix} \text{ GPa.} \tag{1}$$

Following the Bloch theorem [27], the wave propagation in the studied periodic structure can be sought in the form of planar waves with the displacement vector of

$$\mathbf{u}(\mathbf{x}, t) = \mathbf{U}(\mathbf{x}, \mathbf{k}) \exp[i(\mathbf{k} \cdot \mathbf{x} - \omega t)], \tag{2}$$

where $\mathbf{k}$ is the wave vector. $\mathbf{U}(\mathbf{x}, \mathbf{k})$ is the Bloch waveform with the same spatial periodicity as the robocast structure. Thus, the computation domain can be limited to a single unit cell, and the solution for different $\mathbf{k}$ is found in an eigenvalue problem with complex phase-shift boundary conditions, known as Bloch boundary conditions. In particular, to obtain wave dispersion of acoustic waves propagating in the hexagonal plane, periodic boundary conditions for the rectangular unit cell were applied in the form

$$\mathbf{u}(\mathbf{x}) = \mathbf{u}(\mathbf{x} + \mathbf{r}_i) \exp(i\mathbf{k} \cdot \mathbf{r}_i), \quad i = A, B, C, D, \tag{3}$$

where each translation vector $\mathbf{r}_i$ corresponds to the equivalent faces of the unit cell, as shown in Fig. 3 for the $\mathbf{r}_A$, $\mathbf{r}_B$, $\mathbf{r}_C$ vectors lying in x_1x_2 plane. Translation vector $\mathbf{r}_D$ lies in the direction of the x_3 axis, with the magnitude $|\mathbf{r}_D|$ equal to the out-of-plane periodicity of the scaffold h, i.e. the dimension of the unit cell in the x_3 direction.
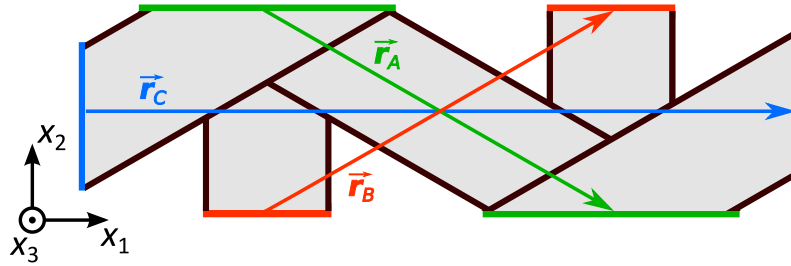
Fig. 3. A sketch showing the geometric relations in the computation unit cell in the x_1x_2 plane. The same colors correspond to the faces at which the periodic boundary conditions are applied; these faces are shifted by the translation vectors $\mathbf{r}_i$ highlighted with the same color.

2.2.2. Modal-based study

To provide a simulation of wave propagation through a larger sample of the structure by a time-domain-like simulation, a very large model would be necessary, implicating high computational demands and time. Therefore, in order to calculate and visualize the propagation of wave-packets with different dominant wavenumber propagating through such structure, we utilize a method based on modal characteristics with the following principle:

1. The dispersion curves obtained by FEM as described in the previous section are fitted with a polynomial function in frequency and interpolated into the whole range of α angles applying the hexagonal symmetry.
2. The excitation is then modeled, given as an initial displacement field in the form of a centered radial cosine function superimposed by a Gaussian pulse, creating a spatial wave packet. Varying the wavelength of the cosine function, the dominant excited wavelength changes, while the long-wavelength part stays constant (given by the size of the Gaussian envelope).
3. The Fourier-transformed excitation, i.e., its modal characteristics, is multiplied by the factor of $\exp[i\boldsymbol{\omega}(\mathbf{k})t]$, where $\boldsymbol{\omega}(\mathbf{k})$ is the angular frequency for each wavenumber and direction of propagation given by the fitted and interpolated dispersion data. Thus, the modal response in time t for each direction and each wavenumber is obtained.

The resulting modal response can be calculated for any chosen time t, and the corresponding displacement field is then obtained by an inverse Fourier transformation.

2.3. Experimental methods

For the comparison with the FEM calculation of elastic constants, a resonant spectrum of the robocast hexagonal scaffold sample was measured by resonant ultrasound spectroscopy (RUS) [28,29]. Furthermore, the propagation of out-of-plane shear waves through the hexagonal scaffold along the principal x_1 and x_2 directions, i.e. in the direction along the rods and in the direction between the rods (see Fig. 1), was also studied experimentally. To obtain the scaffold with the accurate hexagonal periodic arrangement, the non-periodic edges of the robocast hexagonal scaffold were ground away before the measurement. Also, the bottom surface of the scaffold was polished in order to enhance the optical reflectivity for the vibrometer laser, which is used for the detection of out-of-plane displacements during the experiments. This scaffold, shown in Fig. 4 as prepared for the measurements, consists of 24 layers, and has approximate dimensions of $8.54 \times 8.48 \times 3.02$ mm^3.

2.3.1. RUS measurement

The RUS experiment was performed using a setup similar to the one used by Landa et al. [30]. The measured scaffold was placed between and in contact with two piezoelectric transducers on the opposite corners, as shown in Fig. 4(a), and a broadband chirp signal with frequencies sweeping from 0.1 to 1 MHz was sent through T&C AG 1021 Amplifier to one of the piezoelectric transducers. The experiment was controlled by National Instruments PXI digital I/O system and Polytec MSA-500 Micro System Analyzer. The resonant response of the scaffold was detected by a Polytec OFV scanning laser vibrometer system at 240 discrete points on the top plane of the scaffold, allowing to obtain both the frequencies and modal shapes of resonances. Afterward, the measured resonant frequencies with the modal shapes of vibration were compared with a spectrum computed by a forward resonant spectra calculation method described in [31], using the static elastic coefficients of the scaffold as in (1) obtained by the FEM and fulfilling the hexagonal symmetry.

2.3.2. Time-domain measurement

For measuring the propagation of out-of-plane shear waves, the scaffold was contacted to Ultran SRD25-2 shear-wave ultrasonic transducer, using a shear-wave couplant gel, such that the horizontal axis of the scaffold coincided with the axis of the transducer. Single-frequency ultrasonic chirp pulses with the duration of 32 μs and the central frequency either at 0.55 MHz or 1.4 MHz, were sent through the scaffold in both principal directions: along the rods as shown in Fig. 4(b), and in the perpendicular direction, i.e. between the rods. The time signals of the out-of-plane displacement were measured
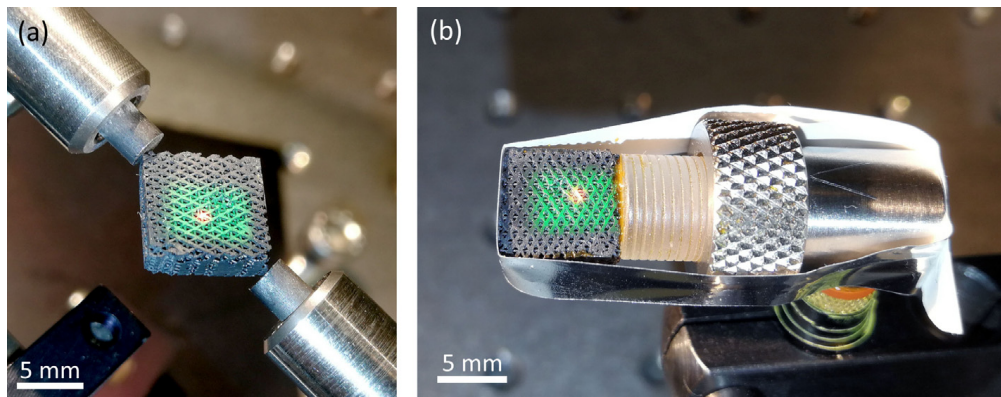
Fig. 4. Photos of the experimental measurements on the hexagonal scaffold. (a) Resonant ultrasound spectroscopy (RUS) where the sample is placed between two piezoelectric transducers. (b) Measurement of the propagation of shear out-of-plane waves where the sample is contacted to shear-wave transducer. The green-illuminated surface shows the area accessible by the red-colored laser detection spot of the Polytec vibrometer measuring system. (For interpretation of the references to color in this figure legend, the reader is referred to the web version of this article.)

by the Polytec OFV scanning laser vibrometer system. The measurement was done at the top surface of the scaffold along 'zigzag' lines following the rod structure in the direction of the propagating wave, i.e. as close as possible to the axis of the shear wave transducer. In each measurement, the line was formed out of ∼100 equidistantly distributed points, with a minimum of 10 points between each of the rod junctions.

3. Results and discussion

3.1. Numerical analysis

The wave solutions were determined for angles α (measured from the x_1 direction and following the notation given in Fig. 1) from 0° to 30° with 5° steps. The direction of the ceramic rods is therefore equal to $\alpha = 30°$.

In each direction, the magnitude of **k** vector was increased from 0 to 4 mm^{-1} in 30 regular steps mapping approximately the inner two thirds of the 1st Brillouin zone. Considering the structure symmetry, the 1st Brillouin zone is hexagonal [32] with the inner radius π/l. The resulting dispersion curves for the longitudinal wave and the shear wave, which has the polarization in the out-of-plane direction (x_3), are given in Fig. 5.

The dispersion curves show that with the increasing wavenumber, i.e., with the wavelength closer to the dimensions of the hexagonal structure, the wave propagation becomes gradually both angular- and frequency-dispersive.

Using the calculations based on modal analysis, the propagation characteristics of wave packets with different dominant frequency through the described structure are studied. Fig. 6 shows the resulting displacement and intensity of longitudinally polarized wave packets at time $\Delta t = 10 \, \mu s$. The chosen dominant wavenumbers correspond to the lines in Fig. 5(a), i.e., to the low-, middle- and high-wavenumber region of the dispersion relation. It is illustrated that, whereas in the low-wavenumber, i.e., the long-wavelength region, the propagation shows no angular dispersion (see Fig. 6(a)), the influence of the structure increases with the shortening wavelength. In the middle region (Fig. 6(b)), the displacement field is still close to radial, but the intensity shows obvious focusing of the energy propagation in the directions of the rods. In the high-wavenumber situation, the displacement is clearly hexagonal, Fig. 6(c). This is even more pronounced in the intensity, shown on the right side of Fig. 6(c), which indicates that the energy is in such a case transmitted almost exclusively through the rods. The wavelength corresponding to $k = 2$ mm^{-1} is $\lambda = \pi$ mm, thus about 5 times larger than the in-plane rod spacing l.

In Fig. 7, a similar study for the case of out-of-plane shear waves at time $t = 25 \, \mu s$ is illustrated. Due to the larger dispersion (see Fig. 5(b)), the effect of focusing is even stronger. The lowest corresponding wavelength is about 3.5 larger than the rod spacing l.

3.2. Experimental analysis

Fig. 8 documents the measurement of resonant frequencies by RUS. In the resonant spectrum, there are around 40 resonant frequencies up to 0.7 MHz, which also have a high quality factor of $Q > 10^3$. Hence, the internal friction Q^{-1} of the scaffold is lower than 10^{-3}, which is comparable to the values in bulk ceramic or even metallic materials [33,34], confirming that there is no significant damping in the scaffold as the individual rods are well interconnected and fused together, without any sliding occurring in the structure which could lead to an increase in the internal friction. The Q^{-1} values for an example set of 7 resonances are shown in Table 1.

Using the sample dimensions and the elastic constants (1) obtained by the FEM model, the resonant spectrum was calculated by a Ritz–Rayleigh approach [31]. The comparison of the calculated and experimentally measured set of
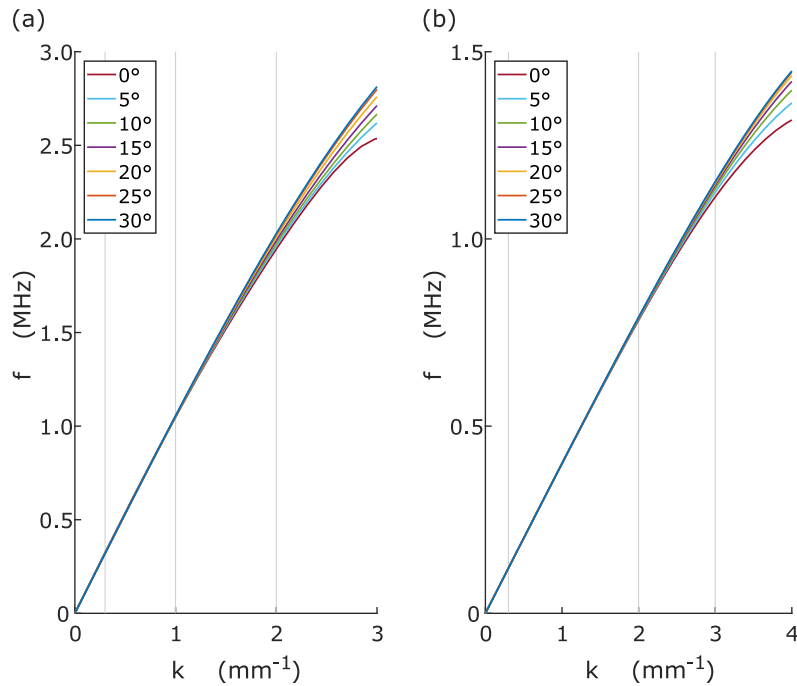
Fig. 5. The dispersion data for the propagation of (a) longitudinal and (b) out-of-plane shear acoustic waves in the direction of the angle α with respect to x_1 axis, i.e., $\alpha = 30°$ corresponds to the direction of the rods. The curves are obtained via a polynomial fit of the FEM data. The vertical lines correspond to wavenumbers chosen for the modal simulations.

Table 1

Comparison of the calculated and experimentally obtained resonant frequencies f of an example set of resonant peaks, with inverse quality factors Q^{-1}.

Mode no.	#1	#6	#8	#12	#13	#17	#31
f_{cal} (kHz)	177.6	319.6	324.1	347.5	383.7	452.1	573.3
f_{exp} (kHz)	169.7	320.4	328.9	357.7	393.9	453.4	567.0
Q_{exp}^{-1} (10^{-3})	0.513	0.492	0.432	0.667	0.711	0.521	0.661

7 resonant frequencies is shown in Table 1, demonstrating a good correlation between the experiment and the FEM calculation.

Considering the sharpness of the resonant peaks and the agreement of calculated and measured resonant frequencies, the results of FEM calculations can be taken as confirmed. Hence, the hexagonal constants (1) describe well the homogenized elastic properties of the scaffold in the low-frequency region.

To compare the low- and high-frequency acoustic behavior, the measurement of time-domain signals of out-of-plane shear wave-packets with the frequency of 0.55 MHz and 1.4 MHz was conducted in two directions, along the axis x_1 and x_2, i.e. in the principal directions between the rods and along the rods. This corresponds to the directions $\alpha = 0°$ and $30°$, respectively, in the dispersion calculations in Fig. 5.

For the frequency of 0.55 MHz (Fig. 9), a rather planar wavefront is observed in both directions, with the tangent in agreement with the velocity calculated by FEM from homogenized elastic properties of the scaffold in low-frequency region. Thus, it can be concluded that in the low-frequency region, the elastic energy propagates in a homogeneous manner along the structure, and the energy propagation is isotropic in the hexagonal plane.

On the other hand, at the frequency of 1.4 MHz (Fig. 10), the energy propagation in both directions is no longer homogeneous. In direction x_1 between the rods (Fig. 10(b)), the inhomogeneous propagation can be seen, forming a standing wave pattern with the antinodes in the scaffold junctions and nodes between them. Clearly, this wave pattern is formed immediately after the first arrival of the shear wave, and thus, it has to be attributed to the shear wave propagation in the periodic scaffold structure, as the interference with the reflections on the sample edges could not affect the wave propagation in such short times. The tangent of the phase front goes to infinity around the junctions, as emphasized by the arrows in Fig. 10(b), indicating the localization of energy in non-propagating vibrations. Fig. 11 shows these signals at a longer time-scale, documenting the fully formed standing waves. As expected from the calculated dispersion curves, for the case of propagating in direction x_2, i.e., along the rods, the effect is not as strong and the wavefront still suggests a more standard wave propagation in the structure with the tangent, i.e., phase velocity, lower than in the case of 0.55 MHz measurement.
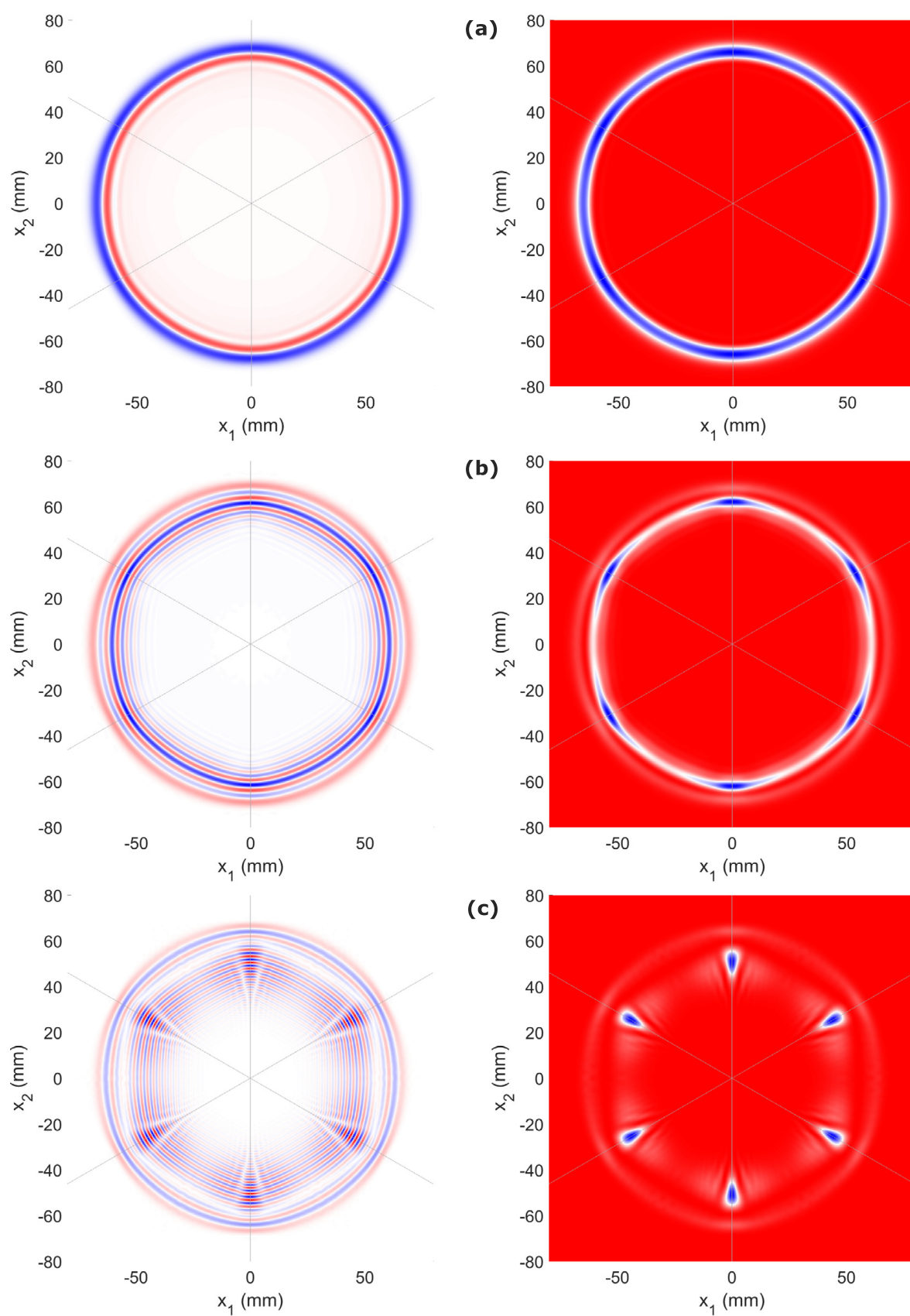
Fig. 6. The displacement field (left) and the corresponding intensity (right) of longitudinal wave at $t = 10\mu s$ for 3 different dominant wavenumbers: (a) $k = 0.3\,\text{mm}^{-1}$, (b) $k = 1\,\text{mm}^{-1}$, (c) and $k = 2\,\text{mm}^{-1}$. The light gray lines serve as the eye-guides of the angles under which the rods are oriented.
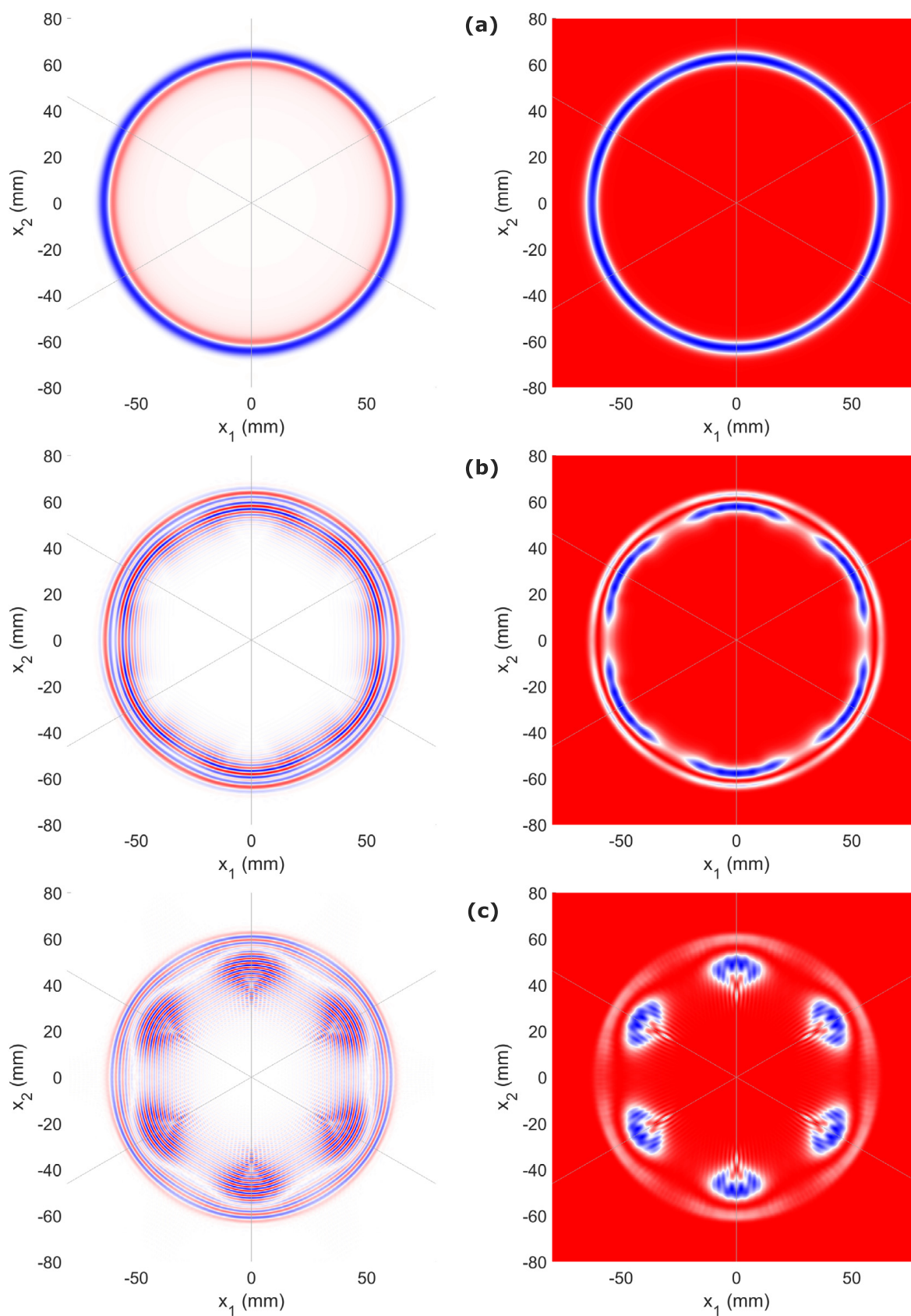
Fig. 7. The displacement field (left) and the corresponding intensity (right) of out-of-plane shear wave at $t = 25\,\mu\text{s}$ for 3 different dominant wavenumbers: (a) $k = 0.3\,\text{mm}^{-1}$, (b) $k = 2\,\text{mm}^{-1}$, (c) and $k = 3\,\text{mm}^{-1}$. The light gray lines serve as the eye-guides of the angles under which the rods are oriented.
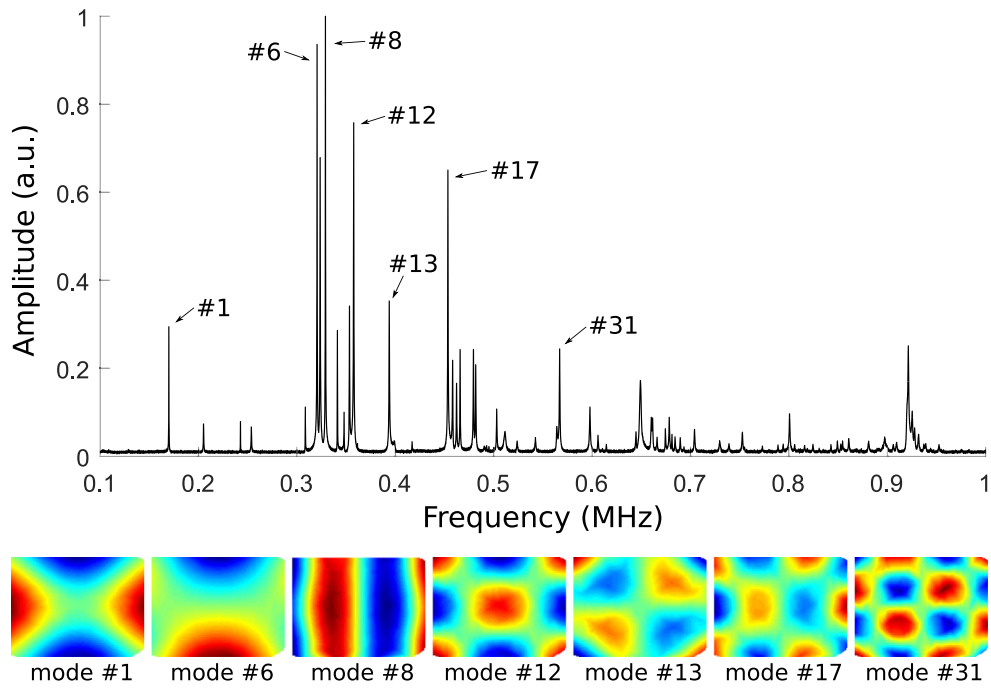
Fig. 8. The measured resonant spectrum of the scaffold, and an example set of calculated mode shapes of vibration associated between the calculation and experiment due to the scanned resonant shapes.
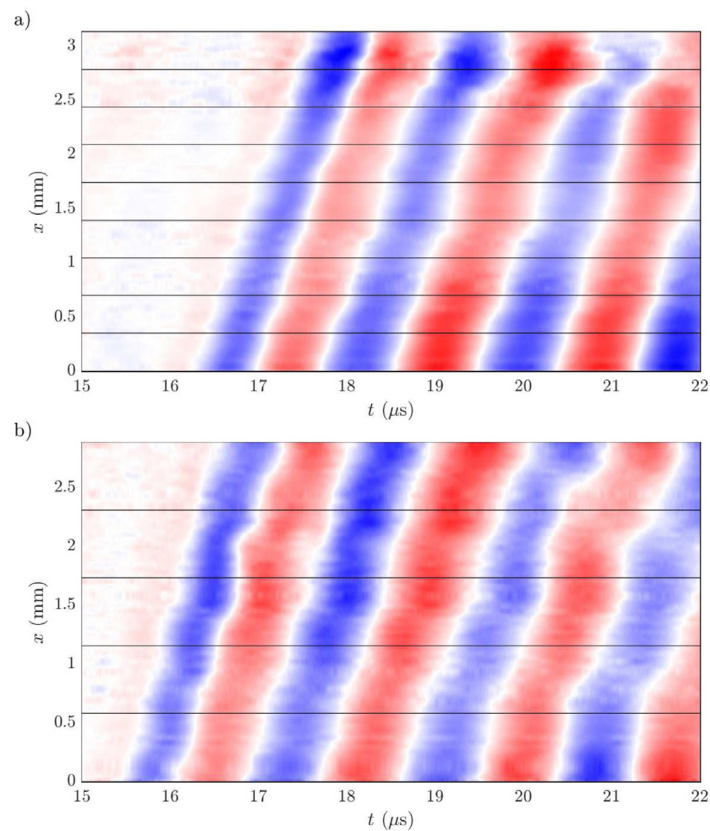
Fig. 9. Time-domain signals of out-of-plane shear wave-packet with frequency 0.55 MHz propagating in directions (a) x_2, i.e., along the rods, and (b) x_1, i.e., between the rods. The black lines denote positions of the rod junctions in the scaffold structure.
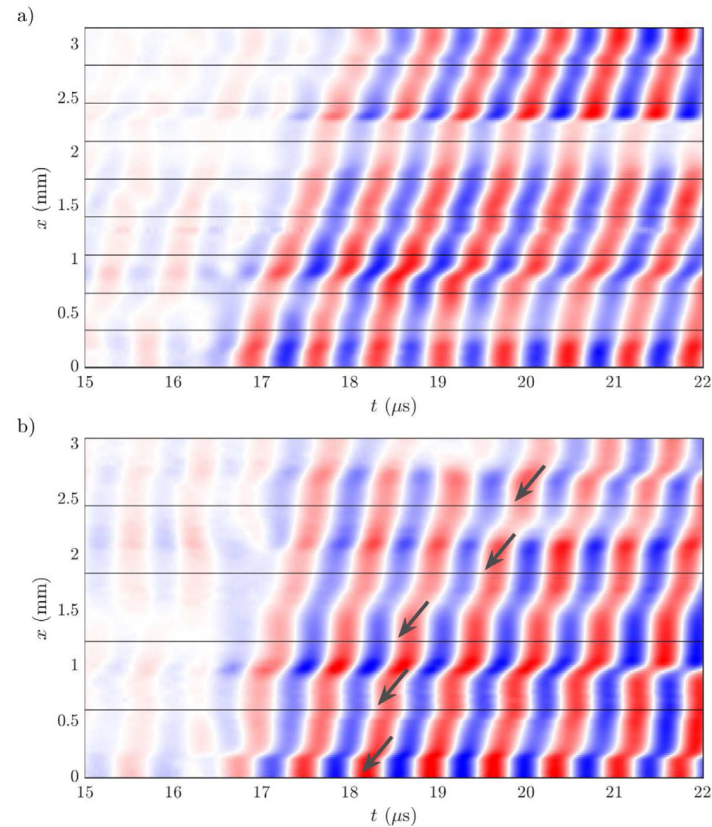
Fig. 10. Time-domain signals of out-of-plane shear wave-packet with frequency 1.4 MHz propagating in directions (a) x_2, i.e., along the rods, and (b) x_1, i.e., between the rods. The black lines denote positions of the rod junctions in the scaffold structure. Black arrows point out the junction-positions where the standing wave antinodes are formed.
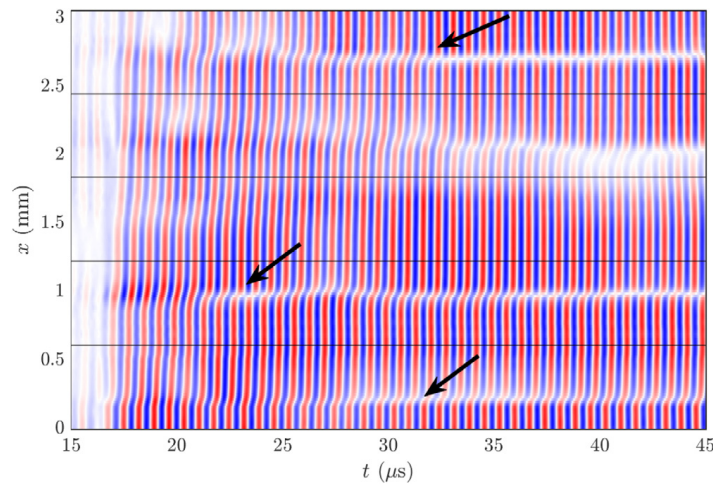
Fig. 11. Time-domain signals of out-of-plane shear wave-packet with frequency 1.4 MHz propagating in direction x_1, i.e., between the rods, shown in a longer time-scale. The black lines denote positions of the rod junctions in the scaffold structure. Black arrows point out the positions of nodes between junctions of the rods.

4. Conclusion

The precise 3D-printing technique of robocasting for creating ceramic architectured scaffolds offers a fast and simple way of constructing phononic crystals with interesting acoustic properties in the MHz range. In this paper, we studied the case of a scaffold with an effective hexagonal symmetry.

With the unit cell model designed to mimic the printed structure, we obtained the dispersion curves of the acoustic modes in several directions by FEM calculations with Bloch boundary conditions. The resulting curves show increasing angular dispersion with higher frequency, i.e., with the corresponding wavelengths comparable to the in-plane rod spacing

of the structure. With the spacing equal to 576 μm, the dispersion is observable already at wavelengths of few millimeters (equivalent to frequencies around 1 MHz in this case).

We studied the energy focusing using the modal-based simulation of propagation of wave packets through a larger area of the hexagonal structure consisting of hundreds of cells. It can be seen that with a higher dominant frequency of the wave packet, the energy propagation is focused more into the direction of the rods. Already at frequencies around 1 or 2 MHz (for shear or longitudinal waves, respectively), the energy propagates entirely through the rods. For higher frequencies, the group velocity is close to zero; hence, there is no energy propagation above a certain point, creating an acoustic band gap.

The RUS experiment successfully confirmed the static and low-frequency elastic properties of the structure as calculated by FEM, also showing the quality of the scaffold structure. The time-domain measurement of the shear wave propagation showed a clear difference between low- and high-frequency signal, with the high-frequency wave-packet creating a standing-wave pattern on the rod junctions, effectively hindering the energy propagation in frequencies close to the bandgap, mainly in the direction between the rods forming the scaffold.

Acknowledgments

References

[1] M.-H. Lu, L. Feng, Y.-F. Chen, Phononic crystals and acoustic metamaterials, Mater. Today 12 (12) (2009) 34–42, http://dx.doi.org/10.1016/S1369-7021(09)70315-3, URL http://www.sciencedirect.com/science/article/pii/S1369702109703153.

[2] Y.-Z. Wang, F.-M. Li, K. Kishimoto, Y.-S. Wang, W.-H. Huang, Elastic wave band gaps in magnetoelectroelastic phononic crystals, Wave Motion 46 (1) (2009) 47–56, http://dx.doi.org/10.1016/j.wavemoti.2008.08.001, URL http://www.sciencedirect.com/science/article/pii/S0165212508000747.

[3] L. D'Alessandro, B. Bahr, L. Daniel, D. Weinstein, R. Ardito, Shape optimization of solid–air porous phononic crystal slabs with widest full 3D bandgap for in-plane acoustic waves, J. Comput. Phys. 344 (2017) 465–484, http://dx.doi.org/10.1016/j.jcp.2017.05.018, URL http://www.sciencedirect.com/science/article/pii/S0021999117303935.

[4] Y. Chen, F. Meng, G. Sun, G. Li, X. Huang, Topological design of phononic crystals for unidirectional acoustic transmission, J. Sound Vib. 410 (2017) 103–123, http://dx.doi.org/10.1016/j.jsv.2017.08.015, URL http://www.sciencedirect.com/science/article/pii/S0022460X1730617X.

[5] Y.F. Li, F. Meng, S. Li, B. Jia, S. Zhou, X. Huang, Designing broad phononic band gaps for in-plane modes, Phys. Lett. A 382 (10) (2018) 679–684, http://dx.doi.org/10.1016/j.physleta.2017.12.050, URL http://www.sciencedirect.com/science/article/pii/S0375960118300021.

[6] M. Ruzzene, F. Scarpa, F. Soranna, Wave beaming effects in two-dimensional cellular structures, Smart Mater. Struct. 12 (3) (2003) 363, http://dx.doi.org/10.1088/0964-1726/12/3/307, URL http://stacks.iop.org/0964-1726/12/i=3/a=307.

[7] S. Yang, J.H. Page, Z. Liu, M.L. Cowan, C.T. Chan, P. Sheng, Focusing of sound in a 3D phononic crystal, Phys. Rev. Lett. 93 (2004) 024301, http://dx.doi.org/10.1103/PhysRevLett.93.024301, URL https://link.aps.org/doi/10.1103/PhysRevLett.93.024301.

[8] P. Celli, S. Gonella, Laser-enabled experimental wavefield reconstruction in two-dimensional phononic crystals, J. Sound Vib. 333 (1) (2014) 114–123, http://dx.doi.org/10.1016/j.jsv.2013.09.001, URL http://www.sciencedirect.com/science/article/pii/S0022460X13007359.

[9] D. Mousanezhad, S. Babaee, R. Ghosh, E. Mahdi, K. Bertoldi, A. Vaziri, Honeycomb phononic crystals with self-similar hierarchy, Phys. Rev. B 92 (2015) 104304, http://dx.doi.org/10.1103/PhysRevB.92.104304, URL https://link.aps.org/doi/10.1103/PhysRevB.92.104304.

[10] K.H. Matlack, A. Bauhofer, S. Krödel, A. Palermo, C. Daraio, Composite 3D-printed metastructures for low-frequency and broadband vibration absorption, Proc. Natl. Acad. Sci. 113 (30) (2016) 8386–8390, http://dx.doi.org/10.1073/pnas.1600171113, URL http://www.pnas.org/content/113/30/8386.

[11] F. Lucklum, M. Vellekoop, Rapid prototyping of 3D phononic crystals using high-resolution stereolithography fabrication, Procedia Eng. 120 (2015) 1095–1098, http://dx.doi.org/10.1016/j.proeng.2015.08.783, URL http://www.sciencedirect.com/science/article/pii/S1877705815024467.

[12] T. Delpero, S. Schoenwald, A. Zemp, A. Bergamini, Structural engineering of three-dimensional phononic crystals, J. Sound Vib. 363 (2016) 156–165, http://dx.doi.org/10.1016/j.jsv.2015.10.033, URL http://www.sciencedirect.com/science/article/pii/S0022460X1500869X.

[13] J. Smay, G. Gratson, R. Shepherd, J. Cesarano, J. Lewis, Directed colloidal assembly of 3D periodic structures, Adv. Mater. 14 (18) (2002) 1279–1283, http://dx.doi.org/10.1002/1521-4095(20020916)14:18<1279::AID-ADMA1279>3.0.CO;2-A, URL https://onlinelibrary.wiley.com/doi/abs/10.1002/1521-4095.

[14] J. Lewis, Direct ink writing of 3D functional materials, Adv. Funct. Mater. 16 (17) (2006) 2193–2204, http://dx.doi.org/10.1002/adfm.200600434, URL https://onlinelibrary.wiley.com/doi/abs/10.1002/adfm.200600434.

[15] K. Cai, B. Román-Manso, J.E. Smay, J. Zhou, M.I. Osendi, M. Belmonte, P. Miranzo, Geometrically complex silicon carbide structures fabricated by robocasting, J. Am. Ceram. Soc. 95 (8) (2012) 2660–2666, http://dx.doi.org/10.1111/j.1551-2916.2012.05276.x, URL https://onlinelibrary.wiley.com/doi/abs/10.1111/j.1551-2916.2012.05276.x.

[16] B. Román-Manso, A. De Pablos, M. Belmonte, M. Osendi, P. Miranzo, Microstructural designs of spark-plasma sintered silicon carbide ceramic scaffolds, Bol. Soc. Esp. Cerám. Vidr. 53 (2014) 93–100, http://dx.doi.org/10.3989/cyv.132014, URL http://boletines.secv.es/upload/20140508120511.20145393.pdf.

[17] B. Román-Manso, F.M. Figueiredo, B. Achiaga, R. Barea, D. Pérez-Coll, A. Morelos-Gómez, M. Terrones, M.I. Osendi, M. Belmonte, P. Miranzo, Electrically functional 3D-architectured graphene/SiC composites, Carbon 100 (2016) 318–328, http://dx.doi.org/10.1016/j.carbon.2015.12.103, URL http://www.sciencedirect.com/science/article/pii/S0008622315305698.

[18] A. Quintanilla, J. Casas, P. Miranzo, M. Osendi, M. Belmonte, 3D-printed Fe-doped silicon carbide monolithic catalysts for wet peroxide oxidation processes, Appl. Catal. B 235 (2018) 246–255, http://dx.doi.org/10.1016/j.apcatb.2018.04.066, URL http://www.sciencedirect.com/science/article/pii/S0926337318303953.

[19] A. Kruisová, H. Seiner, P. Sedlák, M. Landa, B. Román-Manso, P. Miranzo, M. Belmonte, Acoustic metamaterial behavior of three-dimensional periodic architectures assembled by robocasting, Appl. Phys. Lett. 105 (21) (2014) 211904, http://dx.doi.org/10.1063/1.4902810, URL https://aip.scitation.org/doi/10.1063/1.4902810.

[20] M. Koller, A. Kruisova, H. Seiner, P. Sedlak, T. Grabec, B. Roman-Manso, P. Miranzo, M. Belmonte, M. Landa, Ceramic phononic crystals with MHz-range frequency band gaps, Proc. Meet. Acoust. 32 (1) (2017) 045005, http://dx.doi.org/10.1121/2.0000690, URL https://asa.scitation.org/doi/abs/10.1121/2.0000690.

[21] M. Koller, A. Kruisová, H. Seiner, P. Sedlák, B. Román-Manso, P. Miranzo, M. Belmonte, M. Landa, Anisotropic elasticity of ceramic micro-scaffolds fabricated by robocasting, Acta Phys. Pol. A 134 (3) (2018) 799–803, http://dx.doi.org/10.12693/APhysPolA.134.799, URL http://przyrbwn.icm.edu.pl/APP/PDF/134/app134z3p42.pdf.

[22] A. Kruisová, M. Ševčík, H. Seiner, P. Sedlák, B. Román-Manso, P. Miranzo, M. Belmonte, M. Landa, Ultrasonic bandgaps in 3D-printed periodic ceramic microlattices, Ultrasonics 82 (2018) 91–100, http://dx.doi.org/10.1016/j.ultras.2017.07.017, URL http://www.sciencedirect.com/science/article/pii/S0041624X17302408.

[23] J. Hyun, J. Kook, S. Wang, Efficient and stable model reduction scheme for the numerical simulation of broadband acoustic metamaterials, Comput. Math. Appl. 69 (8) (2015) 876–892, http://dx.doi.org/10.1016/j.camwa.2015.01.004, URL http://www.sciencedirect.com/science/article/pii/S0898122115000061.

[24] G. Rosi, N. Auffray, Anisotropic and dispersive wave propagation within strain-gradient framework, Wave Motion 63 (2016) 120–134, http://dx.doi.org/10.1016/j.wavemoti.2016.01.009, URL http://www.sciencedirect.com/science/article/pii/S016521251600010X.

[25] A. Spadoni, M. Ruzzene, S. Gonella, F. Scarpa, Phononic properties of hexagonal chiral lattices, Wave Motion 46 (7) (2009) 435–450, http://dx.doi.org/10.1016/j.wavemoti.2009.04.002, URL http://www.sciencedirect.com/science/article/pii/S0165212509000341.

[26] A. Kruisová, H. Seiner, P. Sedlák, M. Landa, B. Román-Manso, M. Belmonte, Finite elements modeling of mechanical and acoustic properties of a ceramic metamaterial assembled by robocasting, in: Engineering Mechanics 2015, in: Applied Mechanics and Materials, vol. 821, Trans Tech Publications, 2016, pp. 364–371, http://dx.doi.org/10.4028/www.scientific.net/AMM.821.364, URL https://www.scientific.net/AMM.821.364.

[27] L. Brillouin, Wave Propagation in Periodic Structures, second ed., Dover, 1953.

[28] A. Migliori, J. Sarrao, W.M. Visscher, T. Bell, M. Lei, Z. Fisk, R. Leisure, Resonant ultrasound spectroscopic techniques for measurement of the elastic moduli of solids, Phys. B Condens. Matter 183 (1–2) (1993) 1–24, http://dx.doi.org/10.1016/0921-4526(93)90048-B, URL https://www.sciencedirect.com/science/article/pii/092145269390048B.

[29] J. Maynard, Resonant ultrasound spectroscopy, Phys. Today 49 (28) (1996) 6001–6029, http://dx.doi.org/10.1063/1.881483, URL https://physicstoday.scitation.org/doi/10.1063/1.881483.

[30] M. Landa, P. Sedlák, P. Šittner, H. Seiner, L. Heller, On the evaluation of temperature dependence of elastic constants of martensitic phases in shape memory alloys from resonant ultrasound spectroscopy studies, Mater. Sci. Eng. A 481–482 (2008) 567–573, http://dx.doi.org/10.1016/j.msea.2006.12.224, Proceedings of the 7th European Symposium on Martensitic Transformations, ESOMAT 2006. URL http://www.sciencedirect.com/science/article/pii/S0921509307011586.

[31] P. Sedlák, H. Seiner, J. Zídek, M. Janovská, M. Landa, Determination of all 21 independent elastic coefficients of generally anisotropic solids by resonant ultrasound spectroscopy: Benchmark examples, Exp. Mech. 54 (6) (2014) 1073–1085, http://dx.doi.org/10.1007/s11340-014-9862-6, URL http://link.springer.com/10.1007/s11340-014-9862-6.

[32] X. Liu, G. Hu, C. Sun, G. Huang, Wave propagation characterization and design of two-dimensional elastic chiral metacomposite, J. Sound Vib. 330 (11) (2011) 2536–2553, http://dx.doi.org/10.1016/j.jsv.2010.12.014, URL https://www.sciencedirect.com/science/article/pii/S0022460X10008278.

[33] H. Seiner, P. Sedlák, M. Koller, M. Landa, C. Ramírez, M.I. Osendi, M. Belmonte, Anisotropic elastic moduli and internal friction of graphene nanoplatelets/silicon nitride composites, Compos. Sci. Technol. 75 (2013) 93–97, http://dx.doi.org/10.1016/j.compscitech.2012.12.003, URL http://www.sciencedirect.com/science/article/pii/S0266353812004101.

[34] M. Koller, P. Sedlák, H. Seiner, M. Ševčík, M. Landa, J. Stráská, M. Janeček, An ultrasonic internal friction study of ultrafine-grained az31 magnesium alloy, J. Mater. Sci. 50 (2015) 808–818, http://dx.doi.org/10.1007/s10853-014-8641-1, URL https://link.springer.com/article/10.1007.

Paper H

Multifunctional 3D-Printed Cellular MAX-Phase Architectures

Manuel Belmonte, **Martin Koller**, Juan José Moyano, Hanuš Seiner, Pilar Miranzo, María Isabel Osendi, and Jesús González-Julián

Number of total citations[1]: 0 (excluding self-citations: 0)

Contribution of the PhD candidate and the co-authors:

The candidate developed the printable ink based on Cr_2AlC ceramic powder and printed green bodies of the scaffolds during his internship at the Institute of Ceramics and Glass.

Co-authors from the Institute of Ceramics and Glass (M. Belmonte, J. J. Moyano, P. Miranzo, M. I. Osendi) consolidated the scaffolds by SPS and performed their analysis (including differential thermal analysis, scanning electron micrographs, compression tests, electrical and thermal conductivity measurements). H. Seiner organized the internship and supervised the work on the paper. J. González-Julián produced and provided the Cr_2AlC powder.

---

[1]According to the Web of Science database `webofknowledge.com` as of August 2020

Multifunctional 3D-Printed Cellular MAX-Phase Architectures

Manuel Belmonte,* Martin Koller, Juan José Moyano, Hanus Seiner, Pilar Miranzo, María Isabel Osendi, and Jesús González-Julián

The development of porous MAX-phase structures from computer-aided design models and 3D printing strategies is of great interest for the fabricating of cellular parts with geometric and material complexities for advanced technological applications. This is reinforced by the joining of the outstanding properties of MAX phases with the benefits of creating lighter materials with a higher surface area. Here, the additive manufacturing of 3D cellular Cr_2AlC MAX-phase architectures using a direct ink writing technique from concentrated MAX aqueous-based inks is presented. These architectures exhibit multifunctional properties; in particular, high strength and good mechanical cycling behavior, excellent electrical conductivity, tailored heat dissipation, and good thermal cycling resistance, a blend that widens the potential engineering applications of these MAX phases through an innovative approach.

1. Introduction

MAX phases encompass a relatively new family of materials based on nanolayered ternary carbides and/or nitrides, where M is an early transition metal, A corresponds to an A-group element (IIIA or IVA), and X is carbon and/or nitrogen.[1] These phases bridge the gap between ceramics and metals bringing together some of the most interesting properties of both groups of materials, in particular, lightweight, excellent corrosion resistance, and high elastic modulus, all of them typical of their ceramic nature; and, on the other hand, the advantageous machinability of metals, along with their high thermal and electrical conductivities, good thermal shock response, and damage tolerance.[2] Among this family of more than 70 different compositions, aluminum-based MAX phases are the most attractive materials to operate under aggressive environments at high temperature due to the in situ formation of an external, well-adhered, and protective Al_2O_3 layer.[3,4] In this way, Cr_2AlC, Ti_2AlC, and Ti_3AlC_2 MAX phases exhibit the best response under highly demanding conditions, also showing other interesting properties, such as self-crack healing under oxidizing atmospheres.[5] Taking into account these outstanding properties, MAX phases could replace in the near future some of the most advanced superalloys employed in distinct technological applications, such as in gas turbine engines,[6,7] solar receivers in concentrated solar power systems,[8] aerospace structural applications,[9] or claddings in the next generation of nuclear reactors.[10]

The development of highly porous MAX structures is considered the next challenging step, as it certainly opens their potential applications to different areas, for instance, as catalytic supports, electrodes, filters, burners, vibration and sound damping materials, etc. These porous materials would significantly reduce the weight and extraordinarily increase the surface area as compared to bulk materials. Nowadays, porous MAX materials have mostly been processed as foams using three distinct routes, essentially, by introducing a pore former as space holder,[11–14] by foam replication,[15–17] or by the gel-casting method using agarose as gelling agent.[18–20] At present, replicated Ti_3AlC_2 and Ti_2AlC foams have been tentatively used as supports in gas exhauster catalytic converters[15] and electrodes in microbial fuel cells,[21] respectively.

A step forward in the research field of cellular materials is the use of additive manufacturing (AM) techniques to develop robust and multifunctional porous architectures with a precise patterning control of the macroporosity, enabling to fit the application requirements as well. AM processes allow making 3D parts directly from computer-aided design (CAD) models by adding materials in a layer-by-layer way,[22] offering the ability to build components with geometric and material complexities. Until now, some attempts have been carried out to produce near-net-shape dense bulk Ti_3AlC_2 and Ti_3SiC_2 through 3D printing[23–25] and laminated object manufacturing,[26] mostly by infiltrating aluminum or silicon into an additive manufactured TiC part to in situ produce the MAX specimen. However, the control of purity, microstructure, and final dimension tolerance of the MAX component is rather complex. Furthermore, to the best of our knowledge, there is just one work, recently published by Elsayed et al.,[27] that additive manufactured 3D Ti_2AlC

Dr. M. Belmonte, J. J. Moyano, Prof. P. Miranzo, Prof. M. I. Osendi
Institute of Ceramics and Glass (ICV-CSIC)
Kelsen 5, 28049 Madrid, Spain
E-mail: mbelmonte@icv.csic.es
M. Koller, Dr. H. Seiner
Institute of Thermomechanics
Czech Academy of Sciences
Dolejškova 5, 18200 Prague, Czech Republic
Dr. J. González-Julián
Forschungszentrum Jülich GmbH
Institute of Energy and Climate Research
Materials Synthesis and Processing (IEK-1)
52425 Jülich, Germany

**ADVANCED
SCIENCE NEWS**
www.advancedsciencenews.com

**ADVANCED
MATERIALS
TECHNOLOGIES**
www.advmattechnol.de

porous structures by using a direct ink writing technique. The authors presented a deep rheological study of the inks and the printed Ti_2AlC lattices exhibited total porosities between 44 and 63 vol%. The aim of the present work is to develop multifunctional 3D-printed porous MAX structures from high-purity raw Cr_2AlC powders. The structures are manufactured by robocasting (RC), a fast and versatile direct ink writing technique[28,29] that requires concentrated colloidal inks—with as low as possible amount of binder—that must exhibit a pseudoplastic behavior to be extruded through a nozzle or tip. A continuous filament is formed and printed to build the 3D structure according to a CAD model. The control over the ink rheology is critical to assure continuous and smooth flowing, at the same time that the retention of the filament shape is guaranteed to preserve the overall scaffold integrity.

2. Results and Discussion

The rheological results of the Cr_2AlC ink are shown in **Figure 1**a,b. As the shear rate ($\dot{\gamma}$) increased, the apparent viscosity (η) diminished in $\approx$3 orders of magnitude (Figure 1a), which is indicative of a shear thinning behavior of the ink. This pseudoplasticity response allows extruding low viscosity ($\eta \approx 6$ Pa s) Cr_2AlC filaments through the tips of 330 µm of inner diameter in the shear rate region of 30–70 s^{-1} and, at the same time, retains the shape of the filaments once printed due to the increase of viscosity ($\approx 2 \times 10^3$ Pa s) at low shear rates. In addition, the ink exhibited a high shear storage modulus (G') in the linear viscoelastic plateau ($\approx 10^4$ Pa s, Figure 1b) for shear stresses (τ) below 58 Pa and, above it, showed a rapid decrease of G' until crossing the loss modulus curve (G''). This

cross point can be considered as the yield stress ($\tau_y \approx 150$ Pa). According to these high G' and τ_y values, the collapse of the built 3D skeleton should be avoided.

To achieve this printable Cr_2AlC ink, a series of organics were sequentially incorporated to the aqueous-based suspension, where each organics played a specific role. In this way, a combination of high molecular weight polyethylenimine (H-PEI, 1.96 wt%) and low molecular weight PEI (L-PEI, 0.99 wt%), cationic polymers that produce electrostatic and steric repulsion, was employed as dispersant agent to increase the solids content up to 76.0 wt%. This issue is of special relevance, because it directly affects the mechanical resistance of the printed structure and its sinterability. Afterward, a viscosifying agent as hydroxypropyl methylcellulose (MC) was added (0.06 wt%) to the suspension to achieve the pseudoplastic behavior shown in Figure 1a and prevent phase segregations during the ink extrusion. Finally, a 0.37 wt% of ammonium polyacrylate (APA), an anionic polymer acting as flocculant agent, was incorporated to the ink to counterbalance the electrical charges and promote the formation of a strong gel with a high storage modulus (Figure 1b). The resulting ink composition was formed by 20.6 wt% of ultrapure water, 76.0 wt% of Cr_2AlC, and 3.4 wt% of organics (53.8, 37.9, and 8.3 in vol%, respectively).

Cuboid (24 layers and 125 cells) and cylindrical (20 layers and 75 cells) periodic lattices were computer-aided designed (Figure 1c) and, afterward, printed (12.1 × 12.1 × 5.8 mm^3 for cuboid and 5.1 mm of height and 13.9 mm of diameter for cylindrical lattices) with high architecture accuracy and robustness into Cr_2AlC scaffolds, proving the printability of this ink. Prior to sinter these scaffolds, it was necessary to remove the water and organics employed for the ink formulation. In this way, differential thermal analysis (DTA) of the as-printed
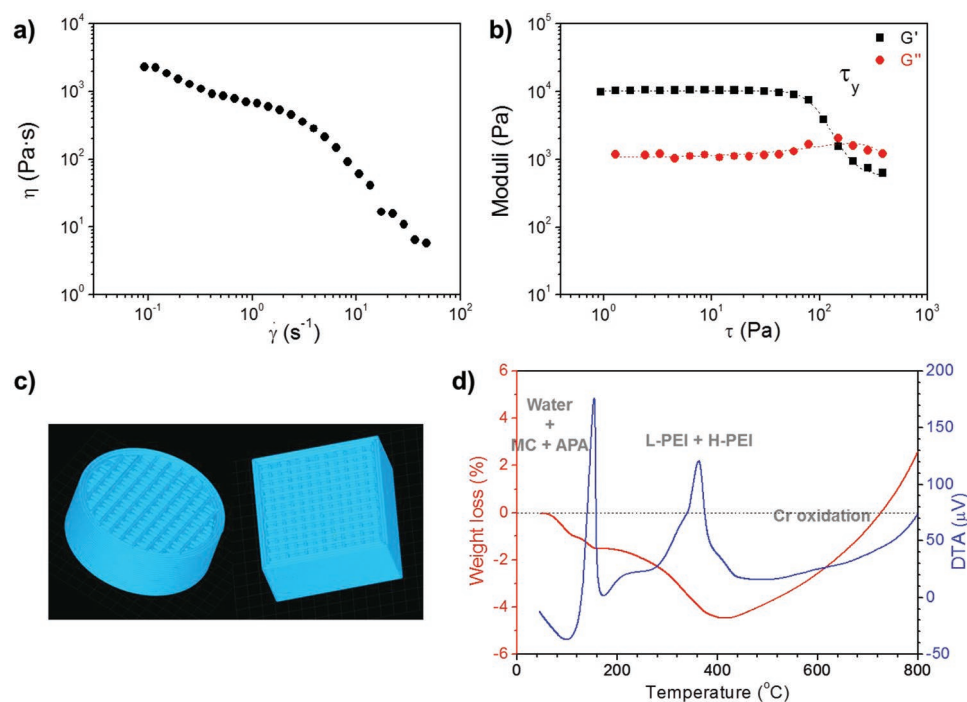

Figure 1. a) Apparent viscosity (η) versus shear rate ($\dot{\gamma}$) and b) shear storage (G') and loss (G'') moduli versus shear stress (τ) of the Cr_2AlC-MAX ink. c) CAD patterned design for cylindrical and cuboid structures. d) DTA and weight loss from TGA of as-printed Cr_2AlC scaffolds.

**ADVANCED
SCIENCE NEWS**
www.advancedsciencenews.com

**ADVANCED
MATERIALS
TECHNOLOGIES**
www.advmattechnol.de

specimens (Figure 1d) showed two main exothermic peaks linked to the combustion of MC and APA, at ≈150 °C, and H-PEI and L-PEI, at ≈360 °C. Besides, thermal gravimetric analysis (TGA, Figure 1d) evidenced a maximum weight loss of 4.5 wt% up to ≈425 °C associated with the complete removal of the organics and some remaining water. For temperatures above this value, the oxidation of Cr_2AlC started to increasingly produce Cr_2O_3 and Al_2O_3. Therefore, the as-printed scaffolds were thermal treated at 425 °C in air for 2 h to completely burn-out the organics, avoiding the oxidation of the MAX phase. Then, the treated scaffolds were pressureless spark plasma sintered (SPSed) at 1200 °C in argon to densify the MAX skeleton and limit its decomposition. In fact, other sintering techniques with longer sintering times and slower heating rates than SPS, such as high-vacuum furnace and pressureless hot pressing, were previously employed but led to considerably lower densities and higher decomposition degrees.

Representative examples of SPSed Cr_2AlC scaffolds are displayed in **Figure 2**a, while the corresponding density and porosity parameters of the sintered scaffolds are summarized in **Table 1**. Cuboid and cylindrical scaffolds exhibited different bulk densities as well as porosities, associated with the distinct patterned designs of the structures, i.e., number of layers and cells, and dimensions of the scaffold. In this way, cuboid scaffolds showed a higher geometrical density (ρ_{geo}) than cylindrical ones (2.06 vs 1.88 g cm^{-3} that corresponds to relative densities of 0.39 and 0.36, respectively). The former structures also presented a lower total porosity (π_{total}) than cylindrical scaffolds (60.6% vs 64.1%), taken this value as the sum of the macroporosity due to the patterned design (π_{macro}), larger for cylindrical scaffolds, and the porosity associated with

the Cr_2AlC struts (π_{strut}) weighted by their volume within the whole structure.

The properties of the 3D MAX materials were determined on the cuboid cellular specimens as this structure was revealed as more convenient for the electrical and thermal measurements. A closer observation of this kind of scaffold by field emission scanning electron microscopy (FESEM) evidenced an excellent retention of the 3D architecture formed by long and straight struts within a printed layer (Figure 2b) that are overlapped between adjacent layers (Figure 2c). The MAX-phase microstructure within the struts (Figure 2d) showed a bimodal distribution of very fine (≈1 μm) and coarse grains (≈5 μm) and, accordingly, significant grain growth occurs during SPS. X-ray diffraction (XRD) analysis confirmed Cr_2AlC as the main crystalline phase in the structures (Figure S1, Supporting Information), although traces of Cr_7C_3 were identified, probably produced by a slight decomposition of Cr_2AlC during the pressureless SPS process. Al_2O_3 traces were also observed in the pattern, which already appeared in the raw material as an effect of the synthesis and grinding process.

3D Cr_2AlC scaffolds exhibited robustness and good mechanical integrity, allowing handling without any signs of damage. In this way, a representative example of the load–displacement curves acquired during compression is shown in **Figure 3**a, displaying the typical response of cellular materials. In fact, a linear elastic region is observed in the first stage of the plot that corresponds to the progressive deformation of the structure—continuous bending/buckling of the Cr_2AlC cells—until reaching the maximum compressive strength (crushing, σ_c). Once the maximum load is attained, a wavy plateau can be observed due to the fracture of the single struts. However, the
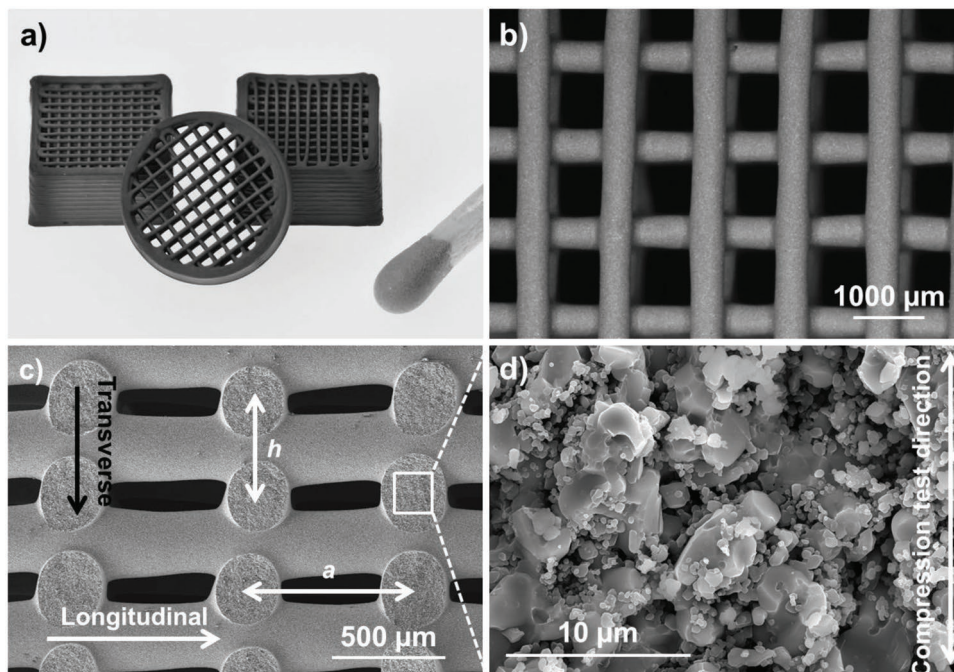
Figure 2. a) Image of the SPSed MAX scaffolds. b–d) FESEM micrographs of a SPSed cuboid scaffold: b) cell-side and c) cross-section views showing the woodpile arrangement with the distance between two adjacent struts (*a*) and between two equivalent layers in the *z*-direction (*h*). Longitudinal and transverse directions for the electrical characterization are also pointed. d) Microstructure at higher magnification (mostly Cr_2AlC grains) of the rod framed highlighted in c), pointing the direction of the compression tests.

Table 1. Geometrical (ρ_{geo}), bulk (ρ_{bulk}), and apparent (ρ_{app}) densities, and total (π_{total}), macro (π_{macro}), and strut (π_{strut}) porosities of the SPSed scaffolds. Data represent the average of the measurements for 14 different specimens.

Scaffold	ρ_{geo} [g cm^{-3}]	ρ_{bulk} [g cm^{-3}]	ρ_{app} [g cm^{-3}]	π_{total} [%]	π_{macro} [%]	π_{strut} [%]
Cuboid	2.06 ± 0.06	3.83 ± 0.02	4.99 ± 0.04	60.6 ± 1.1	46.2 ± 1.3	26.9 ± 0.4
Cylindrical	1.88 ± 0.03	4.40 ± 0.13	5.13 ± 0.01	64.1 ± 0.5	57.2 ± 1.9	16.0 ± 2.6

catastrophic failure of the scaffold did not completely occur, confirmed by the gradual decrease of the stress as the strain increased (see the wavy decreasing line in Figure 3a), although the structure bearing capability slowly decreased as cells progressively failed. The mean σ_c achieved by these 3D Cr$_2$AlC structures was 65.4 ± 2.3 MPa. Present σ_c value was first compared in Figure 3b with the strength of different cellular MAX materials, namely, Ti$_2$AlC[11,18,20] and Cr$_2$AlC[14] foams and 3D-printed Ti$_2$AlC structures.[27] Compressive strength data varied between 1.6 (93% porosity) and 188 MPa (33% porosity). As expected, the compressive strength decreased with the total porosity of the structures,[30] and the collected data fitted to a parabolic equation. In this way, the result obtained in the present work perfectly matches with the predicted behavior, despite most of 3D porous ceramics printed by RC (empty symbols in Figure 3b)[31–36] show inferior strength than MAX foams with similar porosities. This fact could be related to the different

porous architecture of foams and printed cellular materials, in particular, to the different amount of residual porosity in the solid phase (i.e., in the printed struts or in the foam cell walls).

The present 3D-printed Cr$_2$AlC scaffold, 3D Ti$_2$AlC structures,[27] and a very low porosity (32%) 3D-printed Ce-ZrO$_2$/Al$_2$O$_3$ composite structure[34] are the exceptions, all of them having comparable σ_c values to MAX foams of alike porosities. Focusing just on highly porous (≥50%) robocast ceramics (Figure 3c), the compressive strength of the 3D Cr$_2$AlC structures is between 10% and 50% higher than that for 3D Ti$_2$AlC ones, and from 50% to one order of magnitude than other ceramic structures having comparable total porosities (60 ± 10%), which corroborates the success of the printing process and the ink formulation described here. In addition, MAX cuboids were also load cycled (20 times at 3.6 kN, Figure 3d), exhibiting a good mechanical cycling behavior without any apparent degradation. The 3D structure displays an elastic-linear

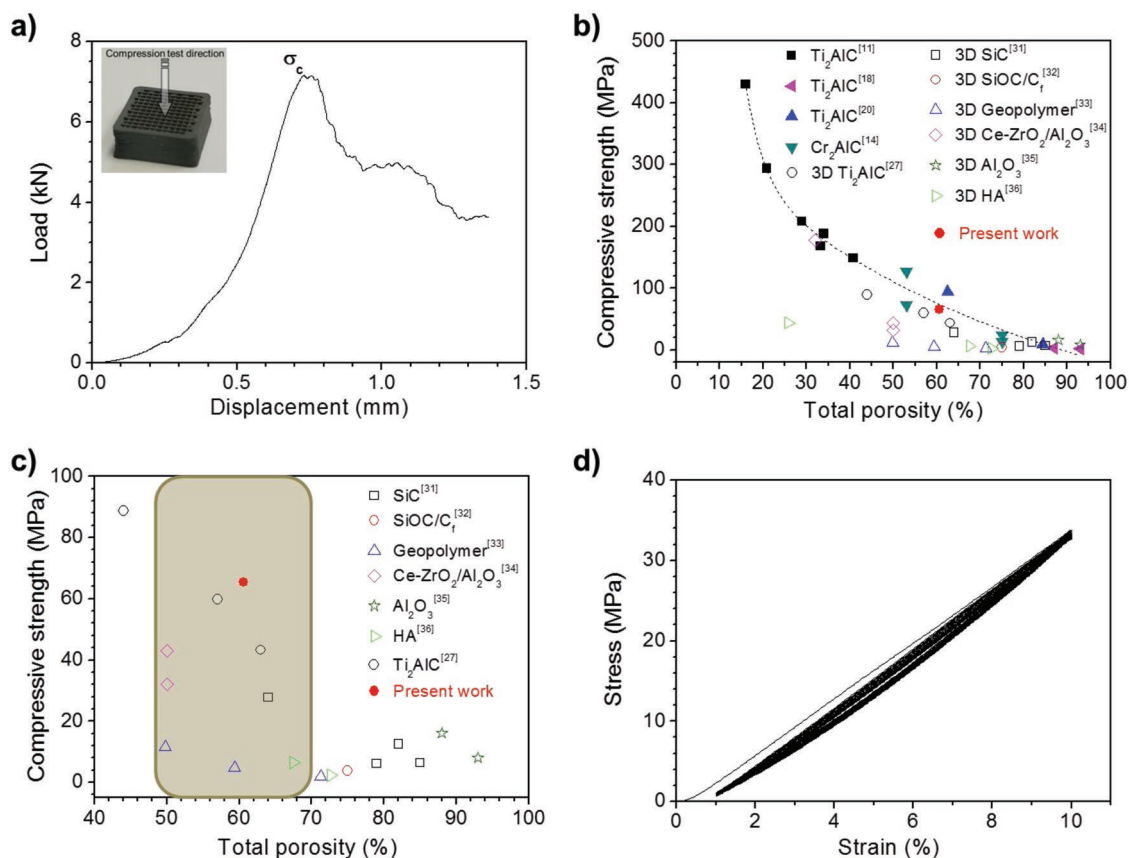**Figure 3.** a) A representative load–displacement curve of SPSed cuboid Cr$_2$AlC scaffold. b) Compressive strength values as a function of the total porosity reported for MAX foams (full symbols) and 3D robocast ceramics (empty symbols). c) A similar plot as in (b) re-scaled to show data for 3D robocast ceramics. d) Stress–strain recorded during 20 cycles for SPSed cuboid Cr$_2$AlC scaffold.

behavior with a small hysteresis loop for the level of deformation tested (10%), recovering the original length and maximum load after each loop.

Effective electrical conductivity (σ_{eff}) data for longitudinal and transverse directions (Figure 2c) confirmed that the electrical transport is favored along the rods and, in fact, the longitudinal direction is 43% more conductive ($\sigma_{eff-L} = 9.0 \times 10^4$ S m^{-1}) than the transverse one ($\sigma_{eff-T} = 6.3 \times 10^4$ S m^{-1}). The σ_{eff} values of the Cr$_2$AlC scaffold are slightly higher than those reported for macroporous Ti$_2$AlC foams (1.1×10^4 S m^{-1}),[16] although a real comparison with that material cannot be done as the total porosity was not provided. Besides, despite the electrical conductivity of the printed Cr$_2$AlC architecture is lower than that measured for fully dense bulk Cr$_2$AlC specimens (1.1×10^6 S m^{-1}), the values are still very high, which would allow using this 3D printing approach for manufacturing porous and lightweight Cr$_2$AlC electrodes for electrochemical reactions.[37]

Differences in the effective electrical conductivity for the transverse and longitudinal directions have also been observed in other conductive 3D-printed porous structures.[38] In that work, the electrical conductivity in SiC/graphene scaffolds was simulated using both a simple resistors model and the finite-elements method. In particular, the resistor model predicts quite correctly that σ_{eff-L} and σ_{eff-T} depend on the intrinsic electrical conductivity of the rods (σ_{rod}), and also on the 3D structure geometry through the mean diameter of the struts ($\varnothing$, 289 µm for Cr$_2$AlC), the distance between two adjacent struts (a, 758 µm), and the distance between two equivalent layers in the z-direction (h, 418 µm)

$$\sigma_{eff-L} = \frac{\varnothing}{2a} \sigma_{rod} \tag{1}$$

$$\sigma_{eff-T} = \frac{h \cdot \varnothing}{a^2} \left(1 - h / 2\varnothing\right) \cdot \sigma_{rod} \tag{2}$$

Using these equations for the present structures, we estimated a σ_{rod} value of $4.2–7.5 \times 10^5$ S m^{-1}, very close to that deduced (7.0×10^5 S m^{-1}) from the well-known Maxwell effective medium theory[39] taking into account the electrical conductivity of the dense bulk material (1.1×10^6 S m^{-1}) and the porosity of the struts (26.9%). Therefore, the resistor model seems to be valid to predict the macroscopic electrical behavior of the present 3D MAX structures. Similarly, we could extend the application of this model for predicting the thermal response of the 3D scaffolds. The thermal conductivity of MAX phases is the sum of the electron ($k_{electron}$) and phonon (k_{phonon}) contributions.[40] The thermal conductivity (k_t) of dense bulk Cr$_2$AlC specimens (**Figure 4**a) varied from 14.3 W m^{-1} K^{-1} at 298 K to 15.4 W m^{-1} K^{-1} at 673 K, slightly increasing with temperature probably because of its mixed electron and phonon conduction. These values are somewhat lower than those reported by Tian et al.[41] for hot-pressed bulk Cr$_2$AlC samples ($\approx$17.5 W m^{-1} K^{-1}), which could be explained by a larger Cr$_2$AlC grain size in the hot-pressed materials ($d_{50} \approx 34$ µm) than in the current spark plasma sintered ones ($d_{50} \approx 15$ µm). According to the Wiedemann–Franz's law,[42] $k_{electron} = L \cdot T / \rho_T$, where L is the Lorentz number (2.44×10^{-8} W Ω K^{-2}), T is the temperature

in Kelvin, and ρ_T is the electrical resistivity of bulk Cr$_2$AlC (9.09×10^{-5} Ω m in the present work at $T = 298$ K). From this equation, the value of the electron contribution is 8.0 W m^{-1} K^{-1} and, hence, the phonon contribution ($k_t - k_{electron}$) would be 6.3 W m^{-1} K^{-1}.

In the case of the 3D-printed cellular scaffolds, it is possible to estimate the effective thermal conductivity (k_{eff}) of the Cr$_2$AlC struts using the Maxwell–Eucken's model, which considers the strut as a heterogenous material formed by the MAX matrix and the porosity inside the struts. In a similar way as we did for the electrical conductivity, thermal conductivity of the dense bulk material was corrected using the porosity of the Cr$_2$AlC struts (26.9%), giving k_{eff} values for the scaffold rods (Figure 4a) that scanned from 9.1 W m^{-1} K^{-1}—at 298 K—to 9.8 W m^{-1} K^{-1}—at 673 K. Introducing these estimated k_{eff} values in the resistor model equations (1) and (2), the k_{eff} in the orthogonal characteristic directions of 3D scaffolds were predicted, attaining values at 298 K of 1.9 and 0.7 W m^{-1} K^{-1} for the longitudinal and transverse directions, respectively (Figure 4a).

Despite this low effective thermal conductivity for the 3D MAX structures, the radiative and convective heat transfer to their surroundings are expected to prevail over conduction during free cooling in these kinds of open cell structures,[31] as demonstrated for highly porous 3D scaffolds of SiC by analyzing the free cooling of their surfaces after a rapid heating at high temperature. A micro-torch gas burner focused during 30 s on 3D MAX cuboids (Figure 4b) rises the temperature on the cell-side up to 925 °C (Figure 4c).

The cooling profile of the cuboids (Figure 4d) was fitted to an expression of the type

$$T(t) = \gamma_0 + A_1 e^{-t/\tau 1} + A_2 e^{-t/\tau 2} \tag{3}$$

with two exponential terms. The first one ($-t/\tau 1$) dominates in the high temperature range, the radiative dissipation mainly governing the cooling process; whereas the second exponential ($-t/\tau 2$) prevails at temperatures below 500 °C and corresponds to the typical functional form for the Newton's cooling law associated with convective cooling. The time constant according to Newton's cooling law[43] is

$$\tau = \frac{\rho \cdot c}{\alpha} \cdot \frac{V}{A} \tag{4}$$

where ρ is the density, c is the specific heat, α is the heat transfer coefficient, and V/A is proportional to the object size.

The cooling profile of the 3D MAX structures showed a good fitting to Equation (3), and it was compared with that previously reported for 3D-printed SiC structures tested under similar conditions.[31] As seen in Figure 4d, the weight of both terms is lower for the 3D MAX than for the SiC 3D structures. As V/A is similar for both 3D materials, differences in their densities (2.06 g cm^{-3} for 3D MAX vs 0.7 g cm^{-3} for 3D SiC, with a MAX/SiC density ratio of $\approx$2.9) would explain the $\approx$2.5 higher time constants for 3D MAX ($\tau 1 = 4.6$, $\tau 2 = 52.0$) than for SiC ($\tau 1 = 1.8$, $\tau 2 = 21.4$). Therefore, the thermal dissipation and thermal inertia in the developed structures could be tailored by tuning the shape and size of the cells and struts and, hence, thermal metamaterials based on MAX phases could be developed to act
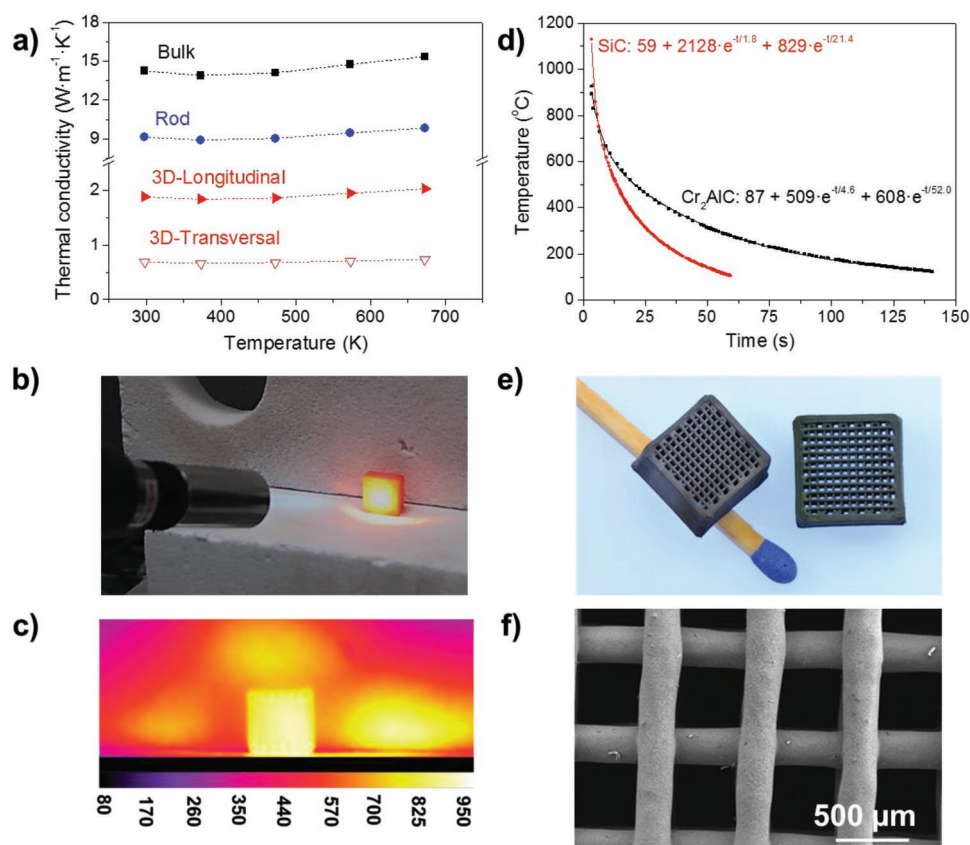
**ADVANCED
SCIENCE NEWS**
www.advancedsciencenews.com

**ADVANCED
MATERIALS
TECHNOLOGIES**
www.advmattechnol.de

Figure 4. a) Thermal conductivity of the dense bulk Cr_2AlC material, one scaffold rod and longitudinal and transverse directions of the 3D scaffolds versus the temperature. b) Experimental setup with the micro-torch and c) thermographic image of the scaffold cell-side after 30 s of heating. d) Experimental cooling curves for 3D Cr_2AlC and SiC structures[31] and exponential fits including the time constants. e) Cuboid scaffolds before (left) and after (right) 200 thermal cycles at 1100 °C treatment and f) SEM image of the Cr_2AlC struts after the thermal cycling.

as thermal concentrators (sinks) or thermal diffusers (cloaks) in particular regions through the 3D printing of patterned porous materials.

The Cr_2AlC scaffolds retained mechanical stability after 200 thermal cycles at 1100 °C (Figure 4e,f), which represents a total time of 400 h at this temperature. No signs of fracture, spallation, or degradation of the structure were observed. However, as expected, Al_2O_3 was formed at the strut surface (Figure S1, Supporting Information), since the onset of the Cr_2AlC oxidation starts at ≈800 °C.[4] Besides, some Cr_2O_3 was also detected in the scaffold composition due to the oxidation of Cr_7C_3 present in the sintered structures.

3. Conclusion

3D cellular Cr_2AlC structures have been additive manufactured by direct ink writing using concentrated aqueous-based dispersions of high-purity MAX powders, which demonstrates the versatility and feasibility of this approach to produce patterned porous MAX scaffolds. The printed and sintered structures, with total porosities around 60%, are lightweight and robust. They exhibit high compressive strength (65 MPa), superior to that of other 3D-printed advanced ceramics of similar porosity, and a good mechanical cycling behavior without apparent

degradation. The functionality of these cellular Cr_2AlC structures is broaden due to its electrical and thermal responses, showing electrical conductivities well above 10^4 S m^{-1} in all printed directions and estimated thermal conductivity up to 1.9 W m^{-1} K^{-1}, the cooling profile being, namely, governed by radiative and convective heat transfer. The combination of all these properties allows designing complex porous MAX components for advanced demanding applications in the energy and catalysis fields (electrodes, volumetric solar receivers, burners, catalytic supports) or in less explored uses, such as vibration and sound damping materials.

4. Experimental Section

Manufacturing of 3D Cr_2AlC Structures: Cr_2AlC MAX powders with a 98% of purity were first synthesized by solid/liquid state reaction from its elemental constituents using the procedure described elsewhere.[44] Briefly, chromium powder (particle size, d_{50} = 85.5 μm, 99.0% pure, Alfa Aesar) was first planetary milled (PM400, Retsch) at 350 rpm for 3 h under argon atmosphere to reduce the particle size. The milled chromium powder, with a mean particle size of 26.5 μm, was mixed with aluminum (d_{50} = 9.1 μm, 99.5% pure, Alfa Aesar) and carbon (d_{50} = 6.9 μm, 99.0% pure, Alfa Aesar) powders in a molar ratio of 2.0:1.1:1.0, respectively. The mixture was compacted and heated up to 1350 °C in argon atmosphere during 3 h using heating and cooling rates of 10 °C min^{-1}. The resultant Cr_2AlC porous sample was ground using

a planetary milling at 300 rpm for 2 h under argon atmosphere with zirconia balls of 5 and 1 mm diameter as grinding media. The final powder presented a unimodal particle size distribution with d_{50} of 0.9 µm and d_{90} of 1.3 µm, exhibiting an excellent uniformity and, hence, the ink characteristics remained constant and no variations on the printing process were observed. The printable MAX ink was developed by mixing in sequential steps ultrapure water, MAX powders, and a series of organics to achieve the required pseudoplastic behavior, which was studied by determining η, G', and G'' of the inks. These tests were performed at a constant temperature of 25 °C using a rheometer equipped with a cone-and-plate geometry (CVO 100 D, Bohlin Instruments). The following organics were selected: H-PEI (PEI 25000, Sigma Aldrich; < 1 wt% of water content) and L-PEI (PEI 2000, Sigma Aldrich; 50 wt% of water content) as dispersants; MC (Methocel F4M, Dow Chemical Co.; 95 wt% of water content) as viscosifier, and APA (Darvan 821-A, R.T. Vanderbilt Company, Inc.; 60 wt% of water content) as flocculant agent. After the addition of any component (water, MAX powders, organics), the ink was homogenized in a planetary centrifugal mixer (ARE-250, Thinky Co.) at 1100 rpm for 30 s. 3D cylindrical and cuboid Cr_2AlC periodic lattices were computer designed (RoboCAD 4.0, 3-D Inks LLC) considering nozzle tips with an inner diameter of 330 µm and a structure formed by 20–24 layers with a linear array of parallel filaments in the x–y plane, each array rotated by 90° in adjacent layers. Afterward, this design was reproduced at room temperature (RT) onto an alumina substrate with a custom three-axis RC system (A-3200, 3-D Inks LLC). The as-printed scaffolds were heat treated in a furnace at 415 °C in air for 2 h with a heating/cooling rate of 3 °C min^{-1}, according to the results attained from the TGA, to burn-out the organics added to the ink and, then, pressureless spark plasma sintered (SPS-510CE; Fuji Electronic Industrial Co., Ltd.) at 1200 °C for 10 min in argon atmosphere, using a heating rate of 125 °C min^{-1} up to 1100 and 50 °C min^{-1} from 1100 to 1200 °C to promote the densification of the MAX skeleton. TGA-DTA (SDT Q600, TA Instruments) were carried out in air from RT to 800 °C at a heating rate of 3 °C min^{-1}. Bulk disks were sintered from the pristine Cr_2AlC powders using a field-assisted sintering furnace (FCT-HPD5, FCT Systeme GmbH) at 1200 °C for 5 min in vacuum (4 Pa) and applying a uniaxial pressure of 50 MPa.

Microstructural Characterization: Geometrical density (ρ_{geo}) was estimated from the weight and the dimensions of the scaffolds. Bulk (ρ_{bulk}) and apparent (ρ_{app}) densities and apparent porosity (π_{app}) of the sintered scaffolds were determined by Archimedes' method (see the Supporting Information). Total porosity (π_{total}) was estimated as the sum of the macroporosity due to the patterned design and the microporosity of the ceramic struts, considering the theoretical density of Cr_2AlC as 5.23 g cm^{-3}. Crystalline phases at the strut surface were identified by XRD (Bruker µ00, Siemens), and the fracture surfaces of struts were observed with an FESEM (Hitachi S-4700).

Mechanical Characterization: Five 3D Cr_2AlC cuboid scaffolds of $10.3 \times 10.3 \times 5.0$ mm^3 were compression tested using a universal testing machine with a load cell of 25 kN (Model EM2/200/FR, Microtest S.A.) with displacement rate of 0.5 mm min^{-1} until crushing. In addition, two additional scaffolds were subjected to cyclic deformation tests during 20 times at 3.6 kN using a 5 kN load cell (ZwickiLine Z5.0 TS, Zwick-Roell). The robocast specimens were previously ground at the top/bottom surfaces (cell-side) to ensure a homogenous distribution of the load on the whole 3D structure. Crushing strength (σ_c) was calculated from the maximum load and the nominal contact surface area.

Electrical Characterization: The effective electrical conductivity (σ_{eff}) at RT of cuboid scaffolds on both the longitudinal (L) and transverse (T) directions was estimated by the four-probe DC method using a potentiostat/galvanostat (Autolab PGSTAT302N) and a current flow between 100 and 3000 mA in steps of 100 mA. In the longitudinal direction (σ_{eff-L}), the current mainly flows along the struts; whereas in the transverse one (σ_{eff-T}), it flows through the struts of successive layers. σ_{eff} values were estimated as: $\sigma_{eff} = l/(A \times R)$, where l is the distance between the inner electrodes, A is the apparent transversal area of the scaffold structure, and R is the resistance obtained from the slope of the current–voltage plot. For comparison purposes, σ_{eff} was also assessed for fully dense bulk specimens.

Thermal Characterization: The thermal conductivity (k_t) of bulk materials from RT up to 800 °C was estimated by measuring the thermal diffusivity in argon atmosphere with a laser flash equipment (Thermaflash 2200, Holometrix Netzsch), once known the density and the specific heat versus the temperature.[41] Nevertheless, this technique is not totally reliable for cellular materials because laser radiation can penetrate into the sample and, hence, the effective thermal conductivity (k_{eff}) of the 3D-printed structure was estimated using the Maxwell–Eucken's model[45] for the porosity rod correction and a simple model of thermal resistances. Besides, the temperature profile of 3D MAX structures placed on an insulating fiber mat was recorded using a thermal imaging infrared camera (FLIR A325sc) when the cell-side was heated using a micro-torch gas burner with a butane/air mixture during 30 s and, then, cooled down, estimating the cooling rate. The distance between the micro-torch and the scaffold surface was ≈6 cm. Additional thermal tests were performed in the scaffolds using an elevator furnace (Carbolite Gero) under continued cycling conditions of 2 h at 1100 °C, followed by a fast cooling at ambient air for 15 min. The cycling program was automatically repeated 200 times. Afterward, the samples were characterized by XRD and SEM.

Supporting Information

Supporting Information is available from the Wiley Online Library or from the author.

Conflict of Interest

The authors declare no conflict of interest.

Keywords

3D MAX phase, direct ink writing, electrical, mechanical, thermal

[1] M. W. Barsoum, *MAX Phases: Properties of Machinable Ternary Carbides and Nitrides*, Wiley-VCH, Weinheim, Germany **2013**.
[2] B. M. Radovic, M. W. Barsoum, *Am. Ceram. Soc. Bull.* **2013**, *92*, 20.
[3] D. J. Tallman, B. Anasori, M. W. Barsoum, *Mater. Res. Lett.* **2013**, *1*, 115.
[4] J. Gonzalez-Julian, T. Go, D. E. Mack, R. Vaßen, *J. Am. Ceram. Soc.* **2018**, *101*, 1841.
[5] A. S. Farle, C. Kwakernaak, S. Van der Zwaag, W. G. Sloof, *J. Eur. Ceram. Soc.* **2015**, *35*, 37.
[6] C. W. Strock, S. Amini, *US 2016/0289844 A1*, **2016**.
[7] H. P. Bossmann, M. Bahraini, *Eur. 3168204 A1*, **2017**.
[8] J. Sarwar, T. Shrouf, A. Srinivasa, H. Gao, M. Radovic, K. Kakosimos, *Sol. Energy Mater. Sol. Cells* **2018**, *182*, 76.

**ADVANCED
SCIENCE NEWS**

www.advancedsciencenews.com

**ADVANCED
MATERIALS
TECHNOLOGIES**

www.advmattechnol.de

[9] S. P. Munagala, in *Aerospace Materials and Material Technologies* (Eds: N. Prasad, R. Wanhill), Springer, Singapore **2017**, pp. 455–465.

[10] E. N. Hoffman, D. W. Vinson, R. L. Sindelar, D. J. Tallman, G. Kohse, M. W. Barsoum, *Nucl. Eng. Des.* **2012**, *244*, 17.

[11] L. Hu, R. Benitez, S. Basu, I. Karaman, M. Radovic, *Acta Mater.* **2012**, *60*, 6266.

[12] C. L. Zhou, T. W. L. Ngai, L. Lu, Y. Y. Li, *Mater. Lett.* **2014**, *131*, 280.

[13] B. Velasco, E. Gordo, S. A. Tsipas, *J. Alloys Compd.* **2015**, *646*, 1036.

[14] J. Gonzalez-Julian, S. Onrubia, M. Bram, C. Broeckmann, R. Vassen, O. Guillon, *J. Am. Ceram. Soc.* **2018**, *101*, 542.

[15] Z. Sun, Y. Liang, M. Li, Y. Zhou, *J. Am. Ceram. Soc.* **2010**, *93*, 2591.

[16] C. R. Bowen, T. Thomas, *Ceram. Int.* **2015**, *41*, 12178.

[17] S. Karimi, T. Go, R. Vaßen, J. Gonzalez-Julian, *Mater. Lett.* **2019**, *240*, 271.

[18] M. Potoczek, E. Guzi de Moraes, P. Colombo, *J. Eur. Ceram. Soc.* **2015**, *35*, 2445.

[19] T. Fey, M. Stumpf, A. Chmielarz, P. Colombo, P. Greil, M. Potoczek, *J. Eur. Ceram. Soc.* **2018**, *38*, 3424.

[20] M. Potoczek, A. Chmielarz, M. D. deM. Innocentini, I. C. P. da Silva, P. Colombo, B. Winiarska, *J. Am. Ceram. Soc.* **2018**, *101*, 5346.

[21] K. Schneider, *Ph.D. Thesis*, University of Bath **2014**.

[22] N. Guo, M. C. Leu, *Front. Mech. Eng.* **2013**, *8*, 215.

[23] B. Nan, X. Yin, L. Zhang, L. Cheng, *J. Am. Ceram. Soc.* **2011**, *94*, 969.

[24] Y. Ma, X. Yin, X. Fan, N. Travitzky, P. Greil, *J. Ceram. Sci. Technol.* **2015**, *6*, 87.

[25] M. M. M. Carrijo, H. Lorenz, I. Filbert-Demut, G. M. de Oliveira Barra, D. Hotza, X. Yin, P. Greil, N. Travitzky, *Ceram. Int.* **2016**, *42*, 9557.

[26] M. Krinitcyn, Z. Fuc, J. Harris, K. Kostikov, G. A. Pribytkov, P. Greil, N. Travitzky, *Ceram. Int.* **2017**, *43*, 9241.

[27] H. Elsayed, A. Chmielarz, M. Potoczek, T. Fey, P. Colombo, *Addit. Manuf.* **2019**, *28*, 365.

[28] J. A. Lewis, *Adv. Funct. Mater.* **2006**, *16*, 2193.

[29] E. Peng, D. Zhang, J. Ding, *Adv. Mater.* **2018**, *30*, 1802404.

[30] L. J. Gibson, M. F. Ashby, *Cellular Solids Structure and Properties*, Cambridge University Press, Cambridge, UK **1999**.

[31] A. Gomez-Gomez, J. J. Moyano, B. Roman-Manso, M. Belmonte, P. Miranzo, M. I. Osendi, *J. Eur. Ceram. Soc.* **2019**, *39*, 688.

[32] G. Franchin, L. Wahl, P. Colombo, *J. Am. Ceram. Soc.* **2017**, *100*, 4397.

[33] G. Franchin, P. Scanferla, L. Zeffiro, H. Elsayed, A. Baliello, G. Giacomello, M. Pasetto, P. Colombo, *J. Eur. Ceram. Soc.* **2017**, *37*, 2481.

[34] L. Goyos-Ball, E. Garcia-Tuñón, E. Fernandez-Garcia, R. Diaz, A. Fernandez, C. Prado, E. Saiz, R. Torrecillas, *J. Eur. Ceram. Soc.* **2017**, *37*, 3151.

[35] C. Minas, D. Carnelli, E. Tervoort, A. R. Studart, *Adv. Mater.* **2016**, *28*, 9993.

[36] J. Rolečeka, L. Pejchalová, F. J. Martínez-Vázquez, P. Miranda, D. Salamon, *J. Eur. Ceram. Soc.* **2019**, *39*, 1595.

[37] V. D. Jovic, M. W. Barsoum, *US 7,001,494 B2*, **2006**.

[38] B. Roman-Manso, F. M. Figueiredo, B. Achiaga, R. Barea, D. Perez-Coll, A. Morelos-Gomez, M. Terrones, M. I. Osendi, M. Belmonte, P. Miranzo, *Carbon* **2016**, *100*, 318.

[39] J. M. Montes, F. G. Cuevas, J. Cintas, *Appl. Phys. A* **2008**, *92*, 375.

[40] J. D. Hettinger, S. E. Lofland, P. Finkel, T. Meehan, J. Palma, K. Harrell, S. Gupta, A. Ganguly, T. El-Raghy, M. W. Barsoum, *Phys. Rev. B* **2005**, *72*, 115120.

[41] W. Tian, P. Wang, G. Zhang, Y. Kan, Y. Li, D. Yan, *Scr. Mater.* **2006**, *54*, 841.

[42] R. Franz, G. Wiedemann, *Ann. Phys. Chem.* **1853**, *165*, 497.

[43] M. Vollmer, *Eur. J. Phys.* **2009**, *30*, 1063.

[44] J. Gonzalez-Julian, S. Onrubia, M. Bram, O. Guillon, *J. Ceram. Soc. Jpn.* **2016**, *124*, 415.

[45] A. Eucken, *Fortchg. Gebiete Ingenieurw. B3 Forschungsheft.* **1932**, *16*, 353.

Summary of the presented articles

The papers presented in this section deal with elastic, acoustic and mechanical properties of robocast scaffolds. The paper [F] shows how the geometry of the scaffolds (given by the rod spacing and the mutual orientation of the rods in the neighboring layers) strongly affects the acoustic properties. Polar distributions of phase and group velocity of the tetragonal and orthorhombic scaffolds are shown in Figure 3.13, as determined by the PhD candidate from the macroscopic elastic coefficients.
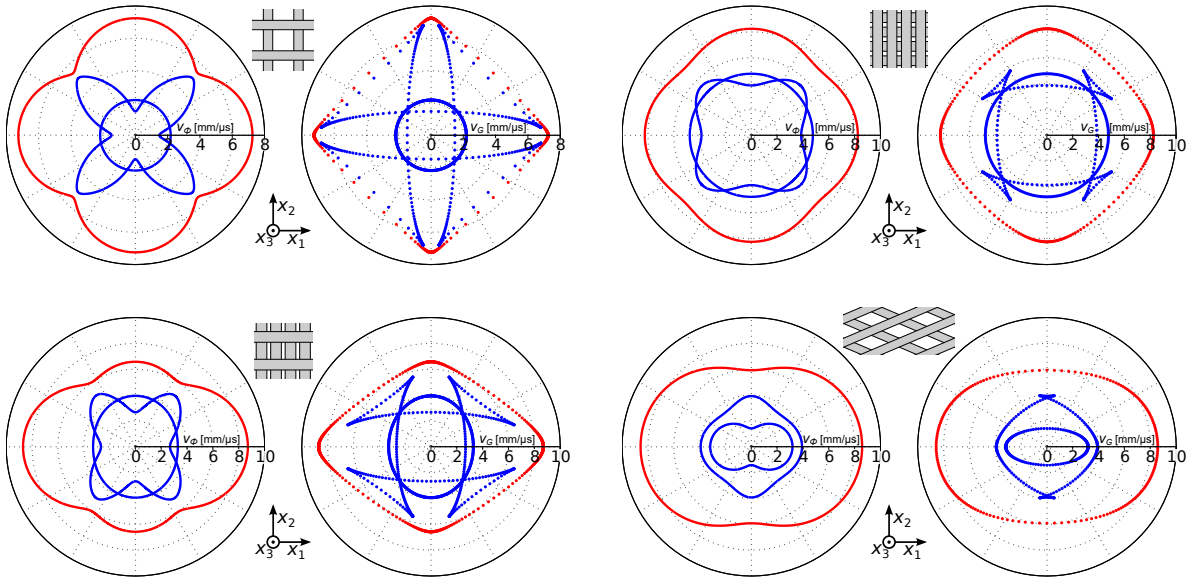
Figure 3.13: Plots of the phase velocity v_ϕ and the group velocity v_G in the x_1x_2 plane for the tetragonal and orthorhombic scaffolds [F]. The red outer curves represent quasi-longitudinal waves and the blue curves represent quasi-transverse waves.

For the scaffolds with a perpendicular orientation of the rods, the acoustic energy is predominantly focused along the direction of the rods, which is visualized by the density of the group velocity points in Figure 3.13. The level of the acoustic energy focusing is quite strong for the tetragonal scaffold with larger in-plane spacing, which is shown in the upper left part of Figure 3.13, and it is quite similar to the results from [172], shown in Figure 3.11, where the acoustic properties of another tetragonal scaffold with little different dimensions were studied both numerically and experimentally. Therefore, the paper [F] shows the consistency with [172], and it extends this study to the other types of scaffolds. In the tetragonal scaffold with much lower in-plane spacing of the rods, seen in the upper right part of Figure 3.13, the acoustic energy focusing is less pronounced due to the much more dense structure, which also leads to the overall higher values of the phase and group velocities. The orthorhombic scaffold with different in-plane spacing in the x_1 and x_2 direction, seen in the lower left part of Figure 3.13, follows the attributes of the acoustic wave propagation of the tetragonal scaffolds, i. e. the acoustic energy is focused here along the rods to some extent, and the higher velocity values correspond to the direction of the denser arrangement of the rods.

The acoustic properties of the second orthorhombic scaffold shown in the lower right part of Figure 3.13 are significantly different, as the acoustic energy is focused along the direction

of the symmetry axis x_1 but not in the direction of the symmetry axis x_2. Besides that, the hexagonal scaffolds were shown to be macroscopically isotropic under the assumption that the wavelength of the propagating waves is much higher than the in-plane spacing of the rods. The idea that the acoustic energy is focused along the direction of the ceramic rods also in the hexagonal scaffolds when the wavelength is sufficiently short and comparable to the periodicity of the scaffold structure was already mentioned in paper [F], but a more thorough study was performed later and published in paper [G].

The paper [G] studies the acoustic energy focusing in the hexagonal scaffolds in more detail both experimentally and theoretically. The measured resonant spectrum of the hexagonal scaffold is shown in Figure 3.14, along with several modal shapes of vibration. The resonant spectrum consists of sharp resonant peaks with a high quality factor $Q > 10^3$ for the majority of peaks (and thus internal friction Q^{-1} is below 10^{-3}), which indicates the good consolidation of the hexagonal scaffold. Moreover, the resonant frequencies well correspond to the frequencies calculated by the FEM analysis, confirming that the macroscopic elastic properties of this scaffold can be described by the homogenized elastic properties in the frequency range of the measured resonant spectrum, i. e. up to 1 MHz.
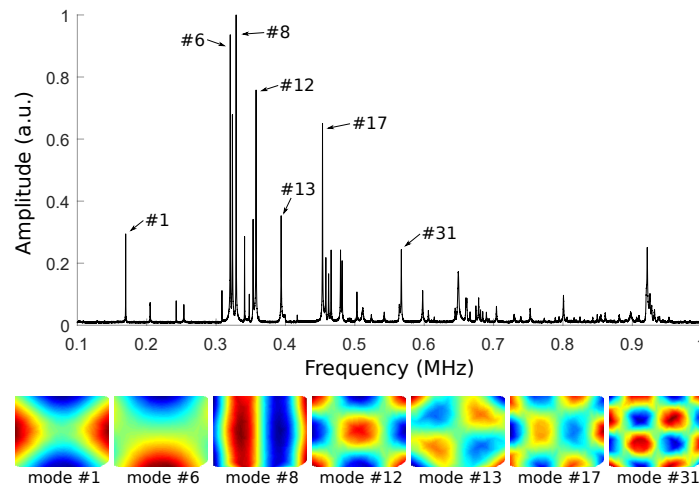
Figure 3.14: Measured resonant spectrum of the hexagonal scaffold with several modal shapes of vibrations [G].

The shear wave propagation in the principal direction of the scaffold (i. e. along the rods and then between the rods) was studied at 0.55 MHz and 1.4 MHz. At the lower frequency of 0.55 MHz, the shear waves propagate in the same way in both directions, with a rather planar wavefront. The tangent to the wavefront corresponds to the shear wave velocity calculated from the elastic coefficients determined by the FEM study. According to the dispersion curves, shown in Fig. 5 in paper [G], the shear wave propagation along the rods and between them should be indeed very similar at 0.55 MHz. On the other hand, there should be a quite different behavior at 1.4 MHz, which is close to the first shear wave frequency band gap. As seen in Figure 3.15, the character of the shear wave propagation differs in these principal directions at 1.4 MHz, where the planar wavefront is still observed for the propagating along the ceramic rods. For the direction of propagation between the rods, fully formed standing wave patterns

are formed, with the antinodes at the rod junctions and nodes between them, as highlighted in Figure 3.15b), and 3.15c). In other words, the paper [G] shows that the ultrasonic wave propagation is also directionally dependent for the hexagonal scaffolds when the wavelengths are comparable to rod spacing of the periodic scaffolds, i. e. at sufficiently high frequencies. At the frequency of 1.4 MHz, the shear wave can still propagate along the direction of the rods, while in the perpendicular direction, a standing wave is formed, which indicates a shear wave band gap.
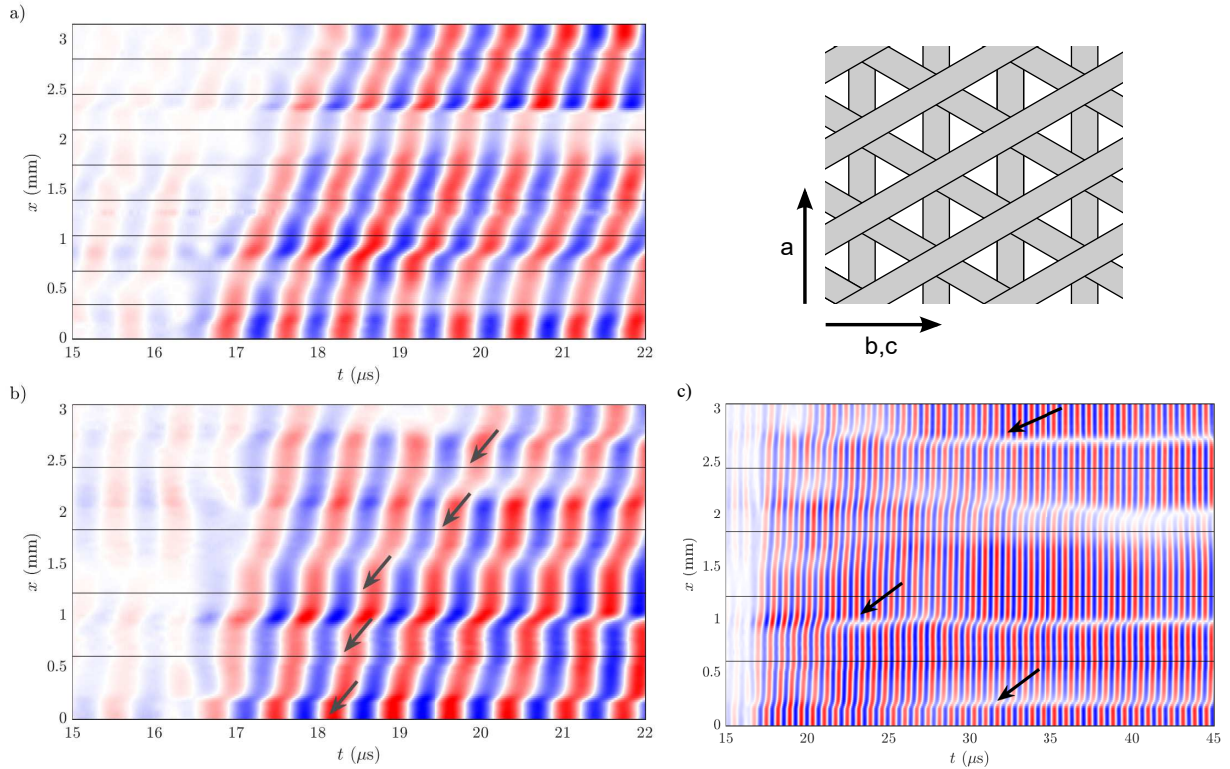
Figure 3.15: Time-domain signals of out-of-plane shear wave packets with frequency 1.4 MHz propagating in directions: a) along the rods, b) between the rods, and c) between the rods in a longer time scale. The black lines denote the positions of the rod junctions in the scaffold structure, and the black arrows highlight the forming standing waves [G]. The sketch in the upper right corner indicates the propagation directions that correspond to the respective subfigures.

The paper [H] summarized the work performed by the PhD candidate during his internship at the Institute of Ceramic and Glass (ICV-CSIC) in Madrid. Within this internship, the PhD candidate developed a printable ink based on Cr_2AlC MAX-phase powder and then printed the cylindrical and cuboid ceramic green bodies of robocast scaffolds. The scaffolds, which some of them are shown in Figure 3.16, were then sintered and characterized by the co-authors of the paper [H] from the ICV-CSIC.
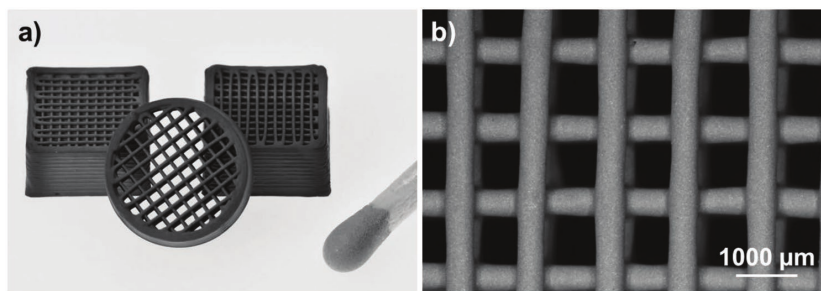
Figure 3.16: Cr$_2$AlC robocast scaffold produced by the PhD candidate: a) image of the cylindrical and cuboid printed green bodies, b) SEM micrograph of the sintered scaffold from the top view [H].

Chapter 4

Conclusions

This thesis deals with the ultrasound characterization of materials prepared by the spark plasma sintering (SPS) technique. The laser-based resonant ultrasound spectroscopy (RUS) has been utilized for studying the elastic properties of the several types of SPSed materials, and it has been complemented with the measurements of the ultrasound waves propagation.

Main outcomes of the thesis regarding the methodology of the utilized ultrasonic methods are

- the RUS method is suitable for characterization of SPSed materials, regardless of whether they are homogeneous materials, composites (both metal-matrix based and ceramic-matrix based) or architectured scaffolds,

- as the laser-based RUS is fully contactless, the studied sample can be put into a low-pressure chamber, where its elastic and anelastic properties are determined at well-defined conditions; this allows us to determine quite precisely the full set of elastic constants from a single spectrum of the studied sample,

- the structural changes and the relaxation processes within the materials are characterized by the laser-based RUS by determining the temperature evolutions of elastic moduli and internal friction,

- the analysis of the ultrasonic wave propagation discovers the direction-dependent and frequency-dependent acoustic properties of architectured materials.

Main conclusions regarding the mechanical properties of the SPSed materials are

- the SPS method does not induce any measurable elastic anisotropy when the powders to be sintered consisted of spherical or randomly-oriented particles,

- the incorporation of laminar graphene-based fillers to the ceramic matrix induces a macroscopic transverse isotropic symmetry due to the preferential orientation of the fillers,

- the elastic properties of the metal-matrix composites are given by the elasticity of the particular phases when they are fully sintered, but a rapid decrease of the elastic moduli indicates an increased porosity or unsintered particles,

- the high-temperature performance of the metal-matrix composites is influenced by the dislocation mobility, which allows ductile behavior but increases the damping,

140

- the robocast scaffolds with a perpendicular orientation of the rods in the neighboring layers are elastically anisotropic in the low-frequency limit, focusing the acoustic energy along the direction of the rods,

- the scaffolds with hexagonal symmetry are macroscopically in-plane isotropic in the low-frequency limit, but the acoustic energy is also focused along the rods near the frequency of the shear band gap.

In summary, this thesis has confirmed that the ultrasonic methods are capable of detecting a variety of material properties or internal processes without damaging the studied materials, either from the resonant spectra millimeter-sized samples or from the attributes of propagating ultrasonic waves. The aims of the thesis, specified in section 1.1, have thus been fulfilled.

This thesis has shown the applicability of the RUS method for characterizing of spark plasma sintered materials, and the PhD candidate will carry out further research in this topic. As the laser-based RUS has been proved as a versatile experimental method for determining the elastic properties of a wide range of materials, its prospective development primarily lies in further extending the accessible temperature range. A low-temperature RUS device, which uses liquid nitrogen as a coolant, has already been put in operation at the Institute of Thermomechanics, but another high-temperature chamber, which would use a more advanced heat source, would be beneficial for studying the elastic properties of materials at much higher temperatures.

References

[1] S.-X. SONG, Z. WANG, G.-P. SHI, Heating mechanism of spark plasma sintering, *Ceramics International* **39** (2) (2013) 1393–1396. `doi:10.1016/j.ceramint.2012.07.080`.

[2] U. ANSELMI-TAMBURINI, S. GENNARI, J. E. GARAY, Z. A. MUNIR, Fundamental investigations on the spark plasma sintering/synthesis process: II. Modeling of current and temperature distributions, *Materials Science and Engineering: A* **394** (1) (2005) 139–148. `doi:10.1016/j.msea.2004.11.019`.

[3] S. MUÑOZ, U. ANSELMI-TAMBURINI, Temperature and stress fields evolution during spark plasma sintering processes, *Journal of Materials Science* **45** (2010) 6528–6539. `doi:10.1007/s10853-010-4742-7`.

[4] J. WAN, R.-G. DUAN, A. K. MUKHERJEE, Spark plasma sintering of silicon nitride/silicon carbide nanocomposites with reduced additive amounts, *Scripta Materialia* **53** (6) (2005) 663–667. `doi:10.1016/j.scriptamat.2005.05.037`.

[5] L. GAO, H. Z. WANG, J. S. HONG, H. MIYAMOTO, K. MIYAMOTO, Y. NISHIKAWA, S. DÍAZ DE LA TORRE, Mechanical Properties and Microstructure of Nano-SiC–Al$_2$O$_3$ Composites Densified by Spark Plasma Sintering, *Journal of the European Ceramic Society* **19** (5) (1999) 609–613. `doi:10.1016/S0955-2219(98)00232-5`.

[6] Z. SHEN, M. JOHNSSON, Z. ZHAO, M. NYGREN, Spark Plasma Sintering of Alumina, *Journal of the American Ceramic Society* **85** (8) (2002) 1921–1927. `doi:10.1111/j.1151-2916.2002.tb00381.x`.

[7] R. CHAIM, Densification mechanisms in spark plasma sintering of nanocrystalline ceramics, *Materials Science and Engineering: A* **443** (1) (2007) 25–32. `doi:10.1016/j.msea.2006.07.092`.

[8] J. D. MAYNARD, The use of piezoelectric film and ultrasound resonance to determine the complete elastic tensor in one measurement, *The Journal of the Acoustical Society of America* **91** (3) (1992) 1754–1762. `doi:10.1121/1.402455`.

[9] A. MIGLIORI, J. L. SARRAO, W. M. VISSCHER, T. M. BELL, M. LEI, Z. FISK, R. G. LEISURE, Resonant ultrasound spectroscopic techniques for measurement of the elastic moduli of solids, *Physica B: Condensed Matter* **183** (1) (1993) 1–24. `doi:10.1016/0921-4526(93)90048-B`.

[10] A. MIGLIORI, J. L. SARRAO, *Resonant Ultrasound Spectroscopy*, John Wiley & Sons, 1997, 202 p.

[11] R. G. LEISURE, F. A. WILLIS, Resonant ultrasound spectroscopy, *Journal of Physics: Condensed Matter* **9** (28) (1997) 6001–6029. `doi:10.1088/0953-8984/9/28/002`.

[12] M. LANDA, H. SEINER, P. SEDLÁK, L. BICANOVÁ, J. ZÍDEK, L. HELLER, Resonant Ultrasound Spectroscopy Close to Its Applicability Limits, *Horizons in World Physics* **268** (2009) 97–136.

[13] P. SEDLÁK, H. SEINER, J. ZÍDEK, M. JANOVSKÁ, M. LANDA, Determination of All 21 Independent Elastic Coefficients of Generally Anisotropic Solids by Resonant Ultrasound Spectroscopy: Benchmark Examples, *Experimental Mechanics* **54** (2014) 1073–1085. `doi:10.1007/s11340-014-9862-6`.

[14] L. D. LANDAU, E. M. LIFSHITZ, *Theory of Elasticity*, 3rd Edition, Reed Educational and Professional Publishing Ltd., 1986, 187 p.

[15] J. D. ACHENBACH, *Wave Propagation in Elastic Solids*, North-Holland Series in Applied Mathematics and Mechanics, Elsevier, 1975, 425 p.

[16] D. ROYER, E. DIEULESAINT, *Elastic Waves in Solids I: Free and Guided Propagation*, Springer, 2000, 374 p.

[17] R. TRUELL, C. ELBAUM, B. B. CHICK, *Ultrasonic Methods in Solid State Physics*, Academic Press, 1969, 464 p.

[18] J. L. ROSE, *Ultrasonic Waves in Solid Media*, Cambridge University Press, 1999, 454 p.

[19] J. D. N. CHEEKE, *Fundamentals and Applications of Ultrasonic Waves*, CRC Press, 2002, 462 p.

[20] H. KOLSKY, *Stress waves in solids*, Dover Publications, 1963, 213 p.

[21] H. F. POLLARD, *Sound Waves in Solids*, Pion Limited, 1977, 366 p.

[22] A. S. NOWICK, B. S. BERRY, *Anelastic Relaxation in Crystalline Solids*, Academic Press, 1972, 677 p.

[23] A. B. BHATIA, *Ultrasonic Absorption: An Introduction to the Theory of Sound Absorption and Dispersion in Gases, Liquids and Solids*, Dover Publications, 1985, 427 p.

[24] R. SCHALLER, G. FANTOZZI, G. GREMAUD, Mechanical Spectroscopy Q^{-1} 2001: With Applications to Materials Science, Vol. **366–368** of Materials Science Forum, Trans Tech Publications Ltd., 2001, 683 p. `doi:10.4028/www.scientific.net/MSF.366-368`.

[25] A. CAZZANI, M. ROVATI, Extrema of Young's modulus for cubic and transversely isotropic solids, *International Journal of Solids and Structures* **40** (7) (2003) 1713–1744. `doi:10.1016/S0020-7683(02)00668-6`.

[26] R. F. S. HEARMON, *An Introduction to Applied Anisotropic Elasticity*, 1st Edition, Oxford University Press, 1961, 136 p.

[27] G. LI, J. R. GLADDEN, High Temperature Resonant Ultrasound Spectroscopy: A Review, *International Journal of Spectroscopy* (2010) 206362. `doi:10.1155/2010/206362`.

[28] A. REUSS, Berechnung der Fließgrenze von Mischkristallen auf Grund der Plastizitätsbedingung für Einkristalle, *Zeitschrift für Angewandte Mathematik und Mechanik* **9** (1) (1929) 49–58. `doi:10.1002/zamm.19290090104`.

[29] W. VOIGT, *Lehrbuch der Kristallphysik*, 1928, 978 p.

[30] M. LEVY, H. E. BASS, R. STERN (Eds.), Modern Acoustical Techniques for the Measurement of Mechanical Properties, Vol. 39 of *Experimental Methods in the Physical Sciences*, Academic Press, 2001, 436 p.

[31] R. G. LEISURE, K. FOSTER, J. E. HIGHTOWER, D. S. AGOSTA, Internal friction studies by resonant ultrasound spectroscopy, *Materials Science and Engineering: A* **370** (1) (2004) 34–40. `doi:10.1016/j.msea.2003.08.070`.

[32] J. L. SNOEK, Letter to the editor: Mechanical after effect and chemical constitution, *Physica* **6** (7) (1939) 591–592. `doi:10.1016/S0031-8914(39)90061-3`.

[33] J. L. SNOEK, Effect of small quantities of carbon and nitrogen on the elastic and plastic properties of iron, *Physica* **8** (7) (1941) 711–733. `doi:10.1016/S0031-8914(41)90517-7`.

[34] M. WELLER, The Snoek relaxation in bcc metals–From steel wire to meteorites, *Materials Science and Engineering: A* **442** (1) (2006) 21–30. `doi:10.1016/j.msea.2006.02.232`.

[35] C. ZENER, Internal friction in an alpha-brass crystal, *Trans. AIME* **152** (1943) 122–126.

[36] C. ZENER, Stress Induced Preferential Orientation of Pairs of Solute Atoms in Metallic Solid Solution, *Physical Review* **71** (1947) 34–38. `doi:10.1103/PhysRev.71.34`.

[37] M. HIRSCHER, U. BROSSMANN, R. HENES, Measurement of the Zener Relaxation in High-Purity FeCr Single Crystals, *Material Transactions* **41** (1) (2000) 82–86. `doi:10.2320/matertrans1989.41.82`.

[38] B. DAMSON, M. WELLER, M. FEUERBACHER, B. GRUSHKO, K. URBAN, Mechanical spectroscopy of quasicrystals, *Journal of Alloys and Compounds* **310** (1) (2000) 184–189. `doi:10.1016/S0925-8388(00)00944-0`.

[39] A. V. GRANATO, K. LÜCKE, *The Vibrating String Model of Dislocation Damping*, in: W. P. MASON (Ed.), Applications to Quantum and Solid State Physics, Part A, Vol. **4** of *Physical Acoustics*, Academic Press, 1966, pp. 225–276. `doi:10.1016/B978-0-12-395663-7.50017-0`.

[40] P. G. BORDONI, Elastic and Anelastic Behavior of Some Metals at very Low Temperatures, *The Journal of the Acoustical Society of America* **26** (4) (1954) 495–502. `doi:10.1121/1.1907363`.

[41] M. KOLLER, P. SEDLÁK, H. SEINER, M. ŠEVČÍK, M. LANDA, J. STRÁSKÁ, M. JANEČEK, An ultrasonic internal friction study of ultrafine-grained AZ31 magnesium alloy, *Journal of Materials Science* **50** (2015) 808–818. `doi:10.1007/s10853-014-8641-1`.

[42] D. B. FRASER, R. C. LECRAW, Novel Method of Measuring Elastic and Anelastic Properties of Solids, *Review of Scientific Instruments* **35** (9) (1964) 1113–1115. `doi:10.1063/1.1718976`.

[43] Y. SATO, T. USAMI, Basic Study on the Oscillation of Homogeneous Elastic Sphere – Part I: Frequency of the Free Oscillations, *Geophysics Magazine* **31** (1) (1962) 15–24.

[44] N. SOGA, O. L. ANDERSON, Elastic properties of tektites measured by resonant sphere technique, *Journal of Geophysical Research* **72** (6) (1967) 1733–1739. `doi:10.1029/JZ072i006p01733`.

[45] H. H. DEMAREST, Cube-Resonance Method to Determine the Elastic Constants of Solids, *The Journal of the Acoustical Society of America* **49** (3B) (1971) 768–775. `doi:10.1121/1.1912415`.

[46] I. OHNO, Free vibration of a rectangular parallelepiped crystal and its application to determination of elastic constants of orthorhombic crystals, *Journal of Physics of the Earth* **24** (4) (1976) 355–379. `doi:10.4294/jpe1952.24.355`.

[47] I. OHNO, S. YAMAMOTO, O. L. ANDERSON, J. NODA, Determination of elastic constants of trigonal crystals by the rectangular parallelepiped resonance method, *Journal of Physics and Chemistry of Solids* **47** (12) (1986) 1103–1108. `doi:10.1016/0022-3697(86)90141-1`.

[48] E. MOCHIZUKI, Application of group theory to free oscillations of an anisotropic rectangular parallelepiped, *Journal of Physics of the Earth* **35** (2) (1987) 159–170. `doi:10.4294/jpe1952.35.159`.

[49] E. MOCHIZUKI, Sphere-resonance method to determine elastic constants of crystal, *Journal of Applied Physics* **63** (12) (1988) 5668–5673. `doi:10.1063/1.340300`.

[50] I. OHNO, Rectangular parallellepiped resonance method for piezoelectric crystals and elastic constants of alpha-quartz, *Physics and Chemistry of Minerals* **17** (1990) 371–378. `doi:10.1007/BF00212204`.

[51] Y. SUMINO, I. OHNO, T. GOTO, M. KUMAZAWA, Measurement of elastic constants and internal frictions on single-crystal MgO by rectangular parallelepiped resonance, *Journal of Physics of the Earth* **24** (3) (1976) 263–273. `doi:10.4294/jpe1952.24.263`.

[52] Y. SUMINO, O. NISHIZAWA, T. GOTO, I. OHNO, M. OZIMA, Temperature variation of elastic constants of single-crystal forsterite between $-190°$ and $400°$C, *Journal of Physics of the Earth* **25** (4) (1977) 377–392. `doi:10.4294/jpe1952.25.377`.

[53] Y. SUMINO, O. L. ANDERSON, I. SUZUKI, Temperature coefficients of elastic constants of single crystal MgO between 80 and 1,300 K, *Physics and Chemistry of Minerals* **9** (1983) 38–47. `doi:10.1007/BF00309468`.

[54] I. SUZUKI, O. L. ANDERSON, Y. SUMINO, Elastic properties of a single-crystal forsterite Mg_2SiO_4, up to 1,200 K, *Physics and Chemistry of Minerals* **10** (1983) 38–46. `doi:10.1007/BF01204324`.

[55] T. GOTO, O. L. ANDERSON, Apparatus for measuring elastic constants of single crystals by a resonance technique up to 1825 K, *Review of Scientific Instruments* **59** (8) (1988) 1405–1408. `doi:10.1063/1.1139677`.

[56] T. GOTO, O. L. ANDERSON, I. OHNO, S. YAMAMOTO, Elastic constants of corundum up to 1825 K, *Journal of Geophysical Research: Solid Earth* **94** (B6) (1989) 7588–7602. `doi:10.1029/JB094iB06p07588`.

[57] D. G. ISAAK, O. L. ANDERSON, T. GOTO, I. SUZUKI, Elasticity of single-crystal forsterite measured to 1700 K, *Journal of Geophysical Research: Solid Earth* **94** (B5) (1989) 5895–5906. `doi:10.1029/JB094iB05p05895`.

[58] D. G. ISAAK, O. L. ANDERSON, T. GOTO, Measured elastic moduli of single-crystal MgO up to 1800 K, *Physics and Chemistry of Minerals* **16** (1989) 704–713. `doi:10.1007/BF00223321`.

[59] O. L. ANDERSON, Rectangular parallelepiped resonance–A technique of resonance ultrasound and its applications to the determination of elasticity at high temperatures, *The Journal of the Acoustical Society of America* **91** (4) (1992) 2245–2253. `doi:10.1121/1.403658`.

[60] J. R. GLADDEN, G. LI, R. ADEBISI, S. FIRDOSY, T. CAILLAT, V. RAVI, High-temperature elastic moduli of bulk nanostructured n- and p-type silicon germanium, *Physical Review B* **82** (2010) 045209. `doi:10.1103/PhysRevB.82.045209`.

[61] A. MIGLIORI, W. M. VISSCHER, S. E. BROWN, Z. FISK, S.-W. CHEONG, B. ALTEN, E. T. AHRENS, K. A. KUBAT-MARTIN, J. D. MAYNARD, Y. HUANG, D. R. KIRK, K. A. GILLIS, H. K. KIM, M. H. W. CHAN, Elastic constants and specific-heat measurements on single crystals of La_2CuO_4, *Physical Review B* **41** (4) (1990) 2098–2102. `doi:10.1103/PhysRevB.41.2098`.

[62] A. MIGLIORI, W. M. VISSCHER, S. WONG, S. E. BROWN, I. TANAKA, H. KOJIMA, P. B. ALLEN, Complete elastic constants and giant softening of c_{66} in superconducting $La_{1.86}Sr_{0.14}CuO_4$, *Physical Review Letters* **64** (1990) 2458–2461. `doi:10.1103/PhysRevLett.64.2458`.

[63] A. STEKEL, J. L. SARRAO, T. M. BELL, M. LEI, R. G. LEISURE, W. M. VISSCHER, A. MIGLIORI, Method for identification of the vibrational modes of a rectangular parallelepiped, *The Journal of the Acoustical Society of America* **92** (2) (1992) 663–668. `doi:10.1121/1.403991`.

[64] M. LEI, J. L. SARRAO, W. M. VISSCHER, T. M. BELL, J. D. THOMPSON, A. MIGLIORI, U. W. WELP, B. W. VEAL, Elastic constants of a monocrystal of superconducting $YBa_2Cu_3O_{7-\delta}$, *Physical Review B* **47** (1993) 6154–6156. `doi:10.1103/PhysRevB.47.6154`.

[65] J. L. SARRAO, S. R. CHEN, W. M. VISSCHER, M. LEI, U. F. KOCKS, A. MIGLIORI, Determination of the crystallographic orientation of a single crystal using resonant ultrasound spectroscopy, *Review of Scientific Instruments* **65** (6) (1994) 2139–2140. `doi:10.1063/1.1144712`.

145

[66] J. MAYNARD, Resonant Ultrasound Spectroscopy, *Physics Today* **49** (1) (1996) 26–31. `doi:10.1063/1.881483`.

[67] W. M. VISSCHER, A. MIGLIORI, T. M. BELL, R. A. REINERT, On the normal modes of free vibration of inhomogeneous and anisotropic elastic objects, *The Journal of the Acoustical Society of America* **90** (4) (1991) 2154–2162. `doi:10.1121/1.401643`.

[68] P. S. SPOOR, J. D. MAYNARD, A. R. KORTAN, Elastic Isotropy and Anisotropy in Quasicrystalline and Cubic AlCuLi, *Physical Review Letters* **75** (1995) 3462–3465. `doi:10.1103/PhysRevLett.75.3462`.

[69] V. KUOKKALA, R. B. SCHWARZ, The use of magnetostrictive film transducers in the measurement of elastic moduli and ultrasonic attenuation of solids, *Review of Scientific Instruments* **63** (5) (1992) 3136–3142. `doi:10.1063/1.1142566`.

[70] H. OGI, H. LEDBETTER, S. KIM, M. HIRAO, Contactless mode-selective resonance ultrasound spectroscopy: Electromagnetic acoustic resonance, *The Journal of the Acoustical Society of America* **106** (2) (1999) 660–665. `doi:10.1121/1.427607`.

[71] H. OGI, K. TAKASHIMA, H. LEDBETTER, M. L. DUNN, G. SHIMOIKE, M. HIRAO, P. BOWEN, Elastic constants and internal friction of an SiC-fiber-reinforced Ti-alloy-matrix crossply composite: measurement and theory, *Acta Materialia* **47** (9) (1999) 2787–2796. `doi:10.1016/S1359-6454(99)00124-X`.

[72] M. HIRAO, H. OGI, *EMATs for Science and Industry: Noncontacting Ultrasonic Measurements*, Kluwer Academic Publishers, 2003.

[73] S. SATO, K. INAGAKI, V. E. GUSEV, O. B. WRIGHT, Resonant ultrasound spectroscopy using optical excitation and detection, *AIP Conference Proceedings* **463** (1) (1999) 424–426. `doi:10.1063/1.58208`.

[74] H. GUO, A. LAL, Characterization of micromachined silicon nitride membrane using resonant ultrasound spectroscopy, *Proceedings of the 2001 IEEE Ultrasonics Symposium* **2** (2001) 863–866. `doi:10.1109/ULTSYM.2001.991857`.

[75] J. PLESEK, R. KOLMAN, M. LANDA, Using finite element method for the determination of elastic moduli by resonant ultrasound spectroscopy, *The Journal of the Acoustical Society of America* **116** (1) (2004) 282–287. `doi:10.1121/1.1760800`.

[76] M. C. REMILLIEUX, T. J. ULRICH, C. PAYAN, J. RIVIÈRE, C. R. LAKE, P.-Y. LE BAS, Resonant ultrasound spectroscopy for materials with high damping and samples of arbitrary geometry, *Journal of Geophysical Research: Solid Earth* **120** (7) (2015) 4898–4916. `doi:10.1002/2015JB011932`.

[77] H. OGI, K. SATO, T. ASADA, M. HIRAO, Complete mode identification for resonance ultrasound spectroscopy, *The Journal of the Acoustical Society of America* **112** (6) (2002) 2553–2557. `doi:10.1121/1.1512700`.

[78] H. OGI, N. NAKAMURA, K. SATO, M. HIRAO, S. UDA, Elastic, anelastic, and piezoelectric coefficients of langasite: resonance ultrasound spectroscopy with laser-Doppler interferometry, *IEEE Transactions on Ultrasonics, Ferroelectrics, and Frequency Control* **50** (5) (2003) 553–560. `doi:10.1109/tuffc.2003.1201468`.

[79] H. OGI, M. FUKUNAGA, M. HIRAO, H. LEDBETTER, Elastic constants, internal friction, and piezoelectric coefficient of $\alpha - \text{TeO}_2$, *Physical Review B* **69** (2004) 024104. `doi:10.1103/PhysRevB.69.024104`.

[80] N. NAKAMURA, H. OGI, M. HIRAO, Elastic constants of chemical-vapor-deposition diamond thin films: resonance ultrasound spectroscopy with laser-Doppler interferometry, *Acta Materialia* **52** (3) (2004) 765–771. `doi:10.1016/j.actamat.2003.10.012`.

[81] N. NAKAMURA, H. OGI, M. HIRAO, Resonance ultrasound spectroscopy with laser-Doppler interferometry for studying elastic properties of thin films, *Ultrasonics* **42** (1) (2004) 491–494. `doi:10.1016/j.ultras.2004.01.048`.

[82] H. OGI, N. NAKAMURA, M. HIRAO, Advanced resonant ultrasound spectroscopy for measuring anisotropic elastic constants of thin films, *Fatigue & Fracture of Engineering Materials & Structures* **28** (8) (2005) 657–663. `doi:10.1111/j.1460-2695.2005.00885.x`.

[83] M. LANDA, V. NOVÁK, P. SEDLÁK, L. MAÑOSA, P. ŠITTNER, Elastic Properties of Structural Phases in Shape Memory Alloys Investigated by Resonant Ultrasound Spectroscopy, *Materials Science Forum* **482** (2005) 351–354. `doi:10.4028/www.scientific.net/MSF.482.351`.

[84] H. SEINER, P. SEDLAK, M. LANDA, Improvement of the Inversion Procedure in Resonant Ultrasound Spectroscopy for Generally Oriented, High Anisotropic Crystals, *2006 IEEE Ultrasonics Symposium* (2006) 2433–2436. `doi:10.1109/ULTSYM.2006.607`.

[85] M. LANDA, P. SEDLÁK, P. ŠITTNER, H. SEINER, V. NOVÁK, Temperature dependence of elastic properties of cubic and orthorhombic phases in Cu–Al–Ni shape memory alloy near their stability limits, *Materials Science and Engineering: A* **462** (1) (2007) 320–324. `doi:10.1016/j.msea.2006.02.472`.

[86] M. LANDA, P. SEDLÁK, P. ŠITNNER, H. SEINER, L. HELLER, On the evaluation of temperature dependence of elastic constants of martensitic phases in shape memory alloys from resonant ultrasound spectroscopy studies, *Materials Science and Engineering: A* **481-482** (2008) 567–573. `doi:10.1016/j.msea.2006.12.224`.

[87] M. LANDA, P. SEDLÁK, H. SEINER, L. HELLER, L. BICANOVÁ, P. ŠITTNER, V. NOVÁK, Modal resonant ultrasound spectroscopy for ferroelastics, *Applied Physics A* **96** (2009) 557–567. `doi:10.1007/s00339-008-5047-4`.

[88] P. SEDLÁK, M. LANDA, H. SEINER, L. BODNÁROVÁ, Non-Contact Resonant Ultrasound Spectroscopy for Elastic Constants Measurement, *NDT.net Journal* 2008-10, 1st International Symposium on Laser Ultrasonics: Science, Technology and Applications (2008).

[89] H. SEINER, M. RŮŽEK, P. SEDLÁK, M. LANDA, Resonant Ultrasound Spectroscopy For Investigation Of Thin Surface Coatings, *WIT Transactions on Engineering Sciences* **64** (2009) 237–248. `doi:10.2495/MC090231`.

[90] M. LANDA, M. RŮŽEK, P. SEDLÁK, H. SEINER, L. BODNÁROVÁ, J. ZÍDEK, Novel approach to material evaluation of thin surface layers by resonant ultrasound spectroscopy, *Journal of Physics: Conference Series* **214** (2010) 012045. `doi:10.1088/1742-6596/214/1/012045`.

[91] M. RŮŽEK, P. SEDLÁK, H. SEINER, A. KRUISOVÁ, M. LANDA, Linearized forward and inverse problems of the resonant ultrasound spectroscopy for the evaluation of thin surface layers, *The Journal of the Acoustical Society of America* **128** (6) (2010) 3426–3437. `doi:10.1121/1.3500671`.

[92] P. SEDMÁK, H. SEINER, P. SEDLÁK, M. LANDA, R. MUŠÁLEK, J. MATĚJÍČEK, Application of resonant ultrasound spectroscopy to determine elastic constants of plasma-sprayed coatings with high internal friction, *Surface and Coatings Technology* **232** (2013) 747–757. `doi:10.1016/j.surfcoat.2013.06.091`.

[93] H. SEINER, J. CIZEK, P. SEDLÁK, R. HUANG, J. CUPERA, I. DLOUHY, M. LANDA, Elastic moduli and elastic anisotropy of cold sprayed metallic coatings, *Surface and Coatings Technology* **291** (2016) 342–347. `doi:10.1016/j.surfcoat.2016.02.057`.

[94] M. JANOVSKÁ, H. SEINER, J. ČÍŽEK, P. SEDLÁK, M. LANDA, Evolution of Elastic Propertiesof Cold Sprayed Metal Coatings at Elevated Temperatures, *Acta Physica Polonica A* **134** (3) (2018) 794–798. `doi:10.12693/APhysPolA.134.794`.

[95] S. HEUER, J. MATĚJÍČEK, M. VILÉMOVÁ, M. KOLLER, K. ILLKOVA, J. VEVERKA, T. WEBER, G. PINTSUK, J. W. COENEN, C. LINSMEIER, Atmospheric plasma spraying of functionally graded steel/tungsten layers for the first wall of future fusion reactors, *Surface and Coatings Technology* **366** (2019) 170–178. `doi:10.1016/j.surfcoat.2019.03.017`.

[96] M. KABLA, H. SEINER, M. MUSILOVA, M. LANDA, D. SHILO, The relationships between sputter deposition conditions, grain size, and phase transformation temperatures in NiTi thin films, *Acta Materialia* **70** (2014) 79–91. `doi:10.1016/j.actamat.2014.02.009`.

[97] M. THOMASOVÁ, P. SEDLÁK, H. SEINER, M. JANOVSKÁ, M. KABLA, D. SHILO, M. LANDA, Young's moduli of sputter-deposited NiTi films determined by resonant ultrasound spectroscopy: Austenite, R-phase, and martensite, *Scripta Materialia* **101** (2015) 24–27. `doi: 10.1016/j.scriptamat.2015.01.009`.

[98] M. THOMASOVÁ, H. SEINER, P. SEDLÁK, M. FROST, M. ŠEVČÍK, I. SZURMAN, R. KOCICH, J. DRAHOKOUPIL, P. ŠITTNER, M. LANDA, Evolution of macroscopic elastic moduli of martensitic polycrystalline NiTi and NiTiCu shape memory alloys with pseudoplastic straining, *Acta Materialia* **123** (2017) 146–156. `doi:10.1016/j.actamat.2016.10.024`.

[99] H. SEINER, L. BICANOVÁ, P. SEDLÁK, M. LANDA, L. HELLER, I. AALTIO, Magneto-elastic attenuation in austenitic phase of Ni–Mn–Ga alloy investigated by ultrasonic methods, *Materials Science and Engineering: A* **521**–**522** (2009) 205–208. `doi:10.1016/j.msea.2008.09.139`.

[100] O. HECZKO, H. SEINER, P. SEDLÁK, J. KOPEČEK, M. LANDA, Anomalous lattice softening of Ni_2MnGa austenite due to magnetoelastic coupling, *Journal of Applied Physics* **111** (7) (2012) 07A929. `doi:10.1063/1.3676412`.

[101] H. SEINER, P. SEDLÁK, L. BODNÁROVÁ, J. DRAHOKOUPIL, V. KOPECKÝ, J. KOPEČEK, M. LANDA, O. HECZKO, The effect of antiphase boundaries on the elastic properties of Ni–Mn–Ga austenite and premartensite, *Journal of Physics: Condensed Matter* **25** (42) (2013) 425402. `doi:10.1088/0953-8984/25/42/425402`.

[102] H. SEINER, O. HECZKO, P. SEDLÁK, L. BODNÁROVÁ, M. NOVOTNÝ, J. KOPEČEK, M. LANDA, Combined effect of structural softening and magneto-elastic coupling on elastic coefficients of Ni–Mn–Ga austenite, *Journal of Alloys and Compounds* **577** (2013) S131–S135. `doi:10.1016/j.jallcom.2012.01.007`.

[103] P. SEDLÁK, H. SEINER, L. BODNÁROVÁ, O. HECZKO, M. LANDA, Elastic constants of non-modulated Ni-Mn-Ga martensite, *Scripta Materialia* **136** (2017) 20–23. `doi:10.1016/j.scriptamat.2017.03.041`.

[104] H. SEINER, J. KOPEČEK, P. SEDLÁK, L. BODNÁROVÁ, M. LANDA, P. SEDMÁK, O. HECZKO, Microstructure, martensitic transformation and anomalies in c'-softening in Co–Ni–Al ferromagnetic shape memory alloys, *Acta Materialia* **61** (15) (2013) 5869–5876. `doi:10.1016/j.actamat.2013.06.035`.

[105] H. SEINER, L. BODNÁROVÁ, P. SEDLÁK, M. JANEČEK, O. SRBA, R. KRÁL, M. LANDA, Application of ultrasonic methods to determine elastic anisotropy of polycrystalline copper processed by equal-channel angular pressing, *Acta Materialia* **58** (1) (2010) 235–247. `doi: 10.1016/j.actamat.2009.08.071`.

[106] M. JANOVSKÁ, P. MINÁRIK, P. SEDLÁK, H. SEINER, M. KNAPEK, F. CHMELÍK, M. JANEČEK, M. LANDA, Elasticity and internal friction of magnesium alloys at room and elevated temperatures, *Journal of Materials Science* **53** (2018) 8545–8553. `doi:10.1007/s10853-018-2136-4`.

[107] H. SEINER, P. SEDLÁK, L. BODNÁROVÁ, A. KRUISOVÁ, M. LANDA, A. DE PABLOS, M. BELMONTE, Sensitivity of the resonant ultrasound spectroscopy to weak gradients of elastic properties, *The Journal of the Acoustical Society of America* **131** (5) (2012) 3775–3785. `doi: 10.1121/1.3695393`.

[108] M. JANOVSKÁ, P. SEDLÁK, H. SEINER, M. LANDA, P. MARTON, P. ONDREJKOVIČ, J. HLINKA, Anisotropic elasticity of DyScO$_3$ substrates, *Journal of Physics: Condensed Matter* **24** (38) (2012) 385404. `doi:10.1088/0953-8984/24/38/385404`.

[109] P. CTIBOR, H. SEINER, J. SEDLACEK, Z. PALA, P. VANEK, Phase stabilization in plasma sprayed BaTiO$_3$, *Ceramics International* **39** (5) (2013) 5039–5048. `doi:10.1016/j.ceramint.2012.11.102`.

[110] M. JANOVSKÁ, P. SEDLÁK, A. KRUISOVÁ, H. SEINER, M. LANDA, J. GRYM, Elastic constants of nanoporous III-V semiconductors, *Journal of Physics D: Applied Physics* **48** (24) (2015) 245102. `doi:10.1088/0022-3727/48/24/245102`.

[111] J. NEJEZCHLEBOVÁ, M. JANOVSKÁ, H. SEINER, P. SEDLÁK, M. LANDA, J. ŠMILAUEROVÁ, J. STRÁSKÝ, P. HARCUBA, M. JANEČEK, The effect of athermal and isothermal ω phase particles on elasticity of β-Ti single crystals, *Acta Materialia* **110** (2016) 185–191. `doi:10.1016/j.actamat.2016.03.033`.

[112] K. VÁCLAVOVÁ, J. STRÁSKÝ, V. POLYAKOVA, J. STRÁSKÁ, J. NEJEZCHLEBOVÁ, H. SEINER, I. SEMENOVA, M. JANEČEK, Microhardness and microstructure evolution of ultra-fine grained Ti-15Mo and TIMETAL LCB alloys prepared by high pressure torsion, *Materials Science and Engineering: A* **682** (2017) 220–228. `doi:10.1016/j.msea.2016.11.038`.

[113] J. NEJEZCHLEBOVÁ, H. SEINER, P. SEDLÁK, M. LANDA, J. ŠMILAUER0VÁ, E. AEBY-GAUTIER, B. DENAND, M. DEHMAS, B. APPOLIAR, On the complementarity between resistivity measurement and ultrasonic measurement for in-situ characterization of phase transitions in Ti-alloys, *Journal of Alloys and Compounds* **762** (2018) 868–872. `doi:10.1016/j.jallcom.2018.05.173`.

[114] J. NEJEZCHLEBOVÁ, M. JANOVSKÁ, P. SEDLÁK, J. ŠMILAUEROVÁ, J. STRÁSKÝ, M. JANEČEK, H. SEINER, Elastic constants of β-Ti15Mo, *Journal of Alloys and Compounds* **792** (2019) 960–967. `doi:10.1016/j.jallcom.2019.03.418`.

[115] S. J. REESE, K. L. TELSCHOW, T. M. LILLO, D. H. HURLEY, On the establishment of a method for characterization of material microstructure through laser-based resonant ultrasound spectroscopy, *IEEE Transactions on Ultrasonics, Ferroelectrics, and Frequency Control* **55** (4) (2008) 770–777. `doi:10.1109/TUFFC.2008.711`.

[116] D. H. HURLEY, S. J. REESE, S. K. PARK, Z. UTEGULOV, J. R. KENNEDY, K. L. TELSCHOW, In situ laser-based resonant ultrasound measurements of microstructure mediated mechanical property evolution, *Journal of Applied Physics* **107** (6) (2010) 063510. `doi: 10.1063/1.3327428`.

[117] S.-K. PARK, S.-H. BIAK, H.-K. CHA, S. J. REESE, D. H. HURLEY, Characteristics of Laser Resonant Ultrasonic Spectroscopy System for Measuring Elastic Constants of Materials, *Journal of the Korean Physical Society* **57** (2010) 375–379. `doi:10.3938/jkps.57.375`.

[118] F. FARZBOD, D. H. HURLEY, Using eigenmodes to perform the inverse problem associated with resonant ultrasound spectroscopy, *IEEE Transactions on Ultrasonics, Ferroelectrics, and Frequency Control* **59** (11) (2012) 2470–2475. `doi:10.1109/TUFFC.2012.2479`.

[119] D. H. HURLEY, S. J. REESE, F. FARZBOD, Application of laser-based resonant ultrasound spectroscopy to study texture in copper, *Journal of Applied Physics* **111** (5) (2012) 053527. `doi:10.1063/1.3692386`.

[120] S. BERNARD, Q. GRIMAL, P. LAUGIER, Resonant ultrasound spectroscopy for viscoelastic characterization of anisotropic attenuative solid materials, *The Journal of the Acoustical Society of America* **135** (5) (2014) 2601–2613. `doi:10.1121/1.4869084`.

[121] Q. ZHANG, F. FAN, R. WANG, H. NIU, P. LAUGIER, A resonant frequency retrieving method for low Q-factor materials based on resonant ultrasound spectroscopy, *Ultrasonics* **99** (2019) 105971. `doi:10.1016/j.ultras.2019.105971`.

[122] F. F. BALAKIREV, S. M. ENNACEUR, R. J. MIGLIORI, B. MAIOROV, A. MIGLIORI, Resonant ultrasound spectroscopy: The essential toolbox, *Review of Scientific Instruments* **90** (12) (2019) 121401. `doi:10.1063/1.5123165`.

[123] R. A. ADEBISI, T. J. LESTHAEGHE, M. R. CHERRY, S. SATHISH, P. A. SHADE, Development of a laser-based resonant ultrasound spectroscopy and a framework for error propagation in the estimated elastic moduli, *AIP Conference Proceedings* **1949** (1) (2018) 170002. `doi:10.1063/1.5031626`.

[124] C. M. DONAHUE, M. C. REMILLIEUX, G. SINGH, T. J. ULRICH, R. J. MIGLIORI, T. A. SALEH, Measuring the elastic tensor of a monolithic SiC hollow cylinder with resonant ultrasound spectroscopy, *NDT & E International* **101** (2019) 29–33. `doi:10.1016/j.ndteint.2018.09.012`.

[125] D. A. HUTCHINS, *Ultrasonic Generation by Pulsed Lasers*, Vol. **18** of Physical Acoustics, Academic Press, 1988, pp. 21–123. `doi:10.1016/B978-0-12-477918-1.50008-4`.

[126] D. ROYER, E. DIEULESAINT, *Elastic Waves in Solids II: Generation, Acousto-optic Interaction, Applications*, Springer, 2000, 446 p.

[127] J. RÄTHEL, M. HERRMANN, W. BECKERT, Temperature distribution for electrically conductive and non-conductive materials during Field Assisted Sintering (FAST), *Journal of the European Ceramic Society* **29** (8) (2009) 1419–1425. `doi:10.1016/j.jeurceramsoc.2008.09.015`.

[128] O. GUILLON, J. GONZALEZ-JULIAN, B. DARGATZ, T. KESSEL, G. SCHIERNING, J. RÄTHEL, M. HERRMANN, Field-Assisted Sintering Technology/Spark Plasma Sintering: Mechanisms, Materials, and Technology Developments, *Advanced Engineering Materials* **16** (7) (2014) 830–849. `doi:10.1002/adem.201300409`.

[129] J. TRAPP, B. KIEBACK, Fundamental principles of spark plasma sintering of metals: part I – Joule heating controlled by the evolution of powder resistivity and local current densities, *Powder Metallurgy* **62** (5) (2019) 297–306. `doi:10.1080/00325899.2019.1653532`.

[130] X. SONG, X. LIU, J. ZHANG, Neck Formation and Self-Adjusting Mechanism of Neck Growth of Conducting Powders in Spark Plasma Sintering, *Journal of the American Ceramic Society* **89** (2) (2006) 494–500. `doi:10.1111/j.1551-2916.2005.00777.x`.

[131] R. MARDER, C. ESTOURNÈS, G. CHEVALLIER, R. CHAIM, Plasma in spark plasma sintering of ceramic particle compacts, *Scripta Materialia* **82** (2014) 57–60. `doi:10.1016/j.scriptamat.2014.03.023`.

[132] N. CHAWAKE, L. D. PINTO, A. K. SRIVASTAV, K. AKKIRAJU, B. S. MURTY, R. S. KOTTADA, On Joule heating during spark plasma sintering of metal powders, *Scripta Materialia* **93** (2014) 52–55. `doi:10.1016/j.scriptamat.2014.09.003`.

[133] L. ZHANG, X. ZHANG, Z. CHU, S. PENG, Z. YAN, Y. LIANG, Effect of heat wave at the initial stage in spark plasma sintering, *SpringerPlus* **5** (2016) 838. `doi:10.1186/s40064-016-2344-9`.

[134] C. COLLARD, Z. TRZASKA, L. DURAND, J.-M. CHAIX, J.-P. MONCHOUX, Theoretical and experimental investigations of local overheating at particle contacts in spark plasma sintering, *Powder Technology* **321** (2017) 458–470. `doi:10.1016/j.powtec.2017.08.033`.

[135] C. MUSA, R. LICHERI, A. M. LOCCI, R. ORRÙ, G. CAO, M. A. RODRIGUEZ, L. JAWORSKA, Energy efficiency during conventional and novel sintering processes: the case of Ti–Al$_2$O$_3$–TiC composites, *Journal of Cleaner Production* **17** (9) (2009) 877–882. `doi:10.1016/j.jclepro.2009.01.012`.

[136] D. CHAKRAVARTY, A. H. CHOKSHI, Direct Characterizing of Densification Mechanisms during Spark Plasma Sintering, *Journal of the American Ceramic Society* **97** (3) (2014) 765–771. `doi:10.1111/jace.12796`.

[137] D. S. PERERA, M. TOKITA, S. MORICCA, Comparative Study of Fabrication of Si$_3$N$_4$/SiC Composites by Spark Plasma Sintering and Hot Isostatic Pressing, *Journal of the European Ceramic Society* **18** (4) (1998) 401–404. `doi:10.1016/S0955-2219(97)00139-8`.

[138] W. YUCHENG, F. ZHENGYI, Study of temperature field in spark plasma sintering, *Materials Science and Engineering: B* **90** (1) (2002) 34–37. `doi:10.1016/S0921-5107(01)00780-2`.

[139] D. TIWARI, B. BASU, K. BISWAS, Simulation of thermal and electric field evolution during spark plasma sintering, *Ceramics International* **35** (2) (2009) 699–708. `doi:10.1016/j.ceramint.2008.02.013`.

[140] M. SUÁREZ, A. FERNÁNDEZ, J. MENÉNDEZ, R. TORRECILLAS, H. U. KESSEL, J. HENNICKE, R. KIRCHNER, T. KESSEL, Challenges and Opportunities for Spark Plasma Sintering: A Key Technology for a New Generation of Materials, in: *Sintering Applications*, IntechOpen, 2013, Chapter 13, pp. 319–342. `doi:10.5772/53706`.

[141] Z. A. MUNIR, U. ANSELMI-TAMBURINI, M. OHYANAGI, The effect of electric field and pressure on the synthesis and consolidation of materials: A review of the spark plasma sintering method, *Journal of Materials Science* **41** (2006) 763–777. `doi:10.1007/s10853-006-6555-2`.

[142] S. R. BAKSHI, V. MUSARAMTHOTA, D. LAHIRI, V. SINGH, S. SEAL, A. AGARWAL, Spark plasma sintered tantalum carbide: Effect of pressure and nano-boron carbide addition on microstructure and mechanical properties, *Materials Science and Engineering: A* **528** (3) (2011) 1287–1295. `doi:10.1016/j.msea.2010.10.009`.

[143] K. VANMEENSEL, A. LAPTEV, S. G. HUANG, J. VLEUGELS, O. VAN DER BIEST, The Role of the Electric Current and Field during Pulsed Electric Current Sintering, in: *Ceramics and Composites Processing Methods*, John Wiley & Sons, Ltd, 2012, Chapter 2, pp. 43–73. `doi:10.1002/9781118176665.ch2`.

[144] R. CHAIM, G. CHEVALLIER, A. WEIBEL, C. ESTOURNÈS, Grain growth during spark plasma and flash sintering of ceramic nanoparticles: a review, *Journal of Materials Science* **53** (2018) 3087–3105. `doi:10.1007/s10853-017-1761-7`.

[145] R. MARDER, C. ESTOURNÈS, G. CHEVALLIER, R. CHAIM, Spark and plasma in spark plasma sintering of rigid ceramic nanoparticles: A model system of YAG, *Journal of the European Ceramic Society* **35** (1) (2015) 211–218. `doi:10.1016/j.jeurceramsoc.2014.08.001`.

[146] Z.-H. ZHANG, Z.-F. LIU, J.-F. LU, X.-B. SHEN, F.-C. WANG, Y.-D. WANG, The sintering mechanism in spark plasma sintering – Proof of the occurrence of spark discharge, *Scripta Materialia* **81** (2014) 56–59. `doi:10.1016/j.scriptamat.2014.03.011`.

[147] V. VISWANATHAN, T. LAHA, K. BALANI, A. AGARWAL, S. SEAL, Challenges and advances in nanocomposite processing techniques, *Materials Science and Engineering: R: Reports* **54** (5) (2006) 121–285. `doi:10.1016/j.mser.2006.11.002`.

[148] S. DIOUF, A. MOLINARI, Densification mechanisms in spark plasma sintering: Effect of particle size and pressure, *Powder Technology* **221** (2012) 220–227. `doi:10.1016/j.powtec.2012.01.005`.

[149] T. SAUNDERS, S. GRASSO, M. J. REECE, Plasma formation during electric discharge (50V) through conductive powder compacts, *Journal of the European Ceramic Society* **35** (3) (2015) 871–877. `doi:10.1016/j.jeurceramsoc.2014.09.022`.

[150] R. LI, Q. LIU, L. TIAN, Y. W. K. A. KHOR, D. ZHANG, Z. DONG, Discharge and densification in the spark plasma sintering of quasicrystal particles, *Journal of Materials Science* **54** (2019) 8727–8742. `doi:10.1007/s10853-019-03489-6`.

[151] D. M. HULBERT, A. ANDERS, J. ANDERSSON, E. J. LAVERNIA, A. K. MUKHERJEE, A discussion on the absence of plasma in spark plasma sintering, *Scripta Materialia* **60** (10) (2009) 835–838. `doi:10.1016/j.scriptamat.2008.12.059`.

[152] D. M. HULBERT, D. JIANG, D. V. DUDINA, A. K. MUKHERJEE, The synthesis and consolidation of hard materials by spark plasma sintering, *International Journal of Refractory Metals and Hard Materials* **27** (2) (2009) 367–375. `doi:10.1016/j.ijrmhm.2008.09.011`.

[153] M. BELMONTE, J. GONZÁLEZ-JULIÁN, P. MIRANZO, M. I. OSENDI, Spark plasma sintering: A powerful tool to develop new silicon nitride-based materials, *Journal of the European Ceramic Society* **30** (14) (2010) 2937–2946. `doi:10.1016/j.jeurceramsoc.2010.01.025`.

[154] L. GAO, Z. SHEN, H. MIYAMOTO, M. NYGREN, Superfast Densification of Oxide/Oxide Ceramic Composites, *Journal of the American Ceramic Society* **82** (4) (1999) 1061–1063. `doi:10.1111/j.1151-2916.1999.tb01874.x`.

[155] M. NYGREN, Z. SHEN, On the preparation of bio-, nano- and structural ceramics and composites by spark plasma sintering, *Solid State Sciences* **5** (1) (2003) 125–131. `doi:10.1016/S1293-2558(02)00086-9`.

[156] S.-Q. GUO, T. NISHIMURA, Y. KAGAWA, J.-M. YANG, Spark Plasma Sintering of Zirconium Diborides, *Journal of the American Ceramic Society* **91** (9) (2008) 2848–2855. `doi:10.1111/j.1551-2916.2008.02587.x`.

[157] J. GURT SANTANACH, A. WEIBEL, C. ESTOURNÈS, Q. YANG, C. LAURENT, A. PEIGNEY, Spark plasma sintering of alumina: Study of parameters, formal sintering analysis and hypotheses on the mechanism(s) involved in densification and grain growth, *Acta Materialia* **59** (4) (2011) 1400–1408. `doi:10.1016/j.actamat.2010.11.002`.

[158] R. CHAIM, Superfast densification of nanocrystalline oxide powders by spark plasma sintering, *Journal of Materials Science* **41** (2006) 7862–7871. `doi:10.1007/s10853-006-0605-7`.

[159] M. BELMONTE, M. I. OSENDI, P. MIRANZO, Modeling the effect of pulsing on the spark plasma sintering of silicon nitride materials, *Scripta Materialia* **65** (3) (2011) 273–276. `doi: 10.1016/j.scriptamat.2011.04.029.`

[160] R. ORRÙ, R. LICHERI, A. M. LOCCI, A. CINCOTTI, G. CAO, Consolidation/synthesis of materials by electric current activated/assisted sintering, *Materials Science and Engineering: R: Reports* **63** (4) (2009) 127–287. `doi:10.1016/j.mser.2008.09.003.`

[161] J. E. SMAY, G. M. GRATSON, R. F. SHEPHERD, J. CESARANO III, J. A. LEWIS, Directed Colloidal Assembly of 3D Periodic Structures, *Advanced Materials* **14** (18) (2002) 1279–1283. `doi:10.1002/1521-4095(20020916)14:18<1279::AID-ADMA1279>3.0.CO;2-A.`

[162] J. A. LEWIS, Direct Ink Writing of 3D Functional Materials, *Advanced Materials Technologies* **16** (17) (2006) 2193–2204. `doi:10.1002/adfm.200600434.`

[163] B. ROMÁN MANSO, *Architectured cellular and bulk ceramic materials based on SiC and graphene/SiC with enhanced transport properties*, Ph.D. thesis, Universidad Autónoma de Madrid (2015).

[164] K. CAI, B. ROMÁN-MANSO, J. E. SMAY, J. ZHOU, M. I. OSENDI, M. BELMONTE, P. MIRANZO, Geometrically Complex Silicon Carbide Structures Fabricated by Robocasting, *Journal of the American Ceramic Society* **95** (8) (2012) 2660–2666. `doi:10.1111/j.1551-2916.2012.05276.x.`

[165] B. ROMÁN-MANSO, Á. DE PABLOS, M. BELMONTE, M. I. OSENDI, P. MIRANZO, Microstructural designs of spark-plasma sintered siliconcarbide ceramic scaffolds, *Boletín de la Sociedad Española de Cerámica y Vidrio* **53** (2) (2014) 93–100. `doi:10.3989/cyv.132014.`

[166] B. ROMAN-MANSO, S. M. VEGA-DÍAZ, A. MORELOS-GÓMEZ, M. TERRONES, P. MIRANZO, M. BELMONTE, Aligned carbon nanotube/silicon carbide hybrid materials with high electrical conductivity, superhydrophobicity and superoleophilicity, *Carbon* **80** (2014) 120–126. `doi:10.1016/j.carbon.2014.08.046.`

[167] C. R. TUBÍO, J. AZUAJE, L. ESCALANTE, A. COELHO, F. GUITIÁN, E. SOTELO, A. GIL, 3D printing of a heterogeneous copper-based catalyst, *Journal of Catalysis* **334** (2016) 110–115. `doi:10.1016/j.jcat.2015.11.019.`

[168] A. QUINTANILLA, J. A. CASAS, P. MIRANZO, M. I. OSENDI, M. BELMONTE, 3D-Printed Fe-doped silicon carbide monolithic catalysts for wet peroxide oxidation processes, *Applied Catalysis B: Environmental* **235** (2018) 246–255. `doi:10.1016/j.apcatb.2018.04.066.`

[169] P. MIRANDA, E. SAIZ, K. GRYN, A. P. TOMSIA, Sintering and robocasting of β-tricalcium phosphate scaffolds for orthopaedic applications, *Acta Biomaterialia* **2** (4) (2006) 457–466. `doi: 10.1016/j.actbio.2006.02.004.`

[170] P. MIRANDA, A. PAJARES, E. SAIZ, A. P. TOMSIA, F. GUIBERTEAU, Fracture modes under uniaxial compression in hydroxyapatite scaffolds fabricated by robocasting, *Journal of Biomedical Materials Research Part A* **83** (3) (2007) 646–655. `doi:10.1002/jbm.a.31272.`

[171] M. HOUMARD, Q. FU, E. SAIZ, A. P. TOMSIA, Sol–gel method to fabricate CaP scaffolds by robocasting for tissue engineering, *Journal of Materials Science: Materials in Medicine* **23** (2012) 921–930. `doi:10.1007/s10856-012-4561-2.`

[172] A. KRUISOVÁ, H. SEINER, P. SEDLÁK, M. LANDA, B. ROMÁN-MANSO, P. MIRANZO, M. BELMONTE, Acoustic metamaterial behavior of three-dimensional periodic architectures assembled by robocasting, *Applied Physics Letters* **105** (21) (2014) 211904. `doi:10.1063/1.4902810.`

[173] A. KRUISOVÁ, H. SEINER, P. SEDLÁK, M. LANDA, B. ROMÁN-MANSO, P. MIRANZO, M. BELMONTE, Finite Elements Modeling of Mechanical and Acoustic Properties of a Ceramic Metamaterial Assembled by Robocasting, *Applied Mechanics and Materials* **821** (2016) 364–371. `doi:10.4028/www.scientific.net/AMM.821.364`.

[174] A. KRUISOVÁ, M. ŠEVČÍK, H. SEINER, P. SEDLÁK, B. ROMÁN-MANSO, P. MIRANZO, M. BELMONTE, M. LANDA, Ultrasonic bandgaps in 3D-printed periodic ceramic microlattices, *Ultrasonics* **82** (2018) 91–100. `doi:10.1016/j.ultras.2017.07.017`.

[175] A. K. GEIM, K. S. NOVOSELOV, The rise of graphene, *Nature Materials* **6** (2007) 183–191. `doi:10.1038/nmat1849`.

[176] C. SOLDANO, A. MAHMOOD, E. DUJARDIN, Production, properties and potential of graphene, *Carbon* **48** (8) (2010) 2127–2150. `doi:10.1016/j.carbon.2010.01.058`.

[177] Y. ZHU, S. MURALI, W. CAI, X. LI, J. W. SUK, J. R. POTTS, R. S. RUOFF, Graphene and Graphene Oxide: Synthesis, Properties, and Applications, *Advanced Materials* **22** (35) (2010) 3906–3924. `doi:10.1002/adma.201001068`.

[178] V. SINGH, D. JOUNG, L. ZHAI, S. DAS, S. I. KHONDAKER, S. SEAL, Graphene based materials: Past, present and future, *Progress in Materials Science* **56** (8) (2011) 1178–1271. `doi:10.1016/j.pmatsci.2011.03.003`.

[179] T. KUILA, S. BOSE, A. K. MISHRA, P. KHANRA, N. H. KIM, J. H. LEE, Chemical functionalization of graphene and its applications, *Progress in Materials Science* **57** (7) (2012) 1061–1105. `doi:10.1016/j.pmatsci.2012.03.002`.

[180] H. PORWAL, S. GRASSO, M. J. REECE, Review of graphene–ceramic matrix composites, *Advances in Applied Ceramics* **112** (8) (2013) 443–454. `doi:10.1179/174367613X13764308970581`.

[181] K. WANG, Y. WANG, Z. FAN, J. YAN, T. WEI, Preparation of graphene nanosheet/alumina composites by spark plasma sintering, *Materials Research Bulletin* **46** (2) (2011) 315–318. `doi:10.1016/j.materresbull.2010.11.005`.

[182] C. RAMIREZ, L. GARZÓN, P. MIRANZO, M. I. OSENDI, C. OCAL, Electrical conductivity maps in graphene nanoplatelet/silicon nitride composites using conducting scanning force microscopy, *Carbon* **49** (12) (2011) 3873–3880. `doi:10.1016/j.carbon.2011.05.025`.

[183] C. RAMIREZ, F. M. FIGUEIREDO, P. MIRANZO, P. POZA, M. I. OSENDI, Graphene nanoplatelet/silicon nitride composites with high electrical conductivity, *Carbon* **50** (10) (2012) 3607–3615. `doi:10.1016/j.carbon.2012.03.031`.

[184] C. RAMÍREZ, S. M. VEGA-DIAZ, A. MORELÓS-GÓMEZ, F. M. FIGUEIREDO, M. TERRONES, M. I. OSENDI, M. BELMONTE, P. MIRANZO, Synthesis of conducting graphene/Si_3N_4 composites by spark plasma sintering, *Carbon* **57** (2013) 425–432. `doi:10.1016/j.carbon.2013.02.015`.

[185] A. CENTENO, V. G. ROCHA, B. ALONSO, A. FERNÁNDEZ, C. F. GUTIERREZ-GONZALEZ, R. TORRECILLAS, A. ZURUTUZA, Graphene for tough and electroconductive alumina ceramics, *Journal of the European Ceramic Society* **33** (15) (2013) 3201–3210. `doi:10.1016/j.jeurceramsoc.2013.07.007`.

[186] O. HANZEL, R. SEDLÁK, J. SEDLÁČEK, V. BIZOVSKÁ, R. BYSTRICKÝ, V. GIRMAN, A. KOVALČÍKOVÁ, J. DUSZA, P. ŠAJGALÍK, Anisotropy of functional properties of SiC composites with GNPs, GO and in-situ formed graphene, *Journal of the European Ceramic Society* **37** (12) (2017) 3731–3739. `doi:10.1016/j.jeurceramsoc.2017.03.060`.

[187] L. S. WALKER, V. R. MAROTTO, M. A. RAFIEE, N. KORATKAR, E. L. CORRAL, Toughening in Graphene Ceramic Composites, *ACS Nano* **5** (4) (2011) 3182–3190. `doi: 10.1021/nn200319d.`

[188] J. DUSZA, J. MORGIEL, A. DUSZOVÁ, L. KVETKOVÁ, M. NOSKO, P. KUN, C. BALÁZSI, Microstructure and fracture toughness of Si_3N_4+graphene platelet composites, *Journal of the European Ceramic Society* **32** (12) (2012) 3389–3397. `doi:10.1016/j.jeurceramsoc.2012.04. 022.`

[189] L. KVETKOVÁ, A. DUSZOVÁ, P. HVIZDOŠ, J. DUSZA, P. KUN, C. BALÁZSI, Fracture toughness and toughening mechanisms in graphene platelet reinforced Si_3N_4 composites, *Scripta Materialia* **66** (10) (2012) 793–796. `doi:10.1016/j.scriptamat.2012.02.009.`

[190] J. LIU, H. YAN, M. J. REECE, K. JIANG, Toughening of zirconia/alumina composites by the addition of graphene platelets, *Journal of the European Ceramic Society* **32** (16) (2012) 4185–4193. `doi:10.1016/j.jeurceramsoc.2012.07.007.`

[191] L. KVETKOVÁ, A. DUSZOVÁ, M. KAŠIAROVÁ, F. DORČÁKOVÁ, J. DUSZA, BALÁZSI, Influence of processing on fracture toughness of Si_3N_4 + graphene platelet composites, *Journal of the European Ceramic Society* **33** (12) (2013) 2299–2304. `doi:10.1016/j.jeurceramsoc. 2013.01.025.`

[192] A. NIETO, D. LAHIRI, A. AGARWAL, Graphene NanoPlatelets reinforced tantalum carbide consolidated by spark plasma sintering, *Materials Science and Engineering: A* **582** (2013) 338–346. `doi:10.1016/j.msea.2013.06.006.`

[193] G. B. YADHUKULAKRISHNAN, S. KARUMURI, A. RAHMAN, R. P. SINGH, A. KAAN KALKAN, S. P. HARIMKAR, Spark plasma sintering of graphene reinforced zirconium diboride ultra-high temperature ceramic composites, *Ceramics International* **39** (6) (2013) 6637–6646. `doi:10.1016/j.ceramint.2013.01.101.`

[194] H. PORWAL, P. TATARKO, R. SAGGAR, S. GRASSO, M. KUMAR MANI, I. DLOUHÝ, J. DUSZA, M. J. REECE, Tribological properties of silica–graphene nano-platelet composites, *Ceramics International* **40** (8) (2014) 12067–12074. `doi:10.1016/j.ceramint.2014.04.046.`

[195] C. RAMIREZ, M. I. OSENDI, Toughening in ceramics containing graphene fillers, *Ceramics International* **40** (7) (2014) 11187–11192. `doi:10.1016/j.ceramint.2014.03.150.`

[196] C. RAMIREZ, P. MIRANZO, M. BELMONTE, M. I. OSENDI, P. POZA, S. M. VEGA-DIAZ, M. TERRONES, Extraordinary toughening enhancement and flexural strength in Si_3N_4 composites using graphene sheets, *Journal of the European Ceramic Society* **34** (2) (2014) 161–169. `doi:10.1016/j.jeurceramsoc.2013.08.039.`

[197] P. KUN, O. TAPASZTÓ, F. WÉBER, C. BALÁZSI, Determination of structural and mechanical properties of multilayer graphene added silicon nitride-based composites, *Ceramics International* **38** (1) (2012) 211–216. `doi:10.1016/j.ceramint.2011.06.051.`

[198] Y. FAN, M. ESTILI, G. IGARASHI, W. JIANG, A. KAWASAKI, The effect of homogeneously dispersed few-layer graphene on microstructure and mechanical properties of Al_2O_3 nanocomposites, *Journal of the European Ceramic Society* **34** (2) (2014) 443–451. `doi:10.1016/j.jeurceramsoc.2013.08.035.`

[199] H. SEINER, P. SEDLÁK, M. KOLLER, M. LANDA, C. RAMÍREZ, M. I. OSENDI, M. BELMONTE, Anisotropic elastic moduli and internal friction of graphene nanoplatelets/silicon nitride composites, *Composites Science and Technology* **75** (2013) 93–97. `doi:10.1016/j.compscitech.2012.12.003.`

[200] C. MAUGE, M. KACHANOV, Effective elastic properties of an anisotropic material with arbitrarily oriented interacting cracks, *Journal of the Mechanics and Physics of Solids* **42** (4) (1994) 561–584. `doi:10.1016/0022-5096(94)90052-3`.

[201] M. KACHANOV, On the concept of approximate elastic symmetry and its application to materials with defects, *International Journal of Fracture* **74** (1996) R33–R38. `doi:10.1007/BF00036268`.

[202] M. KACHANOV, Solids with cracks and non-spherical pores: proper parameters of defect density and effective elastic properties, *International Journal of Fracture* **97** (1999) 1–32. `doi:10.1023/A:1018345702490`.

[203] I. SEVOSTIANOV, M. KACHANOV, On approximate symmetries of the elastic properties and elliptic orthotropy, *International Journal of Engineering Science* **46** (3) (2008) 211–223. `doi:10.1016/j.ijengsci.2007.11.003`.

[204] A. NIETO, A. BISHT, D. LAHIRI, C. ZHANG, A. AGARWAL, Graphene reinforced metal and ceramic matrix composites: a review, *International Materials Reviews* **62** (5) (2017) 241–302. `doi:10.1080/09506608.2016.1219481`.

[205] P. MIRANZO, M. BELMONTE, M. I. OSENDI, From bulk to cellular structures: A review on ceramic/graphene filler composites, *Journal of the European Ceramic Society* **37** (12) (2017) 3649–3672. `doi:10.1016/j.jeurceramsoc.2017.03.016`.

[206] B.-Y. ZHOU, S.-J. FAN, Y.-C. FAN, Q. ZHENG, X. ZHANG, W. JIANG, L.-J. WANG, Recent progress in ceramic matrix composites reinforced with graphene nanoplatelets, *Rare Metals* **39** (2020) 513–528. `doi:10.1007/s12598-019-01306-2`.

[207] H. PORWAL, R. SAGGAR, P. TATARKO, S. GRASSO, T. SAUNDERS, I. DLOUHÝ, M. J. REECE, Effect of lateral size of graphene nano-sheets on the mechanical properties and machinability of alumina nano-composites, *Ceramics International* **42** (6) (2016) 7533–7542. `doi:10.1016/j.ceramint.2016.01.160`.

[208] Y. ZHANG, G. XIAO, C. XU, M. YI, X. MENG, Anisotropic Fracture Toughness and Microstructure of Graphene-Reinforced TiC/Si$_3$N$_4$ Composite, *Journal of Ceramic Science and Technology* **7** (4) (2016) 323–328. `doi:10.4416/JCST2016-00032`.

[209] Y. ZHANG, G. XIAO, M. YI, C. XU, Effect of graphene orientation on microstructure and mechanical properties of silicon nitride ceramics, *Processing and Application of Ceramics* **12** (1) (2018) 27–35. `doi:10.2298/PAC1801027Z`.

[210] W. PIEKARCZYK, Material constants of AlN–graphene composites determined by ultrasound method, *Materials Research Express* **6** (10) (2019) 1050b5. `doi:10.1088/2053-1591/ab415e`.

[211] H. LE FERRAND, Modeling the effect of microstructure on elastic wave propagation in platelet-reinforced composites and ceramics, *Composite Structures* **224** (2019) 111105. `doi:10.1016/j.compstruct.2019.111105`.

[212] A. GÓMEZ-GÓMEZ, C. RAMÍREZ, J. LLORENTE, A. GARCIA, P. MORENO, H. REVERON, J. CHEVALIER, M. I. OSENDI, M. BELMONTE, P. MIRANZO, Improved crack resistance and thermal conductivity of cubic zirconia containing graphene nanoplatelets, *Journal of the European Ceramic Society* **40** (4) (2020) 1557–1565. `doi:10.1016/j.jeurceramsoc.2019.12.016`.

[213] X. ZHANG, N. ZHAO, C. HE, The superior mechanical and physical properties of nanocarbon reinforced bulk composites achieved by architecture design – A review, *Progress in Materials Science* **113** (2020) 100672. `doi:10.1016/j.pmatsci.2020.100672`.

[214] S. YAN, P. HE, D. JIA, X. DUAN, Z. YANG, S. WANG, Y. ZHOU, In-situ preparation of fully stabilized graphene/cubic-leucite composite through graphene oxide/geopolymer, *Materials & Design* **101** (2016) 301–308. `doi:10.1016/j.matdes.2016.03.139`.

[215] Y. SUN, C. ZHANG, B. LIU, Q. MENG, S. MA, W. DAI, Reduced Graphene Oxide Reinforced 7075 Al Matrix Composites: Powder Synthesis and Mechanical Properties, *Metals* **7** (2017) 499. `doi:10.3390/met7110499`.

[216] Z. YIN, J. YUAN, W. XU, K. LIU, S. YAN, Graphene nanosheets toughened TiB_2-based ceramic tool material by spark plasma sintering, *Ceramics International* **44** (8) (2018) 8977–8982. `doi:10.1016/j.ceramint.2018.02.098`.

[217] H. ZOU, Y. ZHANG, L. LIU, L. SHI, W. LI, The toughening mechanism and mechanical properties of graphene-reinforced zirconia ceramics by microwave sintering, *Advances in Applied Ceramics* **117** (7) (2018) 420–426. `doi:10.1080/17436753.2018.1477566`.

[218] J. KOPEČEK, K. BARTHA, R. MUŠÁLEK, Z. PALA, T. CHRÁSKA, P. BERAN, V. RYUKHTIN, P. STRUNZ, J. NOVÁKOVÁ, J. STRÁSKÝ, P. NOVÁK, O. HECZKO, M. LANDA, H. SEINER, M. JANEČEK, Structural characterization of semi-heusler/light metal composites prepared by spark plasma sintering, *Scientific Reports* **8** (2018) 11133. `doi:10.1038/s41598-018-29479-3`.

[219] R. A. PITTS, S. BARDIN, B. BAZYLEV, M. A. VAN DEN BERG, P. BUNTING, S. CARPENTIER-CHOUCHANA, J. W. COENEN, Y. CORRE, R. DEJARNAC, F. ESCOURBIAC, J. GASPAR, J. P. GUNN, T. HIRAI, S.-H. HONG, J. HORACEK, D. IGLESIAS, M. KOMM, K. KRIEGER, C. LASNIER, G. F. MATTHEWS, T. W. MORGAN, S. PANAYOTIS, S. PESTCHANYI, A. PODOLNIK, R. E. NYGREN, D. L. RUDAKOV, G. DE TEMMERMAN, P. VONDRACEK, J. G. WATKINS, Physics conclusions in support of ITER W divertor monoblock shaping, *Nuclear Materials and Energy* **12** (2017) 60–74. `doi:10.1016/j.nme.2017.03.005`.

[220] V. PHILLIPS, Tungsten as material for plasma-facing components in fusion devices, *Journal of Nuclear Materials* **415** (1) (2011) S2–S9. `doi:10.1016/j.jnucmat.2011.01.110`.

[221] O. EL-ATWANI, S. GONDERMAN, M. EFE, G. DE TEMMERMAN, T. MORGAN, K. BYSTROV, D. KLENOSKY, T. QIU, J. ALLAIN, Ultrafine tungsten as a plasma-facing component in fusion devices: effect of high flux, high fluence low energy helium irradiation, *Nuclear Fusion* **54** (8) (2014) 083013. `doi:10.1088/0029-5515/54/8/083013`.

[222] D. STORK, P. AGOSTINI, J. L. BOUTARD, D. BUCKTHORPE, E. DIEGELE, S. L. DUDAREV, C. ENGLISH, G. FEDERICI, M. R. GILBERT, S. GONZALEZ, A. IBARRA, C. LINSMEIER, A. LI PUMA, G. MARBACH, P. F. MORRIS, L. W. PACKER, B. RAJ, M. RIETH, M. Q. TRAN, D. J. WARD, S. J. ZINKLE, Developing structural, high-heat flux and plasma facing materials for a near-term DEMO fusion power plant: The EU assessment, *Journal of Nuclear Materials* **455** (1–3) (2014) 277–291. `doi:10.1016/j.jnucmat.2014.06.014`.

[223] Y. UEDA, J. COENEN, G. DE TEMMERMAN, R. DOERNER, J. LINKE, V. PHILLIPS, E. TSITRONE, Research status and issues of tungsten plasma facing materials for ITER and beyond, *Fusion Engineering and Design* **89** (7–8) (2014) 901–906. `doi:10.1016/j.fusengdes.2014.02.078`.

[224] F. CRESCENZI, H. GREUNER, S. ROCCELA, E. VISCA, J. H. YOU, ITER-like divertor target for DEMO: Design study and fabrication test, *Fusion Engineering and Design* **124** (2017) 432–436. `doi:10.1016/j.fusengdes.2017.02.014`.

[225] J. M. MISSIAEN, J. J. RAHARIJAONA, A. ANTONI, C. PASCAL, M. RICHOU, P. MAGAUD, Design of a W/steel functionally graded material for plasma facing components of DEMO, *Journal of Nuclear Materials* **416** (3) (2011) 262–269. `doi:10.1016/j.jnucmat.2011.05.054`.

[226] T. WEBER, M. STÜBER, S. ULRICH, R. VAßEN, W. W. BASUKI, J. LOHMILLER, W. SITTEL, J. AKTAA, Functionally graded vacuum plasma sprayed and magnetron sputtered tungsten/EUROFER97 interlayers for joints in helium-cooled divertor components, *Journal of Nuclear Materials* **436** (1–3) (2013) 29–39. `doi:10.1016/j.jnucmat.2013.01.286`.

[227] C. LINSMEIER, M. RIETH, J. AKTAA, T. CHIKADA, A. HOFFMANN, J. HOFFMANN, A. HOUBEN, H. KURISHITA, X. JIN, M. LI, A. LITNOVSKY, S. MATSUO, A. VON MÜLLER, V. NIKOLIC, T. PALACIOS, R. PIPPAN, D. QU, J. REISER, J. RIESCH, T. SHIKAMA, R. STIEGLITZ, T. WEBER, S. WURSTER, J.-H. YOU, Z. ZHOU, Development of advanced high heat flux and plasma-facing materials, *Nuclear Fusion* **57** (9) (2017) 092007. `doi:10.1088/1741-4326/aa6f71`.

[228] C. SURYANARAYANA, Mechanical alloying and milling, *Progress in Materials Science* **46** (1) (2001) 1–184. `doi:10.1016/S0079-6425(99)00010-9`.

[229] C. F. BURMEISTER, A. KWADE, Process engineering with planetary ball mills, *Chemical Society Reviews* **42** (2013) 7660–7667. `doi:10.1039/c3cs35455e`.

[230] O. N. SENKOV, M. DUBOIS, J. J. JONAS, Elastic moduli of titanium-hydrogen alloys in the temperature range 20 °C to 1100 °C, *Metallurgical and Materials Transactions A* **27** (1996) 3963–3970. `doi:10.1007/BF02595645`.

[231] H. CONRAD, Thermally activated deformation of α titanium below 0.4 T_M, *Canadian Journal of Physics* **45** (2) (1967) 581–590. `doi:10.1139/p67-050`.

[232] U. ZIEBART, H. SCHULTZ, Dislocation Relaxation Peaks In High Purity Tungsten Single Crystals, *J. Phys. Colloques* **44** (C9) (1983) 691–696. `doi:10.1051/jphyscol:19839104`.

[233] P. GUMBSCH, J. RIEDLE, A. HARTMAIER, H. F. FISCHMEISTER, Controlling Factors for the Brittle-to-Ductile Transition in Tungsten Single Crystals, *Science* **282** (5392) (1998) 1293–1295. `doi:10.1126/science.282.5392.1293`.

[234] P. GUMBSCH, Brittle fracture and the brittle-to-ductile transition of tungsten, *Journal of Nuclear Materials* 323 (2) (2003) 304–312. `doi:10.1016/j.jnucmat.2003.08.009`.

List of publications of the PhD candidate

Papers included in this thesis

[A] **M. KOLLER**, H. SEINER, M. LANDA, A. NIETO, A. AGARWAL, Anisotropic Elastic and Acoustic Properties of Bulk Graphene Nanoplatelets Consolidated by Spark Plasma Sintering. *Acta Physica Polonica A* **128** (4) (2015) 670–674. `doi:10.12693/APhysPolA.128.670`

[B] H. SEINER, C. RAMIREZ, **M. KOLLER**, P. SEDLÁK, M. LANDA, P. MIRANZO, M. BELMONTE, M. I. OSENDI, Elastic properties of silicon nitride ceramics reinforced with graphene nanofillers. *Materials and Design* **87** (2015) 675–680. `doi:10.1016/j.matdes.2015.08.044`

[C] **M. KOLLER**, T. CHRÁSKA, J. CINERT, O. HECZKO, J. KOPEČEK, M. LANDA, R. MUŠÁLEK, M. RAMEŠ, H. SEINER, J. STRÁSKÝ, M. JANEČEK, Mechanical and magnetic properties of semi-Heusler/light-metal composites consolidated by spark plasma sintering. *Materials and Design* **126** (2017) 351–357. `doi:10.1016/j.matdes.2017.04.028`

[D] **M. KOLLER**, A. KRUISOVÁ, R. MUŠÁLEK, J. MATĚJÍČEK, H. SEINER, M. LANDA, On the relation between microstructure and elastic constants of tungsten/ steel composites fabricated by spark plasma sintering. *Fusion Engineering and Design* **133** (2018) 51–58. `doi:10.1016/j.fusengdes.2018.05.056`

[E] **M. KOLLER**, M. VILÉMOVÁ, F. LUKÁČ, P. BERAN, J. ČÍŽEK, H. HADRABA, J. MATĚJÍČEK, J. VEVERKA, H. SEINER, An ultrasonic study of relaxation processes in pure and mechanically alloyed tungsten. *International Journal of Refractory Metals & Hard Materials* **90** (2020) 105233. `doi:10.1016/j.ijrmhm.2020.105233`

[F] **M. KOLLER**, A. KRUISOVÁ, H. SEINER, P. SEDLÁK, B. ROMÁN-MANSO, P. MIRANZO, M. BELMONTE, M. LANDA, Anisotropic elasticity of ceramic micro-scaffolds fabricated by robocasting. *Acta Physica Polonica A* **134** (2018) 799–803. `doi:10.12693/APhysPolA.134.799`

[G] T. GRABEC, **M. KOLLER**, P. SEDLÁK, A. KRUISOVÁ, B. ROMÁN-MANSO, M. BELMONTE, P. MIRANZO, H. SEINER, Frequency-dependent acoustic energy focusing in hexagonal ceramic micro-scaffolds. *Wave Motion* **92** (2020) 102417. `doi:10.1016/j.wavemoti.2019.102417`

[H] M. BELMONTE, **M. KOLLER**, J. J. MOYANO, H. SEINER, P. MIRANZO, M. I. OSENDI, J. GONZÁLEZ-JULIÁN, Multifunctional 3D-Printed Cellular MAX-Phase Architectures. *Advanced Materials Technologies* (2019) 1900375. `doi:10.1002/admt.201900375`

Other papers of the PhD candidate

[I]   H. SEINER, P. SEDLÁK, **M. KOLLER**, M. LANDA, C. RAMÍREZ, M. I. OSENDI, M. BELMONTE, Anisotropic elastic moduli and internal friction of graphene nanoplatelets/ silicon nitride composites. *Composites Science and Technology* **75** (2013) 93–97. `doi:10.1016/j.compscitech.2012.12.003`

[II]   **M. KOLLER**, P. SEDLÁK, H. SEINER, M. ŠEVČÍK, M. LANDA, J. STRÁSKÁ, M. JANEČEK, An ultrasonic internal friction study of ultrafine-grained AZ31 magnesium alloy. *Journal of Materials Science* **50** (2015) 808–818. `doi:10.1007/s10853-014-8641-1`

[III]   **M. KOLLER**, H. SEINER, P. SEDLÁK, J. KOTLAN, P. CTIBOR, R. MUŠÁLEK, M. LANDA, Application of laser-ultrasound for characterization of plasma-sprayed ceramics. *Defect and Diffusion Forum* **368** (2016) 69–72. `doi:10.4028/www.scientific.net/ddf.368.69`

[IV]   **M. KOLLER**, A. KRUISOVA, H. SEINER, P. SEDLAK, T. GRABEC, B. ROMAN-MANSO, P. MIRANZO, M. BELMONTE, M. LANDA, Ceramic phononic crystals with MHz-range frequency band gaps. *Proceedings of Meetings on Acoustics* **32** (2017) 045005. `doi:10.1121/2.0000690`

[V]   S. HEUER, J. MATĚJÍČEK, M. VILÉMOVÁ, **M. KOLLER**, K. ILLKOVA, J. VEVERKA, T. WEBER, G. PINTSUK, J. W. COENEN, C. LINSMEIER, Atmospheric plasma spraying of functionally graded steel/tungsten layers for the first wall of future fusion reactors. *Surface and Coatings Technology* **366** (2019) 170–178. `doi:10.1016/j.surfcoat.2019.03.017`

[VI]   J. CIZEK, M. VILEMOVA, F. LUKAC, **M. KOLLER**, J. KONDAS, R. SINGH, Cold Sprayed Tungsten Armor for Tokamak First Wall. *Coatings* (2019) **9**(12) 836. `doi:10.3390/coatings9120836`

[VII]   M. JANOVSKÁ, P. SEDLÁK, J. CIZEK, **M. KOLLER**, F. ŠIŠKA, H. SEINER, Characterization of bonding quality of a cold-sprayed deposit by laser resonant ultrasound spectroscopy. *Ultrasonics* **106** (2020) 106140. `doi:10.1016/j.ultras.2020.106140`

ORCID: `http://orcid.org/0000-0002-8213-4760`